Theoretical and Spectroscopic Studies of Energy and Charge Transport in Organic Semiconductors

Patrick Charles Tapping
B.Sc. (Hons), MRACI

A thesis submitted in fulfilment of the requirements for the degree of
Doctor of Philosophy

January 2017

Department of Chemistry
The University of Adelaide
North Terrace Campus
Adelaide, South Australia 5005

Supervisors:
A/Prof. Tak W. Kee
Dr. David M. Huang

Contents

Abstract

The performance of organic semiconductor devices is heavily dependent on the precise molecular-level arrangement and overall morphology of the functional layers. In organic photovoltaic applications, exciton mobility, fission/fusion or dissociation, as well as charge transport and separation are some of the morphology-dependent processes that are of interest for efficient device design. In this work a combination of experimental and computational techniques are used to elucidate the behaviour of excitons in conjugated polymer and small-molecule semiconductor systems. While there is an emphasis on photovoltaic applications, many concepts are generally applicable to other organic electronic applications such organic light emitting diodes and photodetectors.

In Chapter 3, a pump-push-probe transient absorption technique is used to observe high-energy “hot” excitons formed by photoexcitation of the conjugated polymer poly(3-hexylthiophene) (P3HT). The work demonstrates the ability to clearly isolate the transient signal of the hot exciton decay processes from the thermalised exciton population, where picosecond and sub-picosecond relaxation of hot excitons through torsional motion in the disordered polymer chain is observed. In addition, the push-induced dissociation of high-energy excitons into free charge carriers is able to be quantified and an upper bound on the exciton binding energy determined.

Spectroscopic experiments on P3HT are accompanied by a hybrid quantum-classical exciton hopping model in Chapter 4. Coarse-grained molecular dynamics are used to obtain realistic structures of P3HT free chains and nanofibre aggregates, to which a Frenkel–Holstein exciton model and Monte Carlo hopping simulation is applied. This novel approach captures exciton transport properties of polymer systems with a monomer-level of detail unachievable with continuum or lattice style models, but at a large scale infeasible with fully quantum calculations. Reasonable quantitative agreement with experimental observables is obtained, offering insight into the morphology-dependence of exciton transport in conjugated polymers. In particular, the observed tendency for exciton migration to the core of the polymer aggregate can explain the relatively poor performance of highly crystalline or nanofibre-based polymer solar cells, as well as the unusually high fluorescence yield of aqueous P3HT nanoparticles.

The effect of disorder in small molecule semiconductor films is investigated in Chapter 5 in the context of singlet exciton fission and triplet fusion under the influence of applied magnetic fields. A model is presented that extends the historical theory of molecular spin interactions in crystalline materials and corrects the current understanding in the literature regarding such disordered solid-phase systems. The possibility of using the fluorescence response to magnetic fields to probe the morphology and degree disorder in the films is demonstrated. Extending the model to solution-phase behaviour is then discussed in Chapter 6, where the potential of improving the light-harvesting ability of solar cells through a molecular triplet–triplet annihilation upconversion process is considered. Molecular dynamics simulations are used to obtain physical parameters and collision geometry of the emitter molecules in solution. The complications of applying a static model of triplet fusion to the dynamic solution-phase behaviour are elucidated and the potential of synthesising an ideal upconversion emitter molecule is discussed.

Declaration

I certify that this work contains no material which has been accepted for the award of any other degree or diploma in my name in any university or other tertiary institution and, to the best of my knowledge and belief, contains no material previously published or written by another person, except where due reference has been made in the text. In addition, I certify that no part of this work will, in the future, be used in a submission in my name for any other degree or diploma in any university or other tertiary institution without the prior approval of the University of Adelaide and where applicable, any partner institution responsible for the joint award of this degree.

I give consent to this copy of my thesis when deposited in the University Library, being made available for loan and photocopying, subject to the provisions of the Copyright Act 1968.

The author acknowledges that copyright of published works contained within this thesis resides with the copyright holder(s) of those works.

I also give permission for the digital version of my thesis to be made available on the web, via the University's digital research repository, the Library Search and also through web search engines, unless permission has been granted by the University to restrict access for a period of time.

Patrick Charles Tapping
January 2017

Acknowledgements

Firstly, this work would not be possible without the assistance of my supervisors Assoc. Prof. Tak W. Kee and Dr David M. Huang. I am incredibly grateful for their time, support and advice as well as the many opportunities they have given me to travel and expand my experience and knowledge.

Many past and current members of the Kee and Huang research groups also deserve thanks. Scott Clafton, Mandy Hei Man Lueng and Takaaki Harada in particular helped introduce me to life in research. Many other deserving people will invariably be left out of any list, so a general thanks goes to everyone who has provided me with advice or assistance over the last few years.

To the other co-author on my publications, Kyra Schwarz, it has been a pleasure to work with you.

The technical staff members at the University of Adelaide, Peter Apoefis and Matthew Bull have been invaluable when it comes to building, testing or repairing all sorts of mechanical and electronic equipment and generally deserve more recognition than these few words.

Much of the work performed during research never makes it in to a finished product. My time studying for this degree and this thesis is no exception, but I do not consider that work wasted. Thanks goes to those who I have worked with on all the projects that did not make it into this document, Drew Evans and Rick Fabretto to name just a few. Particular thanks to Bernd Fischer and Korbinian Kalternecker for hosting me in their lab during my time in Germany and introducing me to terahertz spectroscopy.

Finally, my parents Jeffrey and Carmel have been great inspiration and have encouraged scientific endeavour for literally as long as I can remember. Thanks to you both for your eternal support and encouragement.

Publications

This thesis is based on the following publications that detail some of the research undertaken during the period of candidature:

1. Tapping, P. C.; Kee, T. W. Optical Pumping of Poly(3-hexylthiophene) Singlet Excitons Induces Charge Carrier Generation. *J. Phys. Chem. Lett.* **2014**, *5*, 1040–1047
2. Tapping, P. C.; Clafton, S. N.; Schwarz, K. N.; Kee, T. W.; Huang, D. M. Molecular–Level Details of Morphology–Dependent Exciton Migration in Poly(3-hexylthiophene) Nanostructures. *J. Phys. Chem. C* **2015**, *119*, 7047–7059
3. Tapping, P. C.; Huang, D. M. Comment on "Magnetic Field Effects on Singlet Fission and Fluorescence Decay Dynamics in Amorphous Rubrene". *J. Phys. Chem. C* **2016**, *120*, 25151–25157.
4. Tapping, P. C.; Blacket, S.; Ackling, S.; Huang, D. M. Molecular Understanding of Photochemical Upconversion for Efficient Solar Cells. **2016**. Manuscript in preparation.

Additionally, contributions have been made to the following publications:

5. Yang, J.; Wen, X.; Xia, H.; Sheng, R.; Ma, Q.; Kim, J.; Tapping, P. C.; Harada, T.; Kee, T. W.; Huang, F.; Cheng, Y.-B.; Green, M.; Ho-Baillie, A.; Huang, S.; Shrestha, S.; Patterson, R.; Conibeer, G. Exploring Hot Carrier Thermalization in Perovskites by Ultrafast Optical Characterization. *Nat. Commun.* **2017**. Accepted for publication. DOI: 10.1038/ncomms14120
6. Cao, W.; Lin, Y.; Patterson, R.; Wen, X.; Tapping, P. C.; Kee, T. W.; Veetil, B. P.; Zhang, P.; Zhang, Z.; Zhang, Q.; Reece, P.; Bremner, S.; Shrestha, S.; Conibeer, G. Difference in Hot Carrier Cooling Rate between Langmuir–Blodgett and Drop Cast PbS QDs Films Due to Strong Electron–Phonon Coupling. **2017**. Manuscript submitted for publication.

Abbreviations

BBO β-barium borate

DET Dexter excitation transfer

DoS density of states

EET excitonic energy transfer

ESA excited-state absorption

FET field effect transistor

FRET Förster resonance energy transfer

FWHM full width half maximum

GSB ground-state bleach

HOMO highest occupied molecular orbital

IC internal conversion

ISC inter-system crossing

LCD liquid crystal display

LED light emitting diode

LEES local exciton excited state

LEGS localised exciton ground state

LJ Lennard-Jones

LUMO lowest unoccupied molecular orbital

MD molecular dynamics

MEH-PPV poly[2-methoxy-5-(2-ethylhexyloxy)-1,4-phenylenevinylene]

MSD mean-squared displacement

NIR near infra-red

OD optical density

OLED organic light emitting diode

OPA optical parametric amplifier

OPLS optimised potentials for liquid simulations

OPLS-AA optimised potentials for liquid simulations – all atoms

P3HT poly(3-hexylthiophene)

P3MT poly(3-methylthiophene)

PCBM phenyl-C_{61}-butyric acid methyl ester

PEDOT poly(3,4-ethylenedioxythiophene)

PPV poly(phenylenevinylene)

PSS poly(4-vinylbenzenesulfonic acid)

QEES quasi-extended exciton state

RDF radial distribution function

SE stimulated emission

SFG sum frequency generation

TCSPC time correlated single photon counting

TDC transition density cube

TDM transition dipole moment

THF tetrahydrofuran

TTA triplet–triplet annihilation

TTA-UC triplet–triplet annihilation upconversion

ZINDO/S Zerner's intermediate neglect of differential overlap - spectra

List of Figures

List of Tables

CHAPTER 1

Introduction

1.1 Introduction

In little over a century, the electronics industry has completely changed our way of life. Landmark inventions such as the incandescent lamp, valve tube, transistor, integrated circuit or light emitting diode (LED) could each be seen as revolutionary devices developed in isolation, but in reality, technology progresses through a combination of incremental improvements in theory, manufacturing techniques, materials and marketing.

To date, modern electronics has been built on the back of metals such as copper, aluminium and gold; and semiconductors based on inorganic materials like silicon, germanium or gallium arsenide. While these are not in danger of becoming obsolete any time in the near future, a new breed of electronics is emerging. Organic electronics leverage the power of chemistry to synthesise new materials with specifically engineered physical and electronic properties. Organic devices promise benefits such as mechanical flexibility and simplified manufacturing techniques using low-cost materials. Some organic electronic devices are already in use today; the most visible example being organic light emitting diode (OLED) displays in consumer products like mobile phones and televisions. Further large-scale commercial applications of organic electronics still require improvements in efficiency, device longevity and ultimately cost. Achieving these goals requires a fundamental understanding of the energy and charge transport behaviour at the molecular level.

One of the difficulties in the design of organic semiconductor devices is that the performance is heavily dependent on the microstructure of the semiconductor active layer. The relatively disordered, heterogeneous nature of organic semiconductor solids means that knowing the chemical structure of the constituent molecules gives little indication of the actual device performance. As the electronic properties depend on both quantum effects and large scale morphology, a fundamental understanding is crucial but challenging to achieve.

This work attempts to address how structure and morphology such as molecular packing and orientation affect the electronic properties of organic semiconductors, with a focus on energy transport processes. A better understanding of these relationships will ultimately assist the design of better, more efficient devices.

1.2 Organic Semiconductors

The categorisation of a material as an electrical conductor, semiconductor or insulator is determined by the density of states (DoS) at the material's Fermi level.[7] Conductors such as metals have a high DoS at their Fermi level, thus electrons and electron holes are free to move through the material by migrating through the multitude of partially occupied states. Insulator and semiconductor materials are both characterised by a zero density of states at the Fermi level; the Fermi level lies in the band-gap between the valence and conduction bands. If the size of the band-gap is large, all electrons are trapped in the filled valence band, thus there can be no net movement of charge and the material is considered an electrical insulator. If the band-gap is small, electrons may cross from the valence to the conduction band due to thermal or optical excitation. The resulting partially-occupied bands allow electrons and holes to become mobile. In this situation the material is considered a semiconductor.

In small organic molecules, molecular orbital theory defines discrete electronic energy levels and occupancies.[8] Discussion of a molecule's electronic properties revolves around the individual highest occupied molecular orbital (HOMO) and lowest unoccupied molecular orbital (LUMO) energies rather than broad valence and conduction bands. If, however, many molecules are packed together such as in a molecular crystal, the array of HOMO and LUMO energy levels start to merge. Although in most cases there remains somewhat distinct, localised states as opposed to the continuous band structure of a traditional inorganic semiconductor, this array of HOMO and LUMO states are often referred to as the valence and conduction bands. In this sense, most organic materials have a large band-gap and are considered electrical insulators. Extensive conjugation in a molecule allows for a delocalised π-electron system and acts to lower the HOMO–LUMO gap. As such, organic semiconductors are almost exclusively molecules with highly conjugated or polyaromatic systems.[9–11]

In traditional inorganic semiconductor materials, the addition of impurities can manipulate the DoS around the valence and conduction bands, and therefore control the band gap.[12] Organic materials can be doped in a similar fashion.[13,14] Taken to the extreme, the crystallisation of charge-transfer complexes can lead to conductive organic solids.[15]

One major benefit of organic semiconductor materials is their synthetic origin, thus there is a large variety of chemical modifications available during production that can manipulate their physical and electronic properties. Tuning of the valence or conduction band energy level,[16,17] charge separation ability,[18,19] physical strength and flexibility[20,21] and solution processability[22,23] are just some of the characteristics that can be targeted by structural modification of the organic semiconductor molecules.

1.2.1 Applications

Organic semiconductors can potentially be used in any application where conventional inorganic semiconductors are already in use. Diodes and transistors,[24–26] photodetectors,[27,28] OLEDs[29–32] and photovoltaics[33–35] have all been demonstrated. Additionally, organic materials offer interesting new properties, enabling new use case scenarios. In particular, mechanical flexibility is seen as a significant benefit, allowing electronic devices to be built into paper, fabrics or applied to surfaces.[36–39] The ability to manufacture transparent devices is also a significant opportunity for display and lighting applications,[40,41] where the panel is transparent when not illuminated. Semitransparent photovoltaic cells could be used in places such as window tinting, where traditional solar panels would be unsuitable.[42,43]

Currently, the most visible use of organic semiconductors are OLED displays used in small electronic devices, mobile phones and televisions. As opposed to LCDs, each pixel generates its own light. Since full back-lighting of the LCD panel is not required, power consumption is lowered and contrast is improved as there is no light leakage

Figure 1.1: An OLED display on a mobile phone.* Reduced power consumption and increased contrast are two significant advantages over liquid crystal displays (LCDs) in this application. The curved edges on this model demonstrate the flexible nature of the display panel.

through what should be a black LCD pixel. The mechanical flexibility of OLEDs are sometimes put to use with curved screens on televisions and phones, as demonstrated in Figure 1.1. There is, however, still room for improvement in OLED technology. Power efficiency improvements are always desirable, particularly for battery powered devices. Limited lifespan of the emitter molecules can also cause “burn in”, where pixels that are more often illuminated degrade, leaving a persistent image on the display.[44]

Organic solar cells are in effect the opposite of OLEDs, instead converting incident light into electricity. Despite organic photovoltaics being the subject of intense research over the last fifteen years or more,[33,45] widespread commercial use is yet to occur.

Figure 1.2: A commercially available organic solar cell† manufactured through a roll-to-roll printing method.

Organic solar cells are available for purchase, such as those shown in Figure 1.2, but currently the cost-to-power ratio does not make them economically competitive with other technologies. Reducing the cost of manufacturing has been a clear goal, and one that organic devices are particularly suited. The raw materials do not include rare and expensive metals nor require the energetically-expensive high-temperature refinement of silicon wafers. Soluble organic semiconductors allow fast and automated production techniques such as “roll-to-roll” printing.[46–48] Careful design of the light-harvesting donor and electron-acceptor molecules can induce self-assembly of the active

---

[*] Samsung Galaxy S6 Edge `http://www.samsung.com/au/galaxy-s6/`

[†] InfinityPV Foil `http://infinitypv.com/infinitypro/opv/foil`

layer structure during the printing process, with the bulk-heterojunction motif being the most prominent example.[49–54]

The flip-side to the cost-to-power ratio is device efficiency. Efficiency of organic devices has been reported at above 10%, on par with amorphous silicon, but around half the efficiency of the crystalline silicon cells in common use today.[55] Note that while these numbers may seem poor, the Shockley–Queisser limit defines an upper efficiency bound for a single-junction solar cell of around 32% under solar irradiation;[56] nevertheless there is clearly room for improvement.

There are many sources of loss in an organic photovoltaic cell. Identifying and overcoming them requires an intricate and molecular-level understanding of the fundamental processes involved. Ultimately, the recombination of photogenerated excitons must be minimised in favour of charge-carrier generation,[57–59] which relies on an optimum balance of energy levels of the donor and acceptor materials.[18,60] The nanoscale morphology of the active layer is also highly influential in this regard, and must additionally promote effective charge-carrier transport to the electrodes.[61–63] Relatively minor changes in the the physical construction of the device's layers or electrodes can also make a significant impact on the performance of the device.[42,64] Novel approaches to enhancing solar cell efficiency include techniques such as photon downconversion or upconversion to better match the solar spectrum to the semiconductor band gap, potentially overcoming the Shockley–Queisser limit.[65–67] Some theoretical and practical aspects of these techniques are considered in Chapters 5 and 6.

Unfortunately, any single improvement to an organic solar cell design does not occur in isolation, and there is a delicate balance to ensure an optimal device efficiency. The projects presented in this thesis each have a focus on addressing solar cell efficiency in some way, though the theory is often generally applicable to other optoelectronic applications.

1.2.2 Conjugated Polymers

Conjugated polymers, sometimes referred to as conducting polymers, are characterised by a continuous series of conjugated bonds along the entire length of the polymer backbone. Here, conjugation refers to a pattern of alternating single and double or triple bonds through the molecular structure. Individual monomer units often have aromatic nature, but this is not a requirement. Structures of some common conjugated polymers are shown in Figure 1.3. The simplest example is polyethyne (**1**), first formed by the polymerisation of ethyne (acetylene) in the mid twentieth century.[68] Further development on the family of linearly conjugated polymers and the recognition of their interesting electrical characteristics reached a renaissance in the 1970s,[69–71] with the work by Alan Heeger, Alan MacDiarmid and Hideki Shirakawa ultimately being awarded with a Nobel Prize in Chemistry in the year 2000 for the discovery and development of conductive polymers.[72]

Polyethyne itself is not a particularly useful due to its low solubility and high reactivity. Alternate monomer units in the conjugated backbone, plus chemical substitutions along the chain can be made to manipulate the physical and electronic properties of the polymer.[73–76] Substituted polythiophenes and poly(phenylenevinylene)s (PPVs) are typical examples. P3HT (**3**) has become somewhat of the "fruit fly" of polymer solar cell research, as it is stable, soluble and well characterised.[77] Although greater efficiencies have been achieved with lower band-gap polymers,[78,79] simple bulk-heterojunction

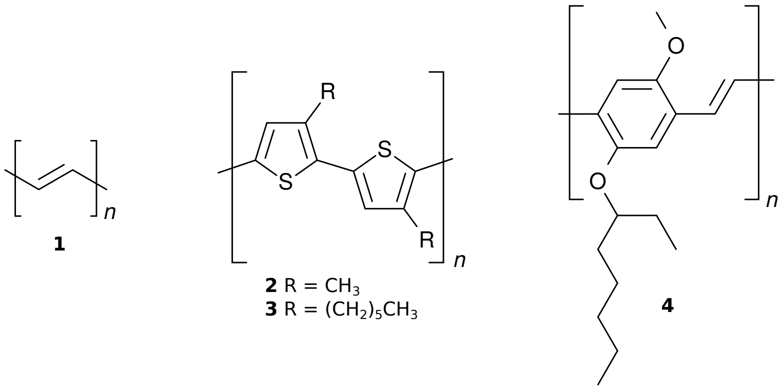

Figure 1.3: Structures of the conjugated polymers **1** polyethyne, **2** poly(3-methylthiophene) (P3MT), **3** poly(3-hexylthiophene) (P3HT) and **4** poly[2-methoxy-5-(2-ethylhexyloxy)-1,4-phenylenevinylene] (MEH-PPV). The structures shown in **2** and **3** are the regioregular variants, with strict head-to-tail type bonding of the monomer units.

designs readily achieve efficiencies of 5%.[62] MEH-PPV (**4**) is a common alkyloxy substituted PPV, popular due to its early success in the production of OLEDs.[80,81]

The physical properties of conjugated polymers differ somewhat to other polymers due to the increased stiffness afforded by the π bonding system. These properties are readily modified by the polymer tacticity or character of the sidechain substitutions. For substituted polythiophenes like P3HT, pure head-to-tail (regioregular) links as shown in **3** create a polymer with significantly different physical and electronic properties to random linkages (regiorandom), as steric crowding of the hexyl sidechains will restrict planarisation of the thiophene rings. While regioregular P3HT is able to form semicrystalline structures in the solid phase, regiorandom P3HT remains amorphous.[82–85]

The properties of conjugated polymers are also heavily influenced by morphology, created by the local ordering of the chains. Under appropriate conditions, conjugated polymers will readily self-assemble into complex structures such as nanoparticles or nanofibres which display radically different physical and optical characteristics compared to amorphous or solution phase structures.[86–93] Simplistically, twists and bends in the polymer backbone act to reduce the orbital overlap of the conjugated π system, effectively creating conjugation breaks and dividing the chain into spectroscopic segments. These segments, termed chromophores, are the localised sites responsible for the light absorption and emission in the polymer system. The precise definition of a chromophore requires a quantum mechanical description of the exciton delocalisation over the disordered polymer chain.[94–96] Chapter 4 in particular investigates the role of polymer morphology on the mobility of excitons in the context of charge generation in polymer-based solar cells.

Conjugated polymers are not intrinsically conducting, but doping can effectively create organic metals. In its pure solid state, the poly(3,4-ethylenedioxythiophene) (PEDOT) (**5**, Figure 1.4) is highly insoluble, but when combined with the anionic polymer poly(4-vinylbenzenesulfonic acid) (PSS) (**6**) it becomes heavily p-doped, creating a conductive and water-dispersible polymer.[97] This combination is commonly used as a flexible and transparent conducting or hole-transport layer in optoelectronic devices, though other anions such as chloride or tosylate are also common dopants.[98–102]

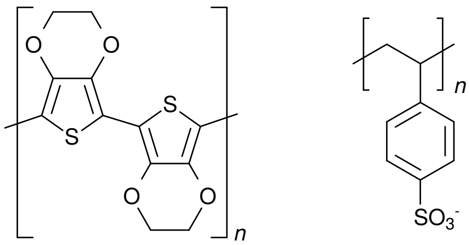

5 **6**

Figure 1.4: Structures of the conjugated polymer **5** PEDOT and **6** the commonly used (non-conjugated) polymer dopant PSS.

1.2.3 Small Molecule Semiconductors

The first work on small molecule organic semiconductors was on crystals of polyaromatic molecules such as anthracene and tetracene, where their interesting optical properties made them a target for much research.[103–108]

The first solar cells based on an organic light harvesting material were inspired by photosynthesis and simply used chlorophyll sandwiched between metal electrodes.[109] Despite the low efficiency, this milestone demonstrated the potential applications of organic electronic devices. The introduction of dedicated electron-acceptor layers and the stacking of multiple semiconductor junctions provided incremental improvements.[110] The discovery and use of fullerenes as highly efficient electron acceptor materials, and the blending of the donor and acceptor materials (the bulk heterojunction) had shown success with conjugated polymer-based solar cells and were also demonstrated in small molecule based devices.[111,112] More recently, polymer-based solar cells tend to be favoured over small molecule devices although oligomer-based devices, straddling the border between the two extremes, have also demonstrated good success.[113] Oligomer type molecules that integrate both the electron donor and acceptor regions into their structure are also the subject of recent research to precisely manipulate charge separation and the self-assembly of the heterojunction microstructure.[19,114,115]

Perhaps the most significant breakthrough for the application of small molecule semiconductors was in the construction of the first OLED,[116] where they still find widespread use today. Early OLEDs used fluorescent molecules which rely on the generation and emission from singlet excitons. This intrinsically limits efficiency to below 25% due to spin statistics. Dramatically improved efficiency was obtained by taking advantage of emission from the triplet state through the incorporation of phosphorescent molecules in a p-i-n junction type construction.[117–119] More recently, molecules with a small energy gap between the singlet and triplet levels have been shown to reach 100% internal quantum efficiency through thermally activated delayed fluorescence.[120–124]

Because impurities in organic crystals act as trap sites and restrict charge carrier mobility,[125] it has only been relatively recently that high efficiency field effect transistor (FET) devices have been constructed from single crystals of small molecules such as rubrene and tetracene.[126–130] Construction of flexible and transparent FETs are of interest for use in switching OLED pixels in an active matrix display.[26,31]

The ability to synthesise and modify organic molecules is a distinct advantage over inorganic semiconductors, allowing the physical and electronic properties to be readily modified. Rubrene (**7**, Figure 1.5) is a substituted tetracene, which exhibits enhanced solubility and charge carrier mobility.[131,132] Substituted perylene (**8**) and fullerene derivatives such as PCBM (**9**) find use as electron acceptor materials in organic

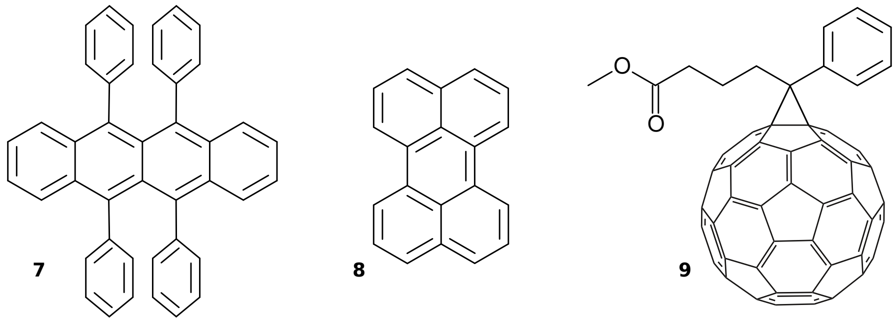

Figure 1.5: Structures of **7** rubrene, **8** perylene and **9** phenyl-C_{61}-butyric acid methyl ester (PCBM).

solar cells.[18,133–135]

In Chapter 5, the quantum mechanical spin considerations in the fission of singlet excitons to a triplet-pair in amorphous rubrene (**7**) films is discussed. In Chapter 6 both rubrene and perylene (**8**) are studied in the context of emitter molecules in a photochemical upconversion device.

1.3 Energy and Charge Transport

1.3.1 Optical Processes

The interaction of light with an optically active molecule is fundamental to the operation of an optoelectronic device like a solar cell or OLED. Small molecule organic semiconductors or conjugated polymer chromophores act no differently to any other molecule in this regard: photon absorption or emission is directly associated with an electronic transition within the molecule. The most common optical processes are summarised in Figure 1.6. Photon absorption usually occurs *via* the HOMO to LUMO

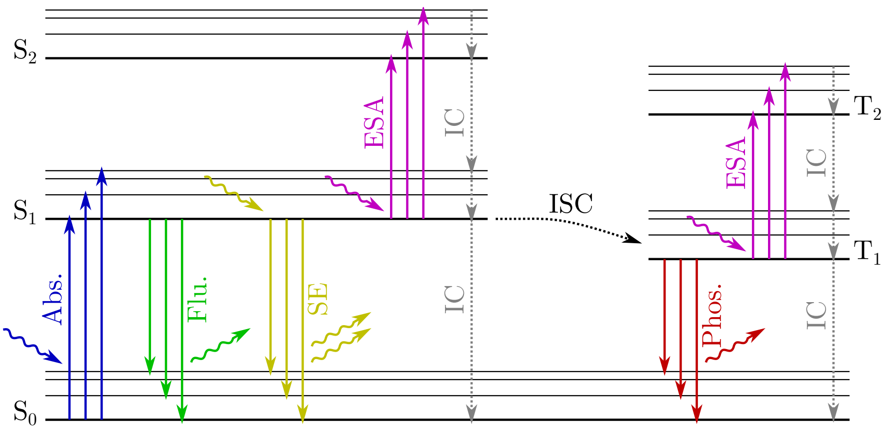

Figure 1.6: Some optical processes available to a chromophore include ground-state absorption (Abs.) of a photon to produce a singlet excited state, radiative decay by fluorescence (Flu.) from the singlet excited state, stimulated emission (SE) from the singlet excited state, excited-state absorption (ESA) by the singlet excited state to produce a high-energy singlet state, inter-system crossing (ISC) from the singlet to triplet manifold, radiative decay by phosphorescence (Phos.) from the excited triplet state, and various non-radiative internal conversion (IC) decay processes.

transition, promoting the molecule from its ground S_0 state to produce the first excited singlet state S_1. In an organic semiconductor material, the individual variations in each chromophore's HOMO and LUMO energies creates the band structure, so this becomes the equivalent of the valence to conduction band transition. From the excited S_1 state, a spontaneous radiative transition back to the ground state produces fluorescence. The radiative S_1 to S_0 transition may also be induced by an incident photon of equivalent energy, this process of stimulated emission (SE) effectively "clones" the incoming photon. Inter-system crossing (ISC) from the singlet to triplet manifold requires the spin flip of an electron, usually giving the first excited triplet state T_1. As the T_1 to S_0 transition is spin-forbidden, lifetimes of the excited triplet state are generally much longer than that of the singlet excited state. Radiative decay from the T_1, although spin-forbidden, does occur slowly and is termed phosphorescence. Absorption to induce transitions other than from HOMO to LUMO are known as excited-state absorption (ESA) and will generate higher-energy states such as S_n, T_n. Non-radiative decay is possible through a number of means, known collectively as internal conversion (IC) processes.

1.3.2 Excitons, Polarons, Charge Carriers

In an organic semiconductor material, absorption of a photon to induce the HOMO to LUMO transition as shown in Figure 1.6 is analogous to promoting an electron to the semiconductor conduction band, leaving a positively charged electron hole in the valance band. The low relative permittivity of the material means that Coulombic attraction between the electron and hole is strong, thus they are not free to migrate independently through the material and are instead bound together within some finite distance.[136,137] This bound excited state is termed an exciton, and can be described quantum mechanically as the electron and hole acting together as a virtual particle.[104,138–140] If there is a strong coupling between the motion of the exciton and the nuclei of material lattice, the exciton can become localised (sometimes referred to as self-trapping).[141,142] In conjugated polymers, conformational disorder and chemical defects along the polymer backbone act to localise the exciton onto short conjugated segments, often referred to as chromophores.[143–145] The binding energy of the exciton is on the order of 1 eV or less,[146] and so may be dissociated into its constituent electron and hole by means such as input of excess photon energy,[1,147] or at the interface with another material like PCBM (**9**, Figure 1.5) that can act as an electron acceptor.[134,148] Exciton dissociation is at the heart of charge generation in organic solar cells. In an LED, the opposite process occurs; electrons and holes are injected into the semiconductor to form excitons, which then radiatively recombine to give the emission of photons.

In a semiconductor, the separated electron or hole are the fundamental carriers of negative or positive charge, respectively. Due to the interactions between the localised charge and the nuclei, distortion of the material lattice can occur and act to stabilise the charge carrier. The distortion is coupled to the vibrations (phonon modes) of the lattice as the charge carrier moves through the material. The coupled charge carrier and lattice distortion is known as a polaron.[149–153] The charged nature of polarons distinguishes them from the excitons. They can be neutralised by encounter with a free charge of opposite polarity, and the more significant distortion on the lattice gives them a greater effective mass and thus slower speed of migration through the material.

1.3.3 Energy Transfer Mechanisms

1.3.3.1 Dipolar Coupling Mechanism

In conjugated polymers, exciton transport occurs through a process referred to as excitonic energy transfer (EET).[154] When chromophores are weakly coupled, as is generally the case, this occurs through discrete "hopping" events between chromophores. This is a dipolar coupling mechanism governed by Förster resonance energy transfer (FRET).[155] The rate of exciton exchange between the donor and acceptor is therefore dependent on the separation distance, orientation and spectral overlap the chromophores.

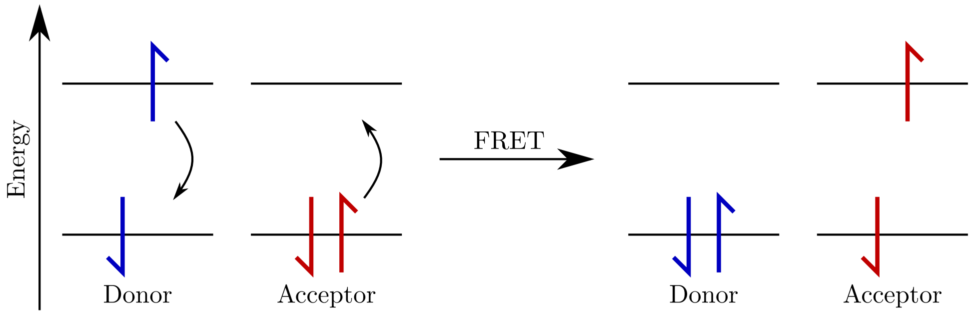

Figure 1.7: FRET transfers energy between a donor and acceptor chromophores *via* a non-radiative dipole coupling mechanism. The transitions on the individual donor and acceptor molecules must be spin-allowed, thus FRET usually occurs between singlet states as shown here.

As FRET is a resonance energy transfer process, no electron exchange takes place, as shown in Figure 1.7. This means that while the donor and acceptor sites must be relatively close in space (within around 10 nm), they do not need to be in intimate contact. The electronic transitions of both the donor and acceptor need to be spin allowed, however, so the hopping mechanism is generally restricted to singlet excitons.[156] EET can however also be facilitated by other mechanisms, such as electron exchange described in Section 1.3.3.2, and quantum-coherent energy transfer has been shown to occur in pure MEH-PPV polymer systems and P3HT/PCBM blends.[157–159]

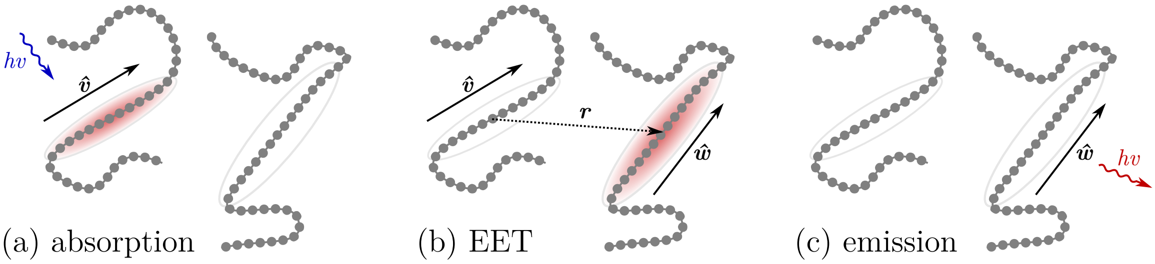

(a) absorption (b) EET (c) emission

Figure 1.8: Example of energetic processes that may occur in a conjugated polymer system. Light is absorbed (a), exciting a chromophore with dipole moment in the direction shown by $\hat{\boldsymbol{v}}$. EET occurs (b), with the generated exciton hopping to a new, lower-energy chromophore site with dipole moment direction shown by $\hat{\boldsymbol{w}}$. The vector $\boldsymbol{r}$ is the separation between the centres of the donor and acceptor chromophore sites. Emission occurs (c) by radiative recombination of the exciton. The photon emitted by fluorescence is lower in energy and exhibits a rotated polarisation relative to the absorbed photon.

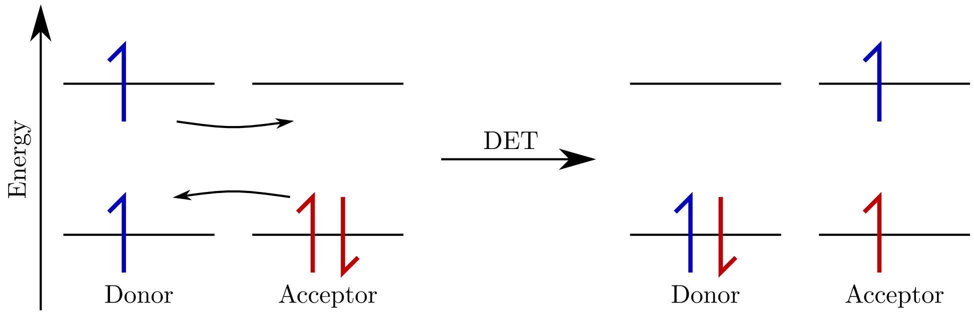

Figure 1.9: DET is an electron exchange mechanism, therefore requiring the donor and acceptor to be within ~10 Å to allow sufficient orbital overlap. The total spin of the donor-acceptor pair must be conserved during the process; here the exchange occurs between a triplet state donor and singlet state acceptor.

Exciton transfer in a conjugated polymer is illustrated in Figure 1.8. In this schematic, an incident photon is absorbed to produce a singlet exciton. The exciton in initially localised on the chromophore with transition dipole moment in the direction shown by the unit vector $\hat{\boldsymbol{v}}$. A nearby chromophore has a transition dipole moment in the direction $\hat{\boldsymbol{w}}$ and the centre-of-mass separation between the two chromophores is shown by the vector $\boldsymbol{r}$. EET occurs, transferring the exciton energy to the distant chromophore. Subsequently, further hopping events may occur to other chromophores, the exciton may be dissociated at a heterojunction interface or, as shown, the exciton may radiatively recombine to emit a photon.

Exciton migration is generally an energetically downhill process,[160] thus the emitted photon will be of longer wavelength than that absorbed; this is one reason why conjugated polymers generally show a large Stokes shift.[69] The disordered alignment of the chromophores also results in any polarisation of the excitation light being lost in the fluorescence.[161] Both these phenomena occur over a finite time period and are able to be observed using time-resolved fluorescence or fluorescence anisotropy experiments, as described in Sections 2.1.2 and 2.1.2.1.

The scheme shown in Figure 1.8 is highly simplified. It does not take into consideration factors such as the relative energy of the chromophore sites (spectral overlap), excited state conformational changes or delocalisation of the exciton over the disordered polymer chain. For example, the scheme assumes the point dipole approximation where the orientational component to the dipolar coupling is simply given by $\kappa = \hat{\boldsymbol{v}} \cdot \hat{\boldsymbol{w}} - 3(\hat{\boldsymbol{v}} \cdot \hat{\boldsymbol{r}})(\hat{\boldsymbol{w}} \cdot \hat{\boldsymbol{r}})$. Improved Förster-type models have been developed that more accurately reflect the quantum mechanical nature of the exciton and complex chromophore geometry.[161–164] Chapter 4 discusses many of these aspects during the implementation of a detailed exciton hopping simulation method.

1.3.3.2 Electron Exchange Mechanisms

If two molecules are in very close proximity so that there is sufficient orbital overlap, electron exchange may occur. This requires separation distances on the order of the molecules' van der Waals radii, typically 10 Å or less. The transfer of an excited state through this mechanism is termed Dexter excitation transfer (DET),[165] as illustrated in Figure 1.9. As there is electron exchange between the donor and acceptor, there is no spin restrictions on the individual molecules, though the combined total spin of the donor plus acceptor must be constant.[156] For example, in Figure 1.9 the donor is an excited triplet state and the acceptor in its singlet ground state. Following the DET process, the acceptor is now in the excited triplet state and the donor has returned to the singlet ground state. For this reason, DET type exchange processes are often encountered in interactions of triplet states.

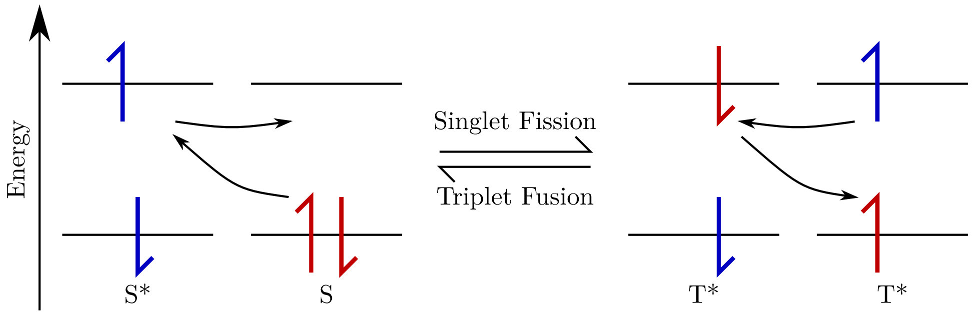

Figure 1.10: Fission of a singlet exciton into a pair of triplets. The reverse process is the fusion of two triplet excitons into a singlet. Like DET, the total spin of the system is conserved.

Singlet fission and triplet fusion can be considered special cases of electron exchange. The processes are shown in Figure 1.10, where the forward reaction is singlet fission and the reverse being triplet fusion.[166] Like DET, the total spin of the system is conserved, the difference being that the excitation energy is split between the two sites during the singlet fission process. Both singlet fission and triplet fusion are of interest in enhancing the efficiency of optoelectronic devices. In photovoltaic applications, splitting a singlet exciton generated from absorption of a high-energy photon into a pair of triplet excitons can, in principle, increase the quantum efficiency through generation of two electrons for each incident photon.[67,167] Similarly, it is possible to harvest the otherwise wasted photons with energy below the band gap of the semiconductor through a triplet fusion process, called triplet–triplet annihilation upconversion (TTA-UC).[168–171] Modern OLED technology already makes use of the triplet state for enhancement of efficiency, where spin statistics would otherwise limit generation of the fluorescent singlet state from uncorrelated electron–hole pairs to 25%.[172–175] If analogous techniques can be applied in photovoltaics, singlet fission into a pair of triplets has the potential to further improve performance.[176]

Chapters 5 and 6 address singlet-fission and triplet–triplet annihilation processes in the context of theoretically increasing solar cell efficiency beyond the Shockley–Queisser limit.

1.4 Morphology and Electronic Properties

Morphology refers to the spatial arrangement of the organic semiconductor molecules or polymer conjugated chains over a range of length scales. At the smallest level, this can mean the orientation of a pair of adjacent molecules or polymer chromophores; at the largest this describes the construction of a device on the micrometre scale. At the intermediate level, local crystal defects or sizes of amorphous versus semicrystalline domains are of interest.

A striking example of the effect of morphology is during the formation of conjugated polymer nanoparticles or nanofibre structures. In a good solvent, the polymer chains

Figure 1.11: P3HT in a series of mixtures of good (chloroform) and marginal (anisole) solvents showing a gradient between well-solvated free chains and nanofibre aggregate formation. Each solution has a polymer concentration of $0.5\,\mathrm{g\,L^{-1}}$. The sample on the left is 75% chloroform by volume, ranging down to 55% on the right. The optical properties of the polymer change dramatically with the different arrangements of the chains.

are isolated with an extended conformation, but in a poor solvent the polymer chains can self-assemble into aggregates with measurably different electronic properties.[87] The aggregation process is easily observable as a dramatic colour change of the polymer solution, as shown in Figure 1.11. These solutions were produced with a mixed solvent method,[92,177] in this case using P3HT in a blend of a good solvent (chloroform) and a marginal solvent (anisole) at room temperature. Nanofibres may also be grown by exploiting the properties of a marginal solvent, where the polymer is soluble at high temperatures, but forms semicrystalline aggregates at lower temperatures.[90] Similar chromatic shifts are seen in the formation of conjugated polymer nanoparticles. When the solvated polymer is injected into aqueous solution, the hydrophobic chains rapidly collapse to form a nanoparticle suspension.[178–180]

Being able to control the morphology of conjugated polymers in this way is of great interest, particularly in the manufacture of organic solar cells. The charge carrier mobility and efficiency of a bulk heterojunction type device is heavily influenced by the thickness of the active layer and the size and alignment of the donor and acceptor domains formed during manufacture.[181–183] In rapid “roll-to-roll’ printing techniques, the morphology of the active layer can be controlled with simple methods such as the solvent mix during deposition,[184,185] or with subsequent thermal annealing to modify the size of the crystalline domains.[62,63,186]

Spectroscopic techniques exist that are able to observe the optical properties of a single, isolated polymer chain. In this scenario, the optical properties can be related to the chain conformation and disorder using relatively simple models based on planarity and conjugation length (the one dimensional “particle-in-a-box”) and FRET.[187,188] As the system size increases, so too does the complexity of the interactions. Semicrystalline polymer aggregates will display noticeably different behaviour depending on the particular stacking arrangement of the chains, leading to the H- and J-type aggregate models that describe the relative alignment of the chromophore transition dipole moments and the subsequent effects on absorption and emission wavelengths.[189–195] Figure 1.12 illustrates how the excitation energy of a pair of adjacent chromophores can change depending on their spatial arrangement.[139] In the case of a face-to-face stacking of the chromophores (H aggregate motif), the transition dipole moments (TDMs) will be arranged parallel. The overall dipole moment of the pair will be strongest for the parallel transition, but this requires greater energy to overcome the head-to-head type arrangement of the individual dipoles. Conversely for the inline stacking (J aggregate motif), the strongest, in-phase transition will require a lower excitation energy due to

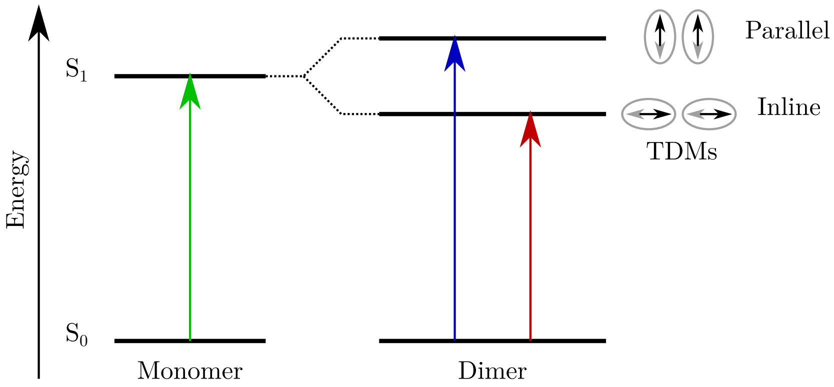

Figure 1.12: Energy level diagram indicating the difference in excitation energies of a pair of coupled chromophores depending on their spatial arrangement. The parallel, face-to-face stacking represents a H-type aggregate, in which the excitation energy is greater to overcome the unfavourable head-to head arrangement of the individual chromophore dipoles. Conversely, the inline, end-to-end stacking of a J-type aggregate displays a lower excitation energy due to the favourable head-to-tail dipole arrangement.

the favourable head-to-tail arrangement of the chromophore dipoles. A real conjugated polymer system will generally comprise a complex blend of H, J and HJ aggregate motifs. Chapter 4 presents a detailed model that links the local chain conformation and larger scale structure of a conjugated polymer system to the exciton transport and observed optical properties.

Small molecule organic semiconductor devices are similarly affected by morphology of the active layers. In molecular crystals, defect sites caused by impurities create energy barriers that trap charge carriers.[125] This phenomena can drastically reduce the efficiency of devices such as organic FETs.[129,130] In OLEDs, physical defects in the organic active layer can act to short-circuit the device,[196] so careful control over the structure of the device layers is critical. For example, roughness of the substrate surface or electrodes can propagate through to subsequent layer, degrading performance.[197] The interfaces between layers are also affected by morphology. A good interface will allow effective electron or hole injection,[198] and techniques like thermal annealing have demonstrated enhanced performance by improving the interfaces to the active layer.[199]

The efficiency of singlet fission and triplet fusion processes are affected by the relative orientation of the two exciton sites. This may be observed experimentally in crystals of small organic molecules with different crystal packing,[200] or in molecules specially synthesised to modify the exciton site geometry.[201,202] The theory of exciton spin interactions including singlet fission and triplet fusion was studied extensively in the late 1960's by Merrifield.[166,203–205] While the theory was oriented towards interactions in ordered molecular crystals, it is general enough to apply to more disordered systems. Chapter 5 applies the model to singlet fission and triplet fusion processes in disordered rubrene films and corrects some errors in the current literature understanding of the theory for these type of disordered systems. The revised theoretical model for triplet–triplet interactions is detailed in Section 2.2.3.

Triplet fusion is an integral step in a photochemical upconversion system, which may be used to enhance the efficiency of photovoltaic devices by enabling the harvest of sub-bandgap photons.[67] Typically, these systems are based on a TTA-UC process, using a solution-based mixture of sensitiser and emitter molecules.[168,169,206–209] Solution-phase could be considered the epitome of disordered systems, yet on the molecular scale, the orientation of emitter molecule collisions are not completely uncorrelated. In Chapter 6, the role of the emitter molecule structure on the geometry of the pair interactions and the subsequent effect on upconversion efficiency are investigated, with the goal of engineering the ideal emitter molecule for a solution-based TTA-UC system.

CHAPTER 2
Methods

2.1 Experimental Methods

This section outlines several ultrafast spectroscopic techniques used in this work. Ultrafast spectroscopy uses pulsed lasers as the light source, typically with a pulse duration measured in femtoseconds (10^{-15} s). It is the short pulse duration that allows these techniques to achieve their high time resolution.

The methods described in Sections 2.1.1 and 2.1.2 used the output of a regenerative amplifier as the source for all laser pulses. A 532 nm continuous-wave Nd:YVO$_4$ laser at 8 W (Spectra-Physics, Millenia Prime) pumped a mode-locked Ti:Sapphire oscillator (Spectra-Physics, Tsunami) producing 800 nm pulses at a rate of 80 MHz. These were used as the seed pulses for the regenerative amplifier (Spectra-Physics, Spitfire Pro XP 100F) which was pumped by a 20 W 1 kHz Q-switched Nd:YLF laser (Spectra-Physics, Empower). The output from the amplifier consisted of 800 nm pulses with a duration of 100 fs and a 1 kHz repetition rate.

The experimental apparatus are described here in a general manner. Experiment-specific details including as pulse power, spot sizes and polarisation are given in the relevant experimental sections of Chapter 3 and 4.

2.1.1 Transient Absorption Spectroscopy

2.1.1.1 Pump-Probe

Pump-probe spectroscopy refers to the use of a "pump" laser that is absorbed by the sample to generate the photoexcited state, and a "probe" laser that is used to measure the absorbance of the sample after some time interval. The absorbance data is obtained as a function of wavelength λ and time t, and is typically represented as the change in absorbance (A) or optical density (OD) relative to the steady-state absorbance as

$$\Delta\mathrm{OD}(\lambda, t) \equiv \Delta\mathrm{A}(\lambda, t) = \mathrm{A}(\lambda, t)_{\mathrm{pump}} - \mathrm{A}(\lambda, t)_{\mathrm{no\ pump}} \tag{2.1}$$

The absorbance in the absence of the pump $\mathrm{A}(\lambda, t)_{\mathrm{no\ pump}}$ is equivalent to the steady-state absorption spectrum, but a series of alternate pump-on and pump-off measurements are collected to reduce noise induced by fluctuations in the laser intensity. The probe may be a monochromatic laser to study a particular transition of interest or, as described below, a broadband "white light" supercontinuum which is able to measure absorptions across a wide spectral range with a single laser shot. By delaying the relative arrival time of the pump and probe pulses, the time resolution of the spectrum is achieved. The dynamics and decay of the excited species is then able to be observed from the composition of the many individual pump-probe measurements.

Using the energy level diagram in Figure 1.6 for reference, the pump wavelength is typically selected to match the S$_0$ to S$_1$ absorption, producing a sample population in the S$_1$ state. The subsequent probe may then measure several phenomena. The reduced population of the S_0 ground state means the normal ground state absorption is diminished. This is observed as a negative ΔOD across similar wavelengths as the steady-state absorption spectrum and is called a ground-state bleach (GSB). A probe photon tuned to the same wavelength as the fluorescence (S_1 to S_0 transition) can cause stimulated emission (SE), as shown in Figure 1.6. As emission of light is the opposite of absorption, SE is observed as a negative ΔOD across similar wavelengths as the steady-state fluorescence spectrum. The SE spectrum may have a markedly different appearance to the fluorescence spectrum, for as the steady-state spectrum comprises the sum of all light ever emitted from the system, the SE may evolve rapidly over time as excited-state relaxation or reorganisation processes occur. Excited species may absorb an additional photon from the probe to reach a higher-lying excited state, for example through the S_1 to S_n or T_1 to T_n transitions. This excited-state absorption (ESA) is seen as a positive ΔOD signal, usually in the lower-energy regions of the spectrum.

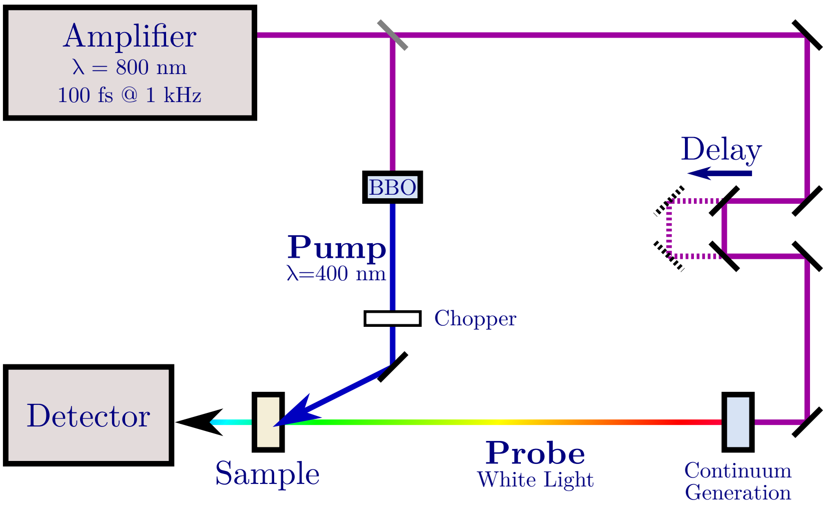

Figure 2.1: Schematic of the pump-probe transient absorption apparatus.

Pump-probe experiments were conducted using a commercial transient absorption spectrometer (Ultrafast Systems, Helios). A schematic diagram of the apparatus is shown in Figure 2.1. Pump pulses at 400 nm were generated by second harmonic frequency doubling of the amplifier output using a 0.5 mm thick β-barium borate (BBO) crystal. An optical chopper was used to mechanically modulate the pump pulses at a frequency of 500 Hz in order to obtain the change in OD due to the pump pulse as per equation 2.1. A white light continuum was generated for use as the probe. The probe in the visible or near infra-red (NIR) range was generated using a 3.2 or 12.7 mm sapphire crystal, respectively. The arrival time of the probe relative to the pump was determined using a computer controlled delay line to achieve the time-resolution. A pair of linear detectors were used, one as a reference (not shown) in addition to the signal that passes through the sample. The detectors were CMOS based for use in the visible range (Ultrafast Systems, CAM-VIS-2) and InGaAs for use in the NIR.

2.1.1.2 Pump-Push-Probe

Pump-push-probe transient absorption spectroscopy is an extension of the pump-probe experiment and involves the use of a second excitation beam line to act as the "push".

As with pump-probe, the pump generates an excited state population. The wavelength of the push pulse is tuned to an ESA band and arrives after a designated time period. The probe arrival is delayed relative to the pump and push to obtain the time resolution. With two excitation pulses, the data may be represented as either ΔOD as with the pump-probe experiment (eq 2.1) or as the change in ΔOD due to the push pulse as

$$\Delta\Delta\mathrm{OD}(\lambda,t) \equiv \Delta\Delta\mathrm{A}(\lambda,t) = \Delta\mathrm{A}(\lambda,t)_{\mathrm{pump+push}} - \Delta\mathrm{A}(\lambda,t)_{\mathrm{pump}} \tag{2.2}$$

It is possible to obtain both the ΔA and ΔΔA data in a single experiment by mechanically chopping both the pump and push lasers at different rates. In this way all four combinations of spectra (both-off, pump-only, push-only, pump+push) are collected on consecutive laser shots.

Pump-push-probe transient absorption spectroscopy offers the benefit of being able to isolate and observe the dynamics of the highly excited states. That is, while pump-probe experiments generally observe transitions to or from the lowest-lying S_1 or T_1 states, pump-push-probe experiments are able to isolate transitions or phenomena that involve the higher-lying S_n or T_n states, such as the internal conversion (IC) or other relaxation processes, inter-system crossing (ISC) or exciton dissociation.

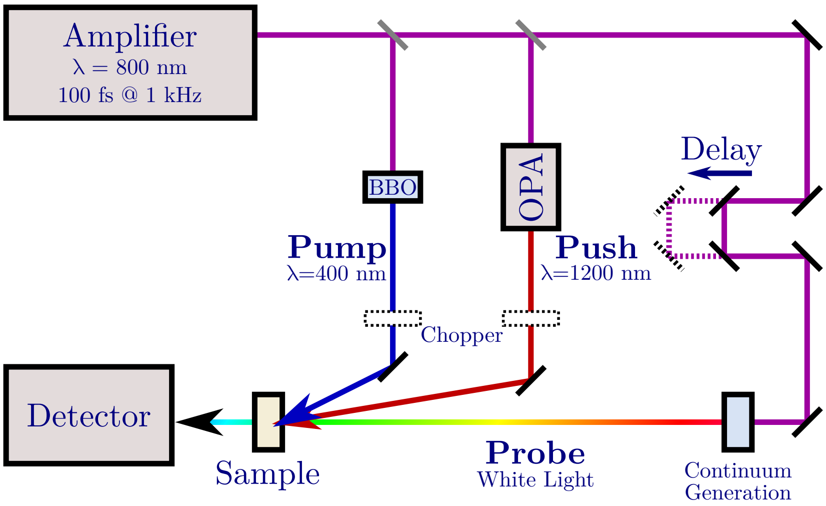

Figure 2.2: Schematic of three-pulse transient absorption apparatus.

The transient absorption spectrometer used for the pump-probe experiments as described in Section 2.1.1.1 was modified in order to perform the three-pulse pump-push-probe experiments and is shown schematically in Figure 2.2. Push pulses of 900 or 1200 nm were generated using an optical parametric amplifier (OPA) (Light Conversion, TOPAS-C). Modulation of the push by a mechanical chopper at 500 Hz was used to obtain the ΔΔOD data.

2.1.2 Fluorescence Upconversion

Fluorescence upconversion is a method of obtaining time-resolved fluorescence data. It is distinguished from other time-resolved fluorescence techniques such as time correlated single photon counting (TCSPC) by offering very high time resolution at the expense of some sensitivity.

Two laser pulses are used, termed the “pump” and the “gate”. The pump pulse is absorbed by the sample to generate the photoexcited state. The fluoresced light from the sample is then collected and focussed onto a BBO crystal. The gate pulse is not directed on to the sample, but is instead used to trigger the time window of fluorescence detection. This is achieved by focussing the gate pulse onto the same BBO crystal. Through sum frequency generation (SFG), photons of a higher energy are produced — this is the upconversion of the fluorescence. The fluorescence wavelength of interest is selected via rotation of the BBO crystal to achieve the required phase matching condition. The upconverted fluorescence has a shorter wavelength than the pump laser, so is able to be filtered from any residual pump and fluorescence light.

Following photoexcitation, fluorescence is continuously emitted by the sample. The upconverted fluorescence is only produced in the presence of the gate however, so by progressively delaying the arrival time of the gate, the time-resolved data is obtained. In this way, the time resolution becomes limited by the duration of the laser pulses, rather than the speed of the electronic detectors.

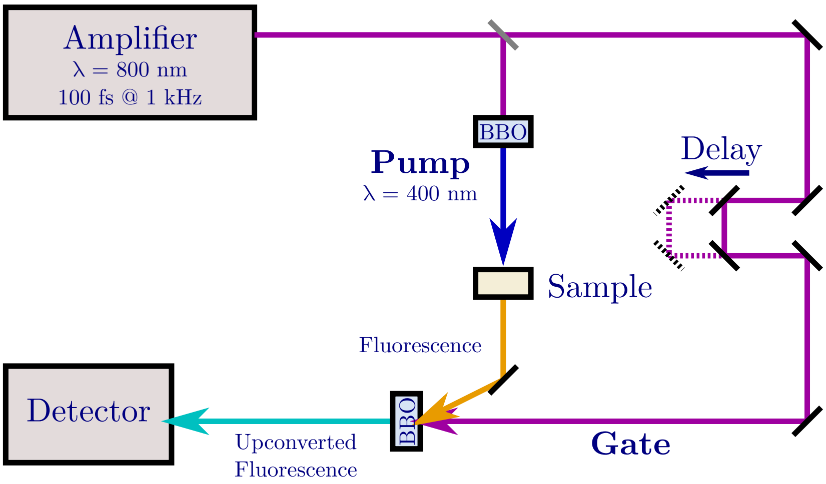

Figure 2.3: Schematic of fluorescence upconversion apparatus.

A schematic diagram of the fluorescence upconversion apparatus (Ultrafast Systems, Halcyone) is shown in Figure 2.3. The 400 nm pump pulse was generated by second harmonic generation of the amplifier output using a BBO crystal. The gate pulse was the raw 800 nm amplifier output and the relative pump-gate delay was determined by a computer controlled delay line. The intensity of the upconverted fluorescence was detected using a photomultiplier tube attached to a monochromator.

2.1.2.1 Fluorescence Anisotropy

Time-resolved spectroscopic experiments such as those described in Sections 2.1.1 and 2.1.2 are typically conducted with the relative polarisation of the excitation (pump) and detection (probe or gate) set at 54.7°. This particular value is called the "magic angle" and is equal to $\arctan\sqrt{2}$, the angle made between the diagonal of a cube and any one of the adjoining edges. As the chromophores in a three-dimensional sample can be arbitrarily orientated, detection at the magic angle negates any effect of anisotropy.

In some situations the anisotropic behaviour of a system may be of interest. For example, as shown in Figure 1.8, exciton transport through a system of disordered chromophores will cause the polarisation of the fluoresced photon to become rotated relative to the excitation. By observing the polarisation of the fluorescence over time, the rate of exciton migration or degree of disorder in the sample can be observed. Experiments of this nature are called time-resolved fluorescence anisotropy.

The anisotropy $r(t)$ is a correlation function between the intensity of the fluorescence at time t with polarisation parallel $I(t)_{\parallel}$ and perpendicular $I(t)_{\perp}$ to the excitation polarisation:

$$r(t) = \frac{I(t)_{\parallel} - I(t)_{\perp}}{I(t)_{\parallel} - 2I(t)_{\perp}} \tag{2.3}$$

The value of the anisotropy function ranges from 0.4 for fully correlated absorption and emission, to zero for emission that has a completely random polarisation. Negative values of the function are also possible, with the minimum value of -0.2 indicating the emission polarisation is being specifically rotated 90° relative to the excitation. These limiting values are obtained by considering the the angle θ between a pair of absorbing and emitting chromophores where the anisotropy is[210]

$$r = \frac{1}{5}\left(3\cos^2\theta - 1\right). \tag{2.4}$$

The apparatus used in this work for the fluorescence anisotropy experiments is that used for the fluorescence upconversion experiments described in Section 2.1.2. The parallel and perpendicular intensity measurements were taken by consecutive experiment runs by rotating the gate polarisation using a half-wave plate.

2.2 Theoretical Methods

2.2.1 Molecular Dynamics

Molecular dynamics (MD) is a computational method based on a classical description of the interactions between particles in a system. Typically the particles will be representative of atoms in molecules, but this is by no means a requirement. The technique determines the behaviour of the particles using Newton's equations of motion, thus may be applied to large systems of 10^5 or more particles and used to simulate interactions over time scales up to approximately 1 µs. (These limitations are predominantly related to current computer memory size and processing power rather than fundamental restrictions of MD.)

In general terms, Newton's equations of motion state that the acceleration of a particle is the second derivative of its position, and acceleration is in turn related to the force on the particle *via* its mass. More formally, for N particles

$$\boldsymbol{F}_i(\boldsymbol{r}^N) = m_i \frac{\mathrm{d}^2\boldsymbol{r}_i}{\mathrm{d}t^2} = -\nabla_i \boldsymbol{U}(\boldsymbol{r}^N) \tag{2.5}$$

where $\boldsymbol{F}_i$ is the force vector on particle i, $\boldsymbol{r}^N$ is the positions of the particles, m_i is the mass of particle located at $\boldsymbol{r}_i$ and $\boldsymbol{U}$ is a function called the force field that describes the potential energy surface for the interacting particles.

The force field will typically be a composition of several bonded and non-bonded particle interactions and is specific to the particular system being simulated. Generally, the force field will take the form

$$U = U_{\mathrm{VDW}} + U_{\mathrm{ES}} + U_{\mathrm{bond}} + U_{\mathrm{angle}} + U_{\mathrm{dihedral}} \tag{2.6}$$

where U_{VDW} and U_{ES} are the non-bonded van der Waals and electrostatic (Coulombic) interactions, U_{bond} is the bond stretch, U_{angle} the bond angle and U_{dihedral} the dihedral angle potentials. By numerically integrating eq 2.5 the positions of the particles is evolved. The time period for the integration (the timestep) is chosen to be shorter than the fastest phenomena in the system to minimise numerical error, typically $\sim$1 fs where chemical bond vibrations are involved. The particular form of the potential functions varies, and parameters are often determined empirically. Some generalised force field parameter sets exist, such as the optimised potentials for liquid simulations (OPLS).[211–216] The details of parameterising a specific force field based on OPLS are shown in the Supporting Information of Chapter 6.

2.2.1.1 Coarse-Grained Molecular Dynamics

Molecular dynamics often uses fully atomistic models, where each atom in a molecule is mapped to a particle, but the efficiency of the simulation can be enhanced through rational simplification of the system. The process of coarse-graining aims to reduce the number of particles used to represent the system while retaining the larger-scale physical properties and behaviour. A coarse-grained system will typically also benefit from the elimination of the most rapid degrees of freedom, such as C−H bonds, allowing for a longer integration time step. Due to the reduction in the number of particle interactions, MD can then be applied to larger systems or is able to achieve longer simulation times with the same computing resources.

A coarse-grained MD model is applied in Chapter 4 to obtain structures for aggregates of the polymer poly(3-hexylthiophene) (P3HT). Details of development of the force field and parameters are found in the work of Schwarz et al.[217] A diagram representing the atomistic to coarse-grained mapping is shown in Figure 2.4. Each system contains 100, 300-unit polymer chains which would consist of over 7.5×10^5 particles in a fully atomistic system. The coarse-grained model reduces the number of particle sites by approximately an order of magnitude, allowing the large system size and long simulation time period required for the formation of the polymer aggregates.

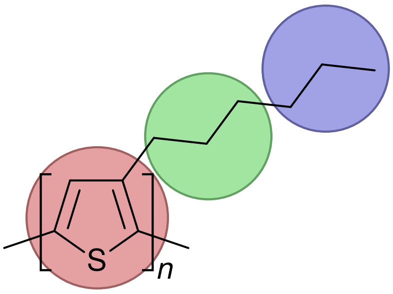

Figure 2.4: Atomistic to coarse-grained mapping of particle sites on P3HT. The thiophene ring, plus first three and last three methyl groups make up the three coarse-grain sites. The complexity of the model is reduced from 25 atoms to 3 coarse-grain particles.

2.2.2 Frenkel–Holstein Exciton Model

The Frenkel–Holstein exciton model is a quantum mechanical treatment of the exciton in a conjugated polymer as a particle that can be delocalised in one dimension along the polymer chain. It is an extension of the Frenkel model that includes the effect of coupling to the motion of the polymer nuclei. The nuclei motion is described classically by a single normal coordinate, linked to the C=C stretching mode of the conjugated polymer backbone. In this way, the relaxation process from the vertically excited state with the initial ground-state nuclear geometry to the excited but vibrationally relaxed state is simulated.

Application of the Frenkel–Holstein model to a disordered polymer system comprising N monomers results in N eigenstates, each of which describe a possible wavefunction of the exciton with energy given by the associated eigenvalue. The low-energy eigenstates describe the favoured exciton states, where the centre-of-mass and localisation length of the exciton can then be derived from the wavefunctions and positions of the corresponding monomers. In this way, the effective chromophore sites and energies in the polymer system can be determined quantum mechanically, without relying on arbitrary criteria, such as intermonomer torsional angle thresholds to define conjugation breaks.[94–96]

The Frenkel-Holstein model is described in detail and applied as part of a mesoscale exciton migration simulation in Chapter 4

2.2.3 Quantum Mechanical Model of Triplet–Triplet Spin Interactions

Chapters 5 and 6 consider singlet exciton fission and triplet exciton fusion processes. As described in Section 1.3.3.2, the interconversion between a singlet exciton and a triplet exciton pair are spin-allowed processes as the total spin of the system is conserved. The quantum mechanical theory of these exciton interactions was studied extensively by Merrifield in the late 1960s,[166,203–205] but focussed on ordered, crystalline materials. While the theory is general enough to apply to disordered systems such as amorphous solids or solutions, recent publications describing such a model have been flawed. Chapter 5 details these issues, describes the development of a corrected model and then applies it to experimental data on singlet fission in amorphous rubrene films. Chapter 6 investigates triplet fusion in solution as part of a triplet–triplet annihilation upconversion (TTA-UC) process. The quantum mechanical model of the triplet–triplet spin interactions is common to both projects and is described in detail in this section.

The spin Hamiltonian for two interacting triplets in a magnetic field consists of four terms:

$$\hat{H} = \hat{H}_{\mathrm{SS_A}} + \hat{H}_{\mathrm{SS_B}} + \hat{H}_{\mathrm{magnetic}} + \hat{H}_{\mathrm{AB}}. \tag{2.7}$$

These are the zero-field intramolecular spin–spin splitting terms $\hat{H}_{\mathrm{SS}}$ for molecules A and B, the Zeeman term $\hat{H}_{\mathrm{magnetic}}$ describing the effect of an applied magnetic field, and the intermolecular spin–spin coupling term $\hat{H}_{\mathrm{AB}}$.

The zero-field intramolecular term for a single molecule,

$$\hat{H}_{\mathrm{SS}} = D\left(\hat{S}_z^2 - \frac{1}{3}\hat{S}^2\right) + E\left(\hat{S}_x^2 - \hat{S}_y^2\right), \tag{2.8}$$

in the $\{|x\rangle, |y\rangle, |z\rangle\}$ basis defined with respect to the molecular symmetry axes x, y and z is[166]

$$\hat{H}_{\mathrm{SS}} = \begin{bmatrix} \frac{D}{3} - E & 0 & 0 \\ 0 & \frac{D}{3} + E & 0 \\ 0 & 0 & -\frac{2D}{3} \end{bmatrix} \tag{2.9}$$

where x, y, and z are refer to the long, short and perpendicular axes of the molecule, respectively (see Figure 5.1) and D and E are the molecular zero-field splitting parameters. The elements of this matrix and all other terms in the total spin Hamiltonian are readily derived by noting that the single-molecule two-electron spin operators $\hat{S}_x$, $\hat{S}_y$, and $\hat{S}_z$ acting on the two-electron spin states $|x\rangle$, $|y\rangle$, and $|z\rangle$ obey the relation $S_j\,|k\rangle = i\hbar\varepsilon_{jkl}\,|l\rangle$, where ε_{jkl} is the permutation symbol. (For convenience, we have taken $\hbar$ to be 1 in all of the results presented.) The zero-field term $\hat{H}_{\mathrm{SS_A}}$ for molecule A in the $\{|x\rangle_{\mathrm{A}}, |y\rangle_{\mathrm{A}}, |z\rangle_{\mathrm{A}}\}$ basis defined with respect to the molecular symmetry axes x, y, and z of molecule A is given by eq 2.9. The zero-field term $\hat{H}_{\mathrm{SS_B}}$ for molecule B in the $\{|x\rangle_{\mathrm{B}}, |y\rangle_{\mathrm{B}}, |z\rangle_{\mathrm{B}}\}$ basis defined with respect to the same x, y, and z axes can be obtained by applying a rotation operation:

$$\hat{H}_{\mathrm{SS_B}} = \hat{R}^{\mathrm{T}}\hat{H}_{\mathrm{SS}}\hat{R}, \tag{2.10}$$

where

$$\hat{R} = \begin{bmatrix} \cos\alpha\cos\gamma - \sin\alpha\cos\beta\sin\gamma & \sin\alpha\cos\gamma + \cos\alpha\cos\beta\sin\gamma & \sin\beta\sin\gamma \\ -\cos\alpha\sin\gamma - \sin\alpha\cos\beta\cos\gamma & -\sin\alpha\sin\gamma + \cos\alpha\cos\beta\cos\gamma & \sin\beta\cos\gamma \\ \sin\alpha\sin\beta & -\cos\alpha\sin\beta & \cos\beta \end{bmatrix} \tag{2.11}$$

and α, β and γ are the Euler angles that would rotate molecule A onto molecule B using the $ZX'Z''$ convention for the sequence of rotations. In the $\{|xx\rangle$, $|xy\rangle$, $|xz\rangle$, $|yx\rangle$, $|yy\rangle$, $|yz\rangle$, $|zx\rangle$, $|zy\rangle$, $|zz\rangle\}$ basis of pair states defined with respect to the molecular symmetry axes of molecule A (where $|xx\rangle \equiv |x\rangle_{\mathrm{A}}\,|x\rangle_{\mathrm{B}}$ and so on),

$$\hat{H}_{\mathrm{SS_A}} = \begin{bmatrix} \frac{D}{3} - E & 0 & 0 & 0 & 0 & 0 & 0 & 0 & 0 \\ 0 & \frac{D}{3} - E & 0 & 0 & 0 & 0 & 0 & 0 & 0 \\ 0 & 0 & \frac{D}{3} - E & 0 & 0 & 0 & 0 & 0 & 0 \\ 0 & 0 & 0 & \frac{D}{3} + E & 0 & 0 & 0 & 0 & 0 \\ 0 & 0 & 0 & 0 & \frac{D}{3} + E & 0 & 0 & 0 & 0 \\ 0 & 0 & 0 & 0 & 0 & \frac{D}{3} + E & 0 & 0 & 0 \\ 0 & 0 & 0 & 0 & 0 & 0 & -\frac{2D}{3} & 0 & 0 \\ 0 & 0 & 0 & 0 & 0 & 0 & 0 & -\frac{2D}{3} & 0 \\ 0 & 0 & 0 & 0 & 0 & 0 & 0 & 0 & -\frac{2D}{3} \end{bmatrix} \tag{2.12}$$

and

$$\hat{H}_{\mathrm{SS_B}} = \begin{bmatrix} \hat{H}_{\mathrm{SS_B}(1,1)} & \hat{H}_{\mathrm{SS_B}(1,2)} & \hat{H}_{\mathrm{SS_B}(1,3)} & 0 & 0 & 0 & 0 & 0 & 0 \\ \hat{H}_{\mathrm{SS_B}(2,1)} & \hat{H}_{\mathrm{SS_B}(2,2)} & \hat{H}_{\mathrm{SS_B}(2,3)} & 0 & 0 & 0 & 0 & 0 & 0 \\ \hat{H}_{\mathrm{SS_B}(3,1)} & \hat{H}_{\mathrm{SS_B}(3,2)} & \hat{H}_{\mathrm{SS_B}(3,3)} & 0 & 0 & 0 & 0 & 0 & 0 \\ 0 & 0 & 0 & \hat{H}_{\mathrm{SS_B}(1,1)} & \hat{H}_{\mathrm{SS_B}(1,2)} & \hat{H}_{\mathrm{SS_B}(1,3)} & 0 & 0 & 0 \\ 0 & 0 & 0 & \hat{H}_{\mathrm{SS_B}(2,1)} & \hat{H}_{\mathrm{SS_B}(2,2)} & \hat{H}_{\mathrm{SS_B}(2,3)} & 0 & 0 & 0 \\ 0 & 0 & 0 & \hat{H}_{\mathrm{SS_B}(3,1)} & \hat{H}_{\mathrm{SS_B}(3,2)} & \hat{H}_{\mathrm{SS_B}(3,3)} & 0 & 0 & 0 \\ 0 & 0 & 0 & 0 & 0 & 0 & \hat{H}_{\mathrm{SS_B}(1,1)} & \hat{H}_{\mathrm{SS_B}(1,2)} & \hat{H}_{\mathrm{SS_B}(1,3)} \\ 0 & 0 & 0 & 0 & 0 & 0 & \hat{H}_{\mathrm{SS_B}(2,1)} & \hat{H}_{\mathrm{SS_B}(2,2)} & \hat{H}_{\mathrm{SS_B}(2,3)} \\ 0 & 0 & 0 & 0 & 0 & 0 & \hat{H}_{\mathrm{SS_B}(3,1)} & \hat{H}_{\mathrm{SS_B}(3,2)} & \hat{H}_{\mathrm{SS_B}(3,3)} \end{bmatrix} \tag{2.13}$$

where $\hat{H}_{\mathrm{SS_B}(r,c)}$ refers to the row r and column c of a matrix element from eq 2.10.

The magnetic field (Zeeman) term,

$$\hat{H}_{\mathrm{magnetic}} = g\beta \boldsymbol{H} \cdot \left(\hat{\boldsymbol{S}}_{\mathrm{A}} + \hat{\boldsymbol{S}}_{\mathrm{B}} \right), \tag{2.14}$$

where $\boldsymbol{H}$ is the applied magnetic field, the coefficient $g\beta$ determines the magnitude of the influence of the magnetic field, and $\hat{\boldsymbol{S}}_{\mathrm{A}}$ and $\hat{\boldsymbol{S}}_{\mathrm{B}}$ are the two-electron spin operators for molecule A and B, respectively, can be written in the same basis as above

$$\hat{H}_{\mathrm{magnetic}} = ig\beta \begin{bmatrix} 0 & -H_z & H_y & -H_z & 0 & 0 & H_y & 0 & 0 \\ H_z & 0 & -H_x & 0 & -H_z & 0 & 0 & H_y & 0 \\ -H_y & H_x & 0 & 0 & 0 & -H_z & 0 & 0 & H_y \\ H_z & 0 & 0 & 0 & -H_z & H_y & -H_x & 0 & 0 \\ 0 & H_z & 0 & H_z & 0 & -H_x & 0 & -H_x & 0 \\ 0 & 0 & H_z & -H_y & H_x & 0 & 0 & 0 & -H_x \\ -H_y & 0 & 0 & H_x & 0 & 0 & 0 & -H_z & H_y \\ 0 & -H_y & 0 & 0 & H_x & 0 & H_z & 0 & -H_x \\ 0 & 0 & -H_y & 0 & 0 & H_x & -H_y & H_x & 0 \end{bmatrix}, \tag{2.15}$$

where

$$H_x = H \sin \phi_{\mathrm{B}} \cos \theta_{\mathrm{B}}, \tag{2.16}$$

$$H_y = H \sin \phi_{\mathrm{B}} \sin \theta_{\mathrm{B}}, \tag{2.17}$$

$$H_z = H \cos \phi_{\mathrm{B}}, \tag{2.18}$$

where H is the magnetic field strength and θ_{B} and ϕ_{B} are polar coordinates describing the field orientation with respect to the coordinate system defined by the symmetry axes of molecule A.

The intermolecular spin–spin coupling is a dipolar interaction of the form

$$\hat{H}_{\mathrm{AB}} = -\frac{X}{r^3} \left[3 \left(\hat{\boldsymbol{S}}_{\mathrm{A}} \cdot \hat{\boldsymbol{r}} \right) \left(\hat{\boldsymbol{S}}_{\mathrm{B}} \cdot \hat{\boldsymbol{r}} \right) - \hat{\boldsymbol{S}}_{\mathrm{A}} \cdot \hat{\boldsymbol{S}}_{\mathrm{B}} \right], \tag{2.19}$$

where $\hat{\boldsymbol{r}}$ is the unit vector joining the two spins, the coefficient X describes the strength of the interaction and $r = |\hat{\boldsymbol{r}}|$ is the distance between the spins. In the same basis as above,

$$\hat{H}_{\mathrm{AB}} = -\tfrac{X}{r^3}\begin{bmatrix} 0 & 0 & 0 & 0 & 1-3w^2 & 3vw & 0 & 3vw & 1-3v^2 \\ 0 & 0 & 0 & -1+3w^2 & 0 & -3uw & -3vw & 0 & 3uv \\ 0 & 0 & 0 & -3vw & 3uw & 0 & -1+3v^2 & -3uv & 0 \\ 0 & -1+3w^2 & -3vw & 0 & 0 & 0 & 0 & -3uw & 3uv \\ 1-3w^2 & 0 & 3uw & 0 & 0 & 0 & 3uw & 0 & 1-3u^2 \\ 3vw & -3uw & 0 & 0 & 0 & 0 & -3uv & -1+3u^2 & 0 \\ 0 & -3vw & -1+3v^2 & 0 & 3uw & -3uv & 0 & 0 & 0 \\ 3vw & 0 & -3uv & -3uw & 0 & -1+3u^2 & 0 & 0 & 0 \\ 1-3v^2 & 3uv & 0 & 3uv & 1-3u^2 & 0 & 0 & 0 & 0 \end{bmatrix} \tag{2.20}$$

where (u, v, w) is the unit vector joining the centres-of-mass of molecules A and B in the (x, y, z) coordinate system defined by the symmetry axes of molecule A. In Chapter 5 the molecule centres-of-mass are taken to be aligned along the z-axis and $X = D/100$, which simulates intermolecular spin interactions that are approximately two orders of magnitude smaller than the intramolecular interactions at typical molecular separations present in the rubrene film.[218] In Chapter 6, the relative position and separation of the emitter molecules during collisions are extracted from the MD simulations and used to obtain u, v, w and r.

To determine the wavefunction $\{\psi_l\}$ and energies of each of the nine possible spin states l of the triplet pair the complete spin Hamiltonian is diagonalised in the $\{|xx\rangle$, $|xy\rangle$, $|xz\rangle$, $|yx\rangle$, $|yy\rangle$, $|yz\rangle$, $|zx\rangle$, $|zy\rangle$, $|zz\rangle\}$ basis of pair states.

The singlet $|C^l_{\mathrm{S}}|^2$, triplet $|C^l_{\mathrm{T}}|^2$ or quintet $|C^l_{\mathrm{Q}}|^2$ character of each eigenstate can be determined from the projection of the wavefunctions onto the pure singlet, triplet or quintet states:[166,219]

$$C^l_{\mathrm{S}} = \frac{1}{\sqrt{3}}\left(\langle xx| + \langle yy| + \langle zz|\right)|\psi_l\rangle \tag{2.21}$$

$$C^l_{\mathrm{T}_1} = \frac{1}{\sqrt{2}}\left(\langle xy| - \langle yx|\right)|\psi_l\rangle \tag{2.22}$$

$$C^l_{\mathrm{T}_2} = \frac{1}{2}\left(\langle xz| - \langle zx| + i\left(\langle yz| - \langle zy|\right)\right)|\psi_l\rangle \tag{2.23}$$

$$C^l_{\mathrm{T}_3} = \frac{1}{2}\left(\langle xz| - \langle zx| - i\left(\langle yz| - \langle zy|\right)\right)|\psi_l\rangle\,. \tag{2.24}$$

$$C^l_{\mathrm{Q}_1} = \frac{1}{\sqrt{2}}\left(\langle xx| - \langle yy|\right)|\psi_l\rangle \tag{2.25}$$

$$C^l_{\mathrm{Q}_2} = \frac{1}{\sqrt{6}}\left(\langle xx| + \langle yy| - 2\langle zz|\right)|\psi_l\rangle \tag{2.26}$$

$$C^l_{\mathrm{Q}_3} = \frac{1}{\sqrt{2}}\left(\langle yz| + \langle zy|\right)|\psi_l\rangle \tag{2.27}$$

$$C^l_{\mathrm{Q}_4} = \frac{1}{\sqrt{2}}\left(\langle xz| + \langle zx|\right)|\psi_l\rangle \tag{2.28}$$

$$C^l_{\mathrm{Q}_5} = \frac{1}{\sqrt{2}}\left(\langle xy| + \langle yx|\right)|\psi_l\rangle \tag{2.29}$$

where $|C^l_{\mathrm{T}}|^2 \equiv \sum_{i=1}^{3} |C^l_{T_i}|^2$ and $|C^l_{\mathrm{Q}}|^2 \equiv \sum_{i=1}^{5} |C^l_{Q_i}|^2$.

CHAPTER 3

Optical Pumping of Poly(3-hexylthiophene) Singlet Excitons Induces Charge Carrier Generation

Statement of Authorship

Title of Paper	Optical Pumping of Poly(3-hexylthiophene) Singlet Excitons Induces Charge Carrier Generation
Publication Status	Published
Publication Details	Tapping, P. C.; Kee, T. W. *J. Phys. Chem. Lett.* **2014**, *5*, 1040–1047. DOI: 10.1021/jz500217f

Principal Author

Principal Author	Patrick C. Tapping		
Contribution to the Paper	Experimental work, data analysis, construction of figures, writing of manuscript.		
Overall Percentage	85%		
Signature		Date	18/7/16

Co-Author Contributions

By signing the Statement of Authorship, each author certifies that the stated contributions to the following publication are accurate and that permission is granted for the publication to be included in this thesis.

Co-Author	Tak W. Kee		
Contribution to the Paper	Supervision of project, assistance with data analysis and manuscript preparation, corresponding author.		
Signature		Date	22/7/16

Abstract

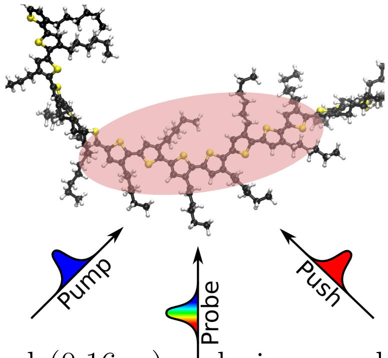

The dynamics of high-energy excitons of poly(3-hexylthiophene) (P3HT) are shown to consist of torsional relaxation and exciton dissociation to form free carriers. In this work we use pump-push-probe femtosecond transient absorption spectroscopy to study the highly excited states of P3HT in solution.

P3HT excitons are generated using a pump pulse (400 nm) and allowed to relax to the lowest-lying excited state before re-excitation using a push pulse (900 nm or 1200 nm), producing high-energy excitons which decay back to the original excited state with both sub-picosecond (0.16 ps) and picosecond (2.4 ps) time constants. These dynamics are consistent with P3HT torsional relaxation, with the 0.16-ps time constant assigned to ultrafast inertial torsional relaxation. Additionally, the signal exhibits an incomplete recovery, indicating dissociation of high-energy excitons to form charge carriers due to excitation by the push pulse. Our analysis indicates that charge carriers are formed with a yield of 11%.

Introduction

The intense research on conjugated polymers is mainly driven by the function of these materials as light harvesting chromophores and electron donors in organic solar cells.[220–223] Polymer based solar cells offer the advantage of solution processability for rapid and low-cost fabrication of mechanically flexible devices. P3HT is one of the most studied conjugated polymers for several important reasons. First, there are well-established synthetic methods by which a high regioselectivity is achieved routinely.[83] Second, P3HT exhibits the ability to aggregate in an ordered fashion to form semicrystalline domains.[224] Recent work has shown that these semicrystalline domains enhance exciton and charge transport.[225] In many cases, long-range order is maintained and P3HT is able to “crystallize” to form nanofibres which are microns in length.[90,193,217] In addition to nanofibres, P3HT is capable of folding into roughly spherical aggregates, *i.e.*, nanoparticles, to give rise to functional properties including charge storage and chemical sensing.[226,227] Furthermore, P3HT nanoparticles provide a good model system for investigating the dynamics of excitons and polarons.[180] The nanoparticle system offers a device-like environment without the significant structural and interfacial heterogeneities found in a thin-film device, thereby improving the understanding between a material’s function and its molecular properties.[227] Finally, the P3HT-fullerene blend is the most widely investigated donor-acceptor system owing to its relatively high solar power conversion efficiency, which is as high as 6.5%.[77,228,229] As a consequence, there is continuing effort in studying P3HT to develop insight into the photovoltaic properties of P3HT-fullerene solar cells.

The use of femtosecond laser spectroscopy has offered a vast level of information about exciton dynamics of P3HT films or aggregates.[180,188,230–236] The photoexcitation event first generates a “hot” singlet exciton with Frenkel-exciton characteristics and a spatial extent of nearly 9 nm, over approximately 20 monomeric units.[188] This delocalized exciton then undergoes rapid self-localisation within the first 100 fs to a size of

$\leq$10 monomers.[232] Furthermore, vibrational relaxation, torsional relaxation and exciton hopping occur on the subpicosecond to >10-picosecond time scales to enable the exciton to relax further.[232,237] The exciton self-localisation and relaxation processes produce a significant Stokes shift in the emission spectrum and exhibit a large decrease in the polarisation anisotropy.[232] In the case of the P3HT-fullerene films or aggregates, there is increasing evidence to suggest that charge carriers are generated at $t \leq 100\,\text{fs}$.[188,238] The large spatial extent of the initially prepared delocalized exciton offers the opportunity for a significant fraction of the "hot" exciton to be quenched by fullerene to generate free carriers. This phenomenon has also been reported for other conjugated polymer-fullerene blends recently.[239–241]

To obtain further insight into the behavior of excitons and charge carriers, more elaborate experimental configurations utilizing three or more optical pulses were employed. Recently, Busby et al. used pump-dump-probe spectroscopy to investigate excited-state self-trapping and ground-state relaxation dynamics of P3HT.[142] Wells and Blank employed two-colour three-pulse photon echo peak shift spectroscopy to demonstrate that the early-time exciton relaxation of P3HT is strongly driven by the coupling between the exciton and the torsional degrees of freedom.[237] Other examples of multipulse spectroscopic investigations include coherent intrachain energy migration using 2D electronic spectroscopy, and charge carrier generation and torsional relaxation using pump-push-probe spectroscopy.[158,242–244] Notably, Gadermaier et al. used pump-push-probe spectroscopy to investigate methyl-substituted ladder-type poly(para)phenyl.[244] In their study, the pump pulse excites the conjugated polymer to generate singlet excitons. The push pulse then arrives at $t < 3\,\text{ps}$ to excite these "hot" excitons. Using this experimental scheme, the authors reported that charge carriers are generated by "pushing" the singlet excitons with a yield of 7%.

In this study, we employ pump-push-probe spectroscopy to study the effect of photoexcitation of singlet excitons of P3HT on torsional relaxation and charge carrier generation dynamics. P3HT is investigated at a low concentration under the single-chains condition to exclude contributions from interchain coupling.[142,234,237] In the experiment, the pump pulse, with a wavelength of 400 nm, generates singlet excitons. The push pulse, which is tuned to the singlet exciton absorption band, arrives approximately 25 ps after the pump pulse to promote the relaxed or "cool" singlet excitons to high-energy, delocalized excitonic states. The probe pulse, which is centered either at the singlet exciton absorption band or the stimulated emission (SE) band, detects the effects of the pump and push pulses. The results show that most of the high-energy excitons undergo rapid relaxation back to the lowest-lying singlet excitonic state due to ultrafast torsional motions of P3HT. Approximately 11% of the high-energy excitons dissociate to form charge carriers, which in turn undergo geminate recombination to produce ground-state P3HT. The results also indicate that the exciton binding energy is $\leq 1\,\text{eV}$. In short, pump-push-probe spectroscopy is used to reveal new insight into the exciton dynamics of P3HT

Results and Discussion

Figure 3.1a shows that P3HT in tetrahydrofuran (THF) has a ground-state absorption band centered around 450 nm and it exhibits a large Stokes shift, with an emission maximum around 575 nm. Upon excitation, a broad excited-state absorption (ESA) band centered around 1100 nm appears in the near-IR region. It shows a lifetime of approximately 500 to 600 ps and has previously been assigned to the singlet exciton.[180,245,246] Fluorescence lifetime results confirm a singlet exciton lifetime of 530 ps, which is in agreement with previously obtained values for P3HT in solution.[232,234,235] Consequently, the pump-probe and pump-push-probe transient absorption data were fitted with a fixed time constant of 530 ps, as is discussed below. The emission signal shows a dynamic red-shift from 0 ps to ~25 ps.[232,234,235] Similarly, a red-shift is also evident in the stimulated emission band of the pump-probe data, with the peak shifting from 575 to 625 nm over a period of approximately 25 ps. These results are shown in Supporting Information. This dynamic red-shift has been observed previously in polythiophene solutions and attributed to a combination of exciton hopping and torsional relaxation.[247] These photophysical processes are shown in Figure 3.1b. Torsional motions between thiophene rings act to increase the planarisation of the polymer, thereby increasing conjugation length and allowing a reduction in the energy of the exciton prior to emission.[142,234] Similarly, the exciton is able to hop from the site of the initial excitation to lower energy chromophores in the polymer chain through excitonic energy transfer (EET), with corresponding dissipation of energy by further torsional and vibrational relaxation.[154]

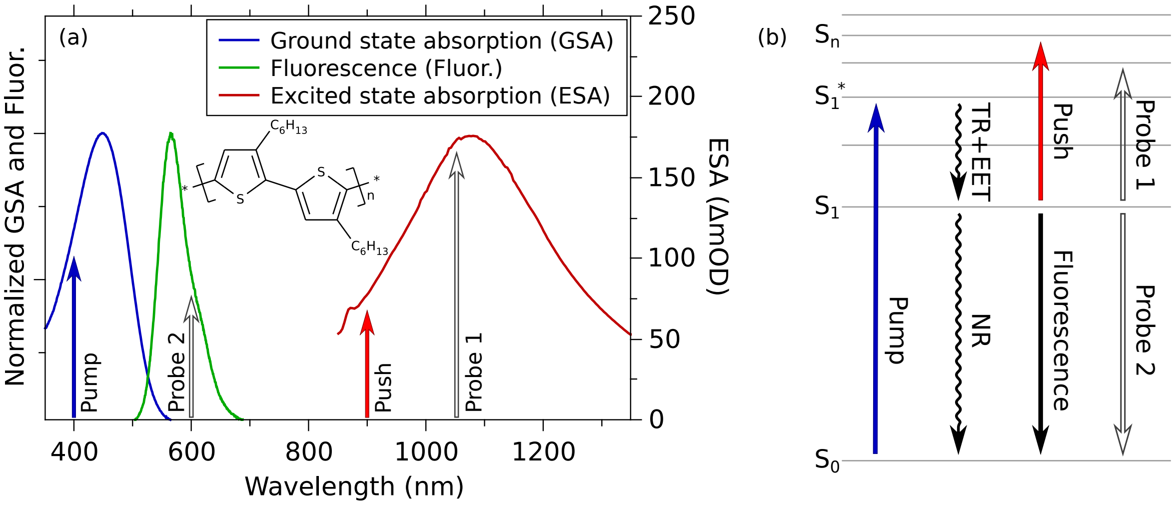

Figure 3.1: (a) Ground-state absorption, fluorescence and excited-state absorption spectra of dilute P3HT in THF. The pump, push, probe 1 and probe 2 wavelengths of 400 nm, 900 nm, 1050 nm and 600 nm, respectively, are indicated with arrows. Inset shows the structure of P3HT. (b) An energy diagram showing the photophysical processes involved in this study. Note that intersystem crossing is not shown and the push pulse is only present in the pump-push-probe experiment. TR: torsional relaxation, EET: excitonic energy transfer, NR: non-radiative deactivation.

Figure 3.2a shows the change in optical density (OD) (ΔOD) at 1050 nm as a function of pump-probe time delay (blue circles). The photophysical processes involved in the pump-probe experiment are shown in Figure 3.1b. First, the 400-nm pump light, which lies within the ground-state absorption spectrum, promotes P3HT from the S_0 to the $S_1{}^*$ state, with which the S_0 state has a large Franck-Condon overlap. The initially prepared exciton is able to dissipate its energy by a combination of torsional relaxation and EET to relax to the lowest-lying excited state, S_1. The 1050-nm probe light (probe 1), which is located near the maximum of the ESA band, monitors the

Table 3.1: Fitting parameters for the pump-probe (ΔOD) and pump-push-probe ($\Delta\Delta$OD) data with $\lambda_{\text{push}} = 900\,\text{nm}$.[a]

expt.	λ_{probe} (nm)	A_1[b]	τ_1 (ps)	A_2	τ_2 (ps)	A_3	τ_3 (ps)	A_4	τ_4 (ps)
ΔOD	1050	–	–	−0.19	2.4	0.14	135	0.66	530[c]
ΔOD	600	–	–	0.18	2.1	−0.22	60	−0.60	530[c]
$\Delta\Delta$OD	1050	−0.80	0.16	−0.09	2.4	−0.07	135[d]	−0.04	530[c]
$\Delta\Delta$OD	600	0.86	0.16	0.08	2.8	0.03	109	0.03	530[c]

[a] The ΔOD and $\Delta\Delta$OD data was fit to a multi-exponential function $f(t) = \sum_n A_n e^{-t/\tau_n}$. All parameters have a relative error of 15%. [b] $\sum_n |A_n| = 1$. [c] Fixed to value obtained from fluorescence lifetime measurements. [d] Fixed to value obtained from pump-probe experiment.

transitions from S_1 to higher-lying states, investigating the behavior of these states.

The black, solid curve shown in Figure 3.2a is the best-fit curve of the pump-probe data using a multi-exponential function of the form $f(t) = \sum_n A_n e^{-t/\tau_n}$ where, for each component, τ_n is the time constant and A_n is the amplitude. The best-fit values are shown in Table 3.1. First, the pump-probe result shows a rapid appearance of the excited-state absorption band immediately after excitation on a time scale near the instrument response function of approximately 150 fs. An additional, slower rise in the signal level with a time constant of 2.4 ps is also present. Furthermore, the result also shows decay components with time constants of 135 ps and 530 ps. The 530 ps time constant, which was fixed in the curve fitting analysis, is the characteristic lifetime of the P3HT exciton, as is discussed above.

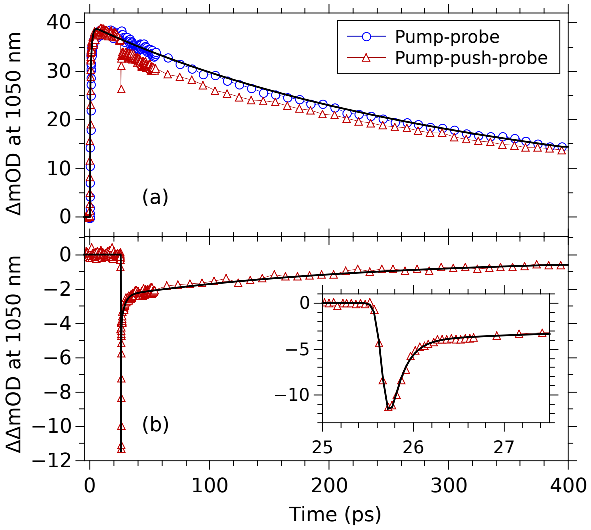

Figure 3.2: (a) The dynamics of the exciton-induced absorption at 1050 nm in the pump-probe (blue circles) and pump-push-probe experiments (red triangles). (b) The change in ΔOD ($\Delta\Delta$OD) due to the push pulse. Fit curves are indicated as solid black curves.

The rising and decaying components of the pump-probe result indicate the following. First, the 2.4 ps rising component, τ_2, is the result of a significant red-shift of the excited-state absorption band up to 1050 nm at early time, as shown in Supporting Information. This red-shift is due to rapid energy dissipation of the initially prepared excited state. The general agreement from a number of studies is that either torsional reorganisation, EET, or both are responsible for these rapid dynamics. Banerji et al. used a global analysis of multicolour fluorescence upconversion data to reconstruct the time-resolved fluorescence spectra of P3HT and concluded that self-localisation of excitons occurs approximately 100 fs following the photoexcitation event.[232] Furthermore, Wells and Blank demonstrated that highly correlated relaxation of P3HT excitons occurs at $t < 200$ fs.[237] The observed dynamic Stokes shift is the result of exciton self trapping mediated by low-frequency torsional modes of P3HT. Recently, Busby et al. used broadband pump-probe and pump-dump-probe spectroscopy to investigate the early-time dynamics of P3HT.[142] They concluded that small-amplitude torsional reorganisation (planarisation) of the thiophene units take place at $t < 1$ ps, while large-amplitude motions occur at $t > 1$ ps. While the long time constant, $\tau_4 = 530$ ps, represents the exciton lifetime,[232,234,235] the process with an intermediate time constant ($\tau_3 = 135$ ps) is attributable to additional slow torsional relaxation.[142,154,187,232,236,247,248]

Figure 3.2a also shows the ΔOD at 1050 nm as a function of pump-probe time delay in the pump-push-probe experiment (red triangles). The pump beam is modulated while the 900-nm push beam is on at all times. The arrival time of the push pulse in the pump-push-probe experiment is 25.8 ps after the pump pulse, which enables the exciton to be sufficiently relaxed before being excited by the push pulse. In this experiment, the exciton is generated in an identical fashion to the pump-probe experiment. However, after the exciton has undergone relaxation to the S_1 state, it is re-excited by the push pulse to a higher-lying state, S_n. The photophysical events in the pump-push-probe experiment are shown in Figure 3.1b. As a result, probing the ESA band as a function of time offers insight into the S_n to S_1 relaxation.

On introduction of the push pulse, the pump-push-probe result shows a significant deviation from the pump-probe transient, as shown in Figure 3.2a. The ΔOD signal at 1050 nm is depleted by approximately 30%, which is a direct measure of the level of excitons promoted by the push pulse to the S_n state. We have also performed a power dependence study of the push pulse while keeping the pump power constant. The results, which are found in Supporting Information, show that the depletion of the ΔOD signal at 1050 nm signal is linear with respect to the range of push powers used in this study. The majority of the ΔOD signal exhibits a rapid recovery, indicating the subsequent relaxation of excitons from the S_n state to the S_1 state. A portion of the signal shows an incomplete recovery over the duration of the experiment, which results in the signal difference in Figure 3.2a at $t > 25.8$ ps. Our analysis indicates that this signal difference is due to exciton dissociation by the push pulse to form free carriers, which is discussed below.

The effect of the push is highlighted in Figure 3.2b, which shows the change in ΔOD, *i.e.*, ΔΔOD. In other words, the data in Figure 3.2b is the difference between the two traces shown in Figure 3.2a, as follows.

$$\Delta\Delta\mathrm{OD}(\lambda, t) = \Delta\mathrm{OD}(\lambda, t)_{\text{push on}} - \Delta\mathrm{OD}(\lambda, t)_{\text{push off}} \tag{3.1}$$

Experimentally, this signal is acquired by modulating the push pulse while keeping the pump pulse on at all times. It is important to note that this simple light modulating arrangement instead of a more elaborate one employed in other studies[142,243] is used here because the push pulse only exhibits an optical response in the presence of the pump light, as shown in Supporting Information. In other words, the push-probe signal is negligible. It is noted that two-photon excitation of P3HT may be possible as the energy of two push photons overlaps with the linear absorption band of P3HT.

However, the push peak intensity used in our study (12.7 GWcm^{-2}) is ~30 times lower than that used in a study involving two-photon excitation of P3HT.[249] Hence, the negligible optical response by the push pulse alone is expected.

Figure 3.2b shows that the depletion of the ΔΔOD signal at $t = 25.8$ ps is followed by a fast recovery over a period of several picoseconds. In addition, it is apparent that there is a portion of the signal that fails to recover completely within the experimental time window. Four exponential decay components are used to fit the ΔΔOD data. The longest time constants τ_3–τ_4 are fixed at 135 ps and 530 ps, corresponding to the decay components in the pump-probe experiment as discussed above. The identical τ_3 and τ_4 values for these two sets of data are chosen on the grounds that apart from the early-time push pulse-associated dynamics, the decaying ΔOD signal with the push pulse (red curve in Figure 3.2a) is simply a portion of that without the push pulse, which can be shown using eq 3.1. In this case, the ΔOD signal with the push pulse is 11% lower than that without it (Figure 3.2a), indicating that the same percentage of the total exciton population is unrecovered after excitation by the push pulse. We argue that the "missing" excitons as a result of the push pulse-excitation are attributable to exciton dissociation to generate charge carriers in P3HT, consistent with the observation in a previous pump-push-probe study on a different conjugated polymer.[244]

It is important to note that in the event of exciton dissociation to form charge carriers, namely the electron and hole-polaron, they are expected to undergo rapid geminate recombination to yield ground-state P3HT because of the close proximity of the charged species.[250] Because the dissociated excitons do not relax back to the S_1 state, this phenomenon manifests as a persistent, negative ΔΔOD signal such as that shown in Figure 3.2b. Therefore, it follows that exciton dissociation should result in a corresponding positive ΔΔOD signal in the spectral region where ground-state P3HT absorbs due to charge recombination. Indeed such a signal is present in our experiment and shown in Supporting Information. The magnitude of this positive ΔΔOD signal is a function of the ground-state absorbance, the level of exciton produced in the photoexcitation event by the pump pulse, the proportion of excitons promoted by the push pulse and the proportion of the unrecovered excitons. Calculation of the expected value for the positive ΔΔOD signal at 465 nm is shown in Supporting Information. The magnitude of the observed ΔΔOD signal and the expected value show excellent agreement and hence the assignment of the unrecovered ΔΔOD signal in the presence of the push pulse to exciton dissociation is strongly supported. Pump-push-probe experiments were also carried out using $\lambda_{\text{push}} = 1200$ nm and the results are shown in Supporting Information. It is interesting that the ΔΔOD dynamics are nearly identical to those with $\lambda_{\text{push}} = 900$ nm. The lack of dependence of the dynamics on push pulse wavelength has implications on the exciton binding energy and is discussed below. With regards to the "missing" excitons, we have also considered that the negative ΔΔOD signal as shown in Figure 3.2b may be due to stimulated deactivation of the exciton by the push pulse. However, this alternative explanation is highly unlikely because the push pulse, which has a wavelength of 900 nm or longer, is sufficiently detuned from any emission wavelengths of P3HT excitons such that stimulated deactivation is expected to be negligible. In short, exciton dissociation by the push pulse is significantly more likely. We have also considered that the persistent ΔΔOD signal in Figure 3.2b may be due to production of triplet excitons as a consequence of charge carrier recombination. Although our ΔOD data show the presence of triplet excitons, which manifests as a long-lived induced absorption band at 820 nm,[235] it is unclear if triplet excitons play a significant role in the ΔΔOD data at the same wavelength (Supporting Information). However, the dynamics and magnitude of the positive ΔΔOD signal at 465 nm indicate that the ground state recovery is complete within picoseconds, which is significantly shorter than the triplet exciton lifetime of hundreds of nanoseconds.[235] Therefore, we believe the contribution of triplet states is insignificant.

To our knowledge, these results are the first observation of exciton dissociation to generate short-lived charge carriers in a conjugated polymer in solution, in which the generation and recombination of charges are confined on a single chain. A number of studies have reported generation of charge carriers in neat polymer films due to photoexcitation.[235,244,251–255] In particular, Cook et al. have reported generation of charge carriers in a P3HT thin-film.[235] By analyzing their kinetic results, they concluded that generation of polarons is an early-time photo-induced event, which takes place prior to the emission of the singlet exciton. While a portion of the charge carriers in films are able to overcome geminate recombination due to sufficiently high charge mobility, the charge carriers in single P3HT chains are confined on the polymer chains and hence are able to undergo rapid geminate recombination. Ultrafast geminate recombination of charges on a conjugated polymer provides a valuable measure of the yield of charge generation due to re-excitation of excitons by the push pulse. As mentioned above, the negative ΔΔOD signal at the push pulse-arrival time in Figure 3.2b indicates excitation of the exciton and the long-lived signal reflects the depletion of excitons due to geminate recombination. As a result, the yield of charge generation can be calculated by taking the ratio between the amplitudes of the two signals. In this case, using the ΔΔOD results with $\lambda_{\text{probe}} = 1050\,\text{nm}$ in Table 3.1, the yield of charge generation is therefore $(|A_3| + |A_4|)/\sum_n |A_n|$, which has a value of ~11%. As mentioned above, Gadermaier et al. used pump-push-probe spectroscopy to investigate a thin film of methyl-substituted ladder-type poly(para)phenyl.[244] An important conclusion from their study is that the charge carrier generation has a strong push arrival time-dependence. Their results show a maximum charge carrier yield at a pump-push delay of ~0.3 ps, which is followed by a significant decrease such that a negligible yield is present at a pump-push delay of ≥ 3 ps. In this study, we have also investigated the dependence of charge carrier generation on the pump-push time delay in which delays ranging from 0.25 to 500 ps were used. Interestingly, no dependence on the pump-push delay was observed. As shown in Supporting Information, throughout the entire lifetime of the exciton the push pulse consistently results in dissociation of ~11% of the high-energy exciton population to yield charge carriers. The dependence of charge carrier generation yield on the pump pulse delay time is possibly related to the early-time dynamics of the polymer. It is known that methyl-substituted ladder-type poly(para)phenyl undergoes vibrational cooling in the first few picoseconds upon photoexcitation and during which time “hot” excitons can be dissociated effectively to form charge carriers.[244] In contrast, early-time dynamics of P3HT are related to torsional relaxation.[142,236] It is conceivable that a significant portion of P3HT excitons are nearly fully relaxed even at the earliest pump-push delay in our study, especially because a recent study shows that ultrafast torsional relaxation occurs on a time scale of ~100 fs.[242] As a consequence, a negligible dependence of charge carrier generation on the pump-push delay is present for P3HT.

The results on charge carrier generation suggest that the exciton binding energy of single P3HT chains in tetrahydrofuran is approximately 1.03 eV or lower, because we have used a λ_{push} as long as 1200 nm, as shown in Supporting Information. Studies have shown that the exciton binding energy of isolated chains is typically 2 to 3 eV.[256–258] However, it must be noted that these results are based on theoretical modelling on single polymer chains alone, *i.e.*, in the absence of any solvent. Furthermore, these studies showed that in a polymer film, owing to a significant level of interchain coupling, dielectric screening of conjugated polymers results in the decrease of exciton binding energy to ∼1 eV. It is well established by experimental measurements that the exciton binding energy in P3HT films is $\leq$ 1 eV.[259] For several other conjugated polymers including MEH-PPV, PFO and P3OT, the exciton binding energies of the films are even lower, ranging from 0.3 to 0.6 eV.[146] Therefore, it is clear that the presence of a dielectric medium, *e.g.*, a solvent such as THF, around the conjugated polymer can lower the exciton binding energy. It is interesting that in a study where electrolytes were added to poly-2,7-(9,9-dihexylfluorene) in THF, an exciton binding energy of 0.2 eV was measured.[260] Overall, the $\leq$ 1 eV exciton binding energy from this study shows good agreement with previous studies.

The two remaining decay components in the ΔΔOD data, with time constants τ_1 and τ_2 of 0.16 ps and 2.4 ps, respectively, are present as a result of the transition from S_n to S_1. A recent study by Clark et al. offers important insight into the ultrafast non-radiative transition from S_n to S_1.[242] By examining oligofluorenes in solution using pump-push-probe spectroscopy, these authors observed a dynamic component in their data with a sub-0.1 ps time constant. Using non-adiabatic excited-state molecular dynamics to model their data, Clark et al. concluded that oligofluorenes can undergo a conformation change on this ultrafast time scale, which is analogous to inertial solvation observed in the 1990s.[261–263] Therefore, in our study it is reasonable to assign the decay component with a time constant of 0.16 ps time to ultrafast torsional relaxation. The slower component with a time constant of 2.4 ps can be assigned to larger amplitude and further torsional relaxation, which has been observed in previous studies.[142,236] It is interesting that the decay time constants and relative amplitudes of these two relaxation components are independent of the pump-push delay time (Supporting Information). These results indicate that the relaxation dynamics of the S_n state are insensitive to whether the original S_1 is a torsionally "hot" or "cool" exciton. This outcome is particularly interesting especially with long pump-push delay times, *e.g.*, 500 ps. In this case, it is reasonable to assume that the S_1 state is fully relaxed, with the singlet exciton localized on a chromophoric segment with a significant conjugation length. In the event that relocalisation of the push pulse-induced high-energy exciton occurs within the same conjugated segment, the S_n to S_1 relaxation is expected to be free of the larger amplitude torsional relaxation. However, the presence of the decay component with a 2.4 ps time constant at all pump-push delay times suggests that the push pulse induces a high level of exciton delocalisation, allowing it to relocalize and undergo relaxation in a different segment of the polymer chain not previously excited by the pump pulse.

Figure 3.3 shows the results of repeating the pump-probe and pump-push-probe experiments, but probing the SE band at 600 nm. Figures 3.3a and 3.3b show the data from the ΔOD and ΔΔOD experiments, respectively. The data appear to mirror that obtained from probing the ESA band (Figure 3.2), which is expected as both are the result of transitions originating from the same electronic state. The similarity of the ESA and SE dynamics is confirmed in the fitting parameters (Table 3.1) where the equivalent components are seen in both the pump-probe and pump-push-probe experiments. A subtle difference between the ESA and SE data is the magnitude of

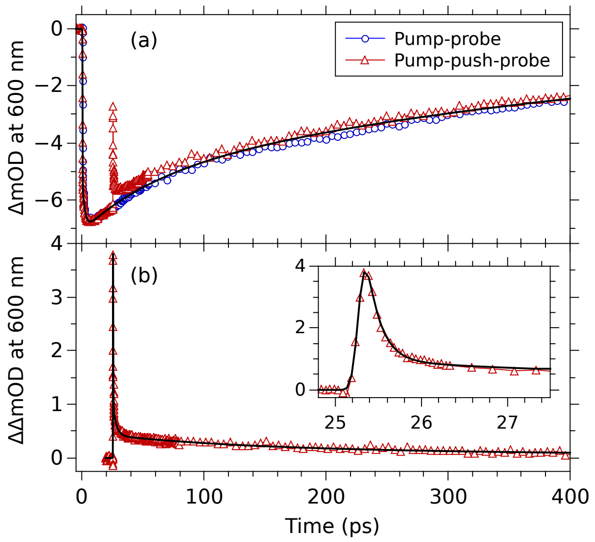

Figure 3.3: The dynamics of stimulated emission at 600 nm in the pump-probe (a, blue circles) and pump-push-probe experiments (a, red triangles). The change in ΔOD due to the push pulse is shown in (b). Fit curves are indicated with black lines.

the sub-picosecond recovery component. This difference can be seen in Figures 3.2a and 3.3a as the extent of the deviation in the signal due to the push pulse. As ΔOD is a indication of the population of excitons, ΔΔOD/ΔOD at the push pulse arrival time should be a measure of the proportion of excitons being affected by the push pulse, and should be identical for both the ESA and SE data. This is not the case however, with this proportion being ∼30% for the ESA and ∼50% for the SE data. The difference can be attributed to dissociation of the exciton into an electron and hole-polaron. The hole-polaron has been observed previously in transient absorption studies of P3HT films, nanoparticles and nanowires, exhibiting an absorption peak overlapping the red-side of the emission.[180,235,246,264] A short-lived hole-polaron absorption induced by the push would manifest as a positive ΔΔOD signal. As a consequence of the overlap between this positive signal and the negative signal of the SE band, an apparently larger than normal decrease in SE due to the push is observed. The ESA data are free from the same effect, as the hole-polaron absorption does not overlap the ESA band. This observation provides further support that the push pulse is causing dissociation of the exciton and production of charge carrier states.

Figure 3.4 summarizes the pump-push-probe results in this study. The pump vertically excites the polymer to form a delocalized singlet exciton which rapidly localizes to a section of the polymer within ∼100 fs to give the S_1 state. Torsional motion between the thiophene rings acts to increase the planarisation of the polymer section, lowering the energy of the exciton. Through the process of EET, the exciton may hop to nearby, lower energy regions of the chain, which themselves can undergo further relaxation due to torsional motion. The arrival of the push pulse then further excites the exciton, producing a high-energy, delocalized state, S_n. From the highly excited state, several relaxation pathways are available. The majority of the high-energy excitons rapidly decay back to the original S_1 state, possibly localizing in a new, previously unvisited conjugated segment of the polymer on a time scale of ∼160 fs, which corresponds to the fastest decay time constant observed in this study. This assignment shows agreement with the expected lifetime of the S_n state of ∼250 fs, which is calculated using the gap

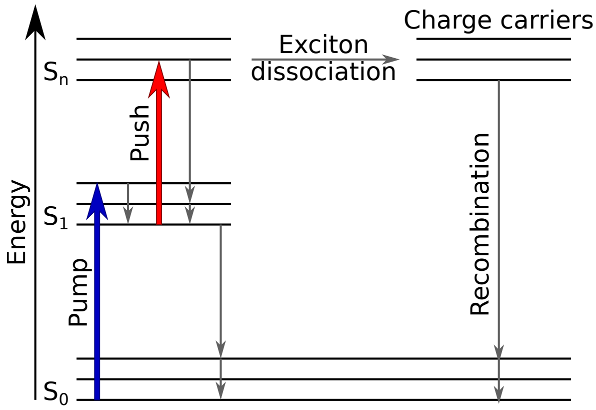

Figure 3.4: Energy level diagram showing the initial excitation by the pump pulse to produce the singlet exciton. The push pulse promotes the exciton to a high-energy, delocalized state which allows dissociation to produce charge carriers.

law.[244,265] The energy gap between the S$_1$ and S$_n$ state is estimated using the peak wavelength of the ESA band of 1075 nm. The delocalisation of the high-energy exciton also provides the opportunity for exciton dissociation to produce charge carrier states (electron and hole-polaron). Owing to the presence of charge carriers on the same polymer chain, geminate recombination occurs rapidly, returning the polymer to the S$_0$ ground-state.

The rate constant of exciton dissociation, k_{ED}, may be calculated using the yield of exciton dissociation, Φ_{ED}, and the lifetime of the S$_n$ state, τ_{S_n} and eq 3.2.

$$\Phi_{ED} = \frac{k_{ED}}{1/\tau_{S_n}} \tag{3.2}$$

Values of 11% and 160 fs are used for Φ_{ED} and τ_{S_n}, respectively. The calculated k_{ED} has a value of $\sim$0.67 ps^{-1}, which corresponds to an exciton dissociation time constant, τ_{ED}, of $\sim$1.5 ps. The $\Delta\Delta$OD data at a wavelength under the ground-state absorption spectrum (Supporting Information), which reports the recovery of the ground-state due to geminate recombination of charge carriers produced during exciton dissociation, shows an increase on a time scale consistent with τ_{ED}. This result indicates that geminate recombination occurs significantly faster than exciton dissociation, which is expected given the close proximity of charge carriers on the polymer chain.

In conclusion, we have used pump-push-probe spectroscopy to show that excitons on isolated P3HT chains in solution may be delocalized by the use of a secondary photoexcitation, a push pulse. Of these high-energy excitons, $\sim$11% were found to dissociate into charge carriers, with the remainder having the possibility of re-localizing on a different region of the polymer chain. Exciton dissociation is present with a push wavelength up to 1200 nm, giving a value for the binding energy of the exciton of $\leq$ 1 eV. The lack of time dependence of the pump-push delay indicates that ultrafast torsional relaxation causes the majority of relaxation of the P3HT exciton on a time scale of $\leq$ 160 fs.

Experimental

Materials and sample preparation. Regioregular P3HT (MW = 50 kg mol^{-1}, 99% regioregular, Rieke Metals) was dissolved in freshly distilled THF (reagent grade, Scharlau) using sonication at 25 °C for one hour to produce 0.1 g L^{-1} solutions, which were then filtered through a 0.2 µm nylon filter.

Steady state spectroscopy. The steady-state absorption spectrum was obtained using a P3HT solution diluted to 0.01 g L^{-1} using a quartz cuvette with a 1 cm pathlength and a Cary 300 UV-visible absorption spectrophotometer. The fluorescence spectrum was obtained on a Perkin-Elmer LS-55 fluorescence spectrometer with the same sample used for the steady-state absorption measurement. Excitation wavelength was 400 nm and excitation and emission slit widths set at 5 nm.

Pump-probe and pump-push-probe spectroscopy. Schematic diagram of the pump-probe/pump-push-probe transient absorption apparatus are supplied in Supporting Information. All laser pulses originated from a Ti:sapphire regenerative amplifier (Spectra-Physics, Spitfire Pro XP 100F) producing 100 fs pulses at a repetition rate of 1 kHz centered at 800 nm. Pump pulses at 400 nm were generated by frequency doubling of the fundamental output using a 0.5 mm BBO crystal. The pump pulse energy was 1.8 µJ with a spot size of 700 µm. Push pulses at 900 nm or 1200 nm were produced using an optical parametric amplifier (Light Conversion, TOPAS-C) with a pulse energy of 1.8 µJ and a spot size of 475 µm. An optical chopper was used to mechanically modulate either the pump or push beams at a frequency of 500 Hz to obtain the ΔOD or $\Delta\Delta$OD values, respectively. A white light continuum was generated for probe pulses by a 3.2 mm thick sapphire crystal for the 600 nm probe light and a 12.7 mm thick sapphire crystal for the 1050 nm probe light, with the arrival time determined by a computer controlled delay line. The probe was split into signal and reference beams and fed to a pair of linear detectors. CMOS sensors were used for the visible (Ultrafast Systems, CAM-VIS-2) and InGaAs diode arrays for the near-IR (Ultrafast Systems, CAM-NIR) wavelengths. Probe spot sizes were 260 µm for the visible and 75 µm for the near-IR, with the energy of the pulses always much less than those of the pump and push pulses. Relative to the probe, the pump and push beam crossing angles were 5° and −4° respectively, with polarisations set at the magic angle of 54.7°. Samples had a concentration of 0.02 g L^{-1} for the visible and 0.1 g L^{-1} for the near-IR experiments and were studied in a quartz cuvette with a 2 mm path length (Starna Cells 21-Q-2) with continuous stirring. By changing the sample after each run of the experiments, each sample was subjected to less than 90 minutes of laser exposure and effects of photobleaching was not observed to exceed 10%. Fitting of the data was performed using a Gaussian instrument response function of 150 fs (FWHM).

Acknowledgements

The authors acknowledge Mr Scott N. Clafton for his assistance in experiment and data analysis, Dr David M. Huang for stimulating discussion, and the Australian Research Council for funding support (LE0989747).

Supporting Information

Ground State Bleaching

Ground state absorbance at 465 nm: $\mathrm{GSA}_{465} = 0.21$
Ground-state bleach (GSB) ΔOD at 465 nm and 25 ps: $\mathrm{GSB}_{465} = -0.0065$
Proportion of excitons produced by pump: $\frac{|\mathrm{GSB}_{465}|}{\mathrm{GSA}_{465}} = 0.031 \equiv 3.1\%$

ΔOD at 1050 nm and 25 ps without push: $\Delta\mathrm{OD}_{1050} = 0.0366$
ΔΔOD at 1050 nm and 25 ps with push: $|\Delta\Delta\mathrm{OD}_{1050}| = 0.0102$
Proportion of excitons affected by push: $1 - \frac{\Delta\mathrm{OD}_{1050} - |\Delta\Delta\mathrm{OD}_{1050}|}{\Delta\mathrm{OD}_{1050}} = 0.28 \equiv 28\%$

Fitting parameters for 3-pulse data show some excitons affected by the push are not recovering: $A_3 + A_4 = 0.11 \equiv 11\%$
As a proportion of total ground state absorbance: $0.21 \times 0.031 \times 0.28 \times 0.11 = 0.00022$

Change in GSB signal due to the push pulse is shown in Figure 3.5, with a change in in ΔOD (ΔΔOD) of 0.0002 appearing within approximately 5 ps. This indicates that some proportion of excitons that absorb the push pulse are rapidly returning to the ground state but are not relaxing back through the normally excited state.

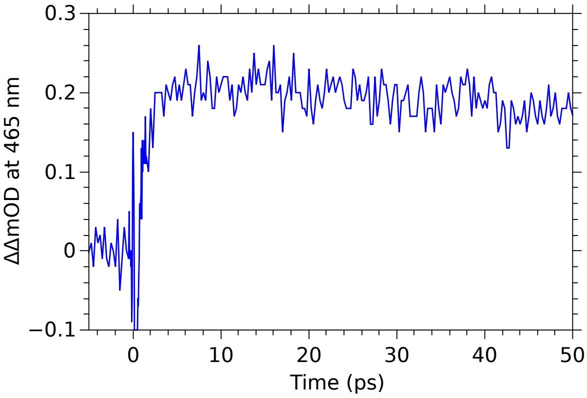

Figure 3.5: Change in the GSB band at 465 nm due to the push pulse. Despite the low signal to noise level it can be seen that the push is causing an increase in ground state population.

Single Strand Assumption

Volume containing a single polymer strand (V_{strand}):
Molecular weight of P3HT sample: $M_{strand} = 50\,000\,\mathrm{g\,mol^{-1}}$
Molecular weight of monomer unit ($C_{10}H_{14}S$): $M_{monomer} = 166.3\,\mathrm{g\,mol^{-1}}$
Number of monomer units per strand: $n = \frac{M_{strand}}{M_{monomer}} = 300$
Length of single monomer unit: $L_{monomer} = 0.39\,\mathrm{nm}$
Contour length of polymer strand: $L_c = n \times L_{monomer} = 117\,\mathrm{nm}$
Persistence length:[76] $L_p = 2.4\,\mathrm{nm}$
Radius of gyration:

$$\begin{aligned} {R_g}^2 &= \frac{1}{3}L_pL_c - {L_p}^2 + 2\frac{{L_p}^3}{L_c}\left(1-\frac{L_p}{L_c}\left[1-e^{-\frac{L_c}{L_p}}\right]\right) \\ &= 8.81\times10^{-17}\,\mathrm{m}^2 \\ R_g &= 9.38\times10^{-9}\,\mathrm{m} \\ &= 9.38\,\mathrm{nm} \end{aligned}$$

Volume of cube containing a strand: $V_{strand} = (2R_g)^3 = 6.6\times10^3\,\mathrm{nm}^3$

Volume allowed in solution for a single polymer strand ($V_{allowed}$):
Concentration of polymer solution: $C = 0.1\,\mathrm{g\,L^{-1}} \equiv 2\,\mu\mathrm{M}$
Avogadro's number: $N_A = 6.022\times10^{23}\,\mathrm{mol^{-1}}$
Strands per unit volume: $N_V = C\times N_A = 1.2\times10^{18}\,\mathrm{L^{-1}} \equiv 1.2\times10^{-6}\,\mathrm{nm^{-3}}$
Volume allowed per strand: $V_{allowed} = \frac{1}{N_V} = 8.3\times10^5\,\mathrm{nm}^3$

Probability of multiple strands interacting:
Expected value: $\lambda = \frac{V_{strand}}{V_{allowed}} = 7.95\times10^{-3}$
Poisson distribution probability of x strands occupying same space:

$P_{(x=0)} = \frac{\lambda^0 e^{-\lambda}}{0!} = 0.99$
$P_{(x=1)} = \frac{\lambda^1 e^{-\lambda}}{1!} = 7.9\times10^{-3}$
$P_{(x=2)} = \frac{\lambda^2 e^{-\lambda}}{2!} = 3.1\times10^{-5}$
$P_{(x=3)} = \frac{\lambda^3 e^{-\lambda}}{3!} = 8.3\times10^{-8}$

Time-Resolved Fluorescence

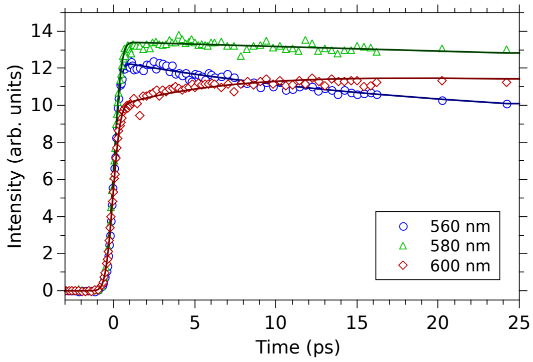

Figure 3.6: Results of the fluorescence upconversion experiments showing differing dynamics at each wavelength, indicating dynamic red-shifting of the emission is occurring.

Spectral Evolution

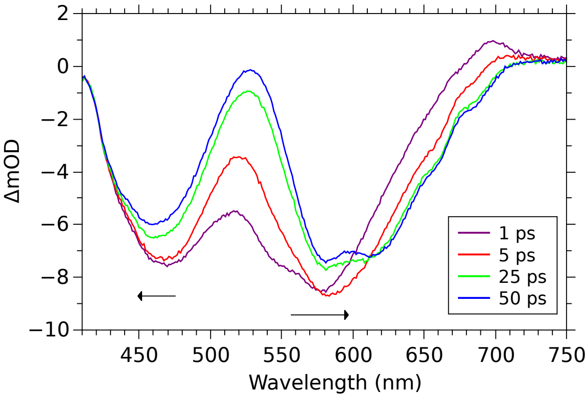

Figure 3.7: Evolution of the visible spectrum during the pump-probe experiment. The arrows indicate the red-shifting of the SE peak and a slight blue-shifting of the GSB peak.

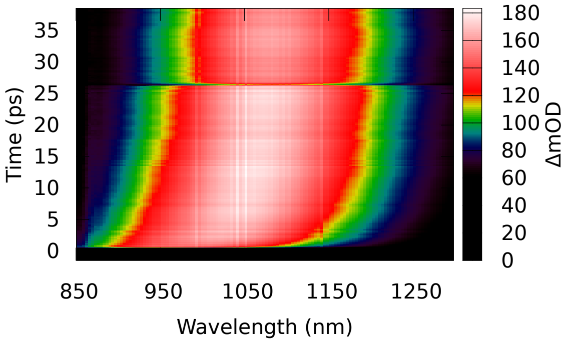

Figure 3.8: Evolution of the ESA peak during the pump-push-probe ΔOD experiments. Red-shifting of the peak is observed over the course of the experiment. The arrival of the push-pulse can be seen at $t = 25\,\text{ps}$.

Push Time and Power Dependency

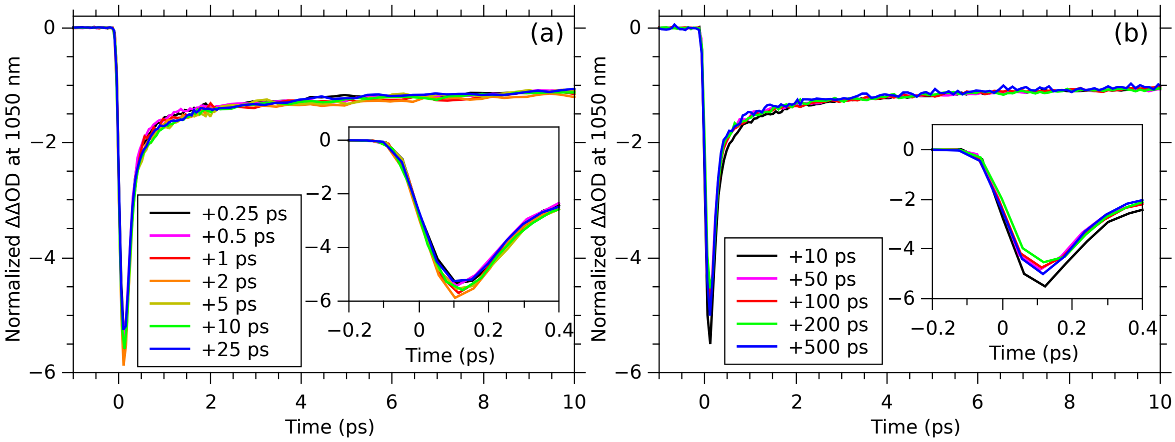

Figure 3.9: Dependency of the change in excited state absorption on the arrival time of the push pulse after the initial excitation. All curves have been normalised to the change in ΔOD 15 ps after the push pulse. Results from time intervals between 0.25 and 25 ps are shown in (a), with corresponding fitting parameters in Table 3.3. Additional experiments were conducted with pump-push delays over the entire lifetime of the exciton, (b), confirming the lack of time dependence.

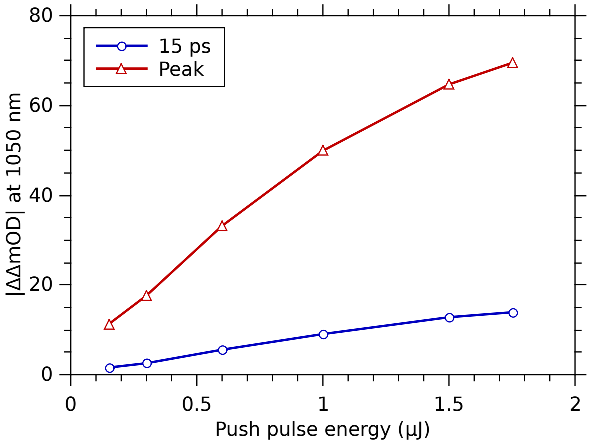

Figure 3.10: Dependency of the excited state absorption on the power of the push pulse showing the magnitude of the change in ΔOD at 15 ps after the arrival of the push pulse, and at the peak change in ΔOD at approximately 150 fs.

Push-Probe Experiment

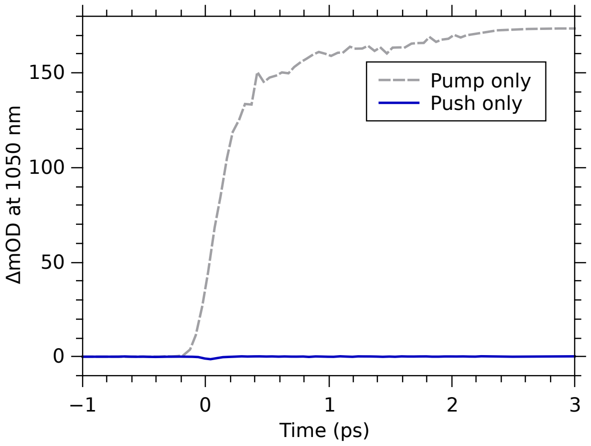

Figure 3.11: Change in optical density at 1050 nm in the presence of either the 900 nm push pulse (solid line) or the 400 nm pump pulse (dashed line) only. The absence of the induced absorption band from the 900 nm experiment shows that excitons are only produced by the 400 nm pump pulse.

Triplet Exciton Population

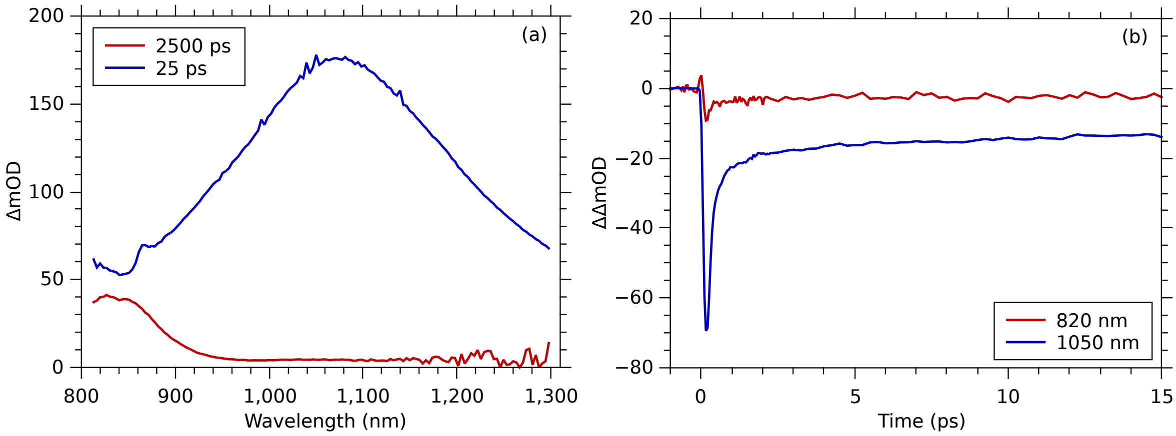

Figure 3.12: (a) Triplet excitons are observed in the ΔOD data as a long-lived absorption peak centered around 820 nm, most visible at the maximum experimental time window of 2.5 ns after the singlet exciton absorption has decayed. (b) The change in ΔOD at 820 nm does not show evidence of a significant increase in triplet excitons due to the push pulse.

Fitting Parameters

Table 3.2: Fitting parameters for the pump-probe (ΔOD) data.[a]

expt.	$A_1{}^b$	τ_1 (ps)	A_2	τ_2 (ps)	A_3	τ_3 (ps)
$\Delta\mathrm{OD}_{1050}$	−0.19	2.4	0.14	135	0.66	530^c
$\Delta\mathrm{OD}_{600}$	0.18	2.1	−0.22	60	−0.60	530^c

[a] The ΔOD data was fit to a multi-exponential function $f(t) = \sum_n A_n e^{-t/\tau_n}$. All parameters have a relative error of 15%. [b] $\sum_n |A_n| = 1$. [c] Fixed to value obtained from fluorescence lifetime measurements.

Table 3.3: Fitting parameters for the pump-push-probe ($\Delta\Delta\mathrm{OD}_{1050}$) data with $\lambda_{\mathrm{push}} = 900\,\mathrm{nm}$.[a]

push (ps)	$A_1{}^b$	τ_1 (ps)	A_2	τ_2 (ps)	A_3	τ_3 (ps)	A_4	τ_4 (ps)
+0.25	−0.83	0.16	−0.06	2.6	−0.09	135^c	−0.03	530^d
+0.5	−0.83	0.17	−0.05	4.4	−0.09	135^c	−0.03	530^d
+1	−0.83	0.17	−0.06	3.9	−0.09	135^c	−0.03	530^d
+2	−0.83	0.17	−0.06	4.5	−0.08	135^c	−0.03	530^d
+5	−0.80	0.17	−0.08	2.6	−0.08	135^c	−0.04	530^d
+10	−0.80	0.16	−0.08	2.6	−0.08	135^c	−0.04	530^d
+25	−0.80	0.16	−0.09	2.4	−0.07	135^c	−0.04	530^d

[a] The $\Delta\Delta$OD data was fit to a multi-exponential function $f(t) = \sum_n A_n e^{-t/\tau_n}$. All parameters have a relative error of 15%. [b] $\sum_n |A_n| = 1$. [c] Fixed to value obtained from pump-probe experiment. [d] Fixed to value obtained from fluorescence lifetime measurements.

Table 3.4: Fitting parameters for the pump-push-probe ($\Delta\Delta\mathrm{OD}_{1050}$) data with $\lambda_{\mathrm{push}} = 1200\,\mathrm{nm}$.[a]

push (ps)	$A_1{}^b$	τ_1 (ps)	A_2	τ_2 (ps)	A_3	τ_3 (ps)	A_4	τ_4 (ps)
+0.25	−0.78	0.22	−0.09	4.7	−0.11	135^c	−0.01	530^d
+0.5	−0.77	0.26	−0.09	8.5	−0.11	135^c	−0.02	530^d
+1	−0.74	0.30	−0.11	5.7	−0.13	135^c	−0.02	530^d
+2	−0.77	0.26	−0.10	5.2	−0.11	135^c	−0.02	530^d
+5	−0.74	0.32	−0.12	4.7	−0.13	135^c	−0.02	530^d
+10	−0.78	0.24	−0.10	4.5	−0.10	135^c	−0.02	530^d
+25	−0.76	0.29	−0.11	4.2	−0.11	135^c	−0.03	530^d

[a] The $\Delta\Delta$OD data was fit to a multi-exponential function $f(t) = \sum_n A_n e^{-t/\tau_n}$. All parameters have a relative error of 15%. [b] $\sum_n |A_n| = 1$. [c] Fixed to value obtained from pump-probe experiment. [d] Fixed to value obtained from fluorescence lifetime measurements.

Table 3.5: Fitting parameters for the pump-push-probe ($\Delta\Delta OD_{600}$) data with $\lambda_{push} = 900\,\mathrm{nm}$.[a]

push (ps)	$A_1{}^b$	τ_1 (ps)	A_2	τ_2 (ps)	A_3	τ_3 (ps)	A_4	τ_4 (ps)
+0.25	0.86	0.16	0.08	2.8	0.03	109	0.03	530^c

[a] The ΔΔOD data was fit to a multi-exponential function $f(t) = \sum_n A_n e^{-t/\tau_n}$. All parameters have a relative error of 15%. [b] $\sum_n |A_n| = 1$. [c] Fixed to value obtained from fluorescence lifetime measurements.

Experimental Section

Fluorescence lifetime measurement. Fluorescence lifetimes were measured using a fluorescence upconversion spectrometer (Ultrafast Systems, Halcyone). A continuous wave 532 nm Nd:YVO_4 laser at 8 W (Spectra-Physics, Millenia Prime) pumped a mode-locked Ti:Sapphire oscillator (Spectra-Physics, Tsunami) to produce 800 nm pulses at a rate of 80 MHz. A pulse picker selected pulses at a rate of 40 MHz that were then split into excitation and gate beams. The excitation wavelength of 400 nm was generated by second harmonic frequency doubling of the oscillator output. The gate pulse polarisation was set to the magic angle (54.7°) with respect to the excitation pulse to negate the effects of anisotropy.

Each run of the experiments consisted of the averaging of three scans with each time point sampled for three seconds.

Samples were tested in a quartz cuvette with a 2 mm path length (Starna Cells 21-Q-2) and stirred continuously during the experiments.

Pump-probe and pump-push-probe spectroscopy. A schematic diagram of the apparatus used for the pump-probe and pump-push-probe experiments is shown in Figures 2.1 and 2.2.

CHAPTER 4

Molecular-Level Details of Morphology-Dependent Exciton Migration in Poly(3-hexylthiophene) Nanostructures

Statement of Authorship

Title of Paper	Molecular–Level Details of Morphology–Dependent Exciton Migration in Poly(3-hexylthiophene) Nanostructures
Publication Status	Published
Publication Details	Tapping, P. C.; Clafton, S. N.; Schwarz, K. N.; Kee, T. W.; Huang, D. M. *J. Phys. Chem. C* **2015**, *119*, 7047–7059. DOI: 10.1021/acs.jpcc.5b00705

Principal Author

Principal Author	Patrick C. Tapping		
Contribution to the Paper	Experimental work, development of exciton hopping code, data analysis, construction of figures, writing of manuscript.		
Overall Percentage	85%		
Signature		Date	18/7/16

Co-Author Contributions

By signing the Statement of Authorship, each author certifies that the stated contributions to the following publication are accurate and that permission is granted for the publication to be included in this thesis.

Co-Author	Scott N. Clafton		
Contribution to the Paper	Fluorescence anisotropy data on P3HT nanofibres.		
Signature		Date	21/09/16

Co-Author	Kyra N. Schwarz		
Contribution to the Paper	Development of coarse-grained MD force field for P3HT.		
Signature		Date	19/07/2016

Co-Author	Tak W. Kee		
Contribution to the Paper	Supervision of experimental work, assistance with review and editing of manuscript.		
Signature		Date	22/7/16

Co-Author	David M. Huang		
Contribution to the Paper	Supervision of project, running of MD simulations, assistance with writing and editing of manuscript, corresponding author.		
Signature		Date	22/7/16

Abstract

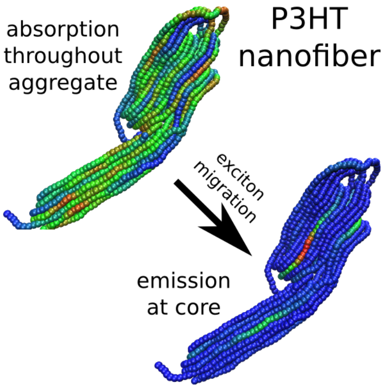

The morphology dependence of exciton transport in the widely used conjugated polymer poly(3-hexylthiophene) (P3HT) is elucidated by combining an accurate mesoscale coarse-grained molecular dynamics simulation model of P3HT structure with a Frenkel–Holstein exciton model. This model provides a more realistic representation than previously achieved of the molecular-level details of exciton transport on large length scales relevant to electronic applications. One hundred 300-monomer regioregular P3HT chains are simulated at room temperature for microseconds in two implicit solvents of differing solvent quality in which the polymer chains adopt contrasting morphologies: nanofibre-like aggregates or well-separated extended conformations. The model gives reasonable quantitative agreement with steady-state absorption and fluorescence and time-resolved fluorescence experiments, and provides valuable insight into the mechanism of exciton transport in conjugated polymers. In particular, exciton transfer in nanofibre aggregates is shown to occur mainly through interchain hops from chromophores on the aggregate surface towards the aggregate core, a behaviour with important implications for organic electronic applications. Furthermore, the counterbalancing effects of greater orientational order and faster exciton transport in nanofibre aggregates than in extended chains is found to explain the puzzling observation of similar fluorescence anisotropy decay rates in nanofibres and free chains.

Introduction

The study of conjugated polymers is motivated by their use as electron donor or acceptor materials in the active layers of organic electronic devices such as solar cells[53] and light-emitting diodes.[266] Despite efficiencies of organic solar cells lagging behind those of conventional silicon devices, organic devices remain appealing because of their low-temperature and solution-based fabrication, which allows flexible and transparent solar cells to be made using low-cost high-throughput production methods.[43,78] Nevertheless, efficiency improvements would help to encourage the more widespread adoption of organic photovoltaics.[267]

The microstructure of the bulk heterojunction — the bicontinuous network of donor and acceptor materials in the active layer — has been shown to play a crucial role in charge generation, separation, and transport in organic solar cells, and hence in the overall device efficiency.[61,63,186,268] Developing a comprehensive understanding of the effects of bulk heterojunction morphology on device performance is challenging, given the crucial role that polymer structure on a wide range of length scales — from the molecular level up to the device scale — has on electronic properties.[269]

Theory and computation can provide valuable insight into the role of bulk heterojunction morphology in controlling device performance and could eventually lead to the rational design of organic solar cells. Most computational approaches to addressing the morphology dependence of the electronic properties of conjugated polymers and polymer-based devices fall into one of two classes, neither of which has been entirely satisfactory in treating the range of length scales that are important in conjugated-polymer devices. On the one hand are models in which the polymer structure is represented in full atomistic detail and electronic properties are computed using quantum chemical methods.[270–276] While such models are generally accurate, the high computational expense limits their use to systems of up to hundreds of atoms, and so polymer conformations cannot be effectively simulated. On the other hand are continuum or lattice models, in which the polymer structure and exciton or charge transport are described by a reduced set of variables on a grid.[277–282] Although simulations on experimental length and time scales are readily accessible using such models, molecular-level structure and chain topology are neglected.

Between these two extremes are mesoscale coarse-grained models in which groups of atoms are represented by a smaller number of interaction sites, allowing multiple chains of thousands of monomers to be feasibly simulated while retaining details about chain connectivity that are crucial to energy and charge-transport mechanisms.[95,247,283–286] However, previous calculations of this nature have used rather approximate models of polymer structure, with conformations usually generated from a random distribution and solvent effects neglected, which is unlikely to provide a accurate representation of the complexity of a real system.

In this work, we address this issue by starting with realistic structures of the polymer P3HT, obtained using an accurate, coarse-grained molecular dynamics model parameterised to reproduce the local structure and dynamics of an atomistic P3HT model.[217] Large multi-chain systems are simulated in two different solvents in which the P3HT chains adopt two conformationally distinct morphologies. P3HT was one of the first conjugated polymers used in the manufacture of organic solar cells[287] and is one of the most widely studied conjugated polymers, with over 1,400 scientific publications on this polymer in 2014 alone, according to Web of Science. P3HT readily exists in a variety of morphologies including amorphous bulk phases, nanoparticles, and semicrystalline nanofibres, which has significant effects on its physical, optical, and electronic properties.[87,88,91,288] We then use a Frenkel–Holstein exciton model[95,96,160,285] to determine the locations and energies of chromophores — a method that scales reasonably up to hundreds of polymer chains — in polymer conformations extracted from the coarse-grained molecular dynamics simulations. Finally, we perform kinetic Monte Carlo simulations of inter-chromophore exciton transfer using transfer rate coefficients derived from the Fermi Golden Rule, assuming a point-dipole approximation for inter-monomer interactions. We verify that the simulations reproduce experimental measurements and use them to provide new molecular-level insight into the mechanism of exciton migration through self-assembled P3HT nanostructures.

Computational Methods

Coarse-grained Molecular Dynamics

The solution-phase structure of P3HT was simulated using molecular dynamics of a coarse-grained polymer model, which has been described in detail in a previous publication.[217] Briefly, each hexylthiophene monomer was represented by a set of three spherical beads corresponding to the centres-of-mass of the thiophene ring and the first three methyl groups and last three methyl groups of the hexyl sidechain, respectively. This atomistic-to-coarse-grained mapping is shown diagrammatically in Figure 4.1a.

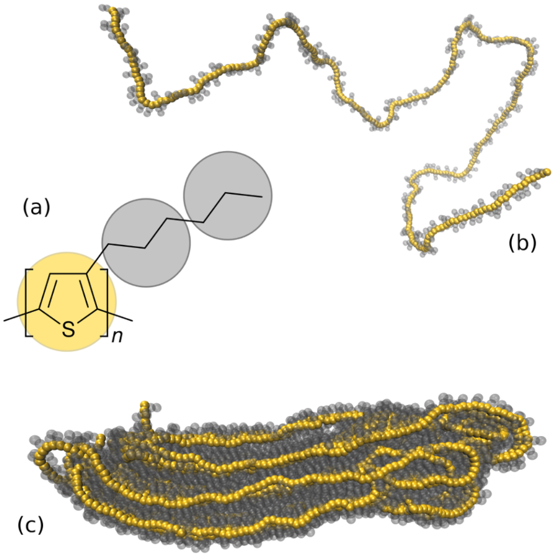

Figure 4.1: (a) Mapping of P3HT atomistic to coarse-grained sites and example structures of (b) a free chain and (c) a nanofibre aggregate. The polythiophene backbone is indicated in yellow, with the alkyl sidechain units shown in gray. The view of the nanofibre is looking down through the π-stacking direction, showing the alkyl sidechain interactions.

Simulations of the polymers were carried out in implicit solvent using Langevin dynamics at constant volume and temperature, with the interactions between coarse-grained sites parametrized so as to match the local structure and dynamics measured in constant-pressure simulations of an atomistic model of P3HT in an explicit solvent, anisole. This coarse-grained P3HT model was found to agree with the experimental phase behavior of P3HT in anisole, showing a transition between a non-aggregated and aggregated state as the temperature dropped below around 35 °C.[217] The size of the simulated aggregates also matched the widths of P3HT nanofibre aggregates measured experimentally. To model P3HT in a better solvent than anisole (e.g. tetrahydrofuran (THF)) in which the polymer chains are fully solvated and form extended structures at room temperature, the non-bonded polymer–polymer pair interactions were reduced by 10% of their value in the coarse-grained P3HT model in implicit anisole.

For convenience, we will refer to the simulations at room temperature of P3HT in implicit anisole and of P3HT in the better solvent as “nanofibre” and “free chain” simulations, respectively, to describe the polymer morphologies formed in these simulations. Note that the nanofibre aggregates simulated are not entire nanofibres as would be produced experimentally, but instead constitute several π-stacked layers in a section of a nanofibre.[217] Examples of the coarse-grained structures that result from these two solvent models are shown in Figures 1b and c. Both the nanofibre and free chain systems consisted of one hundred 300-monomer P3HT chains in a cubic simulation box with periodic boundary conditions enforced. Simulations were carried out at constant volume and temperature using Langevin dynamics, starting from an initial configuration of randomly placed and oriented chains with inter-monomer dihedral angles selected from a Boltzmann distribution of the inter-monomer torsional potential. The temperature was set to 293 K.

Nanofibre simulations were carried out at three different P3HT concentrations with total system volumes of 6.7×10^6, 9.8×10^5, and $4.3 \times 10^5\,\text{nm}^3$ for 2480, 1040, and

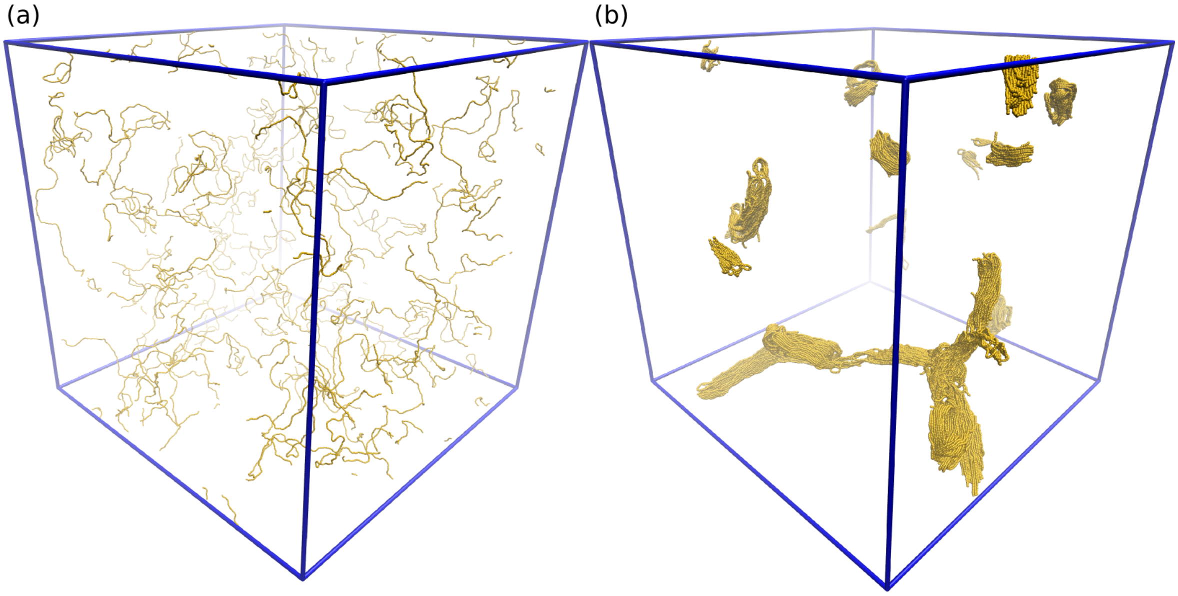

Figure 4.2: Snapshots from molecular dynamics simulations of 100 P3HT (a) free chains in good solvent and (b) nanofibre aggregates formed in a marginal solvent (anisole) at 0.13 and 1.0 wt% P3HT concentration respectively. For clarity, alkyl sidechains are not shown.

240 ns, respectively, to model 0.13, 1.0, and 2.0 wt% systems in anisole. P3HT has been shown experimentally to form nanofibres in anisole at concentrations between 0.005 and 1.0 wt%.[90] The 1.0 and 2.0 wt% simulations were started from configurations obtained by rapidly compressing the configuration of the 0.13 wt% simulation after 1.76 µs in a constant pressure simulation over a period of 0.5 ns. A single free chain simulation was carried out for 544 ns with the same system volume as the 0.13 wt% nanofibre system. It was verified that any measured quantities discussed below ceased to display systematic variations with time within the time scale of the simulations. Figure 4.2 shows examples of the resulting configurations for the free chain (Figure 4.2a) and nanofibre (Figure 4.2b) systems.

The friction coefficient for the Langevin dynamics in the nanofibre simulations was reduced by a factor of 10 from the value in Ref. 217 to accelerate nanofibre formation. While such a change would affect the dynamics of chain aggregation, it should not impact the thermodynamic stability of the polymer structures formed. Furthermore, both cases correspond to “high” friction in the context of aggregation dynamics, with the time scale of decorrelation of particle velocities in both cases being much shorter than the time scale of aggregation; as such, aggregation in both cases should occur by a similar mechanism of diffusive motion biased by inter-particle interactions.

Exciton Transport Simulations

Frenkel–Holstein Exciton Model

Exciton transport was simulated using a Frenkel–Holstein model developed by Barford and Tozer,[95,160] which accounts for the effects of molecular-level polymer structure on excitation energies and dynamics. Here, it was applied to chains representing P3HT generated from the coarse-grained molecular dynamics simulations described above. The main features of the model as they apply to the present work are given below.

The Frenkel exciton model treats the electron–hole pair as a single particle that can be delocalized in one dimension along the polymer chain.[289,290] The Frenkel–Holstein model extends the Frenkel model by coupling the exciton to the motion of the nuclei in the polymer.[149,150,190,191] The nuclei of the monomer units are treated classically, considering their motion to be described by a normal coordinate. In P3HT, the dominant normal coordinate is linked to the C=C stretching mode, as discussed below. The coupling to the normal mode simulates the relaxation process from the vertically excited state with the initial ground state geometry, to the excited but vibrationally relaxed state with the corresponding change in nuclear coordinates.

The Frenkel–Holstein Hamiltonian is

$$H = \sum_i (E_0 + \alpha_i - A\hbar\omega Q_i)\hat{a}_i^\dagger \hat{a}_i + \sum_{i>j} J_{ij}(\hat{a}_i^\dagger \hat{a}_j + \hat{a}_i \hat{a}_j^\dagger) + \frac{\hbar\omega}{2}\sum_i {Q_i}^2, \tag{4.1}$$

where i and j are numeric labels of the monomer units in a chain and the operators $\hat{a}_i^\dagger$ and $\hat{a}_i$ respectively create or destroy an exciton on monomer i. The on-site excitation energy is given by $(E_0 + \alpha_i)$, where α_i is a Gaussian random variate with standard deviation σ_α, representing energetic disorder caused by local structural fluctuations in the polymer system.[145,160] The electronic coupling between monomers i and j is described by J_{ij}. We only consider nearest-neighbour interactions ($j = i \pm 1$) in eq 4.1, which are expected to be dominant,[285] for which this term can be decomposed into two components,

$$J_{ij} = J^{\mathrm{DD}} + J^{\mathrm{SE}} \cos^2(\phi_{ij}). \tag{4.2}$$

J^{DD} is the through-space dipole–dipole coupling, for which the orientational and distance dependence between adjacent monomers is considered negligible. J^{SE} is the through-bond superexchange contribution, which is modulated by $\cos^2(\phi_{ij})$, where ϕ_{ij} is the dihedral angle between monomers i and j. In this way the planar arrangement of monomer units equates to maximum π-conjugation and therefore minimizes the excitation energy. The coupling of the exciton to the normal coordinate is described by the exciton–phonon coupling parameter, A, with Q_i being the dimensionless displacement at site i associated with the normal mode with angular frequency ω. The eigenstates of eq 4.1 define the wavefunctions of the exciton center-of-mass particle, with the corresponding eigenvalue giving the energy for the state.

When there is no coupling to the normal coordinate ($Q_i = 0$), eq 4.1 reduces to the Frenkel Hamiltonian, which is used to determine the vertically excited states. The lowest energy eigenstates of eq 4.1 define the absorbing chromophores, or localised exciton ground states (LEGSs), and therefore can be identified as those eigenstates that satisfy the inequality

$$\left|\sum_i \psi_{mi} \left|\psi_{mi}\right|\right| \geq 0.95, \tag{4.3}$$

where ψ_{mi} is the value of the wavefunction of state m on monomer i.[291] This criterion selects states for which 95% of the wavefunction density is in the main peak of the wavefunction and therefore discriminates against those states whose wavefunctions change sign and have both significant positive and negative amplitudes. The remaining higher-energy states describe local exciton excited states (LEESs), which have nodes but span the same chain segments as LEGSs, and quasi-extended exciton states (QEESs), which have nodes and spatially overlap more than one LEGS. These higher energy states contribute to the simulated absorption spectrum, but upon excitation are assumed to relax rapidly to the LEGS with maximum wavefunction overlap.[292] Note that for the monomer basis used to describe the eigenstates of the Hamiltonian in eq 4.1, a system of N monomers generates N eigenstates, which include both LEGSs and higher lying excited states. As a consequence, the number of LEGSs is generally significantly smaller than the number of eigenstates. An example of the wavefunctions of the LEGSs found on a P3HT chain is shown in Figure 4.3.

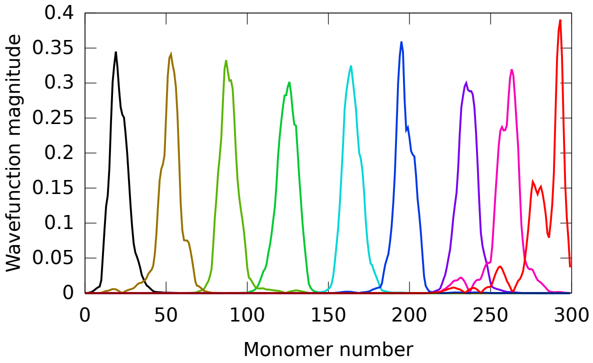

Figure 4.3: Computed wavefunction magnitudes for LEGSs on a 300-monomer polymer chain. The nine different states in this particular case are colour-coded for clarity.

Coupling to the normal coordinate ($Q_i \neq 0$) gives the wavefunctions and energies of electronically excited but vibrationally relaxed chromophores. This process is greatly simplified by assuming that the wavefunction is identical to that of the vertically excited state. This assumption has been validated by density matrix renormalisation group calculations performed by Marcus et al. on a Frenkel–Holstein model of disordered poly(*para*-phenylene) and by Barford and Tozer on poly(*para*-phenylenevinylene).[95,96] These calculations showed minimal variance between the wavefunctions of the vertically excited and vibrationally relaxed states. In the large-polaron limit applicable to conjugated polymers, the dimensionless displacement of monomer i depends on the exciton density in state m according to[150,285]

$$Q_{mi} = A|\psi_{mi}|^2. \tag{4.4}$$

As ψ_{mi} is assumed to be equal to the previously determined wavefunction of the LEGS m, the final term in eq 4.1 can thus be used to directly compute the vibrational relaxation energy,

$$E_{\mathrm{r}m} = \frac{A^2\hbar\omega}{2}\sum_i |\psi_{mi}|^4, \tag{4.5}$$

and therefore the energy of the emissive chromophores.

Exciton Localisation

The exciton center-of-mass, $\boldsymbol{R}_m$, for each LEGS m can be determined from the wavefunctions by

$$\boldsymbol{R}_m = \sum_i \boldsymbol{R}_i {\psi_{mi}}^2, \tag{4.6}$$

where $\boldsymbol{R}_i$ is the spatial position of monomer i. The root-mean-squared deviation of the wavefunction along the polymer chain is used to find the localisation length and therefore effective conjugation length, l_m, of the chromophore m by

$$l_m = \left(\frac{12\pi^2}{\pi^2 - 6}\right)^{\frac{1}{2}} \left[\sum_i i^2 {\psi_{mi}}^2 - \left(\sum_i i {\psi_{mi}}^2\right)^2\right]^{\frac{1}{2}}, \tag{4.7}$$

as described by Makhov and Barford.[144]

Monte Carlo Hopping Simulations

Exciton transport in the model occurs through a Förster-type resonance energy transfer process.[69,271,272] With the location and energy of the absorbing or acceptor and emissive or donor chromophores determined *via* the Frenkel–Holstein model, the nonradiative energy transfer rate between each donor and acceptor can be calculated. The transfer rate between a donor and acceptor pair, k_{DA}, depends on the distance between the chromophores and the alignment of their transition dipole moments as well as the spectral overlap of the donor and acceptor, and is calculated using the Fermi Golden Rule,

$$k_{\mathrm{DA}} = \frac{2\pi}{\hbar} {J_{\mathrm{DA}}}^2 X_{\mathrm{DA}}. \tag{4.8}$$

The electronic coupling between the donor (D) and acceptor (A) chromophores, which is assumed to comprise point-dipole interactions between monomers on the different chromophores not accounted for in the nearest-neighbour Hamiltonian (eq 4.1), is taken as[95]

$$J_{\mathrm{DA}} = \frac{{\mu_0}^2}{4\pi\epsilon_{\mathrm{r}}\epsilon_0} \sum_{\substack{\mathrm{D}i \\ \mathrm{A}j \\ i\neq j}} \frac{\hat{\boldsymbol{r}}_i \cdot \hat{\boldsymbol{r}}_j - 3\left(\hat{\boldsymbol{R}}_{ij} \cdot \hat{\boldsymbol{r}}_i\right)\left(\hat{\boldsymbol{R}}_{ij} \cdot \hat{\boldsymbol{r}}_j\right)}{|\boldsymbol{R}_i - \boldsymbol{R}_j|^3} \psi_{\mathrm{D}i}\psi_{\mathrm{A}j}, \tag{4.9}$$

where μ_0 is the magnitude of the transition dipole moment of a single monomer, ϵ_{r} is the relative permittivity of the polymer, $\hat{\boldsymbol{r}}_i$ is a unit vector in the direction of the transition dipole moment of monomer i, which is assumed to be oriented along the line joining the adjacent monomer centers,[293] and $\hat{\boldsymbol{R}}_{ij}$ is a unit vector between monomers i and j. This equation is equivalent to the line-dipole approximation for Coulombic coupling between chromophores, which gives good agreement with exact results for short chains for inter-chromophore distances more than twice the inter-monomer distance and is essentially exact for all chain lengths when the inter-chromophore distance exceeds three times the inter-monomer distance.[164] Most of the chromophores in our simulations satisfy the latter condition. This approximation may not be so accurate for adjacent π-stacked chromophores in polymer aggregates. We have compared the excitonic coupling between two ordered π-stacked P3HT decamers separated by 3.9 Å in the π-stacking direction from our model with the value from accurate transition density cube (TDC) calculations,[294] and found that our model overestimates the coupling by 50%. On the other hand, our coarse-grained molecular dynamics model overestimates the π-stacking distance in P3HT slightly compared with experiment,[217] resulting in an underestimate of the coupling of around 15% for typical π-stacking distances compared with the TDC calculations. Thus, we expect the excitonic couplings to reproduce reasonably well those in the real system.

Spectral overlap of the donor with the acceptor, X_{DA}, is calculated by treating the donor emission and acceptor absorption spectra as two-level Franck–Condon progressions, with lines replaced by Lorentzian distributions with full width half maximum

(FWHM) of 0.1 eV.[295–297] The effective Franck–Condon factor, F_m, for transitions to the vth vibrational level of chromophore m is determined by

$$F_m = \frac{e^{-S_m} S_m^v}{v!}, \tag{4.10}$$

where S_m is the Huang–Rhys parameter for chromophore m, related to the chromophore length by

$$S_m = \frac{A^2}{2} \sum_i |\psi_{mi}|^4. \tag{4.11}$$

Competing with exciton hopping is radiative decay from the donor chromophores. The radiative rate is determined by

$$k_\mathrm{r} = \frac{n|\boldsymbol{\mu}_m|^2 E^2}{3\pi\epsilon_0 \hbar^4 c^3}, \tag{4.12}$$

where n is the refractive index of the pure polymer, $\boldsymbol{\mu}_m = \mu_0 \sum_i \hat{\mathbf{r}}_i \psi_{mi}$ is the total transition dipole moment of chromophore m, and E is the relaxed energy of the chromophore, which is equivalent to the energy of the emitted photon.

In conjugated polymers, nonradiative decay is a significant exciton deactivation pathway. It is generally accepted that nonradiative transitions follow the energy gap law,[298] with the rate exponentially dependent on the transition energy

$$k_\mathrm{nr} \propto e^{-\gamma E}, \tag{4.13}$$

where γ is a parameter fitted to the molecule. Recently, Dimitrov et al. compared exciton lifetimes of several conjugated polymers to their optical band gaps and confirmed that nonradiative decay rates do appear to show a negative correlation with band gap consistent with eq 4.13.[299] However, a value for the molecular parameter γ was not able to be reliably determined and it was concluded that factors such as polymer structure, the degree of order or crystallinity, and geometric rearrangement between the ground and excited states could have significant influence. Given that k_nr is on the order of $1.6 \times 10^9\,\mathrm{s}^{-1}$ in P3HT,[300,301] the nonradiative lifetime is 600 ps or more, while the vast majority of the exciton migration processes simulated involved fewer than 6 hops (Figure 4.6), each 1–2 orders of magnitude faster than the nonradiative decay rate. Additionally, as the experimentally measured k_{nr} is determined from an ensemble of chromophores, the nonradiative decay rates from the initially excited, high-energy chromophores are expected to be significantly slower according to eq 4.13. It is therefore reasonable to assume that neglecting nonradiative decay should not affect the short time scale dynamics of exciton migration that are the focus of this study, although future development and implementation of a suitable theory for nonradiative decay may improve simulation results involving longer time scales.

Note that only excitation of and energy transfer between local exciton ground states (LEGSs) and the corresponding vibrationally relaxed states is considered in this model. Exciton transfer may not occur exclusively through LEGSs, but this transport mechanism is expected to dominate for several reasons. Firstly, as previously mentioned, these higher excited states are expected to relax rapidly to LEGSs on time scales (∼10s to 100s of fs[285]) much shorter than the time scale of exciton hopping (10s of ps). Secondly, the transition dipole moments (and hence oscillator strengths) of these higher excited states, due to the oscillatory nature of their node-containing wavefunctions,

Table 4.1: Summary of parameters used in exciton transport model for P3HT

	parameter	value
E_0	Nominal on-site excitation energy for a monomer	5.70 eV
σ_α	Standard deviation of on-site excitation energy due to local disorder	0.065 eV
J^{DD}	Nearest neighbour exciton transfer integral: dipole–dipole contribution	-0.95 eV
J^{SE}	Nearest neighbour exciton transfer integral: through bond superexchange contribution	-0.80 eV
μ_0	Dipole moment of a single monomer	2.05×10^{-29} C m
$\hbar\omega$	Energy of normal mode of angular frequency ω	0.18 eV
A	Exciton–phonon coupling	4.5
n	Refractive index of polymer, $n = \sqrt{\epsilon_{\mathrm{r}}}$	1.75

will be smaller than those of the LEGSs,[96,291] so absorption probabilities and exciton transfer rates involving these higher excited states will be correspondingly smaller than those involving LEGSs, particularly for less coiled chains.[96] Finally, following the initial excitation, after which the exciton rapidly finds itself in a LEGS for the reasons mentioned above, further exciton transfer will occur to other LEGSs as the higher lying excited states are energetically inaccessible to the generally energetically downhill exciton transfer process.

The initially excited chromophore is randomly selected with a probability dependent on the degree of spectral overlap of the acceptor with the simulated laser excitation wavelength. At each state, the exciton may either hop to a new site or recombine radiatively. A set of time intervals for these events is determined by $\Delta t = -\ln x/k$, where $k = \{k_{\mathrm{DA}}, k_{\mathrm{r}}\}$ is the set of all rate constants for that donor and x is a random uniform deviate in the interval $[0, 1]$ chosen for each k. The event with the lowest Δt is then selected as the transition to the new state. If the transition is a nonradiative hop to a new chromophore, then the process continues until radiative decay occurs.

The free chain simulation used 68 configurations taken at 8 ns intervals after an 8 ns equilibration period. The nanofibre system combined 63, 130, and 30 configurations of the 0.13, 1.0, and 2.0 wt% systems, respectively, taken at 8 ns intervals after an 1.98 µs period of fibre formation. Each timestep from the free chains and nanofibres was processed 14 and 4 times, respectively, to give ∼1000 configurations for each system. Note that a single configuration will give slightly different chromophore boundaries and energies on each run due to the diagonal disorder α present in the Frenkel–Holstein Hamiltonian. No significant differences in the results were observed when the different concentration nanofibre systems were processed individually. For each configuration, 10^5 excitations were performed.

Model Parameterisation

The parameters used in the Frenkel-Holstein model for P3HT are summarised in Table 4.1. The parameters E_0, J^{DD}, J^{SE}, and μ_0 were determined *via* quantum chemical calculations of methylthiophene oligomers. The hexyl sidechains of P3HT were replaced with methyl groups to reduce computational complexity, as this does not affect the electronic properties of the oligomers significantly, which are dominated by the backbone conjugation.[302,303] Structures were geometry optimised using the AM1 method and the $S_0 \rightarrow S_1$ transition energies computed using ZINDO/S.

The transition energies from ZINDO/S calculations of 3-methylthiophene oligomers agree reasonably well with the energies of the absorption maxima for the $S_0 \rightarrow S_1$ transition of thiophene oligomers in benzene solution[74] and of 3-octylthiophene oligomers in chloroform.[84] Because relatively little energy (compared with $k_\mathrm{B}T$) is required to change the conformation of 3-methylthiophene oligomers significantly from the minimum-energy conformer in which the thiophene rings are coplanar,[217] the calculations were carried out for oligomers whose inter-monomer dihedral angles had been selected randomly from a Boltzmann distribution in the dihedral potential at 298 K.[217] As shown in the Supporting Information, although the calculations underestimate the experimental dimer transition energy by around 0.2 eV, for longer oligomers the calculations and experiments for thiophene oligomers agree within error. Thus, the parameters obtained from the ZINDO/S calculations for the on-site excitation and nearest-neighbour coupling energies are expected to be reasonably accurate.

The value of J^SE was found by the difference in transition energies of methylthiophene dimers with dihedral angles of 180° (planar) and 90° (orthogonal) (see Supporting Information). To determine E_0 and J^DD, the transition energies of oligomers of length 5 to 30 were plotted against the inverse of the number of thiophene units. The equivalent planar coarse-grained structures were built and the transition (LEGS) energies determined using the Frenkel exciton model with the values of $(J^\mathrm{DD} + J^\mathrm{SE})$ and E_0 selected to match, respectively, the slope and intercept from the quantum calculations (see Supporting Information).

The transition dipole moment of a single monomer, μ_0, was determined by plotting the square of the transition dipole moment for methylthiophene oligomers of length 10 to 30 against the number of thiophene units. The linear fit was then extrapolated back to give the magnitude of the transition dipole moment of a single unit.

The refractive index of the pure polymer, n, was obtained from spectroscopic ellipsometry measurements of P3HT films.[304] For simplicity we have ignored the wavelength dependence of the refractive index of P3HT. The selected value is a good estimate for regiorandom P3HT; the refractive index for regioregular P3HT is more heavily wavelength dependent.

In P3HT the energy of the primary normal mode, $\hbar\omega$, corresponds to the C=C stretch at $1450\,\mathrm{cm^{-1}}$ (0.18 eV) that is observed in Raman spectra of P3HT films[305] and in the single-molecule absorption spectrum.[191] The shoulders seen in the UV-visible absorption spectrum of P3HT nanofibres (Figure 4.4) also correspond to this value.

The value for the exciton–phonon coupling parameter, A, was chosen to match the experimentally observed relaxation energy (Stokes shift), and is similar to values used by Barford et al. in exciton transfer simulations of MEH-PPV.[160]

Experimental Methods

Free chains of P3HT in solution were prepared by dissolving regioregular P3HT (Rieke Metals, MW = $50\,000\,\mathrm{g\,mol^{-1}}$, 99% regioregularity) in THF (Scharlau) by sonication at 25 °C for one hour to produce $0.1\,\mathrm{g\,L^{-1}}$ solutions, which were filtered through a 0.2 µm nylon filter. Nanofibres of P3HT were produced by precipitation from anisole (Merck) at a concentration of $0.5\,\mathrm{g\,L^{-1}}$ using the whisker method described by Samitsu et al..[90]

Steady-state absorption spectra were obtained on a Cary 300 UV-visible absorption spectrophotometer using a 1 cm path length quartz cuvette and the free chain or nanofibre solution diluted to 0.01 g L^{-1} in THF or anisole, respectively. Fluorescence spectra were obtained using the same solutions on a Perkin-Elmer LS-55 fluorescence spectrometer with an excitation wavelength of 400 nm and excitation and emission slit widths set at 5 nm.

Time-resolved fluorescence was measured using a fluorescence upconversion spectrometer (Halcyone, Ultrafast Systems). A continuous wave 532 nm Nd:YVO$_4$ laser at 8 W (Millenia Prime, Spectra-Physics) pumped a mode-locked Ti:Sapphire oscillator (Tsunami, Spectra-Physics) to produce 800 nm pulses at a rate of 80 MHz. A pulse picker selected pulses at a rate of 40 MHz that were then split into excitation and gate beams. The excitation wavelength of 400 nm was generated by doubling of the oscillator output using a BBO crystal. For the isotropic emission experiments, the gate pulse polarisation was set to the magic angle (54.7°) with respect to the excitation pulse. Anisotropy measurements were calculated from alternate scans with the gate pulse parallel or perpendicular to the excitation, with anisotropy defined as $r(t) = \frac{I(t)_{\parallel} - I(t)_{\perp}}{I(t)_{\parallel} - 2I(t)_{\perp}}$. Each experiment consisted of the averaging of three runs. For each delay time point a three second sampling time was used for a total of 1.2×10^8 laser excitations. Measurements were taken in a 2 mm quartz cuvette (Starna Cells 21-Q-2) at a concentration of 0.02 g L^{-1} and stirred throughout the duration of the experiments. No photodegradation of the sample was observed over the time scale of the experiments.

Results and Discussion

Model Verification

Figure 4.4 compares the simulated steady-state absorption and fluorescence spectra with those obtained experimentally. The result for the free chains (Figure 4.4a) shows reasonable agreement, although there are quantitative discrepancies, which are not unexpected given the simplicity of the model. While the experimental absorption band is broader than that of the simulations, the onset of absorption at the red edge

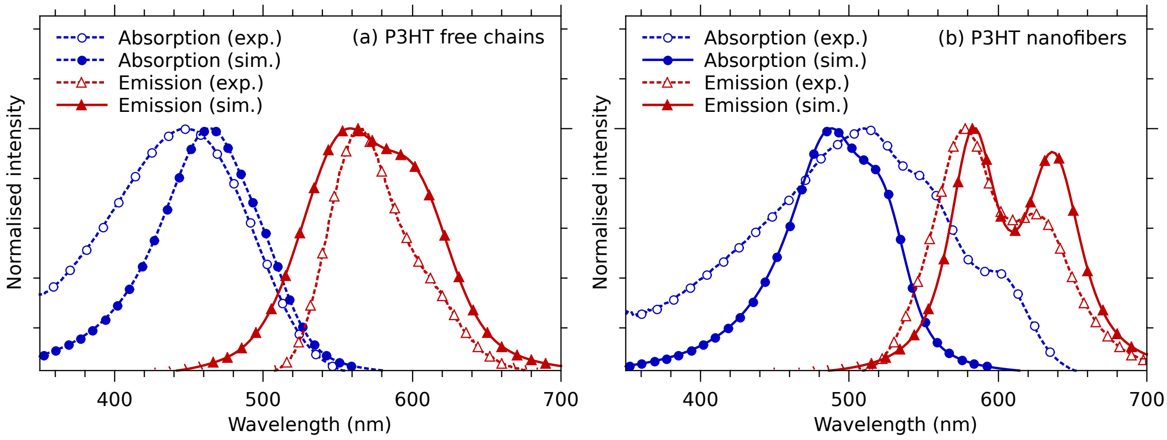

Figure 4.4: Experimental and simulated steady-state absorption and emission spectra for (a) P3HT free chains and (b) nanofibres.

matches well. It is in this low-energy region that the absorption is dominated by LEGSs, indicating that the energies determined from the Frenkel–Holstein model for these states are reasonable. The fluorescence peak of the free chains is also well simulated, showing that the relaxation energies of the LEGSs are also valid. The small shoulder present in the experimental fluorescence peak is reproduced, but somewhat exaggerated in the simulation data, indicating an overestimation of the intensity of the 0–1 vibronic transition.

The experimental absorption and emission spectra of nanofibres (Figure 4.4b) exhibit distinct vibronic structure that is also present in the simulated spectra. In particular, the nanofibre emission shows the two characteristic 0–0 and 0–1 transitions associated with H- and J-type aggregate behavior.[306] These two distinct peaks are reproduced in the simulation data, despite the intensity of the 0–1 transition again being overestimated. The simulated absorption spectrum is also significantly narrower than the experimental nanofibre spectrum. Some of this discrepancy may be due to only relatively small aggregates being simulated rather than complete nanofibres, so that the full distribution of absorbing chromophores may not be captured. On the other hand, agreement is better for the emission spectrum, since emission is expected to occur from a small number of low-energy chromophores as a result of energy funnelling due to exciton transfer, which the simulations are more successfully able to capture.

Importantly, the red-shifting of the absorption and emission peaks in the nanofibre simulations with respect to those in the free chain simulations is captured, indicating that the Frenkel–Holstein model is responding to the structural differences between the two systems and reproducing reasonable energies of the absorptive and emissive chromophores. This result also indicates that the coarse-grained structural model underlying the exciton model accurately captures the structural changes, such as increases in conjugation length, that occur as a result of chain aggregation in P3HT. Although experimentally quantifying chromophore lengths in conjugated polymer systems is complicated by environment, heterogeneity and a suitable definition,[307,308] the computed conjugation lengths of the LEGSs of 20–25 units (Figure 4.3, eq 4.7) are in good agreement with the available data for thiophenes.[308,309]

The exciton transport simulations are also able to reproduce the dynamics of time-resolved fluorescence upconversion experiments (see Supporting Information), which show a dynamic red-shift in the emission occurring over a period of tens of picoseconds, on a time scale that has been attributed to exciton transport,[232,234,310] with different wavelength dependencies for free chains and nanofibres. This result implies the exciton hopping rates calculated in the simulation agree with experimental observations.

Exciton Transport Mechanism

Figure 4.5 shows the mean squared displacement of excitons over time in the free chain and nanofibre systems. The motion of excitons is not clearly diffusive, with an upper limit to exciton displacement being reached asymptotically due to the finite size of the polymer in which the exciton can travel. The free chains are in dilute solution, which means that chains are generally well isolated from each other. This puts an upper limit on exciton travel distance, equal to the chain contour length. In reality, chains are not fully extended, nor are excitations exclusively at the chain termini. The nanofibre aggregates are naturally much larger than a single chain, which immediately allows for greater exciton travel. However, the total displacement is still limited to 7–8 nm due to

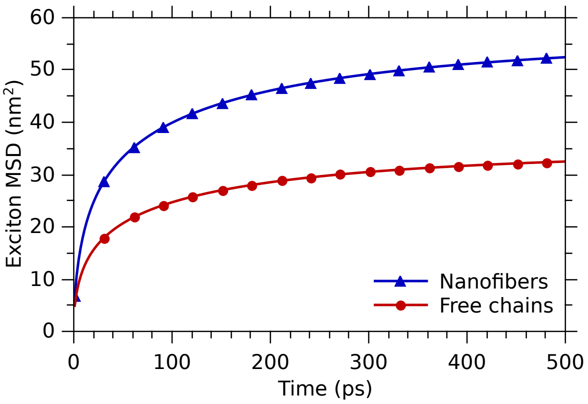

Figure 4.5: Mean-squared displacement (MSD) of excitons in P3HT free chains and nanofibres.

trapping effects coupled with the total exciton lifetime governed by the chromophore radiative rates (eq 4.12). This result from the simulations is in good agreement with the experimental values for exciton diffusion length in crystalline P3HT.[311]

The difference in the mean squared displacements between the free chains and nanofibres correlates with the distribution of hop counts for each system, shown in Figure 4.6. On isolated chains the probability that hopping does not occur, where excitation and emission occur from the same chromophore, is approximately 35%. Where hopping does take place, it is likely that only one or two hops will occur, with the probability of an exciton undergoing more than four hops being negligible. This observation is consistent with single-molecule polarisation spectroscopy experiments on disordered P3HT,[187,188] for which the decay of the correlation between excitation and emission polarisations suggests some degree of energy funnelling to the lowest energy chromophore, but the lack of perfect anisotropy in the single-molecule emission indicates incomplete funnelling to the lowest energy chromophore. The appearance of broad, homogeneous emission spectra from individual molecules also suggests that emission occurs from a variety of chromophores in the molecule. This can be rationalized from the exciton transport simulations, in which the extended and disordered nature of the free chains can cause a relatively large distance and unfavourable orientation between chromophores, preventing the exciton from reaching the lowest energy site prior to emission. As expected, excitons are more mobile in the nanofibres, with only around

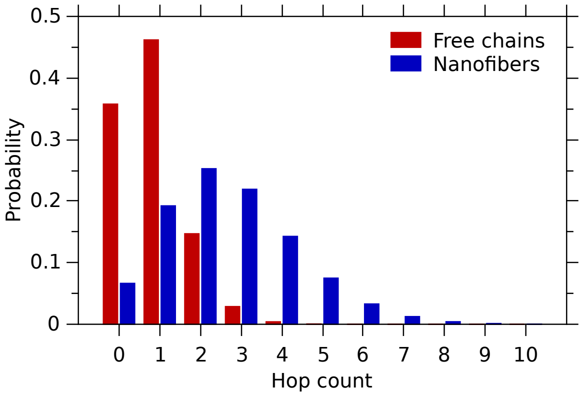

Figure 4.6: Distributions of total number of hops performed by excitons during the simulations.

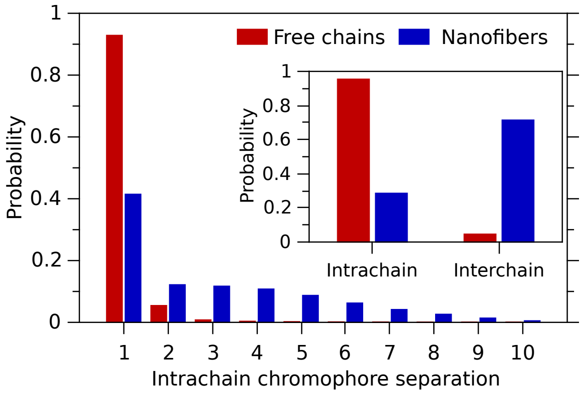

Figure 4.7: Probability distribution of intrachain hops to neighbouring chromophores as a function of intrachain hopping distance in units of chromophore numbers (a value of one equates to a nearest-neighbour hop to an immediately adjacent chromophore, with large values indicating hops to a chromophore at the opposite end of the chain). *Inset:* Probability that an exciton hop is of intrachain or interchain type.

5% of excitons emitting from the initially excited chromophore, as shown in Figure 4.6. Polymer aggregation clearly leads to a larger selection of chromophores in close proximity and allows for a greater selection of lower energy acceptor sites as possible hop destinations.

Exciton hopping events can be categorized as either intra- or interchain. The proportions of each for the free chains and nanofibres are shown in the inset of Figure 4.7. The isolation of the free chains is again evident with hops being almost exclusively within the same chain. For the nanofibres there is a predominance of interchain-type hops, indicating that there are either a greater number of interchain acceptor chromophores in the vicinity, or that they are more strongly coupled by a smaller distance or more favourable orientation (eq 4.9). Analysis of the intrachain-type hops in Figure 4.7 shows that, for both systems, exciton transfer to the nearest-neighbour chromophore is preferred. As the immediately adjacent acceptor chromophore is likely to be both spatially close and possess a favourable orientation with respect to the donor, this result is expected. Similarly, for the free chains, hops to more distant chromophores become increasingly unlikely due to the extended and disordered nature of the chains.

However, with nanofibres the trend for exciton hops between the donor and acceptor separated by two or more chromophores is more complex. The probability of exciton hopping to a site two chromophores away is significantly less than that for a nearest-neighbour type hop, but the probability of hops to sites further along the chain then tapers off slowly. The particular nature of the chain folding is responsible for the above phenomena. A chain that contributes to a nanofibre is likely to fold into segments of length ~25 nm. As shown in Figure 4.8b, these segments are divided into roughly two or three chromophores (chromophores in a free chain are shown in Figure 4.8a for comparison). The remainder of the chain folds back upon itself. The result is that beyond the directly adjacent chromophore, there is a good chance the remainder of the chain is folded back in close proximity. Indeed a plot of Euclidean distance between chromophores on a chain against their separation number along the chain (Figure 4.9a) shows that a chromophore at the opposite end of a chain in a nanofibre aggregate is generally not any more spatially distant than any other on that chain. Furthermore, if hopping events are analysed (Figure 4.9b), it can be seen that hops to the nearest-

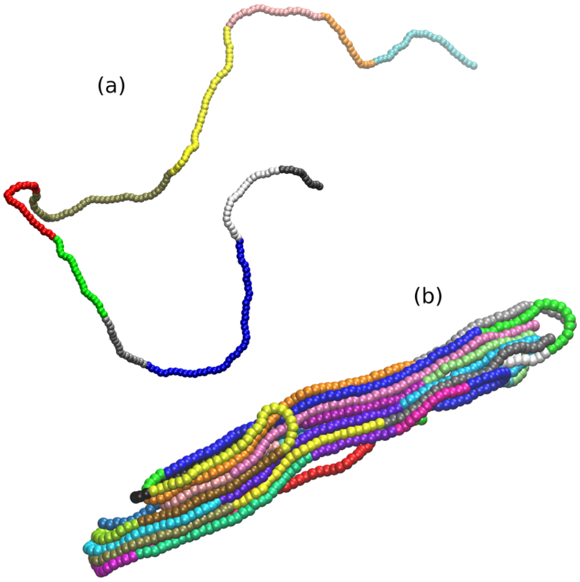

Figure 4.8: Division of polymer chains into spectroscopic units for (a) a free chain and (b) a nanofibre aggregate. Chromophore colours are arbitrary and alkyl sidechains are not shown for clarity.

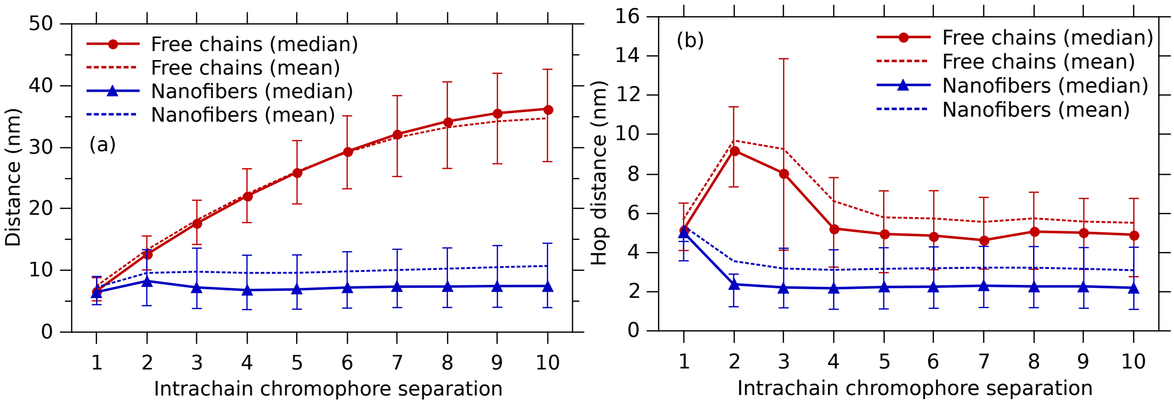

Figure 4.9: Euclidean distance (a) between intrachain chromophores and (b) of intrachain exciton hops versus the linear chromophore separation along the chain length. Error bars show the first and third quartile.

neighbour chromophore in nanofibre aggregates in fact have, on average, the furthest hop distance, and that hops to chromophores elsewhere on the chains are likely due to them being wrapped and aligned closer than the directly adjacent neighbour along the chain. Overall, the results show preference for exciton migration across the chains in nanofibre aggregates rather than along them, most likely in the π-stacking direction due to the close proximity and hence stronger interchain coupling in this direction.[61,294] Nevertheless, nearest-neighbour hops are the most common intrachain transitions in the nanofibre aggregates due to the favourable correlated orientation of the transition dipoles of adjacent chromophores along the chain.

The extended structure of free chains is evident in Figure 4.9a, with the Euclidean distance increasing with intrachain chromophore separation. As a consequence, hops to sites on the chain separated by more than two chromophores are highly unlikely (Figure 4.7), with disorder also making favourable transition dipole alignment less

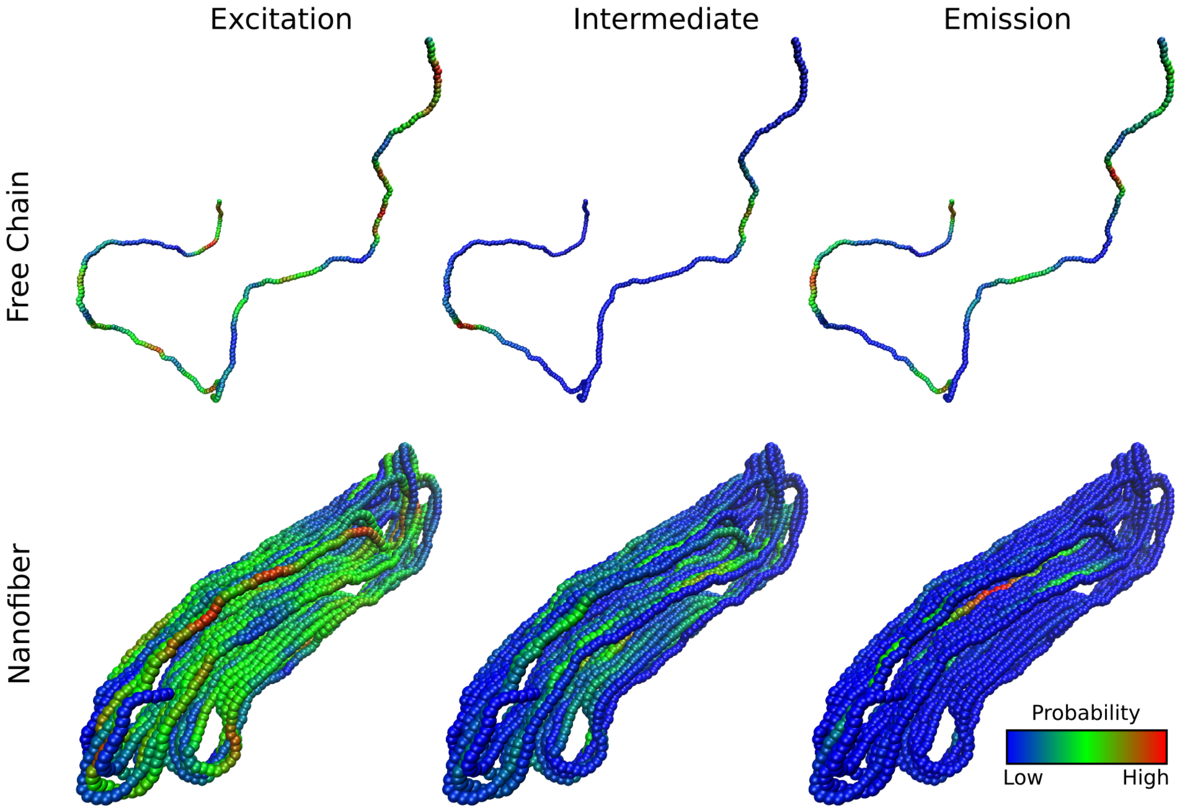

Figure 4.10: Probability heat maps of excitation, intermediate exciton visit, and emission events on a P3HT free chain and nanofibre aggregate.

probable. Figure 4.9b suggests that hops between widely separated chromophores only occurs when the chain ends are occasionally brought close together in space.

Figure 4.10 shows probability maps of excitation, intermediate visit, and emission events for typical free chain and nanofibre systems. Absorption of the simulated 400-nm laser excitation light occurs relatively evenly throughout the polymer chains, although there are a few higher energy sites that are more likely to absorb. These chromophores are well distributed over the extended free chains, but appear to be localized on the outside of the nanofibre structures. Emission sites are again distributed over the length of the free chains, but appear to be localized to just a few sites in the nanofibre, with a tendency for emission to occur from within the core of the structure. The category of intermediate visits is where a site is an exciton transition pathway but does not directly absorb or emit photons. There are only a small number of these sites on the free chains, where there is a chromophore of just the right energy bridging a high-energy absorption and low-energy emission site. This low probability is also reflected in Figure 4.6 for hop counts greater than two. On the nanofibre, the intermediate sites appear to be located between the absorbing sites on the exterior and emissive sites on the interior of the structure. Qualitatively, the heat maps in Figure 4.10 imply there is an energy funnelling effect towards the nanofibre core. This energy-funnelling behaviour was observed in general for the nanofibre aggregates simulated, as illustrated for a number of other aggregates in the Supporting Information.

To confirm this assertion, individual nanofibre aggregates were identified in the nanofibre systems and exciton migration tracked in relation to the center-of-mass of the aggregate. The aggregates were determined by finding clusters of chromophores defined using a density-based clustering algorithm, DBSCAN.[312] In this method, an aggregate is firstly located by detecting a minimum of six chromophore centres-of-mass within a sphere of 7 nm diameter, and the boundary of the aggregate is then found when the chromophore density falls below this threshold. The Supporting Information shows a plot of the mean squared displacement of an exciton from the center-of-mass of its originating nanofibre cluster over time, showing there is an overall tendency for energy funnelling towards the aggregate center. This effect can be explained by the fact that the polymer chains are more ordered in the aggregate core. The more planar structure of the stacked polymer chains in the core results in a longer conjugation length and therefore lower energy chromophores that make favourable acceptor sites. This is backed by an analysis of chromophore conjugation length and chain planarity as a function of distance from the chromophore cluster's center-of-mass (Supporting Information). There is a clear increase in chain planarity closer to the cluster center of mass, with a resulting increase in conjugation length of approximately four thiophene units.

The tendency for excitons to migrate towards the centres of the aggregates has negative implications for charge generation in conjugated polymer solar cells, where exciton migration to and dissociation at the donor–acceptor interface is required. It could be expected that nanofibre-based solar cells would provide greater efficiency than traditional bulk-heterojunction types due to higher charge-carrier mobilities and fibre diameters being comparable to the exciton diffusion length, but these solar cells do not automatically show significant improvements over disordered bulk-heterojunction cells.[92,313,314] Furthermore, more recently developed polymers for photovoltaic applications display high efficiency with amorphous microstructures, with any thermal annealing to induce donor–acceptor phase separation reducing their performance.[78,315] Our simulation results suggest that a contributing factor to the poor performance of photovoltaic devices containing relatively large ordered aggregates is the presence of low-energy trap sites at aggregate cores that funnel excitons away from donor–acceptor interfaces and where exciton recombination eventually occurs. This effect may also be responsible for the unexpectedly high fluorescent quantum yields of conjugated polymer nanoparticle suspensions in water, where the water would otherwise be expected to efficiently quench excitons.[91,178,316] If the exciton is rapidly funnelled from the surface towards the low-energy center of the nanoparticle it would then be effectively protected from the aqueous environment.

The individual nanofibre aggregates identified from the coarse-grained P3HT configurations all show some degree of order, but are never perfectly crystalline. Several structural motifs are observed, similar to what has been reported previously in both computational work and single-molecule spectroscopic experiments on conjugated polymers.[86,187,188,217,317] Notable extremes are "hairpin"-type structures, with regular, linear folding of chains like that shown in Figure 4.1c, and "helices" with a more cylindrical stacking of the chains. To investigate whether these structural differences impact the simulation results, the individual aggregates were isolated using the clustering algorithm described above and sorted using a measure of static anisotropy defined by[86]

$$r_{\mathrm{s}} = \frac{1}{n_{\mathrm{a}}} \sum_{i} \cos^2(\theta_i), \tag{4.14}$$

where θ_i is the angle between the transition dipole moment vector on monomer i and the sum of transition dipole moment vectors of all monomers in the aggregate and

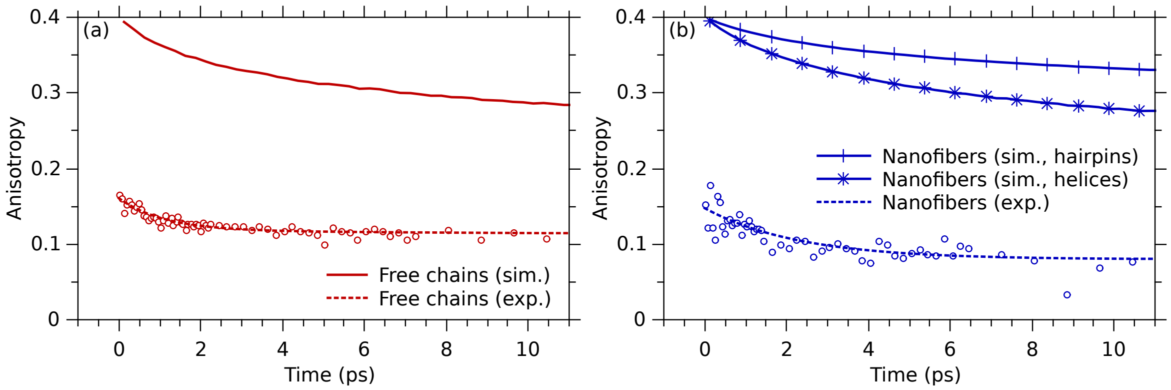

Figure 4.11: Experimental and simulated fluorescence anisotropy. The measured wavelength is that of the respective fluorescence peak of the sample for both experimental and simulation data (570 nm for free chains and 600 nm for the nanofibres).

n_a is the number of monomers in the aggregate. The top and bottom ~30% most anisotropic aggregates were then designated as “hairpins” and “helices”, respectively, and exciton transport simulations carried out for each group separately. No significant differences between the simulation results was observed, with the exception of the fluorescence anisotropy data shown in Figure 4.11b. This difference is expected, as the helical aggregates are more isotropic by definition and should result in greater depolarisation of fluorescence as exciton hopping occurs. Interestingly, fitting of the anisotropy decays in Figure 4.11a and Figure 4.11b (Supporting Information) shows that the rate of depolarisation is similar in both forms of nanofibres as well as in the free chains (~7 ps), with only the magnitude of the final depolarisation differing. This result is consistent with experimental observations, in which there is little difference between the depolarisation rates of free chains and nanofibres, and although the decay time constants are shorter than those of the simulation (~2 ps), they are of the same order of magnitude.

The similarity in the rates of depolarisation is initially unexpected considering the greater mobility of excitons in the nanofibres than in the free chains (Figure 4.5). A comparison of the rate of depolarisation with that of exciton diffusion is given in the Supporting Information. The simulations indicate that excitons in nanofibres move on average 40% further than those in free chains for the same amount of fluorescence depolarisation. This result can be rationalized by considering that although excitons undergo more hops and travel further in the nanofibres, the ordered alignment of the chains acts to better preserve the direction of the transition dipole moment. The end result is a similar rate of fluorescence depolarisation in nanofibres and free chains despite the higher exciton diffusion rate in the nanofibres. Note that in both the simulation and experimental data the rates of depolarisation are consistent with those previously attributed to exciton energy-transfer processes.[232,234,310]

The experimental fluorescence anisotropy data in Figure 4.11 show ultrafast depolarisation occurring in both the free chains and nanofibres on a time scale of < 100 fs, below the response time of the instrument. This differs from the simulation data, in which the anisotropy has an initial value of 0.4, indicating perfect correlation of the excitation and emission polarisations. Ultrafast fluorescence depolarisation is routinely observed in conjugated polymers,[234,271,318] and has been attributed to geometrical changes in the polymer due to the strong coupling between the electronic and the nuclear degrees of freedom.[1,319] Correspondingly, relaxation of the initially generated, delocalized states (QEESs) to more localized ones (LEGSs) occurs on the time scale of the nuclear motion, causing rapid change in the direction transition dipole moment as the wavefunction evolves over the disordered chain.[95,320]

The absence of the ultrafast depolarisation effect in the simulation data highlights some deficiencies in the model. While the higher energy eigenstates of eq 4.1 (QEESs) contribute to the simulated absorption spectrum (Figure 4.4), it is only the LEGSs that are selected for excitation during the Monte Carlo hopping simulation since, as stated previously, the QEESs rapidly relax to the LEGS with maximum wavefunction overlap. Implementing this behaviour would account for some proportion of the ultrafast fluorescence depolarisation. An additional contribution to the ultrafast depolarisation may be due to delocalisation of the initially formed exciton across adjacent chain segments, another effect that is not considered in the simulation model. This could also account for the slightly greater magnitude of depolarisation seen in the experimental nanofibre data, in spite of the nanofibres having greater structural order than the free chains. The lack of these ultrafast depolarisation effects in the model is not expected to affect the longer time-scale exciton dynamics that is more relevant for energy transfer in organic electronic devices. However, the contribution of geometrical changes to the fluorescence depolarisation are harder to quantify as the coarse-grained molecular dynamics that provides the polymer geometry is decoupled from the simulation of the exciton. A static polymer conformation over the lifetime of the exciton is clearly not entirely realistic, but attempting to closely couple the exciton behaviour and the molecular dynamics would require extreme computational costs that would limit application of the model to small system sizes.

Conclusions

In summary, we have used accurate coarse-grained molecular dynamics simulations to generate large, 100-chain systems of regioregular P3HT in two contrasting solvent environments made by modifying the implicit solvent model. Free chains characterized by an extended, disordered conformation were produced in a good solvent and were well isolated in a dilute solution. A marginal solvent and polymer concentrations between $\sim$0.1 and 2.0 wt% resulted in the formation of nanofibre-like aggregates, which exhibited a semicrystalline microstructure. From these systems, a Frenkel–Holstein exciton model was then applied to calculate wavefunctions and energies of chromophores, with parameters derived from quantum chemical calculations. Finally, Monte Carlo simulations of Förster-type exciton migration were performed using the Fermi Golden Rule with chromophore couplings determined by the line-dipole approximation, in which point-dipole interactions between monomer transition dipoles are summed.

The results of the simulations provide reasonable quantitative agreement with experimental steady-state and time-resolved fluorescence data for P3HT nanofibres and solutions. Simulated exciton diffusion lengths are also in agreement with literature experimental data. Furthermore, morphology-dependent mechanisms of exciton transport were observed on the molecular level. Notably, exciton transfer through the nanofibre aggregates occurred generally by interchain hops towards low-energy sites at the core of the aggregate. These “trap” sites are formed due to the higher level of crystallinity resulting in more planar chains and longer chromophore conjugation lengths. This structure-dependent energy funnelling has implications for exciton diffusion to donor–acceptor interfaces in bulk-heterojunction organic solar cells, particularly those employing polymer nanofibres, and for fluorescence yields of conjugated polymer nanoparticles used in fluorescence imaging. Similar rates of fluorescence depolarisation were observed in P3HT free chains and nanofibres in both experimental and simulation data, in spite of exciton mobility being much greater in the nanofibres. This phenomena can be rationalized by the fact that the increased order of the chromophore orientations acts as a counterbalance to help preserve the fluorescence polarisation.

Our methods demonstrate a bridging of the gap between highly accurate atomistic quantum calculations and generalized lattice models of conjugated polymers. A combination of mesoscale models provides realistic polymer conformations and gives molecular-level detail of exciton transport in conjugated polymers on experimentally relevant length and time scales.

Acknowledgements

The authors acknowledge Dr. William Barford for providing an early version of his exciton transport simulation code. This research was undertaken with the assistance of resources provided at the NCI National Facility systems at the Australian National University through the National Computational Merit Allocation Scheme supported by the Australian Government. Computational resources provided by eResearch SA are also gratefully acknowledged.

Supporting Information

Model Parameterisation

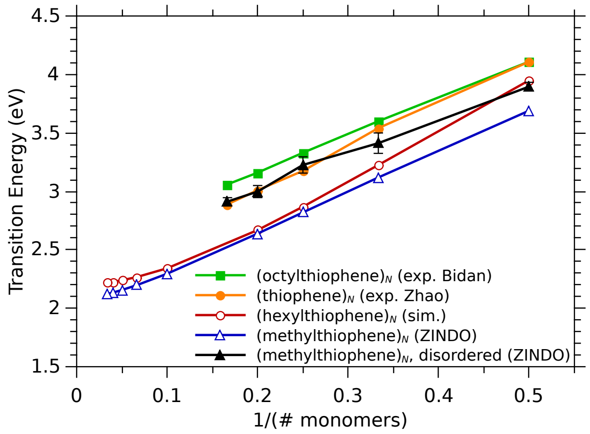

Figure 4.12: Transition energies of thiophene oligomers as a function of the inverse number of monomer units. Transition energies of planar methylthiophene oligomers were computed using the ZINDO/S method (blue open triangles). The values for the sum of the nearest-neighbour exciton transfer integral components, $(J^{\mathrm{SE}} + J^{\mathrm{DD}})$, and nominal on-site excitation energy, E_0, were then selected by fitting the predicted LEGS energies of planar coarse-grained structures (red open circles) to the slope and offset respectively for oligomers of length 5–30 units. Experimental data for octylthiophene oligomers in chloroform[84] (orange filled circles) and thiophene oligomers in benzene[74] (green filled squares) are included for comparison. The experimental oligomers are not expected to be perfectly planar and possess some degree of disorder. For comparison, disordered methylthiophene oligomers were constructed using dihedral angles between the thiophene units selected randomly from the expected Boltzmann distribution at 298 K[217] and their transition energies computed using the ZINDO/S method (black filled trianges). For oligomers of N units, $3(N-1)$ different structures were generated. Error bars are 2 standard errors.

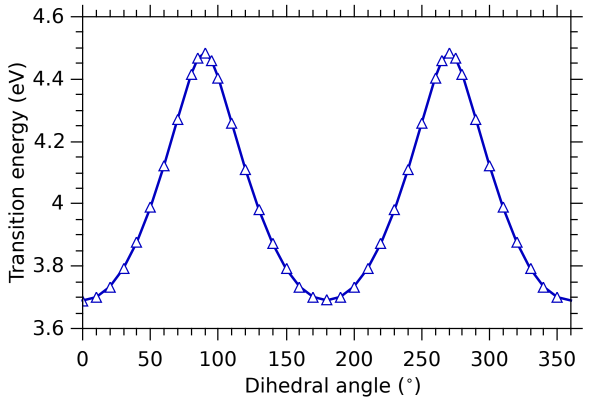

Figure 4.13: Transition energy of a methylthiophene dimer as a function of the dihedral angle between the thiophene units, computed using the ZINDO/S method. The through-bond superexchange contribution of the nearest neighbour exciton transfer integral, J^{SE}, is determined from the difference in transition energy between the planar and orthogonal orientations.

Time-Resolved Fluorescence

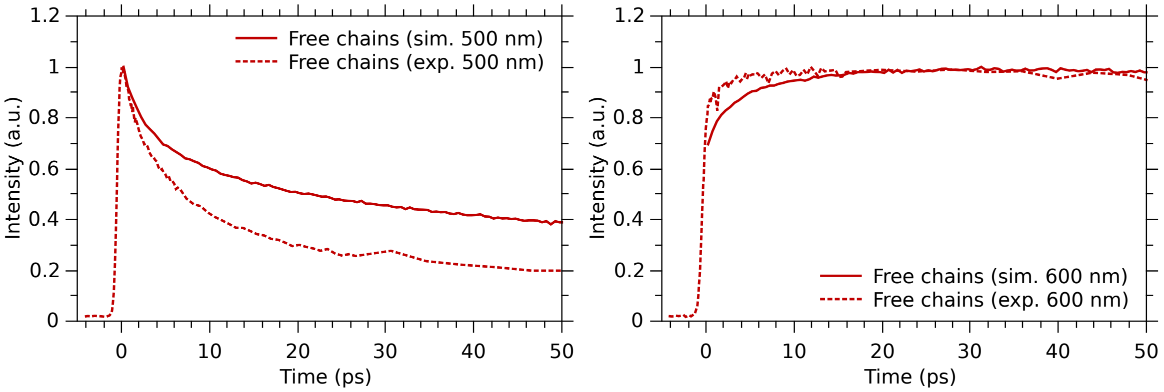

Figure 4.14: Simulated and experimental time-resolved fluorescence of P3HT chains in solution showing the dynamic red-shift of the fluorescence is captured in the simulation. 500 nm is on the blue side of the emission peak, and 600 nm is on the red side. The differing shape of the traces indicates the peak undergoes a red-shift over several picoseconds.

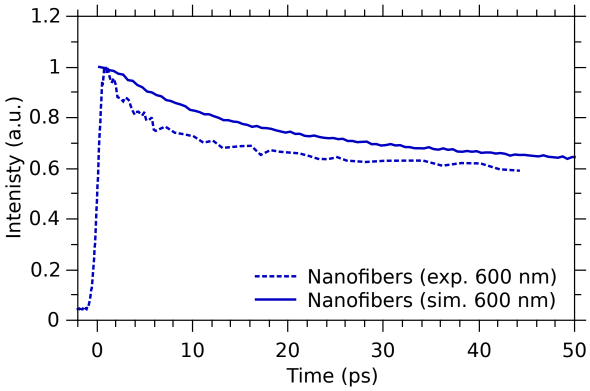

Figure 4.15: Simulated and experimental time-resolved fluorescence of P3HT nanofibres. 600 nm is approximately at the center of the emission peak.

Exciton Migration Preference

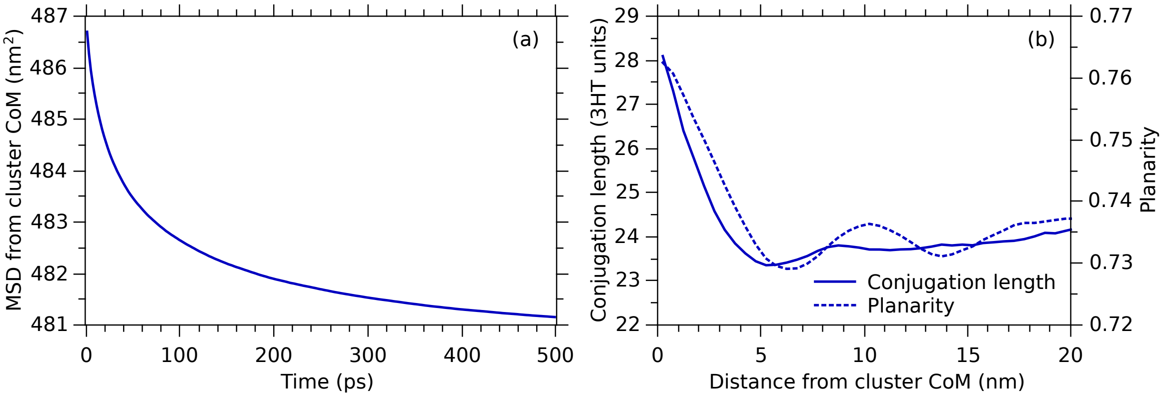

Figure 4.16: (a) Mean squared displacement of the exciton relative to the nanofibre cluster's center of mass. (b) Mean chromophore length and planarity of the polymer relative to the distance from the center of mass of the nanofibre cluster. Planarity is defined as $\frac{3}{2}\cos^2\phi - \frac{1}{2}$, where ϕ is the dihedral angle between monomer units.

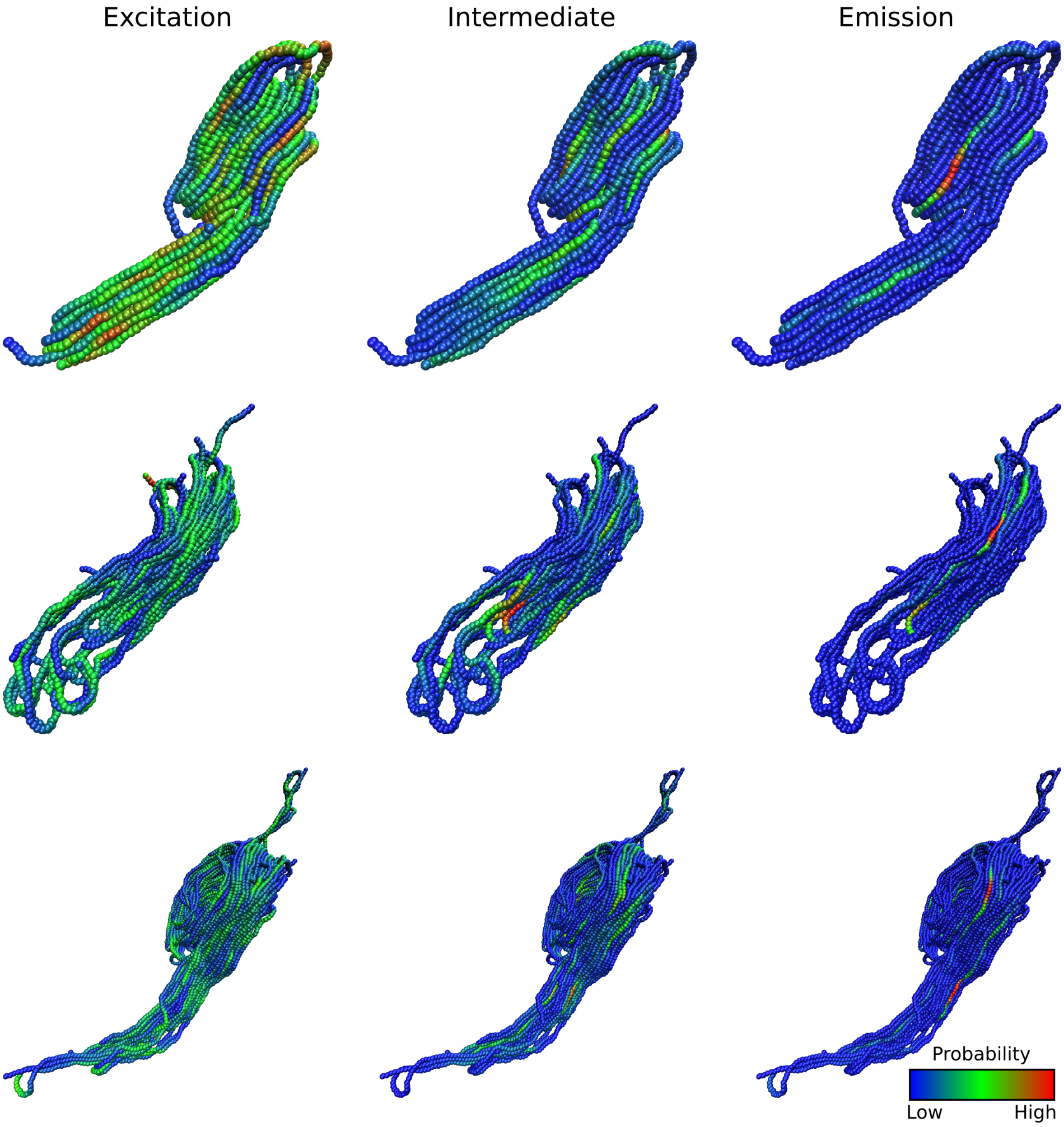

Figure 4.17: Probability heat maps of excitation, intermediate exciton visit, and emission events on P3HT nanofibre aggregates. A large proportion of chromophores act as absorbing sites, while only a small number are sites of high intensity emission. These low-energy “trap” sites are often located at the core, rather than the surface of the aggregate.

Fluorescence Depolarisation Rates

Single-exponential decay fits of the form $A = A_0 + B\exp(-t/\tau)$ were made to the simulated and experimental fluorescence anisotropy data over the first 25 ps to extract the depolarisation time constant, τ. The exciton diffusion coefficient, D_t, was obtained by a linear fit to the exciton mean squared displacement plot over the first 25 ps. The quantity $1/\sqrt{\tau D_\mathrm{t}}$ provides a measure of the degree of fluorescence depolarisation per unit distance travelled by the exciton and gives an indication of the rate of fluorescence depolarisation relative to that of exciton diffusion. The values shown in Table 4.2 indicate that the rate of depolarisation is approximately equal for the free chains and nanofibres. (Note that the different appearance of the anisotropy traces is therefore primarily due to the differing amplitude factors, B.) However, the nanofibres show a significantly faster exciton diffusion rate. As a result, the exciton in nanofibres moves on average 40% further than that in free chains for the same amount of fluorescence depolarisation.

Table 4.2: Comparison of fluorescence depolarisation and exciton diffusion rates over the period of $t = 0$ to $t = 25$ ps.

System	τ (ps)	D_t (nm^2 ps^{-1})	$1/\sqrt{\tau D_\mathrm{t}}$ (nm^{-1})
Free chains	6.6	0.45	0.58
Nanofibres (hairpins)	7.1	0.77	0.43
Nanofibres (helices)	7.0	0.77	0.43
Free chains (exp.)	1.5	–	–
Nanofibres (exp.)	2.0	–	–

CHAPTER 5

Modelling of Magnetic Field Effects on Singlet Fission and Triplet Fusion in Disordered Rubrene Films

Statement of Authorship

Title of Paper	Comment on “Magnetic Field Effects on Singlet Fission and Fluorescence Decay Dynamics in Amorphous Rubrene”
Publication Status	Published
Publication Details	Tapping, P. C.; Huang, D. M. *J. Phys. Chem. C* **2016**, *120*, 25151–25157. DOI: 10.1021/acs.jpcc.6b04934

Principal Author

Principal Author	Patrick C. Tapping		
Contribution to the Paper	Development of simulation code, data analysis, construction of figures, writing of manuscript.		
Overall Percentage	85%		
Signature		Date	18/7/16

Co-Author Contributions

By signing the Statement of Authorship, each author certifies that the stated contributions to the following publication are accurate and that permission is granted for the publication to be included in this thesis.

Co-Author	David M. Huang		
Contribution to the Paper	Supervision of project; assistance with theory, writing and editing of manuscript; corresponding author.		
Signature		Date	22/7/16

Introduction

In a recent paper, Piland, Burdett, Kurunthu and Bardeen[321] (PBKB) present data from time-resolved fluorescence measurements on amorphous rubrene films and explain the observed prompt and delayed fluorescence intensities in terms of competing singlet-fission and triplet-fusion processes. The dynamics of such processes are of interest due to their relevance to strategies for boosting efficiencies of photovoltaic devices.[322] The rate of crossing between the singlet and triplet manifolds depends on the overlap of the pure singlet and the triplet-pair state wavefunctions, which itself can be affected by the molecular orientation and any applied magnetic field. To explain their experimental results, a hybrid quantum–kinetic model is used to simulate fluorescence decays from systems of ordered or disordered rubrene molecular pairs. A spin Hamiltonian is constructed to describe the interactions of the triplet excitons residing on the molecular pair and was used to compute the singlet character of each of the nine triplet-pair states. This quantum-mechanical model of the interactions of triplet excitons and the influence of an applied magnetic field closely follows the theory pioneered by Merrifield in the late 1960s.[166,203–205] The singlet character of the triplet-pair states is then used in a system of kinetic equations to simulate the crossings between the singlet and triplet exciton states, with the fluorescence intensity taken to be proportional to the exciton population in the pure singlet state at any point in time.

The simulations predict markedly different behaviour for the magnetic-field dependence of the fluorescence intensity for ordered and disordered systems at zero and high ($8.1\,\mathrm{kG} = 0.81\,\mathrm{T}$) fields: for a model ordered system, the prompt fluorescence increases with field strength at the expense of the delayed fluorescence due to a reduction in the number of triplet-pair states with singlet character, whereas for a model disordered system, the opposite trend is predicted. As only the behaviour of the ordered system matches the experimental data for the same magnetic fields, it is concluded that singlet exciton migration to ordered regions of the film must occur prior to singlet fission. These results suggest that measurements of magnetic-field effects on fluorescence decay dynamics can provide a sensitive probe of molecular-level morphology in systems that undergo singlet fission.

Although we do not dispute the validity of this interesting method of combining magnetic fields and spectroscopy to probe molecular ordering, we have identified some errors in the quantum-mechanical model presented by PBKB, most crucially in the representation of the pure singlet state in the basis of triplet pair states. The incorrect calculation of the singlet character of the triplet-pair states propagates through to the kinetic model and causes significant qualitative and quantitative discrepancies between their results and those obtained when the pure singlet is correctly represented. In particular, for physically reasonable molecular parameters, the corrected model predicts magnetic-field effects on the fluorescence intensity decays for both ordered and disordered systems that are consistent with the experimental data. Thus, it cannot be concluded from the data that singlet exciton migration occurs to ordered regions of the film prior to singlet fission. Nevertheless, the variation of the spin states with magnetic field does differ for ordered and disordered systems, and we identify a regime of magnetic field strengths much lower ($\ll 0.81\,\mathrm{T}$) than those studied in the experiments in which the fluorescence decay dynamics relative to zero field should be qualitatively different for amorphous and ordered regions of a rubrene film.

Model

It should be noted that the underlying theory presented by PBKB is sound and therefore will not be reiterated here in detail. We refer readers interested in the quantum mechanical theory of interactions of triplet excitons and magnetic fields to the text in question[321] and to previous literature.[166,203–205,219,323] Here we simply present the elements of the theory needed to explain the inconsistencies in the approach used. The construction of the spin Hamiltonian for an interacting pair of triplets and its matrix representation in terms of triplet pair states, as well as other minor differences between our model and that of PBKB, are described in detail in the Supporting Information.

The general form of the spin Hamiltonian is

$$\hat{H}_{\text{total}} = \hat{H}_{\text{magnetic}} + \hat{H}_{\text{zero-field}} + \hat{H}_{\text{AB}} \tag{5.1}$$

where $\hat{H}_{\text{magnetic}}$ describes the Zeeman effect of the magnetic field on the triplet pair, $\hat{H}_{\text{zero-field}}$ is the intramolecular electron spin–spin interaction and $\hat{H}_{\text{AB}}$ is the intermolecular coupling between the triplets on molecules A and B. The zero-field term can in turn be decomposed into the individual spin–spin contributions from the two unpaired electrons on each of the two molecules, A and B:

$$\hat{H}_{\text{zero-field}} = \hat{H}_{\text{SS}_\text{A}} + \hat{H}_{\text{SS}_\text{B}} \tag{5.2}$$

The zero-field term for a molecule such as tetracene (which has the same polyaromatic backbone as rubrene) in the (x, y, z) coordinate system defined by the molecular symmetry axes is[103,166,324]

$$\hat{H}_{\text{SS}} = D\left(\hat{S}_z^2 - \frac{1}{3}\hat{S}^2\right) + E\left(\hat{S}_x^2 - \hat{S}_y^2\right) \tag{5.3}$$

where D and E are the molecular zero-field splitting parameters.

The pure singlet state $|\text{S}\rangle$ that can be formed by the pair of interacting triplets is defined as the eigenstate of the total four-electron $\hat{S}^2 = (\hat{\boldsymbol{S}}_{\text{A}1} + \hat{\boldsymbol{S}}_{\text{A}2} + \hat{\boldsymbol{S}}_{\text{B}1} + \hat{\boldsymbol{S}}_{\text{B}2})^2$ and $\hat{S}_z = (\hat{S}_{z,\text{A}1} + \hat{S}_{z,\text{A}2} + \hat{S}_{z,\text{B}1} + \hat{S}_{z,\text{B}2})$ operators with eigenvalue zero in both cases. Here, “A” and “B” label the two molecules and “1” and “2” label the two unpaired electrons on each molecule. Using standard identities for spin operators,[325] the singlet state is readily shown to be

$$\begin{aligned} |\text{S}\rangle &= 3^{-1/2}\left(|xx\rangle + |yy\rangle + |zz\rangle\right) && (5.4)\\ &\equiv 3^{-1/2}\left(|x\rangle_\text{A}|x\rangle_\text{B} + |y\rangle_\text{A}|y\rangle_\text{B} + |z\rangle_\text{A}|z\rangle_\text{B}\right) && (5.5)\end{aligned}$$

where $|xx\rangle \equiv |x\rangle_\text{A}|x\rangle_\text{B}$ and so on and $|x\rangle_j$, $|y\rangle_j$, and $|z\rangle_j$ are two-electron spin states on molecule $j = \text{A}$ or B,

$$\begin{aligned} |x\rangle_j &= 2^{-1/2}\left(|\beta_1\beta_2\rangle_j - |\alpha_1\alpha_2\rangle_j\right) && (5.6)\\ |y\rangle_j &= i2^{-1/2}\left(|\beta_1\beta_2\rangle_j + |\alpha_1\alpha_2\rangle_j\right) && (5.7)\\ |z\rangle_j &= 2^{-1/2}\left(|\alpha_1\beta_2\rangle_j + |\beta_1\alpha_2\rangle_j\right) && (5.8)\end{aligned}$$

and α and β have their usual meaning as individual up and down electron spins, respectively, quantised along the z axis.

The choice of Cartesian axes x, y, and z used to define the singlet state $|\mathrm{S}\rangle$ is arbitrary, but it is clear from eqs 5.4–5.8 that the axes must be the *same* for *both* molecules A and B. A convenient choice (which we have made) is to take the coordinate system in which the zero-field term for molecule A, $\hat{H}_{\mathrm{SS_A}} = \hat{H}_{\mathrm{SS}}$, is diagonal in the basis $\{|x\rangle_\mathrm{A}, |y\rangle_\mathrm{A}, |z\rangle_\mathrm{A}\}$, which corresponds to x, y, and z being aligned with the molecular symmetry axes of the rubrene backbone. This coordinate system is indicated in Figure 5.1.

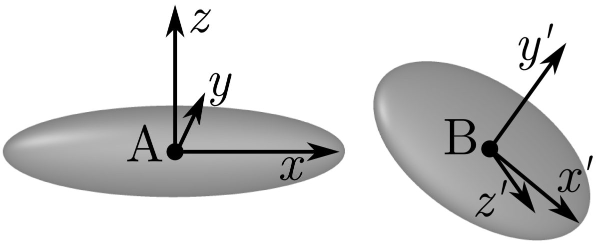

Figure 5.1: Schematic defining the molecular axes of the rubrene pair. The x, y and z axes correspond, respectively, to the long, short and perpendicular axes of the tetracene backbone of molecule A, while the primed x', y' and z' axes refer to the corresponding axes of molecule B, which could be rotated with respect to those of molecule A.

In their paper,[321] PBKB appear to use the definition of the singlet state $|\mathrm{S}\rangle$ given in eqs 5.4 and 5.5, but in actuality define the singlet state as $|\mathrm{S}\rangle \equiv 3^{-1/2}(|x\rangle_\mathrm{A}|x'\rangle_\mathrm{B} + |y\rangle_\mathrm{A}|y'\rangle_\mathrm{B} + |z\rangle_\mathrm{A}|z'\rangle_\mathrm{B})$ in which the two-electron spin states $|x'\rangle_\mathrm{B}$, $|y'\rangle_\mathrm{B}$, and $|z'\rangle_\mathrm{B}$ of molecule B are defined with respect to the molecular symmetry axes x', y', and z' of molecule B. As illustrated in Figure 5.1, the coordinate systems (x, y, z) and (x', y', z') do not coincide in general, and thus the equation above does *not* in general represent the pure singlet state produced by the interacting triplet pair (it is *not* an eigenstate of the total S^2 and S_z operators); it is only the singlet state if the two molecules are perfectly aligned. This error in the representation of the singlet state leads to an incorrect calculation of the projection C^l_S of each eigenstate ψ_l of the spin Hamiltonian (eq 5.1) on to the singlet state,

$$C^l_\mathrm{S} \equiv \langle \mathrm{S}|\psi_l\rangle = 3^{-1/2}\left(\langle xx| + \langle yy| + \langle zz|\right)|\psi_l\rangle \tag{5.9}$$

As a consequence, the rate of crossing between the triplet-pair states and the pure singlet state, which in the kinetic model depends on the singlet character $|C^l_\mathrm{S}|^2$ of each pair state $|\psi_l\rangle$, and the resulting fluorescence decay dynamics are not correctly computed.

The parameters in eq 5.3 are defined such that x, y, and z axes correspond to the molecular symmetry axes: for the tetracene parameters used here, x is the long axis, y is the short axis, and z is perpendicular to the molecular plane. As we have defined the coordinate system for the interacting molecular pair in terms of the symmetry axes of molecule A, in eq 5.1 for the total spin Hamiltonian, the zero-field component for molecule A is $\hat{H}_{\mathrm{SS_A}} = \hat{H}_{\mathrm{SS}}$, but a rotation operation must be applied to $\hat{H}_{\mathrm{SS}}$ to give $\hat{H}_{\mathrm{SS_B}}$, the zero-field component for molecule B, i.e.

$$\hat{H}_{\mathrm{SS_B}} = R^\mathrm{T}\hat{H}_{\mathrm{SS}}R. \tag{5.10}$$

where the rotation matrix R uses the three Euler angles that define the sequence of rotations needed to rotate the axes of molecule A on to the axes of molecule B (see

Supporting Information). PBKB do not apply any such rotation operation to determine $\hat{H}_{\mathrm{SS_B}}$, because they effectively compute the contributions of molecule A and molecule B to the total spin Hamiltonian in different coordinate systems.

We diagonalised the total spin Hamiltonian (eq 5.1) in the $\{|xx\rangle, |xy\rangle, |xz\rangle, |yx\rangle, |yy\rangle, |yz\rangle, |zx\rangle, |zy\rangle, |zz\rangle\}$ basis of pair states to determine the eigenstates $\{\psi_l\}$, from which the singlet character $|C^l_{\mathrm{S}}|^2$ of each eigenstate is readily determined from eq 5.9, since $\langle\gamma\delta|\epsilon\zeta\rangle = \delta_{\gamma\epsilon}\delta_{\delta\zeta}$. (PBKB instead diagonalise the Hamiltonian in the $\{|xx'\rangle, |xy'\rangle, |xz'\rangle, |yx'\rangle, |yy'\rangle, |yz'\rangle, |zx'\rangle, |zy'\rangle, |zz'\rangle\}$, in which the singlet character of the eigenstates can only be determined by first applying a rotation operation to the primed pair states on molecule B.) We then used the singlet character of each eigenstate in a system of ten differential equations,

$$\frac{\mathrm{d}N_{\mathrm{S1}}}{\mathrm{d}t} = -\left(k_{\mathrm{rad}} + k_{-2}\sum_{l=1}^{9}|C^l_{\mathrm{S}}|^2\right)N_{\mathrm{S1}} + \sum_{l=1}^{9}k_2|C^l_{\mathrm{S}}|^2 N_{(\mathrm{TT})l} \tag{5.11a}$$

$$\frac{\mathrm{d}N_{(\mathrm{TT})l}}{\mathrm{d}t} = k_{-2}|C^l_{\mathrm{S}}|^2 N_{\mathrm{S1}} - k_2|C^l_{\mathrm{S}}l|^2 N_{(\mathrm{TT})l} \tag{5.11b}$$

which represent the rate of crossing between the triplet-pair states and the pure singlet state, where k_2 is the rate constant for the crossing into the singlet state from the triplet manifold, k_{-2} is the rate constant for the reverse process, and k_{rad} is the radiative rate from the singlet state. Equations 5.11a and 5.11b are equivalent to the kinetic equations used by PBKB[321] in which mixing of and decay from the triplet states is considered to be negligible. For the purposes of comparison, we have also used the same values for the rate constants:[321] $k_{\mathrm{rad}} = 0.06\,\mathrm{ns}^{-1}$, $k_2 = 0.5\,\mathrm{ns}^{-1}$, and $k_{-2} = 0.5\,\mathrm{ns}^{-1}$.

To simulate the time-resolved fluorescence, the system of equations was solved numerically to find the populations in the singlet N_{S1} and triplet-pair $N_{(\mathrm{TT})}$ states, with the initial condition that all population began in the singlet state. The fluorescence intensity was then assumed to be proportional to the population in the pure singlet state at any instant in time. When an ensemble of orientations of the molecular pairs was simulated, such as in the model of a fully disordered rubrene film, a uniform distribution of molecular or magnetic field orientations were selected from the unit sphere. For each unique orientation of the magnetic field or molecular pair, the singlet character and fluorescence decay kinetics were computed. The final time-resolved fluorescence data was then determined as the mean of the individual fluorescence contributions from each molecular pair.

Results and Discussion

To demonstrate the qualitatively and quantitatively different predictions of the two spin-Hamiltonian implementations, we have first reconstructed the results of PBKB in ref 321 for reference. Figures 5.2a–c show three scenarios for molecular and magnetic-field orientations, in which the singlet character of the nine triplet-pair states is shown to evolve with the strength of an applied magnetic field. Here we have used the method and parameters described in ref 321. Note that the line plots showing the evolution of the singlet character of the pair states with magnetic field are equivalent to the bar charts presented in Figure 5 of ref 321, and the results reproduced here are identical. The three orientation scenarios are the parallel alignment of the molecules, with the magnetic field oriented perpendicular to the molecular planes (Figure 5.2a); non-parallel molecules, with molecule B oriented at 45° to molecule A and the magnetic

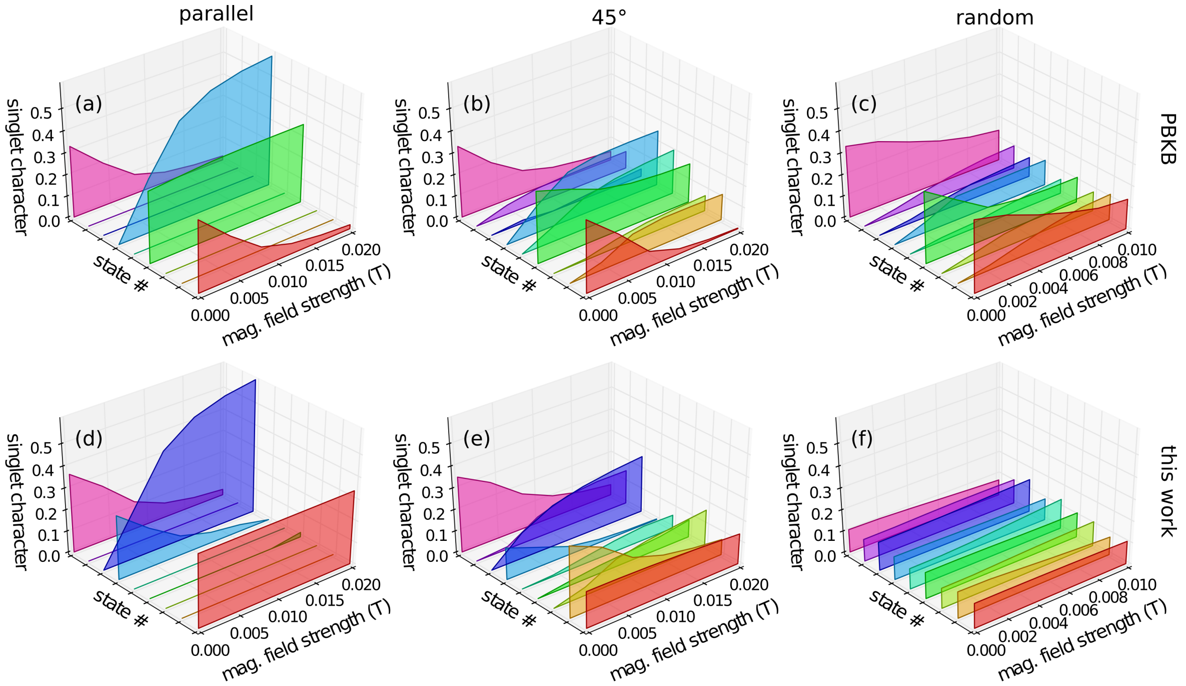

Figure 5.2: (a–c) Reproduction of the singlet-projection plots in Figure 5 of PBKB[321] showing the evolution of the singlet character of each of the nine possible triplet-pair states with magnetic field strength for (a) parallel molecules and magnetic field perpendicular to the molecular planes, (b) second molecule now orientated at 45° to the first, which has its plane perpendicular to the magnetic field, and (c) a random orientation of molecules and magnetic field direction. (d–f) Analogous plots using the model and parameters described in this work.

field oriented perpendicular to the plane of molecule A (Figure 5.2b); and a model of a randomly oriented system constructed from the average of 10^4 combined molecular and magnetic field orientations (Figure 5.2c).

In the first case of the ordered system, the parallel molecular pair naturally share their symmetry axes (x, y, and z coincide with x', y', and z', respectively) and there is no difference between the definitions of the basis vectors or singlet state of PBKB and those presented in this work. There is also no need to apply the rotation operation (eq 5.10). Consequently, the results in this case are a textbook example of the expected behaviour of the system, in which the number of pair states with singlet character evolve from three at zero-field to two towards the high-field limit.[166,205,323,326] The second scenario with the molecules aligned at 45° introduces asymmetry into the system. In this situation it is expected that even at zero magnetic field there should be some mixing of the spin states and consequently more than three of the triplet-pair states should show singlet character. This is in accord with the fact that the singlet character of pair states $|\gamma\delta'\rangle$ of unaligned molecules, where γ and δ span the x, y, and z molecular axes, is $\frac{1}{3}\cos^2\theta_{\gamma\delta'}$, where $\theta_{\gamma\delta'}$ is the angle between the axes.[327] This behaviour is not observed in Figure 5.2b, with the zero-field result identical to that for parallel molecules. The fully disordered system shown in Figure 5.2c was constructed from the average singlet character of many molecular orientations and thus should be expected to show a high degree of spin mixing at zero field.[328] Again the results at zero field are identical to that for the parallel molecules, highlighting that the incorrect definition of the overall singlet state by PBKB and consequent lack of the rotation operation on the zero-field term effectively locks the molecular pair in an identical orientation when evaluating the spin eigenstates.

Figures 5.2d–f show the identical three scenarios for molecular and magnetic field orientations as in Figures 5.2a–c, but the results were this time calculated using the model and parameters presented in this work. In the case of the ordered system with parallel molecules (Figure 5.2d), three states show singlet character at zero field, tending to two at high magnetic field strengths as expected. In the case of molecules at 45° (Figure 5.2e), four states show singlet character at zero field, indicating the model successfully exhibits the effect of the introduced asymmetry of the molecular orientations. With the application of a magnetic field the spin states are mixed further, resulting in eight states with singlet character. For the completely disordered system (Figure 5.2f), on average all nine of the triplet-pair states show singlet character for all magnetic field strengths shown. This behaviour is also seen in the disordered system from PBKB (Figure 5.2c) when a magnetic field is applied.

Note that these disordered scenarios were modelled by averaging the singlet projections over many molecular and magnetic field orientations and that one individual choice of orientation will not cause all nine states to show singlet character simultaneously. Rather, the different orientations will cause the singlet character to be displayed in various subsets of the pair states and it is the averaging process, coupled with the arbitrary eigenstate ordering that is output from the matrix diagonalisation algorithms used, which acts to give the appearance of a uniform distribution of the singlet character as shown. In terms of physical observables such as the time-resolved fluorescence, it is not the average singlet character that is important, but the singlet character of the pair states of each molecular pair that contributes to the fluorescence. The further implications of this averaging process on the simulated time-resolved fluorescence data are discussed below.

In the scenarios shown in Figure 5.2, the magnetic fields are in the mT range, so the systems are not yet in the high-field regime in which the magnetic term of the Hamiltonian dominates the zero-field term. To further illustrate that the model of PBKB does not behave qualitatively correctly, while ours does, in Figure 5.3 we have compared the evolution of the singlet character of the triplet-pair states with magnetic field strength up to very high (100 T) fields. At sufficiently large fields, the orientation of the molecules should become irrelevant as the alignment of the spins is determined solely by the magnetic field orientation. In this example, the two molecules

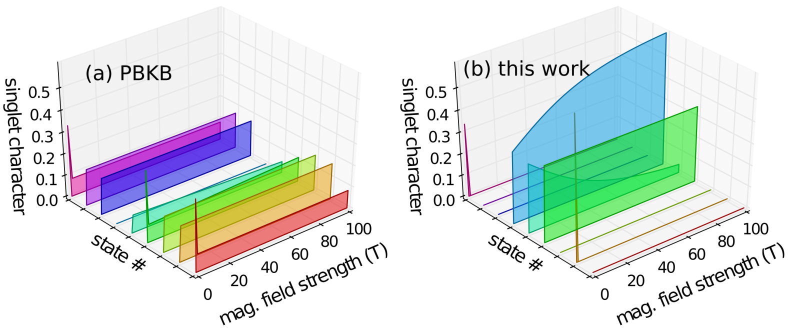

Figure 5.3: Illustration of the behaviour of (a) the model of PBKB[321] and (b) our model in the approach to the high-field limit, where only two pair states are expected to show singlet character.[166,204,323] Molecules are oriented at $\beta = 90°$ with an arbitrarily oriented magnetic field ($\theta_B = 291°$, $\phi_B = 15°$). (See Supporting Information for definition of angles.)

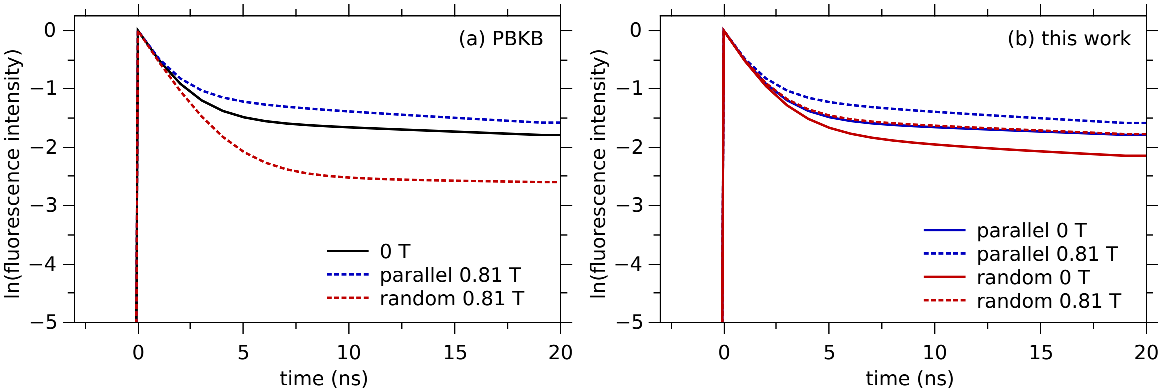

Figure 5.4: Simulated normalised fluorescence intensity decay for parallel or randomly oriented molecular pairs at zero or 0.81 T magnetic field strength for (a) the model of PBKB[321] and (b) our model.

were oriented at 90° so that the corresponding triplet eigenstates of the two molecules would be orthogonal at zero-field. An arbitrary magnetic field orientation was selected at random. Figure 5.3b shows that our model gives the expected two pair states with singlet character at high field,[166,204,323] while the model of PBKB incorrectly gives eight pair states with singlet character and no visible evolution of the states beyond intermediate field strengths.

We now turn to the simulation of the time-resolved fluorescence for the rubrene films. Again, we have first reconstructed the simulated results of PBKB[321] for reference. To model the disordered system with randomly oriented molecules, the average of many molecular and magnetic field orientations were used as described above. A parallel molecular pair was used to model an ordered rubrene film system, with the average of many magnetic field orientations used to simulate the random alignment of the molecular pairs relative to the plane of the film. For each system, a single magnetic field strength of 0.81 T was simulated and compared with the zero-field case, matching the experimental conditions.[321] The predicted singlet character of the pair states was used in the kinetic equation system (eq 5.11a and b) to produce the simulated fluorescence decays shown in Figure 5.4a. For the disordered randomly oriented system, PBKB predicted that the application of the magnetic field acts to decrease the intensity of the prompt fluorescence compared with zero-field. The ordered, parallel system shows the opposite behaviour, with an enhancement of the prompt fluorescence in the presence of the magnetic field. Note that without the magnetic field the behaviour for both the ordered and disordered systems are identical due to the lack of rotation in the zero-field term of the Hamiltonian, meaning the same singlet projections C_{S}^{l} are input to the kinetic equations in each case. The different fluorescence decays are explained by noting that for the randomly oriented case, PBKB predict that three triplet pair-states show singlet character at zero-field, increasing to nine with the application of the magnetic field (Figure 5.2c). With a larger number of dark triplet states in which the excited population can "hide", the population of the radiative singlet state is reduced at early time scales. In the ordered case, the number of pair states with singlet character evolves from three to two with the magnetic field (Figure 5.2a). Fewer triplet-pair states at high magnetic field leads to more of the excited state population being in the radiative singlet state. As only the behaviour of the ordered, parallel system matched their experimental data, PBKB excluded the possibility of singlet fission occurring from disordered sections of the rubrene film and concluded that singlet exciton migration to localised regions of order must occur prior to singlet fission.

Figure 5.4b shows the simulated fluorescence decays for the same ordered and disordered systems described above, but using the model described in this work to compute the singlet character of the triplet-pair states prior to use in the kinetic equations. In the absence of the magnetic field, the ordered system of parallel molecules and the disordered, randomly oriented molecules show different behaviour, in contrast with the data shown in Figure 5.4a. With a magnetic field applied, both the ordered and disordered systems exhibit an enhancement in the prompt fluorescence intensity. This result can again be explained in terms of the number of triplet-pair states displaying singlet character. With the ordered system of parallel molecules, the result is the same as shown in Figure 5.4a, as the definition of the overall singlet state is the same and no rotation of the zero-field terms in the spin Hamiltonian is required. For the disordered system of randomly orientated molecules, however, the number of pair states with singlet character evolves from ≈5 at zero field to ≈3 with the application of the 0.81 T magnetic field. As both the ordered and disordered systems show a reduced number of pair states with singlet character when the magnetic field is applied, so too do they both show an increase in the prompt fluorescence intensity. Critically, this indicates that the parallel and randomly oriented systems replicate the trend seen in the experimental data, and so it is plausible that singlet exciton fission does occur throughout the disordered regions in the film, eliminating the requirement of exciton migration to sites of localised order prior to fission events put forward by PBKB in their work.[321]

Nevertheless, our model does predict a regime of magnetic field strengths substantially lower than that studied experimentally by PBKB in which the time-resolved fluorescence from ordered versus disordered rubrene films may be expected to be qualitatively different. Figure 5.5 shows the simulated fluorescence intensity relative to the zero-field intensity at short times for several magnetic field strengths for the same systems of parallel or disordered molecules studied in Figure 5.4. So a positive value indicates that the prompt fluorescence intensity is enhanced compared with the zero-field case, while a negative value indicates that it is diminished. (The simulated curves over longer time scales are given in the Supporting Information.) As already shown in Figure 5.4b, the prompt fluorescence is enhanced compared with zero field for both the ordered parallel and disordered random systems at a magnetic field strength of 0.81 T. On the other hand, at a low field strength of 0.02 T, the prompt fluorescence is diminished compared with zero field for both systems as the field spreads the singlet character over a larger number of “dark” triplet pair states. But the rate at which the pair states are mixed by the field differs for the ordered and random systems and so at an intermediate field strength of 0.1 T, the two systems display opposite behaviour, with the prompt fluorescence enhanced relative to zero field for the random system, but diminished for the ordered, parallel system. Thus, we suggest that repeating the experiments at 0.1 T instead of 0.81 T may reveal whether singlet fission indeed occurs from the ordered rather than disordered regions of a rubrene film.

Finally, we note that for the simulated scenarios shown in Figures 5.4b and 5.5 we computed the singlet character of the triplet-pair states for each combination of molecular and magnetic field orientation, which were then used separately as input to the kinetic equations. The simulated fluorescence was thus determined as the average of the fluorescence over each individual molecular pair in the system, which physically describes how the emission from each molecular pair contributes to the total measured

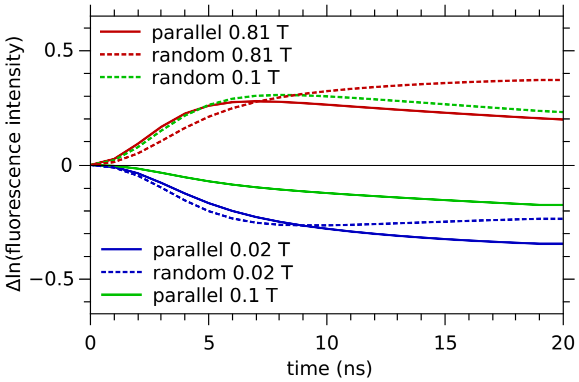

Figure 5.5: Simulated normalized time-resolved fluorescence intensity with application of a magnetic field relative to zero field for parallel or randomly oriented molecular pairs at several field strengths.

fluorescence. This method contrasts with that described by PBKB,[321] who calculated the average of the singlet projections for the entire ensemble and used this average singlet character in the kinetic equations. We have shown in Figure 5.2f that averaging the singlet character over the many orientations overestimates the number of pair states showing singlet character. A figure demonstrating the effect of the two different averaging methods on the simulated fluorescence data is shown in the Supporting Information.

Conclusions

In summary, we have identified errors in the quantum-mechanical model used by PBKB to simulate time-resolved fluorescence decays from amorphous rubrene films. In particular, the incorrect representation of the overall singlet state and thus the singlet character of the triplet-pair states leads to significant qualitative and quantitative errors in the simulated effect of an applied magnetic field on the evolution of the singlet character and fluorescence. PBKB's simulation results led to the conclusion, which we have demonstrated is not substantiated by a more accurate model, that singlet exciton migration must occur in disordered rubrene films to regions of localised order prior to singlet fission. Nevertheless, we show that time-resolved fluorescence experiments at lower magnetic fields than those studied by PBKB may be able to distinguish between singlet fission from ordered or disordered regions of a rubrene film, supporting their suggestion that measurements of magnetic-field effects on fluorescence decay dynamics can provide a sensitive probe of molecular-level morphology in systems that undergo singlet fission.

Acknowledgements

We thank Timothy Schmidt, Andrew Danos, Simon Blacket and Louis Ritchie for fruitful discussions.

Supporting Information

Spin Hamiltonian for the Triplet Pair State

Complete description of the spin Hamiltonain for singlet to triplet–triplet interaction is given in Section 2.2.3.

Additional Notes on PBKB Hamiltonian

Piland, Burdett, Kurunthu and Bardeen (PBKB)[321] incorrectly use a plus instead of a minus sign in the first term of eq 5.3 for the single-molecule zero-field component of the spin Hamiltonian. This does not change the eigenstates but shifts all the eigenvalues up by $4D/3$. (However, in the Hamiltonian matrix in the Supporting Information of their paper,[321] only one of the eigenvalues, corresponding to the $|z\rangle$ state, is shifted.)

The Hamiltonian matrix in the Supporting Information of the paper by PBKB[321] has the opposite sign for all terms in the above matrix involving the y-component of the magnetic field. This is equivalent to using a left-handed coordinate system rather than the conventional right-handed coordinate system that we have assumed here (i.e. the y axis points in the opposite direction to the conventional direction).

In PBKB,[321] the zero-field splitting parameters $D = -6.2 \times 10^{-3}\,\mathrm{cm}^{-1}$ and $E = 2.48 \times 10^{-2}\,\mathrm{cm}^{-1}$ for crystalline tetracene[324] are used, even though there are two tetracene molecules per triclinic unit cell[329] and the axes in eq 5.3 are then defined by the crystal unit cell. The molecular parameters for tetracene (obtained from EPR experiments),[324] $D = 5.2 \times 10^{-2}\,\mathrm{cm}^{-1}$ and $E = -5.2 \times 10^{-3}\,\mathrm{cm}^{-1}$, which differ substantially from the crystal parameters, are more appropriate when considering the triplet spin interactions between molecular pairs as a function of relative molecular orientation. Thus, we have used the molecular parameters in our work. PBKB note that identical results were obtained when using the tetracene molecular parameters, but we believe that this may be an artefact of the incorrect calculation of the zero-field term in the Hamiltonian (see Figure 5.6).

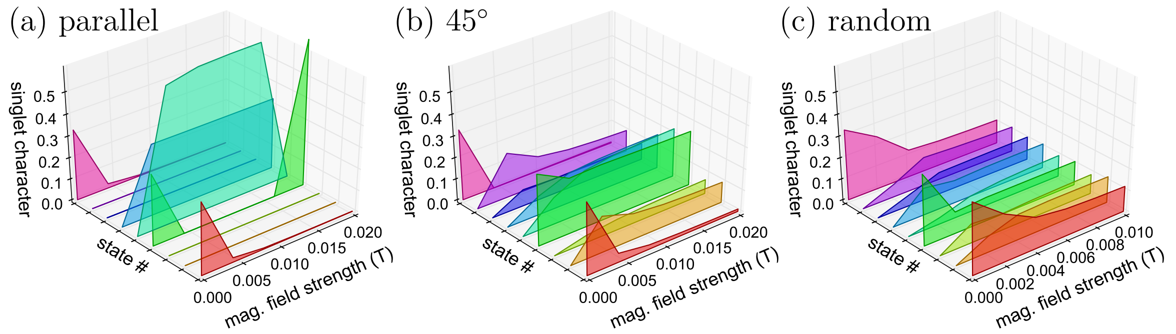
(a) parallel (b) 45° (c) random

Figure 5.6: Effect of using the crystalline instead of molecular zero-field splitting parameters on the singlet character of the triplet pair states. The molecular and magnetic field orientation scenarios (a), (b) and (c) are identical to those in Figure 2 of the main text. The spin-Hamiltonian model of PBKB[321] was used with the parameters $D = 5.2 \times 10^{-2}\,\mathrm{cm}^{-1}$ and $E = -5.2 \times 10^{-3}\,\mathrm{cm}^{-1}$ from molecular tetracene,[324] $g\beta = 5\,\mathrm{cm}^{-1}\,\mathrm{T}^{-1}$ and $X = 10^{-4}\,\mathrm{cm}^{-1}$.

Given the g-factor of 2.002[324] and the Bohr magneton of $0.4669\,\mathrm{cm}^{-1}\,\mathrm{T}^{-1}$, $g\beta = 0.9338\,\mathrm{cm}^{-1}\,\mathrm{T}^{-1} \approx 1\,\mathrm{cm}^{-1}\,\mathrm{T}^{-1}$. Both this value and a value of $5\,\mathrm{cm}^{-1}\,\mathrm{T}^{-1}$ are mentioned by PBKB.[321] We were only able to reproduce their results with $g\beta = 5\,\mathrm{cm}^{-1}\,\mathrm{T}^{-1}$, as shown in Figure 5.7.

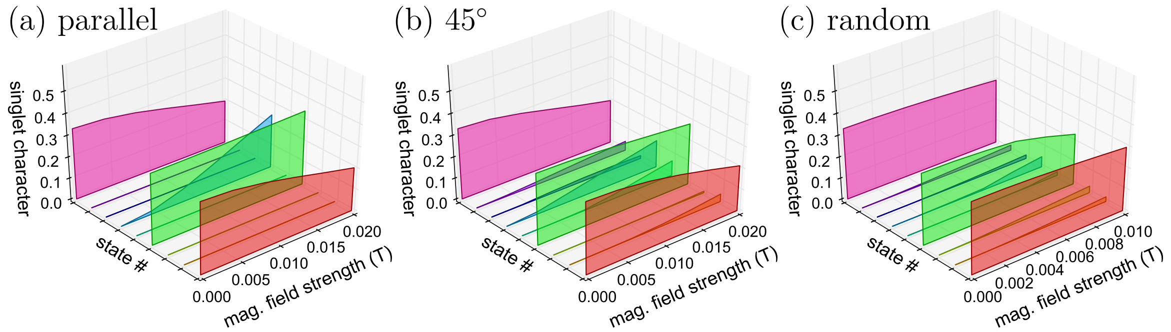

Figure 5.7: Effect of the $g\beta$ magnetic parameter on the singlet character of the triplet pair states. The molecular and magnetic field orientation scenarios (a), (b) and (c) are identical to those in Figure 2 of the main text. The spin-Hamiltonian model of PBKB[321] was used with the parameters $D = -6.2 \times 10^{-3}\,\mathrm{cm}^{-1}$ and $E = 2.48 \times 10^{-2}\,\mathrm{cm}^{-1}$ for crystalline tetracene and $X = 10^{-4}\,\mathrm{cm}^{-1}$. Here, the literature value[324] of $g\beta = 1\,\mathrm{cm}^{-1}\,\mathrm{T}^{-1}$ for tetracene was used. The results shown in Figure 5 of PBKB[321] could only be reproduced using $g\beta = 5\,\mathrm{cm}^{-1}\,\mathrm{T}^{-1}$.

Simulated Time-Resolved Fluorescence

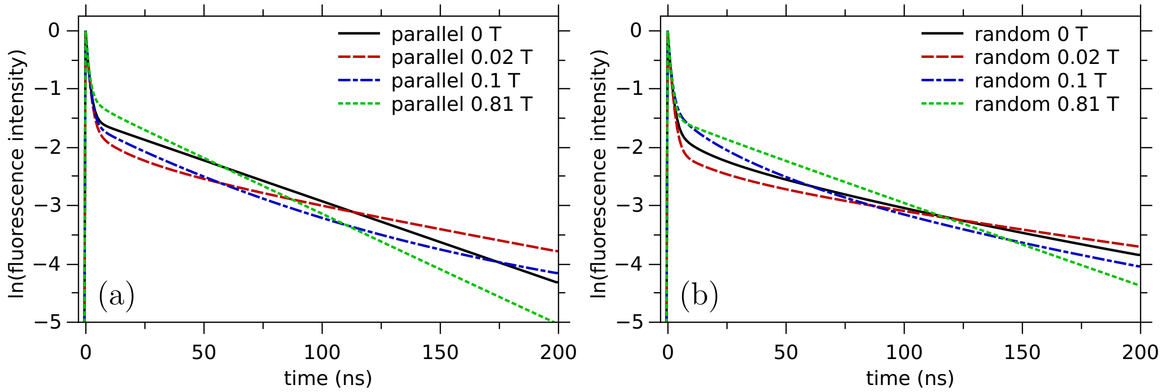

Figure 5.8: Simulated normalised time-resolved fluorescence intensity using our spin-Hamiltonian model and parameters showing the effect of the magnetic field on the proportions of early and delayed fluorescence. The same parameters used by PBKB[321] were employed in the kinetic model. Both the (a) ordered system of parallel molecules and (b) disordered system of randomly oriented molecules give the same qualitative behaviour compared with the zero-field case at the lowest and highest magnetic field strengths. At the lowest field strength (red dashes) the magnetic field helps to distribute singlet character across the triplet-pair states, decreasing the prompt fluorescence intensity and enhancing the delayed fluorescence. At the highest field strengths (green dots) the magnetic field forces the alignment of the spins, reducing the number of triplet-pair states with singlet character and increasing the prompt fluorescence intensity. Our simulations predict an intermediate magnetic field strength (blue dash-dot) at which the ordered and disordered systems will display opposite behaviours.

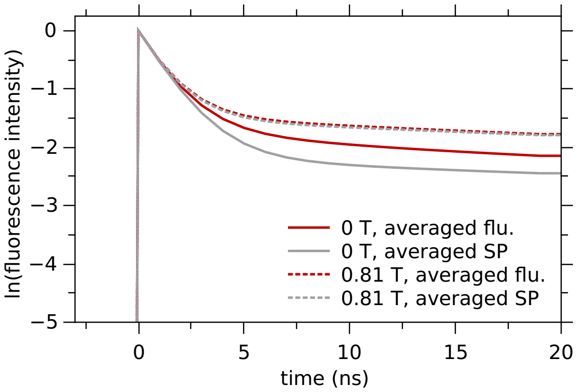

Figure 5.9: Comparison of simulated fluorescence decays using two alternate averaging methods when multiple molecular and/or magnetic field orientations are involved, in this case for the disordered system. The method used in PBKB[321] averaged the singlet projections (SP) for all orientations prior to use in the system of kinetic equations. In this work, we used the singlet projections of each individual orientation as input to the differential equations and subsequently average the simulated fluorescence (flu.). This method more accurately models the physical processes that determine the measured fluorescence; specifically, each molecule pair undergoes emission that contributes to the fluorescence intensity, but at a rate that differs for each pair and depends on the molecular configuration and orientation with respect to the magnetic field. As described in the main text, the process of averaging the singlet projections can act to artificially spread the singlet character over all nine triplet-pair states and consequently underestimates the intensity of the prompt fluorescence.

CHAPTER 6

Molecular Effects in Photochemical Upconversion by Triplet–Triplet Annihilation in Solution

Statement of Authorship

Title of Paper	Molecular Understanding of Photochemical Upconversion for Efficient Solar Cells
Publication Status	Unpublished and Unsubmitted Work Written in a Manuscript Style
Publication Details	Tapping, P. C.; Blacket, S.; Ackling, S.; Huang, D. M. **2016**. Manuscript in preparation.

Principal Author

Principal Author	Patrick C. Tapping		
Contribution to the Paper	Development of TTA simulation code, data analysis, construction of figures, writing of manuscript.		
Overall Percentage	80%		
Signature		Date	18/7/16

Co-Author Contributions

By signing the Statement of Authorship, each author certifies that the stated contributions to the following publication are accurate and that permission is granted for the publication to be included in this thesis.

Co-Author	Simon Blacket		
Contribution to the Paper	Running of MD simulations, data analysis, construction of Figures 6.2–3, 6.12–14, 6.21–22, 6.29–30.		
Signature		Date	21/7/2016

Co-Author	Sophia Ackling		
Contribution to the Paper	Development of MD force field for toluene.		
Signature		Date	22/7/16

Co-Author	David M. Huang		
Contribution to the Paper	Supervision of project; assistance with theory, writing and editing of manuscript; corresponding author.		
Signature		Date	22/7/16

Abstract

Solar cell efficiency may be improved through integration of an upconverting layer to facilitate harvesting of sub-bandgap photons, for example through a solution-based process of sensitised triplet–triplet annihilation upconversion (TTA-UC). Molecular dynamics (MD) simulations of emitter molecules are coupled with a quantum mechanical description of disordered triplet–triplet spin interactions to investigate the influence of diffusion rate, molecular shape, and collision geometry on the upconversion efficiency. The qualities of a good emitter molecule are discussed. Close contact of the polyaromatic core of the emitters is found to be the primary influence of annihilation efficiency, followed by diffusion rate and finally molecular orientation during collisions. A dynamic model of the triplet pair interaction reproduces behaviour observed in solution-phase experiments, where magnetic fields have an exclusively negative effect on TTA-UC. In contrast, the use of a static molecular arrangement predicts an enhancement in TTA-UC with intermediate field strengths, replicating results from solid-state experiments. Using the explicit emitter trajectories obtained from the MD simulations, the model shows that the motion of the triplet-pair during a collision is sufficient to cause significant mixing of the spin states. By inducing spin alignment, applied magnetic fields result in exclusively negative effects on upconversion efficiency by decreasing the rate of this mixing.

Introduction

Solar power offers a scalable and sustainable means to meet society's ever increasing demand for energy, with solar irradiance of the Earth's surface exceeding the world's power usage by several orders of magnitude.[330] Currently silicon-based photovoltaic cells provide the majority of solar electricity production, and economies of scale in manufacturing have reduced their cost-per-watt significantly in recent times. However, to become a viable option, the deployment of photovoltaics on the terawatt-scale requires further improvements to this ratio. Many next-generation technologies are emerging that hope to achieve the ideal of cheap, easily manufactured photovoltaics using non-toxic and readily available materials.[55,331] Regardless of the specific technology, any solar cell using a single band gap is intrinsically limited in efficiency to approximately 33% due to the nature of the solar spectrum, as described by the Shockley–Quiesser limit.[56] The primary factor is that the band gap of a single-junction cell can never be tuned to capture the full energy of the solar spectrum. Photons with energy greater than the band gap are absorbed, but excess photon energy cannot be converted to electrical power and is lost as heat. If the photon energy is lower than the band gap, the cell is simply unable to harvest it, thus these wavelengths are transmitted to be absorbed or reflected by the inactive substrate. Currently this limitation is overcome by layering multiple cells tuned to different parts of the spectrum, but such multi-junction cells are more expensive and difficult to produce. An alternative approach is to instead tune the spectrum of the incident light through the addition of a conversion layer. Upconversion combines the energy of two low-energy photons to create a single, higher-energy photon, while downconversion describes the splitting of a high-energy photon in to two lower-energy photons. Such processes are readily achievable in the laboratory using nonlinear optics with high-intensity laser light, but this approach does not work with unconcentrated sunlight. In this case, upconversion can instead be achieved through a photochemical process, whereby a long-lived triplet state acts as an intermediate energy store.

TTA-UC uses a blend of sensitiser and emitter molecules. The sensitiser is required to absorb the low-energy wavelengths and rapidly enter its triplet state *via* intersystem crossing; typically a metalloporphyrin is used, but pure organic molecules have also been demonstrated.[170,332] Emitter molecules generally contain a polyaromatic structure, the ideal having a T_1 state half the energy of S_1, and its T_2 state greater than the S_1 energy. Triplet energy transfer from an excited sensitiser causes a ground-state emitter to be excited directly to its triplet state. In a solution-phase system such as those discussed herein, this occurs through collisions between sensitiser and emitter molecules. Colliding pairs of excited emitter molecules may then undergo triplet–triplet annihilation (TTA) to form a variety of products. One possible product has an emitter returning to the ground-state while the other enters the higher-lying S_1 state. Fluorescence from the singlet excited state is spin-allowed thus occurs rapidly, emitting a photon of greater energy than those absorbed by the sensitiser. Solution-based TTA-UC systems are the most common and are the focus of this work,[168,169,206–209] but recently a variety of solid-state examples have been demonstrated based on integrating the sensitiser and emitters into systems such as polymer matrices, nanoparticles or metal-organic frameworks.[333–335] Triplet diffusion mechanisms and molecular freedom will vary in the solid-phase, but much of the theory discussed here applies equally to solid-state systems.

Given a pair of uncorrelated triplet emitters, annihilation should be naively expected to give a choice of nine products with equal probability; one singlet, three triplet and five different quintet states. Experimentally, yield of the desired singlet product has been observed to exceed 1/9, indicating that the singlet, triplet and quintet decay pathways are not equally accessible due to energy-level mismatches or other influences.[336] Emitter molecules are generally non-spherical, so the relative orientation of collisions in solution will not be completely uncorrelated. Alignment of the spins comprising the triplets will be influenced by the orientation of the individual molecules, thus the specific geometry of the emitter collisions should be expected to affect the total spin character of the triplet-pair and the resulting distribution of products. Further, as magnetic fields will also act upon the alignment of the spins, the efficiency of TTA-UC will additionally display dependence on any applied magnetic field.

In crystals of polyaromatic molecules such as anthracene, competing singlet fission and triplet fusion processes result in a delayed fluorescence phenomenon which displays significant dependence on the magnetic field strength and orientation relative to the crystal planes.[204] More recently, in a TTA-UC system consisting of a sensitised film of diphenylanthracene, an 11% enhancement of upconversion was measured when a ∼50 mT magnetic field was applied. The theory of triplet–triplet interactions has been studied extensively, notably by Merrifield[205] and Suna[337] circa 1970, with a comprehensive overview provided by Swenberg and Geacintov.[166] These orientational and field strength dependencies can be well described using Merrifield's theory, based on a quantum mechanical description of the spin interactions.

The idea that the upconversion process could be enhanced through engineering emitter molecules that encourage favourable interaction geometry and by the application of magnetic fields is clearly appealing. Although positive magnetic field effects on triplet fusion has been observed in low-temperature solutions,[338] the influence of magnetic fields at room temperature appears to be exclusively negative.[209,328,339] Recently, the dependence on solvent and solvent viscosity in a sensitised TTA-UC system has been reported, in which higher viscosity was shown to assist the triplet fusion process under some conditions.[340] The contrasting magnetic field effects for solid versus solution-based systems has been explained by a process of spin relaxation facilitated by the rapid rotational motion of the emitter molecules.[341,342] To date, attempts to model the solution behaviour have relied on some significant assumptions. Atkins and Evans derived an analytic model of the magnetic field dependence by reducing the physical description of the emitter molecules to their bulk translational and rotational diffusion rates, with spin relaxation introduced through the use of Redfield's theory of spin relaxation.[341–343] Others have either depicted the relative molecular orientations during triplet-pair collisions as a static sandwich arrangement, or as completely uncorrelated interactions through an average of all possible orientations.[328,340,344]

In this work, we examine in detail two different emitter molecules to determine the characteristics which influence effectiveness as an emitter in a solution-based TTA-UC system. We focus only on the behaviour of the excited emitter pairs and do not consider the sensitisation step in this study. Rubrene and perylene are chosen as two commonly used emitters,[171] with sufficiently different size and structure for comparison. For the first time, MD simulations are performed of the emitters in explicit solvent to investigate the collisional dynamics explicitly, examining in particular the effect of intermolecular correlations during collisions that have previously been ignored in theoretical models of solution based TTA. The trajectories provide collision rates and durations, as well as representative geometry of the emitter pairs during the entirety of each interaction. To simulate the yield of the desired singlet product from the TTA process, we employ a spin Hamiltonian derived previously to describe triplet–triplet interactions with arbitrary molecular and magnetic field orientations.[3] The influence of diffusion rate, shape and collision geometry as well as energy levels are addressed. Magnetic field effects on the TTA-UC process in solution are modelled with a novel technique that demonstrates the mechanism of spin relaxation using only the explicit orientations of the emitter molecules during interaction events, without requiring the inclusion of relaxation terms. Finally, the results are discussed as a whole in the context of the rational design of the ideal emitter molecule.

Computational Methods

Molecular Dynamics

Molecular dynamics simulations were performed with the LAMMPS molecular dynamics simulation package,[345–348] using interaction parameters from the all-atom optimised potentials for liquid simulations (OPLS-AA) force field and enforcing periodic boundary conditions to simulate a bulk solution.[211–216] Bond lengths of the minimum-energy geometries of toluene, rubrene and perylene were determined using density functional calculations at the CAM-B3LYP/6-31G** level with D3 dispersion corrections in the TeraChem quantum chemistry package.[349,350] The ground-state geometry of the emitter molecules was assumed throughout the simulations as full quantum mechanical treatment of the dynamics of condensed-phase systems such as these is computationally unfeasible. After energy minimisation of the molecular systems using LAMMPS and the OPLS-AA force field, bond lengths were on average within ∼1% of those found from the quantum calculations. A Nose–Hoover thermostat and barostat was used to simulate constant temperature and pressure conditions (NPT ensemble).[351] Long-range electrostatic interactions were computed using the particle–particle particle–mesh (PPPM) method.[352,353] Carbon–hydrogen bond lengths were constrained with the SHAKE algorithm.[354] Simulation parameters are given in the Supporting Information.

Toluene

Systems of 1000 toluene molecules were simulated at a pressure of 1 atm and temperature of 200 K or 295 K. Molecules were initially placed in a face-centred-cubic lattice arrangement inside a cubic box with side lengths of 80 Å and then allowed to equilibrate over a period of 10 ns, reaching an average volume of 160.3 nm^3 and 179 nm^3 for the 200 K and 295 K systems, respectively. The simulation was then run for a further 8 ns, using a 2 fs integration timestep.

Rubrene or Perylene in Toluene

Systems of 20 emitter molecules (rubrene or perylene) with 8000 toluene molecules were simulated at temperature of 295 K and pressure of 1 atm. An additional simulation of rubrene in toluene was also performed at 200 K. Emitter and solvent molecules were placed randomly in a cubic box with side lengths of 150 Å. Overlapping atoms were first separated by performing a simulation using a soft potential force field and then the systems were allowed to reach their equilibrium volume by running the NPT ensemble over a period of approximately 3.5 ns. Final average simulation box sizes were 1294 nm^3 and 1451 nm^3 for rubrene in toluene at 200 K and 295 K respectively, equivalent to a concentration of 25.7 $\mathrm{mmol\,L^{-1}}$ and 22.9 $\mathrm{mmol\,L^{-1}}$. For perylene in toluene, the final average box size of 1443 nm^3 equated to a concentration of 23.0 $\mathrm{mmol\,L^{-1}}$. The NPT simulation was then run for a further 150 ns for the systems at 295 K and 200 ns for the perylene system at 200 K, with an integration timestep of 2 fs.

Collision Counts, Durations and Orientations

Collision ranges for pairs of emitter molecules were identified from local maxima observed in plots of the radial distribution functions (RDFs). Due to the non-spherical nature of the molecules, these plots showed multiple maxima that correspond to different favourable orientations of the two molecules. Over the course of the MD simulations the number of collisions at each range were counted to determine the rate of association for pairs of molecules. A collision at a particular range was counted if the pairs of molecules entered that range from a greater distance. Once a collision was registered, any interaction between that pair of molecules was not again counted as an additional collision until they separated by at least a distance of twice the molecular length (19.2 Å for perylene and 27.2 Å for rubrene). A collision counted at an inner range did not also count as a collision at any longer ranges. For each collision detected, the inverse of the mean duration that the emitter pair remained within the collision range was used to determine the rate of dissociation of the molecules. To eliminate overestimation of the collision counts due to small, stochastic motions of the emitters, a moving-window time average of the molecular separations was used. The window size of $2w + 1$ was selected so that a unit increase in w resulted in a 0.1% reduction in the total collision counts ($w = 190$ timesteps for perylene and $w = 360$ timesteps for rubrene). In this way, the choice of window size then has minimal effect on the measured collision rate. For each simulation timestep a plane was fitted to each emitter molecule and the Euler angles that describe the relative orientation of the molecules were determined. The relative positions of the centres-of-mass of the molecules was also computed in the coordinate system defined by the symmetry axes of one of the molecules. The Euler angles and spherical polar coordinates used to describe the relative orientation and position, respectively, of the molecules are defined graphically in the Supporting Information. Relative orientations and positions of the molecules were collected for each timestep in which the molecular pair were in the approach phase of a collision. Randomly selected subsets of these collision geometries were used for the later TTA-UC simulation calculations.

Triplet–Triplet Annihilation Rates

Triplet–triplet interactions have been a focus of much study, originating with the theory proposed by Merrifield on triplet exciton interactions and the effect of applied magnetic fields.[203–205] Typically, two general approaches are used, though both are based on the identical quantum mechanical description of spin–spin interactions. Where the annihilation rate is fast compared to the motion of the triplets, a static method is applicable and can predict some of the experimentally observed magnetic field effects in molecular crystals and thin films.[323,355] Conversely, when the motion of the molecules is comparable to the annihilation rate, an extension of the model can account of the dynamic interactions between the molecules and magnetic field.[204,328,337,341,342,344] In this work, we calculate triplet–triplet annihilation rates from the emitter molecule collision orientations found from the MD simulations using both approaches. While the static model is useful to isolate and quantify the various individual contributions to the observed TTA-UC rates, the dynamic model coupled with the explicit molecular geometries obtained from the MD simulations provides unprecedented clarity of the spin relaxation mechanisms present in solution.

In a somewhat simplified picture, the interaction of a pair of excited triplet state emitters ${}^3\mathrm{E}^*$ is described by

$$ {}^3\mathrm{E}^* + {}^3\mathrm{E}^* \underset{k_{-1}}{\overset{k_1}{\rightleftarrows}} \begin{cases} {}^1[\mathrm{E}{\cdots}\mathrm{E}]^* \xrightarrow{k_\mathrm{S}} {}^1\mathrm{E} + {}^1\mathrm{E}^* \\ {}^3[\mathrm{E}{\cdots}\mathrm{E}]^* \xrightarrow{k_\mathrm{T}} {}^1\mathrm{E} + {}^3\mathrm{E}^{**} \\ {}^5[\mathrm{E}{\cdots}\mathrm{E}]^* \end{cases} . \tag{6.1} $$

k_1 is the rate of association of the emitters to form an encounter complex $[\mathrm{E}{\cdots}\mathrm{E}]$. Four products of the encounter complex are assumed to be possible. The pair may simply dissociate without energy transfer at a rate of k_{-1}, resulting in the emitters remaining in their original excited triplet states. The mixing of spins will in the triplet pair allow nine possible combinations of singlet, triplet and quintet states. Statistical probability would predict that the chance of an excited singlet, triplet or quintet product would be 1/9, 3/9 and 5/9 respectively, but the probability of these products also depends on the spin character of the encounter complex, which is affected by the orientation of the individual emitter molecules and any applied magnetic field, and on the rates of the various reaction channels in the kinetic scheme above. The development of a quantum mechanical model for interacting spins of disordered molecular pairs is described in a previous publication.[3] Construction of the Hamiltonian is outlined briefly here with details given in the Supporting Information.

Spin Hamiltonian for a Triplet Pair

The Hamiltonian consists of four terms

$$\hat{H} = \hat{H}_{\mathrm{SS_A}} + \hat{H}_{\mathrm{SS_B}} + \hat{H}_{\mathrm{magnetic}} + \hat{H}_{\mathrm{AB}}. \tag{6.2}$$

The zero-field intramolecular spin–spin coupling is given by $\hat{H}_{\mathrm{SS}}$ for molecule A and B. The effect of an external magnetic field is given by the Zeeman term $\hat{H}_{\mathrm{magnetic}}$, which captures the contributions from both molecules. Finally, $\hat{H}_{\mathrm{AB}}$ describes the intermolecular dipolar interaction, which depends on the distance between the molecules and their spatial arrangement. The zero-field splitting parameters D and E that contribute to $\hat{H}_{\mathrm{SS}}$ were taken to be those of molecular tetracene obtained from EPR experiments.[324] Rubrene is a substituted tetracene, thus the zero-field splitting parameters should be similar. Given the absence of experimental data, and that we are most concerned with comparing the physical characteristics of the emitter molecules on TTA, identical values were also used for perylene which should be on the correct order of magnitude. The intermolecular term was taken to be a dipolar interaction (Supporting Information), as the intermolecular interactions between molecular triplets in polyaromatic hydrocarbons such as anthracene and tetracene are of this nature.[166] We set the parameter controlling the strength of these interactions to $X = |D|$ and used the relative molecular orientation and the collision separation distance of the emitter molecules found from the MD simulations. In this way the influence of the intermolecular interaction term will be around two orders of magnitude smaller than the intramolecular interactions at typical collision distances. Because the intermolecular interactions are small compared with the intramolecular and magnetic field interactions, the specific form of the equation used for these interaction is not very important in terms of determining the spin eigenstates and energies and the resulting triplet–triplet annihilation rate. These interactions must be present for triplet annihilation to occur and to split otherwise degenerate eigenstates, particularly at high magnetic fields.

Static Model

Diagonalising the complete spin Hamiltonian provides the energies and wavefunctions $|\psi_l\rangle$ of each of the nine possible spin eigenstates l of the encounter complex. Projecting the wavefunctions on to the pure singlet state[3]

$$C^l_{\mathrm{S}} = \frac{1}{\sqrt{3}} \left(\langle xx| + \langle yy| + \langle zz| \right) |\psi_l\rangle \tag{6.3}$$

provides the degree of singlet character $|C^l_{\mathrm{S}}|^2$ of each pair state, where the molecular pair spin states $|xx\rangle$, $|yy\rangle$, $|zz\rangle$ ... are defined in the Supporting Information. Similarly, the triplet or quintet character can be obtained by the projections on to the pure triplet or quintet states[219]

$$C^l_{\mathrm{T_1}} = \frac{1}{\sqrt{2}} \left(\langle xy| - \langle yx| \right) |\psi_l\rangle \tag{6.4}$$

$$C^l_{\mathrm{T_2}} = \frac{1}{2} \left(\langle xz| - \langle zx| + i \left(\langle yz| - \langle zy| \right) \right) |\psi_l\rangle \tag{6.5}$$

$$C^l_{\mathrm{T_3}} = \frac{1}{2} \left(\langle xz| - \langle zx| - i \left(\langle yz| - \langle zy| \right) \right) |\psi_l\rangle . \tag{6.6}$$

and

$$C^l_{\mathrm{Q}_1} = \frac{1}{\sqrt{2}} \left(\langle xx| - \langle yy| \right) |\psi_l\rangle \tag{6.7}$$

$$C^l_{\mathrm{Q}_2} = \frac{1}{\sqrt{6}} \left(\langle xx| + \langle yy| - 2\,\langle zz| \right) |\psi_l\rangle \tag{6.8}$$

$$C^l_{\mathrm{Q}_3} = \frac{1}{\sqrt{2}} \left(\langle yz| + \langle zy| \right) |\psi_l\rangle \tag{6.9}$$

$$C^l_{\mathrm{Q}_4} = \frac{1}{\sqrt{2}} \left(\langle xz| + \langle zx| \right) |\psi_l\rangle \tag{6.10}$$

$$C^l_{\mathrm{Q}_5} = \frac{1}{\sqrt{2}} \left(\langle xy| + \langle yx| \right) |\psi_l\rangle \tag{6.11}$$

From the kinetic scheme in eq 6.1, the rate of triplet annihilation resulting in an excited singlet state γ_{S} is then computed using a kinetic equation of the form

$$\gamma_{\mathrm{S}} = \frac{k_1}{9} \sum_{l=1}^{9} \frac{k_{\mathrm{S}}|C^l_{\mathrm{S}}|^2}{k_{-1} + k_{\mathrm{S}}|C^l_{\mathrm{S}}|^2 + k_{\mathrm{T}}|C^l_{\mathrm{T}}|^2}, \tag{6.12}$$

where $|C^l_{\mathrm{T}}|^2 \equiv \sum_{i=1}^{3} |C^l_{T_i}|^2$. Here we note that the quintet character $|C^l_{\mathrm{Q}}|^2$ does not appear in eq 6.12. In our analysis we ignore the effect of quintet products as the required two-electron excitations are unlikely to be energetically accessible.[323,328] Hence we set $k_{\mathrm{Q}} = 0$, representing a closed quintet decay pathway as shown in eq 6.1.

As triplet exciton energy transfer (TEET) decreases exponentially with increasing separation between the molecules,[356–358] the rates of annihilation to form the excited singlet or highly excited triplet species will also be modulated with the intermolecular distance. For this reason the rate constants for TTA via the singlet k_{S} or triplet channel k_{T} were modelled by equations of the form $k = k_0 \exp(-k_\beta r)$. The distance decay factor $k_\beta = 3.44\,\text{Å}^{-1}$ was taken from TEET rates of perylene diimide dimers in benzene derived from quantum calculations.[358] The coefficients k_{S_0} and k_{T_0} were chosen by fitting to time-resolved experiments of rubrene emitters in toluene (Supporting Information).[359] The same value of k_{S_0} was then also used for perylene, while k_{T_0} was approximated as $k_{\mathrm{S}_0}/100$ due to the T_2 energy level of perylene lying significantly higher than S_1 compared to the equivalent energy levels in rubrene.[360,361]

Collisions between pairs of molecules in solution exhibit a variety of orientations and spatial arrangements that will each result in triplet-pair states with different proportions of singlet $|C^l_{\mathrm{S}}|^2$ or triplet character $|C^l_{\mathrm{T}}|^2$. Thus, within each collision range identified for the emitter molecules, a random subset of 500 molecular geometries were sampled from the MD trajectories. Where magnetic field effects were considered, 500 random magnetic field directions were generated to simulate the arbitrary orientation of the molecular pairs in solution. Each molecular orientation was coupled with each magnetic field orientation and used individually as input to the spin Hamiltonian and kinetic equation. The TTA-UC rate for each collision range was then calculated as the average TTA-UC rate for 2.5×10^5 combinations of molecular and magnetic field orientations. Note that although the same number of collision geometries were used at each collision range, the relative frequency of the collisions at each range is expressed through the emitter association rates k_1 obtained from the MD simulations. The final TTA-UC rate γ_{S} was then computed as the sum over all ranges, as a collision at an inner range is not also counted in any outer ranges. We note that the method used here

Table 6.1: Parameters used in the TTA-UC simulations.

	description	value		ref.
D	molecular zero field splitting parameters	5.2×10^{-2}	cm^{-1}	324
E		-5.2×10^{-3}	cm^{-1}	324
X	intermolecular spin–spin coupling coefficient	5.2×10^{-2}	cm^{-1}	
$g\beta$	g-factor times Bohr magneton	0.9338	$\mathrm{cm}^{-1}\,\mathrm{T}^{-1}$	324
k_{S_0}	singlet channel rate constant coefficient	2.66×10^{17}	s^{-1}	359[a]
k_{T_0}	triplet channel rate constant coefficient (rubrene)	6.25×10^{16}	s^{-1}	359[a]
	(perylene)	2.66×10^{15}	s^{-1}	
k_Q	quintet channel rate constant	0	s^{-1}	328
k_β	TEET exponential distance decay coefficient	3.44	$\mathrm{Å}^{-1}$	358

[a] value fitted to referenced experimental data (Supporting Information).

to divide the emitter pair interactions into discrete collision ranges may overemphasise the influence of the collision geometry at the inner ranges. In a physical system, an annihilation event at large separation distance will destroy the triplet-pair and preclude subsequent TTA if the colliding molecules continue their approach. As we are interested in separating out the various molecular factors that contribute to the TTA-UC rate, the division of the emitter pair interactions into discrete collision ranges provides a straightforward means to do so. In addition, any error introduced by this treatment should be small as the effect of the molecular orientations on the TTA-UC rate is far outweighed by the influence of molecular separation distance during collisions.

All parameters used in constructing the spin Hamiltonian and kinetic model are shown in Table 6.1.

Dynamic Model

The kinetic model described by eq 6.12 can reproduce the magnetic field dependence of TTA-UC in the case of static molecular arrangements such as crystalline materials. Of particular interest is the enhancement in TTA-UC that is observed with the application of intermediate-strength magnetic fields.[204,323,355] In the case of high-temperature solutions, the motions of the excited triplet molecules occur on time scales comparable to the annihilation rates k_S, k_T and act as a source of spin relaxation.[341,342] This must be taken into account in order to reproduce the behaviour observed in solution-based experiments where TTA-UC decreases monotonically with the application of magnetic fields.[209,328,339,340] We employ an extension of the static model that accounts for the time evolution of the spin interactions over the course of a triplet-pair collision. The model is based on the spin density matrix approach demonstrated by Johnson and Merrifield and Suna to consider the effect of exciton mobility in molecular crystals,[204,337] and later used by Avakian et al. and Lendi et al. to describe TTA-UC in solution.[328,344] The equation describing the evolution of the spin density matrix ρ is based on the Liouville equation,

$$\frac{\partial \rho}{\partial t} = k_1 \Gamma - i[\hat{H}, \rho] - \frac{1}{2}\{\rho, \Lambda\} - k_{-1}\rho, \tag{6.13}$$

where the square brackets are the commutator and the braces are the anticommutator, Γ is the generation matrix and Λ is the annihilation matrix. The terms in eq 6.13 are most conveniently expressed in a basis of the overall pure singlet, triplet and quintet states of the triplet-pair using eqs 6.3–6.11. The annihilation term $\{\rho, \Lambda\}$ governs the decay through the singlet, triplet or quintet channels at a rate of k_S, k_T or k_Q respectively. Previous studies using the spin density matrix approach have not explicitly considered the individual triplet-pair interactions, instead treating the collisional dynamics as an ensemble average through the inclusion of the generation and dissociation terms.[209,328,339–342,344] The generation term $k_1\Gamma$ is considered to form the triplet-pair from two uncorrelated triplet molecules and so populates the singlet, triplet and quintet states equally at a rate of $\frac{1}{9}k_1$. Similarly, the dissociation term $k_{-1}\rho$ depopulates all states equally at a rate of k_{-1}. The explicit form of the generation an annihilation matrices are given in the Supporting Information.

To capture the dynamic nature of the triplet-pair collisions, we consider every individual triplet-pair collision explicitly. In this manner the association and dissociation of the molecular pairs is controlled by the MD trajectories, thus k_1 and k_{-1} are set as zero and the Liouville equation becomes

$$\frac{\partial \rho}{\partial t} = -i[\hat{H}, \rho] - \frac{1}{2}\{\rho, \Lambda\}. \tag{6.14}$$

The generation of the triplet pairs is taken into account through the initial condition of the spin density matrix, where all 9 pair state are equally populated before the collision. We then evolve the density matrix by integrating eq 6.14 over time using a 10 fs time step. Geometry for the triplet-pair collisions and relative magnetic field orientation are sampled at 1 ps intervals from the MD simulations starting from beyond the interaction distance (10.4 Å for both rubrene and perylene) and used to determine both $\hat{H}$ and Λ at each time step. The simulated TTA-UC is taken as the sum of the decay through the singlet channel over all the molecular collisions throughout the course of the MD simulations. Using this treatment, for each collision of a particular pair of molecules, the spin density matrix can be considered to describe the probability of each outcome if that collision was repeated many times.

Analytic Model

If the initially uncorrelated triplet molecules are considered collide to induce correlation of their spins, then separate and recollide diffusively, an analytical solution to eq 6.13 can be found. Following the work by Atkins and Evans, Redfield theory may be used to calculate the effect of an applied magnetic field H on the spin relaxation rates.[339,341,342]

$$\gamma_\mathrm{S} \propto \lambda_\mathrm{T}\left\{1 - \lambda_\mathrm{T} + \lambda_\mathrm{T} g_\mathrm{T}(H)\right\} \tag{6.15}$$

where λ_T is the probability a colliding triplet pair will produce the singlet state by

$$\lambda_\mathrm{T} = \frac{k_\mathrm{S}\tau_a}{1 + k_\mathrm{S}\tau_a} \tag{6.16}$$

with the value of k_S estimated using the molecular separation of the second peak observed in the RDFs shown in Figure 6.1 (6.5 Å and 6.0 Å for rubrene and perylene, respectively). The translational correlation time is given by

$$\tau_a = \frac{2r_\mathrm{T}}{D_\mathrm{T}} \tag{6.17}$$

where r_T is the radius of the triplet molecule, which we have computed using the HYDROPRO package[362] (6.87 Å and 5.43 Å for rubrene or perylene, respectively) and

D_T is the translational diffusion coefficient of the molecule obtained from the MD simulations (Supporting Information). The function $g(H)$ relates the singlet character of the triplet pair as a function of magnetic field strength using the molecular zero-field splitting parameters, plus the translational and rotational diffusion coefficients derived from Redfield's theory of spin relaxation.[343]

$$\begin{aligned} g(H) = \frac{1}{9}\{8 - [F(6R_{1100}) + F(2T_1^{-1}) + 2F(-2R_{1-11-1}) \\ + 2F(2T_2^{-1}) + 2F(2R_{1010} - 2R_{100-1})]\} \end{aligned} \tag{6.18}$$

where

$$F(s) = \frac{\sinh(\sqrt{s\tau_a})\exp(-\sqrt{s\tau_a})}{\sqrt{s\tau_a}}. \tag{6.19}$$

The longitudinal and transverse spin relaxation times are T_1 and T_2, respectively, and

$$T_1^{-1} = R_{1100} + 2R_{11-1-1} \tag{6.20}$$

$$T_2^{-1} = -R_{1010} - R_{100-1} \tag{6.21}$$

where $R_{mm'nn'}$ are determined via the Redfield relaxation matrix

$$R_{1100} = \frac{2}{15}k(H) \tag{6.22}$$

$$R_{11-1-1} = \frac{4}{15}k(2H) \tag{6.23}$$

$$R_{1-11-1} = -\frac{2}{15}\left[k(H) + 2k(2H)\right] \tag{6.24}$$

$$R_{1010} = -\frac{1}{5}\left[k(0) + k(H) + \frac{2}{3}k(2H)\right] \tag{6.25}$$

$$R_{100-1} = -\frac{2}{15}k(H). \tag{6.26}$$

The magnetic field dependence appears in the function

$$k(H) = \frac{(D^2 + 3E^2)\tau_2}{1 + (g\beta H\hbar^{-1}\tau_2)^2} \tag{6.27}$$

where the isotropic rotational correlation time τ_2 is calculated from the harmonic mean of the rotational diffusion coefficients D_R obtained from the MD simulations (Supporting Information) by

$$\tau_2 = \frac{1}{6D_\mathrm{R}}. \tag{6.28}$$

Results and Discussion

Molecular Dynamics Simulations

The pure toluene simulations resulted in average mass densities of $0.954\,\mathrm{g\,cm^{-3}}$ and $0.865\,\mathrm{g\,cm^{-3}}$ at 200 K and 295 K, respectively, agreeing well with experimental values.[363] Translational diffusion coefficients of the pure toluene, rubrene in toluene and perylene in toluene were calculated from plots of the mean-squared displacement of molecules over time. The diffusion coefficients of toluene were found to be (1.04 ± 0.01)

$\times\ 10^{-6}\,\mathrm{cm^2\,s^{-1}}$ at 200 K and $(1.86 \pm 0.02) \times 10^{-5}\,\mathrm{cm^2\,s^{-1}}$ at 295 K. While the agreement with experimental values is within 11% at 295 K, the simulation data deviates more significantly at 200 K with a relative error of 42% but is still of the correct order of magnitude.[364] The diffusion coefficients of rubrene in toluene were found to be $(4.4 \pm 0.2) \times 10^{-6}\,\mathrm{cm^2\,s^{-1}}$ at 295 K and $(2.50 \pm 0.08) \times 10^{-7}\,\mathrm{cm^2\,s^{-1}}$ at 200 K. For perylene in toluene, a diffusion coefficient of $(1.21 \pm 0.03) \times 10^{-5}\,\mathrm{cm^2\,s^{-1}}$ was found at 295 K, in good agreement with experiment.[365] Experimental data for the translational diffusion coefficient of rubrene in toluene could not be found in the literature. Rotational diffusion coefficients were also calculated from the MD simulations of toluene and rubrene or perylene in toluene. No experimental data exists for rubrene or perylene in toluene, but the simulated results for the pure toluene solvent are in reasonable agreement with experiment. All values for the diffusion coefficients are listed in the Supporting Information. These results indicate that our simulations capture the dynamics of these systems with reasonable accuracy.

RDF plots are shown in Figure 6.1 for the (a) rubrene and (b) perylene simulations at 295 K. Both emitter molecules show several distinct peaks in their RDFs, which each correspond to favourable collision orientations for the pairs of emitters. To more clearly identify the effect of the specific pair geometry on the TTA rates, several molecular separation ranges were defined by the local minima in the RDF plots and treated independently in the subsequent analysis. Three collision ranges with centre-of-mass separations of less than 10 Å were identified for each of the emitter molecules, indicated on Figures 6.1a and b as I–III. The 10 Å outer range cutoff was chosen as the molecules must be in close proximity for electron exchange associated with the TTA process to occur. Table 6.2 lists the collision ranges, plus the corresponding association k_1 and dissociation k_{-1} rates determined from the collision counts and durations. Due to the slow diffusion of rubrene in toluene at 200 K, insufficient emitter pair collisions were observed over the 200 ns MD simulation period and thus the data was not used in further analysis.

The Euler angles and spherical polar coordinates that describe, respectively, the relative orientation and position of the emitter molecules were analysed and identified the geometry favoured at each collision range. Plots detailing the correlations between Euler angles and the spherical polar coordinates plus examples of some preferred molecular collision orientations are provided in the Supporting Information. At their closest collision range, both rubrene and perylene show restrictions on the possible geome-

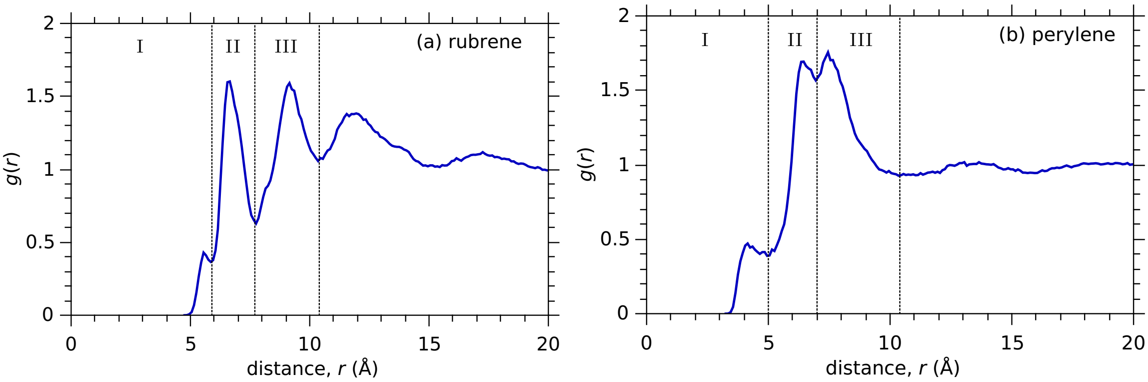

Figure 6.1: Radial distribution function $g(r)$ between pairs of (a) rubrene and (b) perylene emitter molecules at 295 K during the molecular dynamics simulations.

Table 6.2: Collision ranges for rubrene and perylene determined from RDF plots in Figure 6.1 and calculated association k_1 and dissociation k_{-1} rates.

emitter	range	(Å)	k_1 ($\mathrm{ns^{-1}\,M^{-1}}$)	k_{-1} ($\mathrm{ns^{-1}}$)
rubrene	I	0–5.9	2.2	3.05
	II	5.9–7.7	10.0	1.74
	III	7.7–10.4	29.3	1.49
perylene	I	0–5.0	10.4	10.27
	II	5.0–7.0	44.4	6.13
	III	7.0–10.4	71.7	7.55

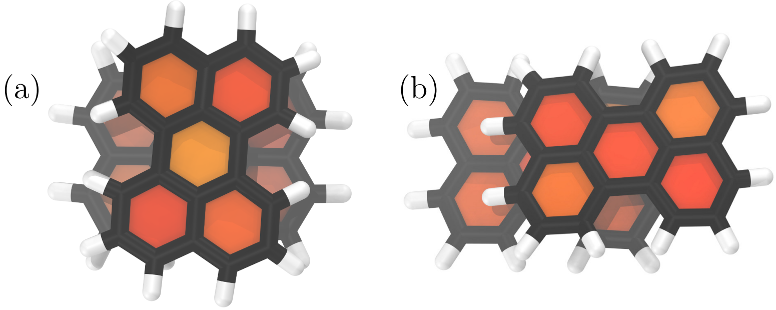

Figure 6.2: Two typical examples of perylene molecules interacting within their closest collision range during a MD simulation. The planar nature of perylene allows for some flexibility in both the (a) in-plane rotation and (b) relative positioning of the molecules.

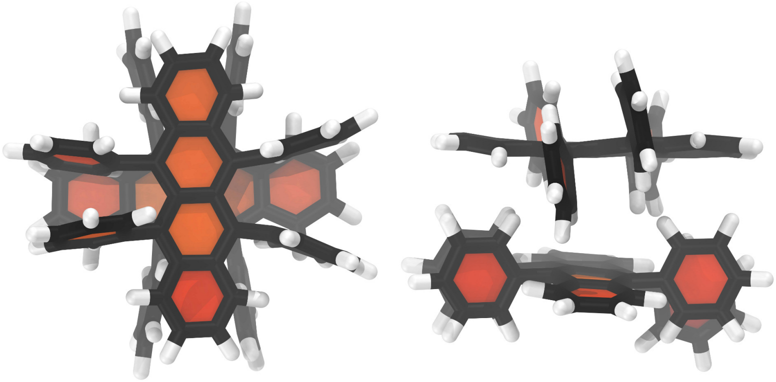

Figure 6.3: Typical example geometry of a pair of rubrene molecules interacting within their closest collision range. The phenyl sidechains of rubrene do not lie co-planar with the tetracene backbone and act to restrict the orientational freedom during collisions.

try, most notably a preference for the polyaromatic backbones to lie co-planar. While perylene pairs have some flexibility with regard to the in-plane rotation and relative position (Figure 6.2), the phenyl substituents of rubrene do not lie in-plane with the tetracene backbone and act to restrict the range of collision geometry. As a consequence, the closest collisions of rubrene pairs strongly favour a co-planar arrangement with the long molecular axes of the two molecules rotated at 90° to one another, as shown in Figure 6.3. With an increasing separation between the molecular pairs, a wider variety of collision geometry becomes possible. However, for the second collision range of both rubrene and perylene there remains a high degree of correlation within the Euler angles and spherical polar coordinates, and at the third collision range the molecular geometry is not yet completely random.

TTA-UC Simulations

We begin by looking at the influences on the TTA process using the static model described by eq 6.12. While the static model can not completely describe the complex nature of the molecular interactions possible in solution, the simplification helps isolate and qualitatively determine the fundamental mechanisms in which the molecular properties can affect the TTA-UC rate. The simulated TTA-UC rate in the absence of magnetic fields was calculated using eq 6.12, giving a rate for rubrene of $\gamma_\mathrm{S} = 1.8 \times 10^6\,\mathrm{s}^{-1}$. Perylene was predicted to give approximately 20 times greater upconversion rate with $\gamma_\mathrm{S} = 4.0 \times 10^7\,\mathrm{s}^{-1}$. Four general factors contribute to the observed upconversion rate: the diffusion rate of the emitter molecules in solution, the orientation during collisions, molecular separation distances during collisions and the relative energy levels of the emitter's S_1 singlet and T_2 triplet states. Each of these factors comes into play by influencing the competing annihilation k_S, k_T and dissociation k_{-1} processes, or by varying the spin character $|C^l_\mathrm{S}|^2$, $|C^l_\mathrm{T}|^2$ of the triplet-pair states. We address each of these factors and attempt to quantify their impact on the upconversion rate below.

Role of Molecular Factors

Diffusion Rate The effect of the diffusion rate of the different emitter molecules impacts the association k_1 and dissociation k_{-1} rates extracted from the MD simulations (Table 6.2). To isolate the effect of the emitter diffusion rate on upconversion efficiency, simulations of rubrene and perylene were performed as before, but exchanging the k_1 and k_{-1} rates between the emitter molecule types while leaving the remaining conditions unchanged.

For the rubrene simulation, substituting the association and dissociation rates of perylene resulted in only a 50% increase in the overall upconversion rate. This result is initially surprising, as the translational diffusion rate of perylene is around 3 times greater than that of rubrene which is then reflected in the difference in frequency of collisions, k_1. The upconversion rate was instead found to closely track the ratio of $k_1 : k_{-1}$ when each collision range was considered in isolation. For example, at its closest collision range perylene has a $k_1 : k_{-1}$ ratio 43% greater than that of rubrene. This indicates that the increased diffusion rate of a smaller emitter molecule such as perylene does have a favourable influence on upconversion efficiency due to an increased collision rate, but the dissociation rate also plays a role. While the collision rate scales with diffusion, the dissociation rate is also influenced by the shape of the emitter. During a collision, the phenyl sidechains of rubrene act to hold the emitters together, delaying the separation and allowing a longer duration for the competing TTA process to proceed. This effect may be responsible for some of the solvent viscosity dependence of TTA-UC recently observed by Yokoyama et al. that was unable to be explained by translational diffusion alone.[340]

From eq 6.12 it can be seen that diffusion rate, which is reflected in k_1, will always have a linear scaling effect on the upconversion rate, but the dissociation rate k_{-1} competes with the annihilation processes and therefore variations in k_{-1} will have maximum influence when $k_{-1} \approx k_\mathrm{S}$. This is demonstrated in a simulation of perylene in which substitution of the rubrene association and dissociation rates showed a slightly greater effect than observed for the equivalent substitution described above for rubrene, more than halving the upconversion rate. This would imply that with more favourable annihilation processes in perylene (larger k_S, k_T in eq 6.1), the rate of the competing emitter pair dissociation k_{-1} will have less significance, allowing the diffusion and therefore association rate k_1 to become more influential.

Molecular Orientation The collision orientation of the emitter molecules affect the TTA-UC rate by modulating the singlet or triplet character of the triplet-pair states, represented by $|C^l_\mathrm{S}|^2$ or $|C^l_\mathrm{T}|^2$ in eq 6.12. The mechanism by which the annihilation products are influenced by the distribution of spin character across the nine triplet-pair states is well known.[203] In summary, the rate of upconversion γ_S is theoretically maximised when the singlet character is distributed evenly across the nine triplet-pair states ($|C^l_\mathrm{S}|^2 = 1/9$ for all l pair states) and minimised when the singlet character is confined to one state only.

The effect of collision orientation of the emitters on the upconversion rate was investigated by performing the simulations of rubrene and perylene, but exchanging the relative molecular orientations of the emitter pairs while preserving the remaining conditions, including the molecular separation distances of the original collisions.

For the rubrene simulation, substituting the collision orientations of perylene enhanced the overall upconversion rate by approximately 5% at zero-field, indicating that the slightly more disordered collisions of perylene do generally result in the singlet character being distributed across more of the triplet-pair states. Conversely, when substituting the orientations of rubrene into the perylene simulations, a reduction in upconversion rate of approximately 10% is seen. The greater effect on the perylene simulation may be rationalised by considering that with closer perylene collisions k_S in eq 6.12 will be larger and hence any orientation effect on the values of $|C^l_\mathrm{S}|^2$ will become enhanced.

In the case of completely disordered collisions the singlet character is expected to be on average distributed across a greater number of triplet-pair states. This was simulated by substituting random orientations into the perylene simulation, resulting in an approximately 20% increase in the upconversion rate at zero field. It should be noted that the concept of a fully disordered system implies that the singlet character is distributed equally amongst the nine triplet-pair states, thus resulting in the theoretical maximum probability of TTA producing the singlet product. In reality, no one combination of molecular orientations will ever distribute the singlet character across all pair states simultaneously. In the same way that macroscopic observables like fluorescence are due to contributions from many individual emission events, when simulating the TTA-UC rate from an ensemble of collisions, the upconversion rate is computed from the average γ_S using each orientation individually, rather than from the average singlet character of the pair states. The implication is that random collision orientations does not in fact provide the maximum disorder required to optimise the distribution of singlet character. The idea that there is a single optimum molecular pair geometry to maximise TTA-UC is discussed later.

Separation Distance As the rate of triplet exciton energy transfer and triplet–triplet annihilation decays exponentially with distance,[356,358] it is expected that the molecular separation during emitter molecule collisions should strongly influence the upconversion efficiency. To demonstrate this effect, the rubrene and perylene simulations were performed, but exchanging the molecular separation distances between the two emitter molecule types.

The rubrene simulation using the collision separations of perylene showed an 8 times increase in upconversion rate at zero field. For the perylene simulation using the separations of the rubrene collisions, an analogous 15 to 20 times reduction in upconversion rate was found. This clearly shows that the separation of the emitter molecules during collisions dominates the rate of upconversion, and additionally acts to amplify any effect of diffusion rate, collision orientations or any applied magnetic field. In eq 6.12, as k_S is increased, the modulation of $|C^l_\mathrm{S}|^2$ and $|C^l_\mathrm{T}|^2$ by molecular orientation or the magnetic field becomes more significant. With the faster annihilation processes, the competing dissociation of the molecular pair k_{-1} becomes less important. Taking this to the limit of extremely large values of k_S, the rate of formation of the triplet-pair through diffusion k_1 becomes the rate limiting step.

Energy Levels The efficiency of the upconversion process relies on the suitable alignment of electronic energy levels of the emitter molecule. In an ideal case, the first singlet state S_1 which we desire to be populated will have an energy roughly twice the energy of the first triplet state T_1, and any higher triplet states will lie far above S_1. In this way, the annihilation process that acts to double the T_1 energy can populate the S_1 state with minimal losses, while decay through the triplet pathway will become energetically inaccessible. In eq 6.1 this ideal scenario would give $k_\mathrm{T} = 0$, leaving the singlet channel as the only TTA decay pathway.

When considering energy levels, both rubrene and perylene can be considered "good" emitters. Rubrene has an S_1 energy very close to twice T_1, with T_2 lying above by around 0.1 eV.[360] The S_1 state of perylene lies below $2\mathrm{T}_1$ by around 0.4 eV with T_2 lying above by around 1 eV.[361] When simulating rubrene with a closed triplet decay channel by setting $k_{\mathrm{T}_0} = 0$, upconversion rate is only enhanced by 2%. For perylene, the reduced availability of the triplet decay pathway compared with rubrene ($k_{\mathrm{T}_0} = 2.66 \times 10^6\,\mathrm{ns}^{-1}$ versus $6.25 \times 10^7\,\mathrm{ns}^{-1}$) results in approximately 10% enhancement in the upconversion rate.

The behaviour of a "poor" emitter, for which the energy of the T_2 state lies closer to twice T_1 than the emissive S_1 state, may be simulated by adjusting the ratio of $k_\mathrm{S} : k_\mathrm{T}$. We discuss the investigation of this possibility below.

Influence of Magnetic Field: Static Model

The discussion thus far has only considered the interactions of the triplet-state emitters in the absence of any magnetic fields. As magnetic fields have an influence on the alignment of the spins in the triplet-state emitter molecules, the idea that an applied magnetic field may enhance the TTA-UC process is an appealing one. In the solid phase, such as anthracene or tetracene crystals,[204,355] or diphenylanthracene (DPA) films[323] a significant enhancement in TTA-UC is observed with intermediate strength magnetic fields, whereas TTA-UC is diminished at high field. In contrast, solution-phase experiments at room temperature display only a monotonic decrease in TTA-UC with applied magnetic fields,[209,328,339,340] although low-temperature experiments have also shown positive effects.[338]

We first look at the influence of an applied magnetic field on the simulated TTA-UC rates of rubrene and perylene using the static model used above. Again, we note that the static model is not a complete description of the TTA-UC process in solution, but

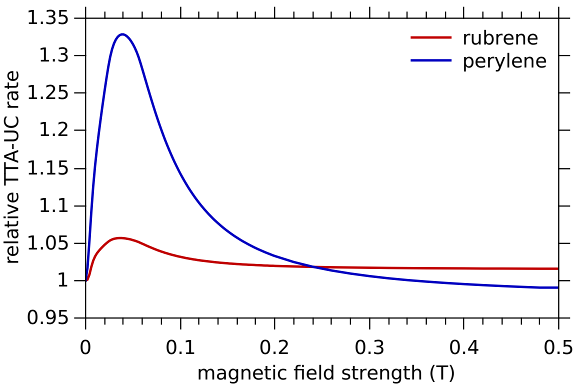

Figure 6.4: Simulated TTA-UC rates of rubrene or perylene emitters as a function of applied magnetic field strength computed using the static model. Data is normalised to the zero-field rate for each emitter ($7.69 \times 10^7\,\mathrm{s^{-1}\,M^{-1}}$ for rubrene and $1.74 \times 10^9\,\mathrm{s^{-1}\,M^{-1}}$ for perylene).

it provides a qualitative picture of the interplay of the molecular factors and applied magnetic field which is less straightforward to deconvolute in the fully dynamic model.

Figure 6.4 shows the simulated TTA-UC rates γ_S calculated using eq 6.12 for rubrene or perylene as a function of magnetic field strength. The data is plotted relative to the respective zero-field rate for each emitter molecule. Both emitter molecules exhibit an enhanced upconversion rate under the influence of low magnetic fields, with maximum improvements of around 5% for rubrene and 30% for perylene reached at approximately 0.04 T, but further increases in the field strength then have a detrimental effect. Perylene eventually shows a reduced upconversion rate relative to the zero-field rate with magnetic field strengths above 0.4 T, though rubrene retains a slightly enhanced upconversion rate within the range of magnetic fields shown.

The response to the applied magnetic field is explained by considering eq 6.12 and remembering that the rate of upconversion γ_S will be maximised when the singlet character is distributed evenly across the nine triplet-pair states. In the case of two identical emitter molecules aligned parallel to each other, the system behaves similarly to the crystalline materials in which singlet-fission and triplet-fusion processes have been studied extensively.[166,203–205,323] At zero field, three pair states show singlet character. With the application of an arbitrarily oriented magnetic field, mixing of the spin states will cause an increase in the number of states displaying singlet character and the rate of upconversion will be increased. As the magnetic field strength increases, the relative orientation of the molecules becomes irrelevant as the alignment of the spins is determined only by the magnetic field direction. Towards the high-field limit three pair states show singlet character, one aligned with the magnetic field direction and two orthogonal to it. The two orthogonal states are degenerate, but the intermolecular term $\hat{H}_\mathrm{AB}$ in the Hamiltonian acts to break this degeneracy so at very high field strengths only two pair states display singlet character and the rate of upconversion is reduced to below that observed at zero field.

If we consider our systems of emitter molecules, at the closest collision range both the rubrene and perylene pairs lie co-planar (see Supporting Information Figures S4 and S10). Perylene pairs have some freedom to rotate within the plane, with some preference for either parallel or orthogonal alignment of their long axes, while rubrene favours only the orthogonal alignment. In the case in which the molecules are aligned parallel, the evolution of singlet character of the pair states with magnetic field follows

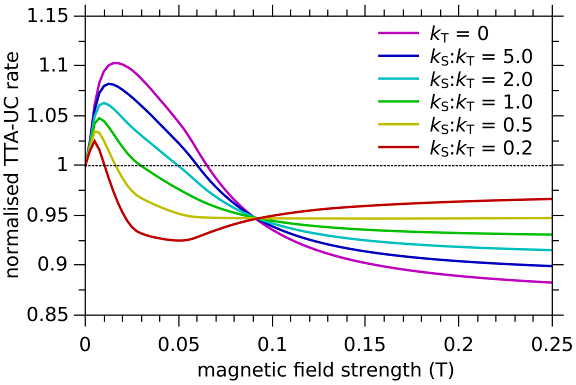

Figure 6.5: Simulated upconversion rate as a function of magnetic field strength demonstrating the varied response as the ratio of singlet k_S to triplet k_T channel annihilation rate constants (eq 6.12) changes. The ratio of k_S and k_T will be affected by the relative S_1 and T_2 energy levels of the emitter molecule.

the ordered, crystalline description above. If, however, the molecules are rotated so that their long axes are at 90° to one another, the $|xx\rangle$ and $|yy\rangle$ spin states become degenerate. Like the high-field case described above, this degeneracy is broken by the intermolecular interaction $\hat{H}_{AB}$, with the result that only two states show singlet character at zero-field. In this situation the number of states with singlet character is still increased with intermediate magnetic fields, resulting in an enhanced upconversion rate, but at the high-field limit the number of states with singlet character can only ever be reduced as low as two, so the upconversion rate will not decrease below the rate seen at zero field. This explains the higher relative TTA-UC rate at high field for rubrene compared with perylene.

We note that if the rate of triplet annihilation k_S is significantly greater than the rate of dissociation k_{-1}, then any affect of an applied magnetic field will become more significant.[323] This is one contribution to the greater enhancement of the TTA-UC rate with magnetic field for perylene observed in Figure 6.4, as the larger magnitude of k_S acts to amplify the effects from distribution of the singlet character across a greater number of pair states. Similarly, at zero or low magnetic field strengths, the benefit from more disordered collisions of perylene is also enhanced by this same effect. As the magnetic field strength increases, however, the orientation differences between the molecules become less relevant as the alignment of the spins by the magnetic field becomes dominant. This phenomena is reflected in our simulations described above in which the difference in upconversion rates because of molecular orientation rapidly tends towards zero beyond intermediate field strengths.

We consider again "good" or "poor" emitter molecules characterised only by their relative singlet and triplet energy levels. If $k_S \approx k_T$, the singlet and triplet annihilation pathways are in competition and small variations in k_S or k_T should then be expected to cause noticeable differences in response to the applied magnetic field. Figure 6.5 shows an example TTA-UC simulation in which the ratio of $k_S : k_T$ was varied between and 5 and 0.2, as well as the scenario of a "good" emitter molecule for which the triplet channel was closed completely ($k_T = 0$). In these scenarios, an ensemble of randomly oriented emitters and magnetic fields was used with parameters as in Table 6.1 except $r = 5\,\text{Å}$, $k_\beta = 0\,\text{Å}^{-1}$, $k_1 = k_{-1} = 1\,\text{ns}^{-1}$ and the values of k_S and k_T were selected so that $k_S + k_T = 2$.

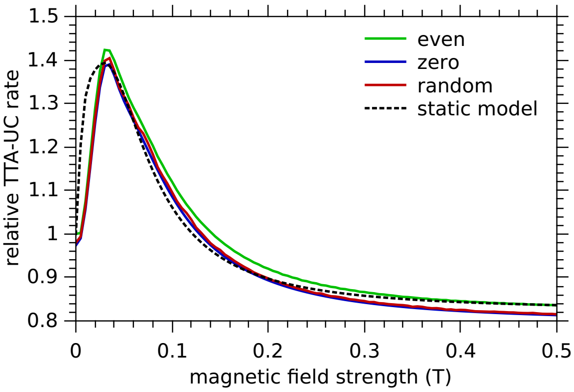

Figure 6.6: Relative TTA-UC rate in response to magnetic field predicted using the spin density matrix approach (eq 6.13), but using a single static molecular pair geometry extracted from the MD simulations. This demonstration shows the dynamic model captures the same effects as the static model (eq 6.12, black dotted curve) when the molecular orientations are fixed. The initial state of the spin density matrix has little relevance; the spin density matrix was initialised as either zero (blue curve) or with a unit of spin distributed between the singlet, triplet and quintet states evenly (green curve) or randomly (red curve), with minimal impact on the results.

Where the triplet decay channel is closed, an enhancement in upconversion rate compared with zero-field is predicted at low magnetic field strength, giving way to a diminished upconversion rate at higher field strengths. Interestingly, with a triplet channel decay rate constant around twice that of the singlet channel, minimal enhancement in upconversion rate is predicted and the application of a magnetic field only has a negative impact on upconversion. In the case that the rate of triplet channel decay dominates the decay through the singlet channel, it appears that the upconversion rate is at a minimum relative to zero-field at intermediate field strength, and further increases in magnetic field promotes a mild recovery in upconversion rate. It should be noted that in this scenario, the normalisation of the plot may be misleading as the absolute value of γ_S will be small and so any change in upconversion rate will also be small in absolute terms. This is, however, a clear demonstration of how the relative S_1 and T_2 energy levels of an emitter molecule may act to shape its response to magnetic fields.

Influence of Magnetic Field: Dynamic Model

We now employ the dynamic model of the triplet interactions in solution using a spin density matrix approach. Figure 6.6 demonstrates the use of the Liouville equation given in eq 6.13, but using a single, static arrangement of a rubrene pair and magnetic field orientation sampled from the closest collision range. The generation and dissociation terms were enabled by setting $k_1 = k_{-1} = 1\,\mathrm{ns}^{-1}$ and the density matrix evolved until the steady-state was reached. The TTA-UC rate was then taken to be proportional to the steady-state density of the pure singlet state $\rho_{1,1}$. To test the influence of the initial state of the density matrix on the results the spin density was distributed either evenly or randomly across the nine pure singlet, triplet and quintet states, or with all elements of the matrix set to zero. Figure 6.6 shows that the spin density matrix approach reproduces the magnetic field response of the static model (black dotted

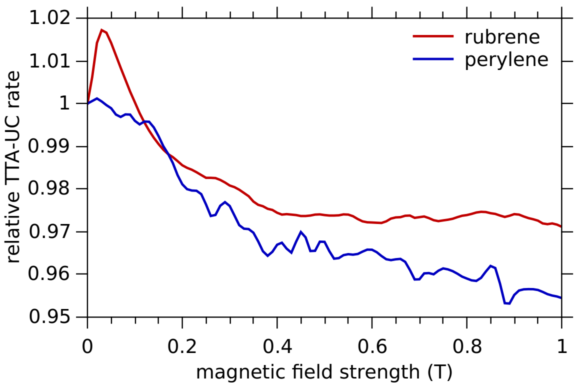

Figure 6.7: Relative TTA-UC response to magnetic field for rubrene or perylene determined via the spin density matrix method of eq 6.14 with the contribution from the individual collisions of the emitter molecules considered explicitly. For each collision, as the spin density matrix evolved, the Hamiltonian and annihilation matrix were recalculated using the geometry sampled from the MD simulations at 1 ps intervals. In contrast to Figure 6.6, the rapid motions of the molecules act as a source of spin relaxation, nullifying any enhancement effect on TTA-UC by the magnetic field.

curve) when a fixed molecular-pair orientation is used, replicating the enhancement in TTA-UC predicted at a magnetic field strength of approximately 0.04 T followed by a diminished rate with the application of higher strength fields. Additionally, the initial condition of the density matrix has minimal influence on the final singlet character of the molecular pair in this situation.

The influence of the motion of the emitter molecules over the course of a collision is now considered. Figure 6.7 shows the magnetic field dependence of the TTA-UC rate for rubrene and perylene using the spin density matrix approach of eq 6.14, with each individual molecular pair collision observed during the MD simulations treated explicitly. For each emitter pair collision, the spin density matrix ρ was initialised with the pure singlet, triplet and quintet states equally populated to represent the triplet-pair comprising a mixture of two uncorrelated triplet states. The association and dissociation of the triplet pairs was determined intrinsically through the MD trajectories, thus the absence of the generation or dissociation terms in eq 6.14. The spin density matrix was then allowed to evolve, with both the Hamiltonian $\hat{H}$ and annihilation matrix Λ updated using the geometry from the MD simulations sampled at 1 ps time intervals. Over the course of each collision, the decay through the singlet component of the annihilation term was taken as the contribution to the upconverted emission intensity.

The behaviour in response to the applied magnetic field shown in Figure 6.7 is markedly different to that predicted by the static model in Figure 6.4 and the dynamic model with a static molecular arrangement demonstrated in Figure 6.6. While rubrene still shows an enhanced TTA-UC rate at low field strength, the enhancement is less than 2%. Perylene displays only a monotonic decrease in upconversion with magnetic field, in stark contrast to the 30% enhancement predicted using the static model. This monotonic decrease is consistent with previous room-temperature solution-phase experiments of TTA-UC.[209,328,339,340]

Given that both the static and dynamic models effectively use the same spin Hamiltonian and molecular geometries, the difference in magnetic field response can be at-

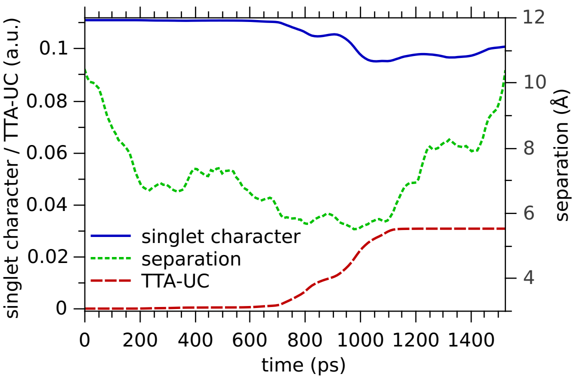

Figure 6.8: Demonstration of the mechanism of the dynamic model of triplet annihilation showing the tracking a rubrene pair during the MD simulation and the contribution of the collision event to the observed upconversion. The molecular separation distance is given by the green dotted curve, and time $t = 0\,\mathrm{ps}$ is defined as when the molecular pair begins to enter the interaction range of 10.4 Å. As the molecules approach, TTA-UC becomes possible (red dashed curve) and singlet character is depleted from the spin density matrix (blue solid curve). When the rotation of the molecules is rapid compared with the collision duration, multiple coupling pathways are opened between the pure singlet and triplet and quintet states, mixing the spin states and assisting the decay through the singlet channel.

tributed to the possibility of mixing of the spin states during the course of the collisions. This is illustrated in Figure 6.8, which tracks an individual collision between a pair of rubrene molecules. At time $t = 0\,\mathrm{ps}$ the molecular pair are separated beyond the interaction distance determined by the exponential dependence of the annihilation rate on intermolecular separation (green dots). The two triplet-state molecules are uncorrelated and have yet to form the triplet-pair complex; thus the singlet character of the pair takes the statistical probability of 1/9 (blue line). No annihilation is possible at this distance, so the contribution of the collision to TTA-UC is zero (red dashes). As the molecules approach, annihilation and decay through the singlet and triplet channels becomes a possibility. Singlet character is drained from the spin density matrix, contributing to the observed TTA-UC (depletion from the triplet states also occurs but is not shown). The spin density matrix is now perturbed, and the mixing of the spin states occurs through the Liouville term in eq 6.13 acting to partially repopulate the pure singlet state from the triplet and quintet states. Crucially, it is the relative rate of this mixing of the spin states compared with the duration of the molecular collision that determines the magnitude of the contribution to the observed TTA-UC. In the static model described by eq 6.12 the emitter pair dissociation k_{-1} competes with annihilation k_S as described above. Similarly, for the dynamic model, Figure 6.8 clearly shows that the longer the emitter molecules are in close contact, the greater the potential contribution to the observed TTA-UC. The differing response to the applied magnetic field displayed by the dynamic model versus the static model is due to the varying intra- and intermolecular spin interactions that are available during the course of the collision. At zero magnetic field and when the tumbling of the molecules is rapid, many coupling pathways are opened between the pure singlet, triplet and quintet states through the rapidly rotating orientation of the molecules' zero-field intramolecular spin-spin coupling components $\hat{H}_{SS}$. This is expressed in the dynamic model by the existence of many varying, non-zero, off-diagonal elements in the Hamiltonian $\hat{H}$, leading to more efficient draining of the spin density matrix through the singlet channel. With the application of magnetic fields, the individual spins on the molecules will begin to be aligned with the magnetic field orientation. As the spin states were already well mixed at zero field due to the tumbling of the molecules, the magnetic field can only reduce the variety in the off-diagonal elements in the Hamiltonian, leading to less efficient decay through the singlet pathway.

In Figure 6.7 perylene displays a monotonic decay of TTA-UC rate with magnetic field, in agreement with the behaviour observed for high temperature solution experiments of perylene and other emitters.[209,328,339,340] The small, planar nature of perylene results in translational and rotational diffusion rates that are fast relative to the collision durations (Supporting Information). Additionally, during collisions the molecules lie co-planar and are relatively free to rotate in-plane as indicated in Figure 6.2. This allows a good degree of mixing between the spin states as described above and produces the exclusively negative magnetic field response. Conversely, rubrene displays a slight enhancement of TTA-UC rate at low magnetic fields. The diffusion rates of rubrene are multiple times slower than those of perylene, and during collisions the phenyl substituents have the effect of locking the molecules together and restricting their relative movement (Figure 6.3). In this situation the individual rubrene molecules are not free to rotate completely independently, so there is not complete mixing of the spin states. Small magnetic fields may then have the possibility of further mixing of the spins and hence the slight enhancement in TTA-UC observed.

Influence of Magnetic Field: Analytic Model

The results shown in Figure 6.7 use the relative molecular orientations extracted directly from the MD simulations and we have shown that there is a significant degree of correlation between the molecular geometries during collisions (Supporting Information). If the emitter molecules are instead assumed to diffuse and rotate isotropically and independently, an analytical solution to the dynamic model given by eq 6.13 can be found. Equations 6.15–6.28 summarise the analytical model presented in Atkins and Evans.[341,342] where the ensemble of molecular orientations are encapsulated by the diffusion coefficients and the size of the molecule. The translational and rotational diffusion coefficients were obtained from the MD simulations and the rubrene or perylene size was taken as the computed hydrodynamic radius. The relative TTA-UC rates for the two emitter molecules calculated using eq 6.15 are shown in Figure 6.9. Both rubrene and perylene display an exclusively diminished TTA-UC rate with the application of magnetic fields. The two emitters show slightly different curve shapes below ∼0.1 T, which is predominantly a consequence of the different rotational diffusion rates between the planar perylene and the bulkier rubrene emitters, but note also that rubrene and perylene share identical zero field splitting parameters for the purposes of these simulations. The relative reduction in TTA-UC rate at high field strengths is primarily determined by the reaction probability λ_T as indicated in eq 6.15, where an increased reaction probability will emphasise any effect of the magnetic field. Equation 6.16 relates the reaction probability to the translational diffusion and the singlet channel decay rate. As the singlet decay rate k_S has a strong distance dependence and only a single molecular pair separation is used as input, the total reduction in TTA-UC rate at high field is somewhat dependent on the choice of this parameter.

The relative TTA-UC rates simulated by the analytic model in Figure 6.9 are similar to that obtained from the fully dynamic model in Figure 6.7, and supports the notion predicted by the static model that the specifics of the molecular orientations

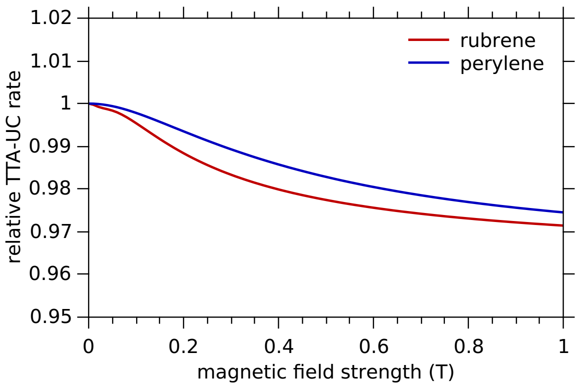

Figure 6.9: Relative TTA-UC response to magnetic field for rubrene or perylene predicted by Atkins and Evans' analytical solution to the dynamic model in eq 6.13.[341,342] The emitter molecules are assumed to diffuse and rotate isotropically, with the motions of the molecules represented only by the isotropic translational and rotational diffusion coefficients.

are relatively unimportant. A crucial difference is that the analytic model always assumes random diffusion and does not account for the case where the molecules are in close proximity and deviation from random diffusion may occur. This effect will be most noticeable for molecules with bulky substituents, and is likely responsible for the slight enhancement in TTA-UC rate for rubrene shown in Figure 6.7.

Optimising Molecular Geometry

The idea that it may be possible to engineer an emitter molecule with a structure optimised for the TTA-UC process is an appealing one, but the results presented in this work hint at why this goal has thus far remained elusive. When considering the static case at zero field, an example of the "best" collision geometry was found by optimising eq 6.12, setting $\theta = \phi = 0°$, $r = 4\,\text{Å}$, $k_\beta = 0\,\text{Å}^{-1}$ and $k_\text{S} = k_1 = k_{-1} = 1\,\text{ns}^{-1}$. The optimised geometry that distributes the singlet character most evenly across the triplet-pair states is shown in Figure 6.10b. Here the Euler angles $\alpha \approx \beta \approx 45°$ describe a rotation where the z axis of the second molecule is at 45° to the x, y and z axes of the first and introduces the maximum achievable disorder to the spin states. As shown in Figure 6.10a, if the triplet decay channel is closed ($k_\text{T} = 0$) this gives approximately 95% of the maximum theoretical TTA-UC rate that would result from perfectly even distribution of the singlet character across all nine triplet-pair states (where 0% denotes the complete absence of TTA-UC). Encouraging emitter molecule collisions with this type of geometry could be imagined by attaching bulky substituents for example. Unfortunately, this type of modification will likely be counter productive due to the negative impact the substituents may have on the translational diffusion, and hence collision rate k_1. Most crucially, any change to an emitter molecule that restricts the close contact of the polyaromatic backbones will have a severely detrimental effect on the TTA-UC rate. For small emitter molecules, a collision angle of 45° as pictured in Figure 6.10b is still compatible with close-range collisions, but for larger molecules this is not likely to be feasible.

The other theoretical extreme is the "worst" collision geometry described earlier where the emitters are co-planar, but rotated in-plane by 90° (Figure 6.10c). When again considering a closed triplet decay channel, this orientation still results in just

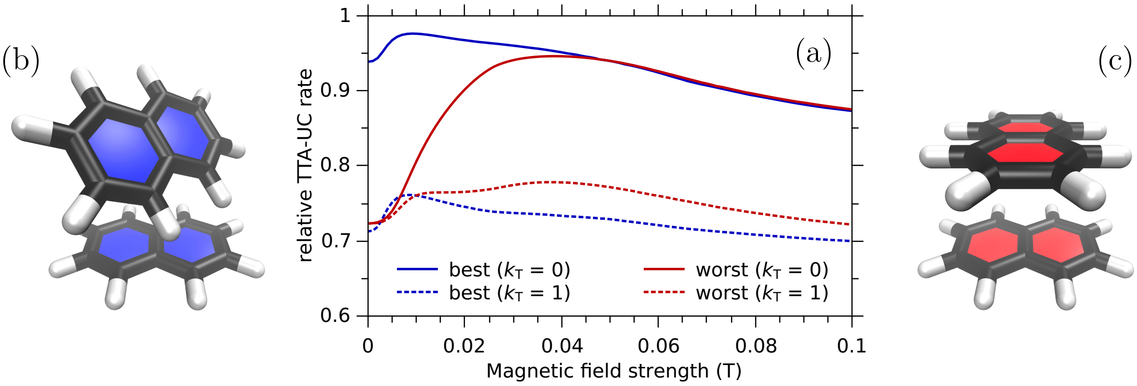

Figure 6.10: (a) TTA-UC rate relative to the maximum theoretical value for two molecular pair orientations as a function of applied magnetic field strength. The chosen orientations were selected for being the best (b, blue) or worst (c, red) case scenarios at zero field. When considering only the singlet character of the pair states ($k_{\mathrm{T}} = 0$, line), the best or worst orientations give approximately 95% or 70% of the theoretical maximum at zero magnetic field strength, respectively. With the application of an arbitrarily oriented magnetic field, a relative TTA-UC rate of 95% can also be achieved for the worst case orientation scenario. If the triplet decay channel is open and competes equally with the singlet channel ($k_{\mathrm{T}} = 1$, dots), orientation plays a negligible role at zero-field and only has a minor influence when a magnetic field is applied. For the best case scenario $\alpha \approx \beta \approx 45^\circ$, $\gamma = 0^\circ$ and for the worst $\alpha = 90^\circ$, $\beta = \gamma = 0^\circ$. Renders of napthalene are used for clarity. Additional parameters were set as $\theta = \phi = 0^\circ$, $r = 4\,\text{Å}$, $k_\beta = 0\,\text{Å}^{-1}$ and $k_{\mathrm{S}} = k_1 = k_{-1} = 1\,\mathrm{ns}^{-1}$.

over 70% of the maximum theoretical TTA-UC rate at zero field. If the emitter pairs are simulated in an arbitrarily oriented magnetic field, the "best" orientation shows little further enhancement of TTA-UC rate, and the applied field has only a detrimental effect beyond 0.01 T. Conversely, the "worst" orientation is able to achieve 95% of the theoretical maximum TTA-UC rate with a magnetic field of approximately 0.04 T, and continues to match the rate of the "best" orientation at greater magnetic field strengths. There is in fact a vast number of individual combinations of molecular orientation, magnetic field direction and strength that can give very close to the theoretical maximum TTA-UC rate. Figure 6.10 shows that in solution, where the orientation of the magnetic field is in an arbitrary direction relative to the molecular pair, poor collision geometry may be compensated by the application of moderate magnetic fields. Interestingly, if the triplet decay channel is open and of the same order as the singlet decay ($k_{\mathrm{S}} = k_{\mathrm{T}} = 1$), both these example molecular orientations show almost identical TTA-UC rate at zero field, and only minor differences with an applied magnetic field.

As a demonstration of how these molecular orientations and the magnetic field interact to distribute the singlet character between the triplet-pair states, Figure 6.11 plots the singlet character $|C_{\mathrm{S}}^{l}|^2$ of each of the nine triplet-pair states as a function of magnetic field for the "best" and "worst" molecular orientation scenarios depicted in Figures 6.10b and c, respectively. A single magnetic field orientation is used, directed along the $+y$ axis of molecule A. For the best-case orientation, seven pair states display singlet character at zero field. Although the spin states are already well mixed purely due to the molecular orientation, the applied magnetic field is able to achieve a further distribution of singlet character across all nine states. In the worst case scenario, only two pair states have singlet character at zero-field, and the magnetic field directed

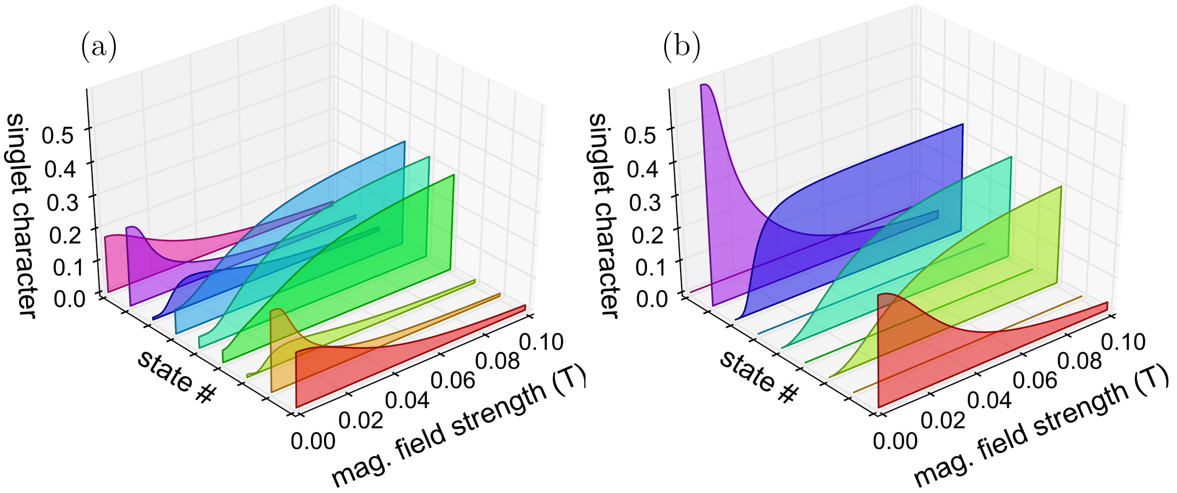

Figure 6.11: Evolution of the singlet character of the triplet-pair states with magnetic field for two molecular pair orientations. The orientations correspond to the "best" and "worst" orientations depicted in Figure 6.10, with the symmetry axes of molecule A defining the x, y and z directions and the magnetic field applied along the $+y$ axis in both cases. The best case orientation is shown in (a) where the number of states with singlet character tends from $7 \rightarrow 9 \rightarrow 3$. The worst case orientation is shown in (b) where the number of states tends from $2 \rightarrow 5 \rightarrow 3$. At very high magnetic fields both systems will eventually result in two states with singlet character. Note that in these scenarios there is a single static magnetic field orientation, though in Figure 6.10 the average of many random field orientations are used.

along the y axis is only able to induce singlet character in a maximum of five states in this case.

An ideal emitter molecule requires rapid diffusion through the solution, thus the static picture of such a molecule is not complete because, as we have shown in this work, it does not account for the intrinsic spin relaxation caused by the fast motions of the molecules. Using the static model, we have shown that the precise molecular orientations of a collision can account for a maximum of approximately 30% difference in observed TTA-UC rate. In the extreme opposite case in which rotational diffusion is rapid, the benefits of any optimal collision orientation are nullified. The spin states are already well mixed at zero field by the rotating molecules and any applied magnetic field will only have a negative impact on the upconversion rate. Our results suggest that any attempted design of the ideal emitter molecule should focus on, in rough order of importance, ensuring close contact of the polyaromatic system during collisions, a rapid diffusion rate, a T_2 state with energy well above S_1, and lastly geometry that favours disordered molecular orientations during collisions.

In solid-state TTA-UC systems, attempting to engineer favourable emitter-pair geometry may be more worthwhile, as the emitters are generally fixed into position and triplet diffusion occurs through exciton hopping events rather than translational motion of the molecules.[333–335] In this case, optimising the emitter pair interactions as shown in Figure 6.10 may provide a significant benefit to device performance.

Conclusions

In summary, we have investigated the influence of several properties of emitter molecules on the efficiency in a photochemical upconversion system based on sensitised triplet–triplet annihilation. The effects of diffusion rate, molecule shape, and collision geometry were quantified using data obtained from MD simulations of rubrene or perylene emitters in an explicit solvent, coupled with a quantum mechanical model of triplet–triplet spin interactions. Most critically, emitter molecules that allow close contact of the polyaromatic core during collisions will assist the required triplet exciton energy transfer and thus facilitate the rapid annihilation of the triplet-pair. In this scenario, the upconversion process will become limited by diffusion through solution, favouring small molecules with high translational diffusion rates. However, as a rapid diffusion rate will generally also reduce the collision duration available for annihilation to occur, efficiency should not be expected to scale linearly with the diffusion rate; correspondingly molecules that adhere or linger somewhat during collisions can be beneficial. The precise molecular orientation of the emitter pair during annihilation is influential, but we estimate the difference in upconversion efficiency between the best and worst possible collision orientations to be below 30%, far outweighed by the influence of separation distance and diffusion rate. Positive magnetic field effects on upconversion have been observed in solid phase systems, which are reproduced by a static model of triplet–triplet spin interactions. This should not be expected in high-temperature solutions, where rapid tumbling of the molecules acts as a source of spin relaxation. By combining the explicit trajectories of the emitter molecules obtained from the MD simulations with a dynamic model of the spin interactions we have modelled this mechanism of relaxation with unprecedented detail. We show that the motion of the emitter pair while interacting during a collision is sufficient to cause mixing of the spin-states. By forcing the alignment of the spins, applied magnetic fields reduce the efficiency of this mixing and cause an exclusively negative effect on the observed upconversion. Molecular design rules for emitters in solution-phase TTA-UC systems are formulated based on the results of this work.

Acknowledgements

We thank Timothy Schmidt, Dane McCamey and Andrew Danos for fruitful discussions. This research was undertaken with the assistance of resources provided at the NCI National Facility systems at the Australian National University through the National Computational Merit Allocation Scheme supported by the Australian Government. Computational resources provided by eResearch SA are also gratefully acknowledged.

Supporting Information

OPLS-AA Force Field Parameters

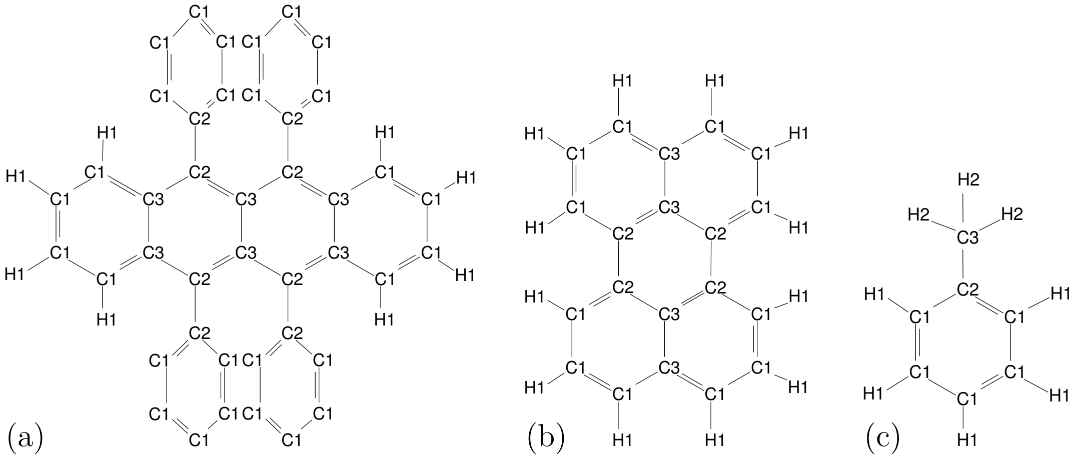

Figure 6.12: Chemical structures of (a) rubrene, (b) perylene and (c) toluene indicating the assignment of the different atom types. Hydrogen atoms on the 'paddle' rings of rubrene are omitted for clarity.

For the MD simulations of rubrene, perylene and toluene molecules, the optimised potentials for liquid simulations – all atoms (OPLS-AA) force field was used.[211–216] Figure 6.12 indicates the different atom types within each molecule of (a) rubrene, (b) perylene and (c) toluene.

Table 6.3: Parameters used in the non-bonded potential, $U_{\mathrm{nb}}(r_{ij}) = 4\varepsilon_{ij}[(\sigma_{ij}/r_{ij})^{12} - (\sigma_{ij}/r_{ij})^{6}] + q_i q_j/(4\pi\varepsilon_0 r_{ij})$, where σ_{ii} is the homonuclear Lennard-Jones (LJ) diameter, ε_{ii} is the homonuclear LJ interaction strength and q_i is the atomic charge. The standard geometric combining rules $\sigma_{ij} = (\sigma_{ii}\sigma_{jj})^{1/2}$ and $\varepsilon_{ij} = (\varepsilon_{ii}\varepsilon_{jj})^{1/2}$ apply.

(a) rubrene and perylene

atom type, i	atom class	mass (amu)	σ_{ii} (Å)	ε_{ii} (kcal mol^{-1})	q_i (e)
C1	CA	12.011	3.550	0.070	−0.115
C2	C!	12.011	3.550	0.070	0.000
C3	CA	12.011	3.550	0.070	0.000
H1	HA	1.008	2.420	0.030	0.115

(b) toluene

atom type, i	atom class	mass (amu)	σ_{ii} (Å)	ε_{ii} (kcal mol^{-1})	q_i (e)
C1	CA	12.011	3.550	0.070	−0.115
C2	CA	12.011	3.550	0.070	−0.115
C3	CT	12.011	3.500	0.066	−0.065
H1	HA	1.008	2.420	0.030	0.115
H2	HC	1.008	2.500	0.030	0.060

Table 6.3 shows the assignment of the atom types to an optimised potentials for liquid simulations (OPLS) atom class, and the parameters used in the non-bonded

potential. In the two-character OPLS atom class, CA denotes an aromatic carbon in a six-membered ring, C! denotes the ipso carbon of biphenyl-like junctions, HA is a hydrogen bound to an aromatic carbon, CT denotes a saturated tetrahedral carbon and HC is a hydrogen bound to a saturated carbon.

Table 6.4: Parameters used in the harmonic bond length potential, $U_{\text{bond}}(l) = k_l(l - l_0)^2/2$, where l_0 is the bond distance and k_l is the force constant for the bonded potential.

(a) rubrene and perylene

bond type	l_0 (Å)	k_l (kcal mol^{-1} Å^{-2})
CA–CA	1.400	938.00
CA–C!	1.400	938.00
C!–C!	1.460	770.00
CA–HA	1.080	734.00

(b) toluene

bond type	l_0 (Å)	k_l (kcal mol^{-1} Å^{-2})
CA–CA	1.400	938.00
CA–CT	1.510	634.00
CA–HA	1.080	734.00
CT–HC	1.090	680.00

Table 6.5: Parameters used in the harmonic bond angle potential, $U_{\text{angle}}(\theta) = k_\theta(\theta - \theta_0)^2/2$, where θ_0 is the equilibrium bond angle and k_θ is the force constant for the bond angle potential. Note that C–C–C represents any applicable combination of CA and C!.

(a) rubrene and perylene

angle type	θ_0 (°)	k_θ (kcal mol^{-1} rad^{-2})
C–C–C	120.0	126.00
CA–CA–HA	120.0	70.00
C!–CA–HA	120.0	70.00

(b) toluene

angle type	θ_0 (°)	k_θ (kcal mol^{-1} rad^{-2})
CA–CA–CA	120.0	126.00
CA–CA–CT	120.0	140.00
CA–CA–HA	120.0	70.00
CA–CT–HC	109.5	70.00
HC–CT–HC	107.8	66.00

Tables 6.4 and 6.5 show the parameters used as part of the bonded potential and harmonic bond angle potential respectively.

Tables 6.6 and 6.7 show the parameters used as part of the proper and improper dihedral potentials respectively.

Table 6.6: Parameters used in the proper dihedral potential, $U_{\text{dihed}}(\phi) = \sum_{n=1}^{5} A_n \cos^{n-1}(\phi)$, where A_n are the coefficients for the proper dihedral potential and ϕ is the proper dihedral angle. Note that X represents any applicable atom and the units of the coefficients are kcal mol^{-1}.

(a) rubrene and perylene

dihedral type	A_1	A_2	A_3	A_4	A_5
X–CA–CA–X	7.250	0.000	−7.250	0.000	0.000
X–CA–C!–X	7.250	0.000	−7.250	0.000	0.000
X–C!–C!–X	1.970	0.000	−1.970	0.000	0.000

(b) toluene

dihedral type	A_1	A_2	A_3	A_4	A_5
X–CA–CA–X	7.250	0.000	−7.250	0.000	0.000
CA–CA–CT–HC	0.000	0.000	0.000	0.000	0.000

Table 6.7: Parameters used in the improper dihedral potential, $U_{\text{improp}}(\varphi) = K[1 + d\cos(n\varphi)]$, where K, d, and n the coefficients for the improper potential and φ is the improper dihedral angle. Note that C represents either CA or C! and that X represents any adjoining carbon atom.

improper type	K (kcal mol^{-1})	d	n
X–X–C–X	1.1	−1	2
X–X–C–HA	1.1	−1	2

Diffusion Coefficients

Table 6.8: Translational diffusion coefficients of toluene, plus rubrene or perylene in toluene obtained from the MD simulations.

	temp. (K)	D_{sim} ($\text{cm}^2\,\text{s}^{-1}$)	D_{exp} ($\text{cm}^2\,\text{s}^{-1}$)	ref.
toluene	200	$1.04 \pm 0.01 \times 10^{-6}$	$1.8 \pm 0.1 \times 10^{-6}$	364
	295	$1.86 \pm 0.02 \times 10^{-5}$	$2.1 \pm 0.1 \times 10^{-5}$	364
rubrene	200	$2.50 \pm 0.08 \times 10^{-7}$	–	
	295	$4.4 \pm 0.2 \times 10^{-6}$	–	
perylene	295	$1.21 \pm 0.03 \times 10^{-5}$	$1.29 \pm 0.04 \times 10^{-5}$	365

Table 6.9: Rotational diffusion coefficients of toluene, plus rubrene or perylene in toluene obtained from the MD simulations. The x, y and z molecular axes are defined as the long, short and perpendicular axes, respectively.

	temp. (K)	axis	R_{sim} (s^{-1})	R_{exp} (s^{-1})	ref.
toluene	200	x	1.0×10^{10}	$5 \pm 3 \times 10^{10}$	366
		y	1.2×10^{10}	$1.5 \pm 0.8 \times 10^{10}$	366
		z	0.6×10^{10}	$2 \pm 1 \times 10^{10}$	366
	295	x	7.5×10^{10}	$1.0 \pm 0.5 \times 10^{11}$	366
		y	1.0×10^{11}	$4 \pm 2 \times 10^{10}$	366
		z	6.6×10^{10}	$1.0 \pm 0.5 \times 10^{11}$	366
rubrene	200	x	7.9×10^{7}	–	
		y	6.3×10^{7}	–	
		z	8.3×10^{7}	–	
	295	x	1.8×10^{9}	–	
		y	1.6×10^{9}	–	
		z	2.1×10^{9}	–	
perylene	295	x	1.3×10^{10}	–	
		y	1.5×10^{10}	–	
		z	9.4×10^{9}	–	

Emitter Molecule Collision Orientations

Definitions of Euler Angles and Spherical Polar Coordinates

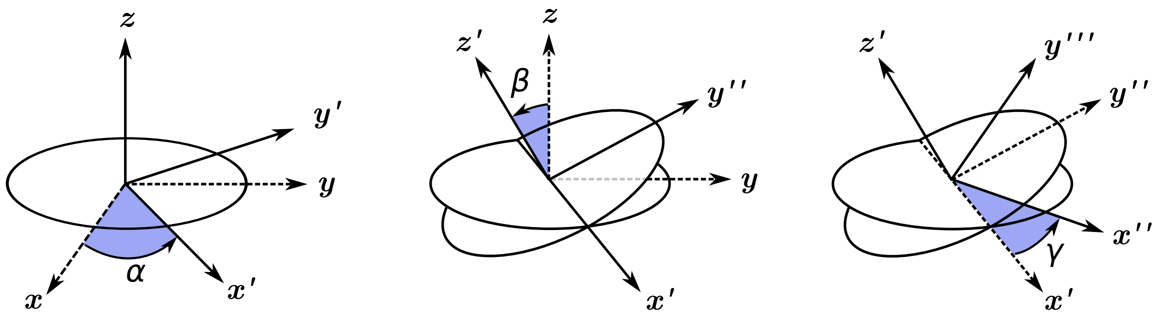

Rotation about z-axis **Rotation about x'-axis** **Rotation about z'-axis**

Figure 6.13: Description of the Euler angles (α, β, γ) used to relate the orientation of molecule B relative to molecule A. The rotations are carried out in the order: a rotation of α about the z-axis, a rotation of β about the now rotated x-axis (the x'-axis) and a rotation of γ about the now rotated z-axis (z'-axis). Positive angles equate to anticlockwise rotations.

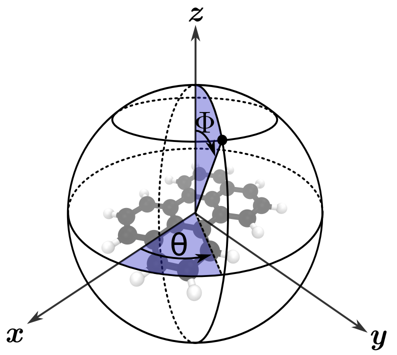

Figure 6.14: Relative positions of emitter pairs using the spherical polar coordinates (θ, ϕ). The axes shown are those of the reference molecule A, and the filled black dot indicates the centre of mass of molecule B.

Collision Angle Correlations

The (red) Euler angle combinations of α, β and γ describe the relative orientations of the molecular pairs found during collisions defined in Figure 6.13. The central 3D density plot shows the most probable combinations of all three angles, with the 2D heatmap plots showing the correlations between pairs of angles. The 2D heatmaps can be thought of as projections of the 3D density cube as if looking through the top, front-left and front-right faces. No attempt has been made to compensate for symmetry of the molecules or equivalence of Euler angle combinations.

The (blue) spherical polar coordinates θ and ϕ describe the relative arrangement in space of the molecular pair, as defined in Figure 6.14.

Collision ranges are defined by the peaks observed in the radial distribution functions shown in Figure 6.1.

Rubrene

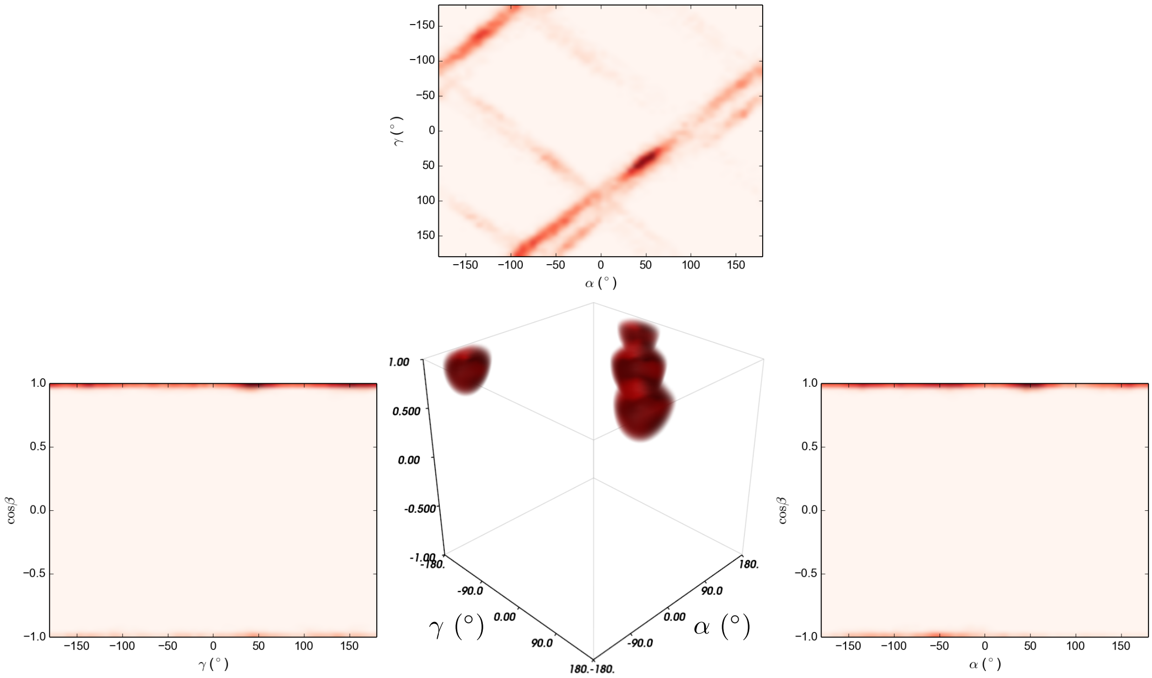

Figure 6.15: Rubrene, first range, Euler angle correlations.

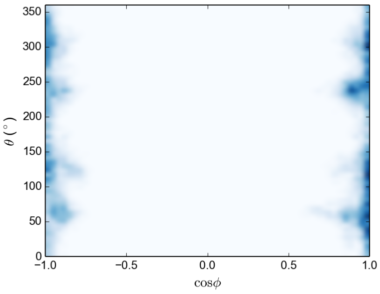

Figure 6.16: Rubrene, first range, spherical polar coordinate correlations.

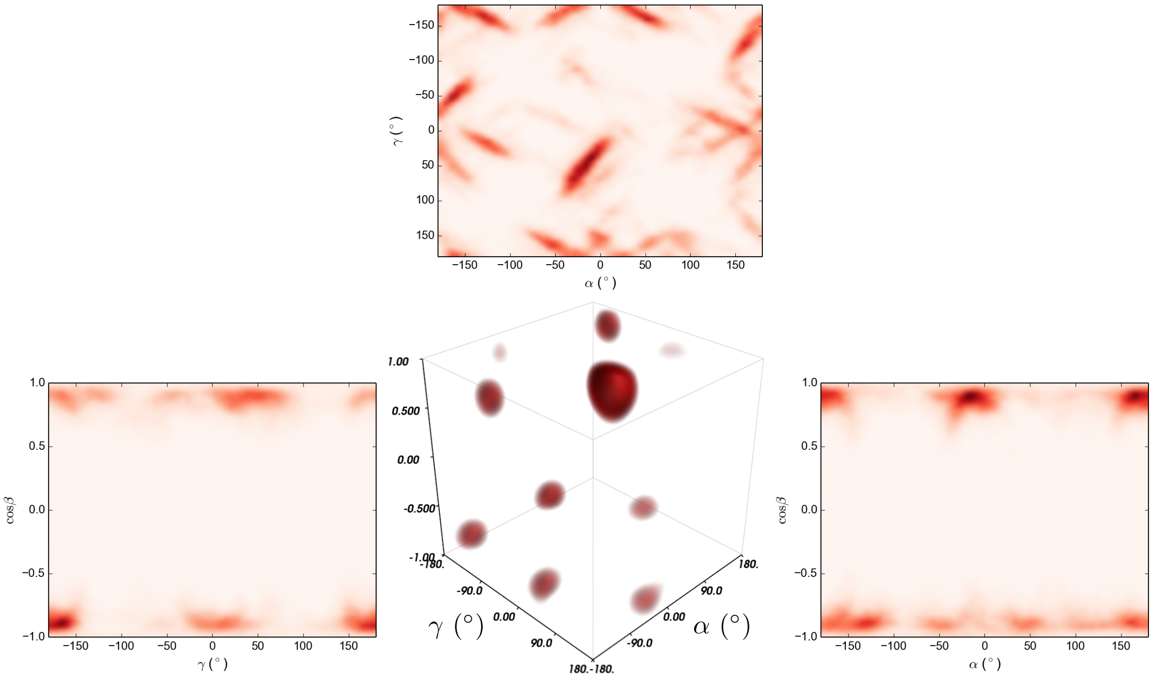

Figure 6.17: Rubrene, second range, Euler angle correlations.

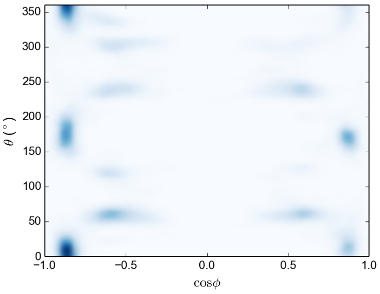

Figure 6.18: Rubrene, second range, spherical polar coordinate correlations.

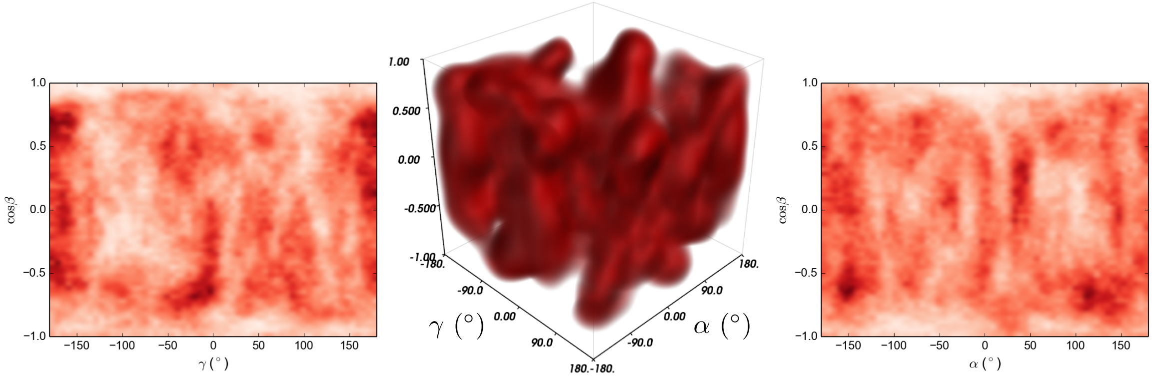

Figure 6.19: Rubrene, third range, Euler angle correlations.

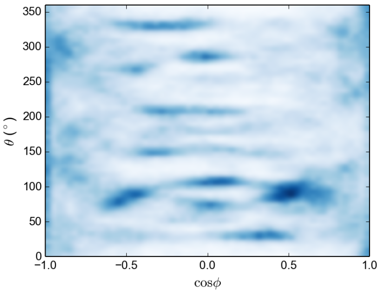

Figure 6.20: Rubrene, third range, spherical polar coordinate correlations.

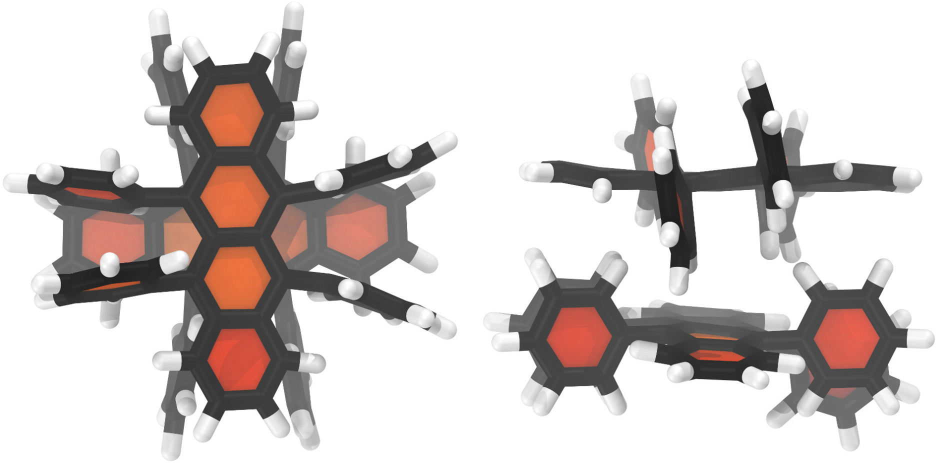

(a) Top view. **(b)** Side view.

Figure 6.21: Interaction of two rubrene molecules at a separation of 4.9 Å–5.9 Å showing the approximately parallel arrangement of the molecules and a 90° alignment of the vector along the length of the backbones.

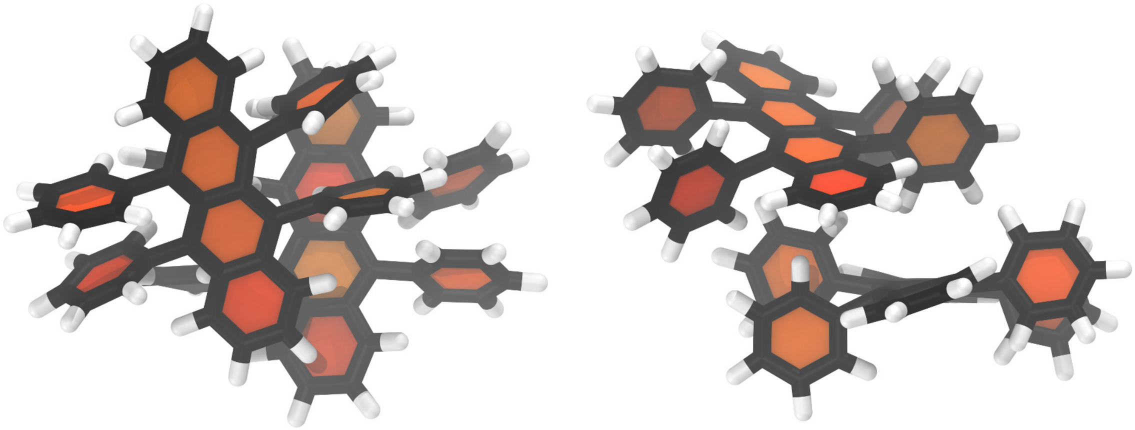

(a) Top view. **(b)** Side view.

Figure 6.22: Interaction of two rubrene molecules at a separation of 5.9 Å–7.7 Å showing an approximate angle of 25° between the planes of their anthracene backbone and a 30° alignment of the vector along the length of the backbones.

Perylene

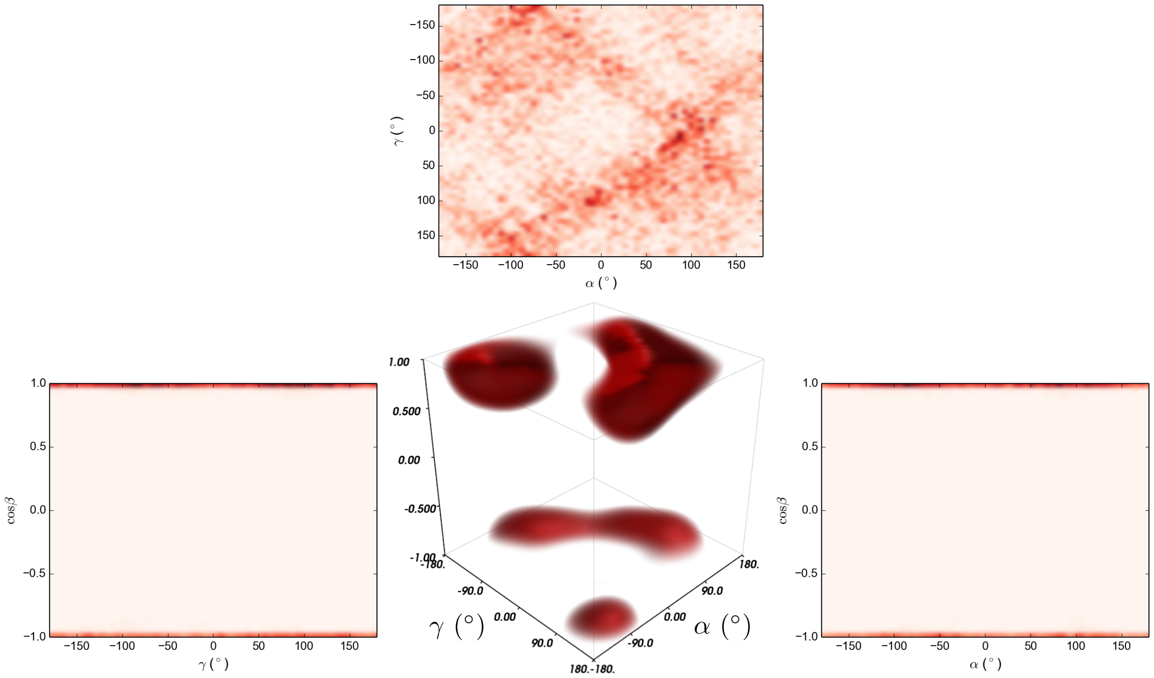

Figure 6.23: Perylene, first range, Euler angle correlations.

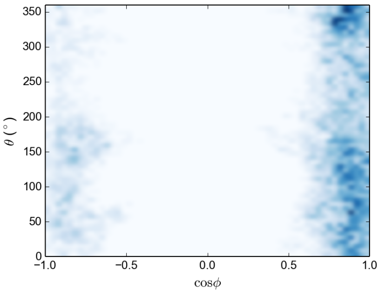

Figure 6.24: Perylene, first range, spherical polar coordinate correlations.

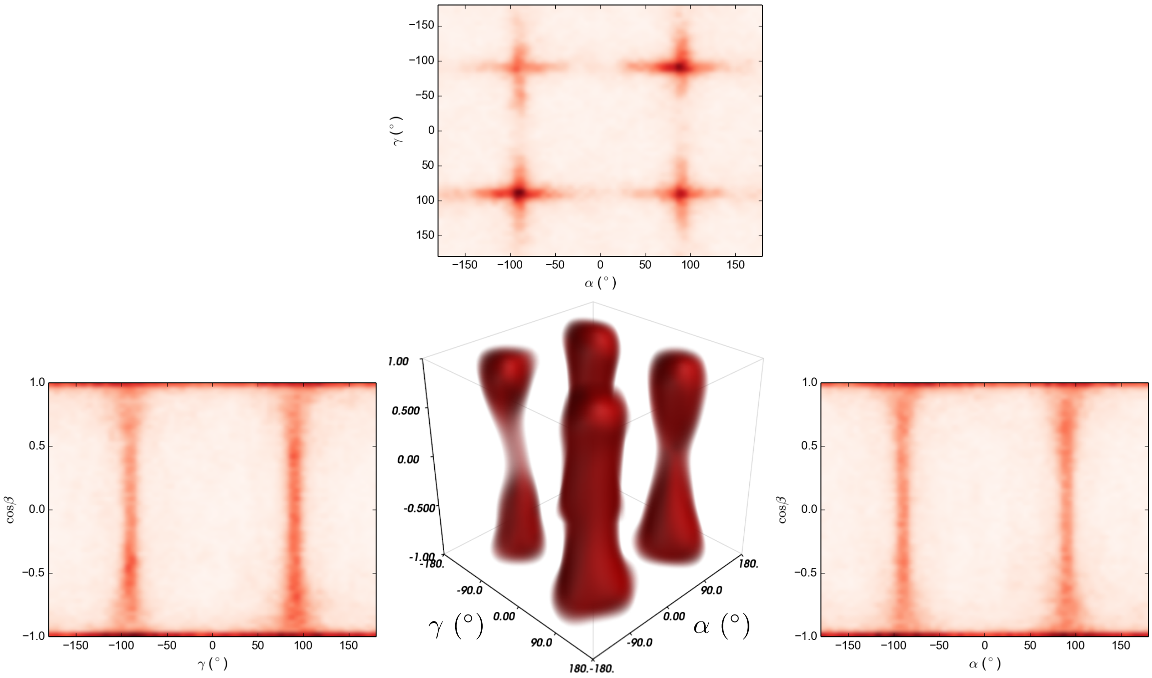

Figure 6.25: Perylene, second range, Euler angle correlations.

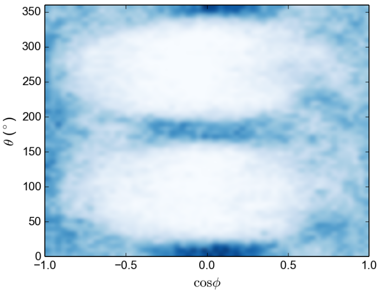

Figure 6.26: Perylene, second range, spherical polar coordinate correlations.

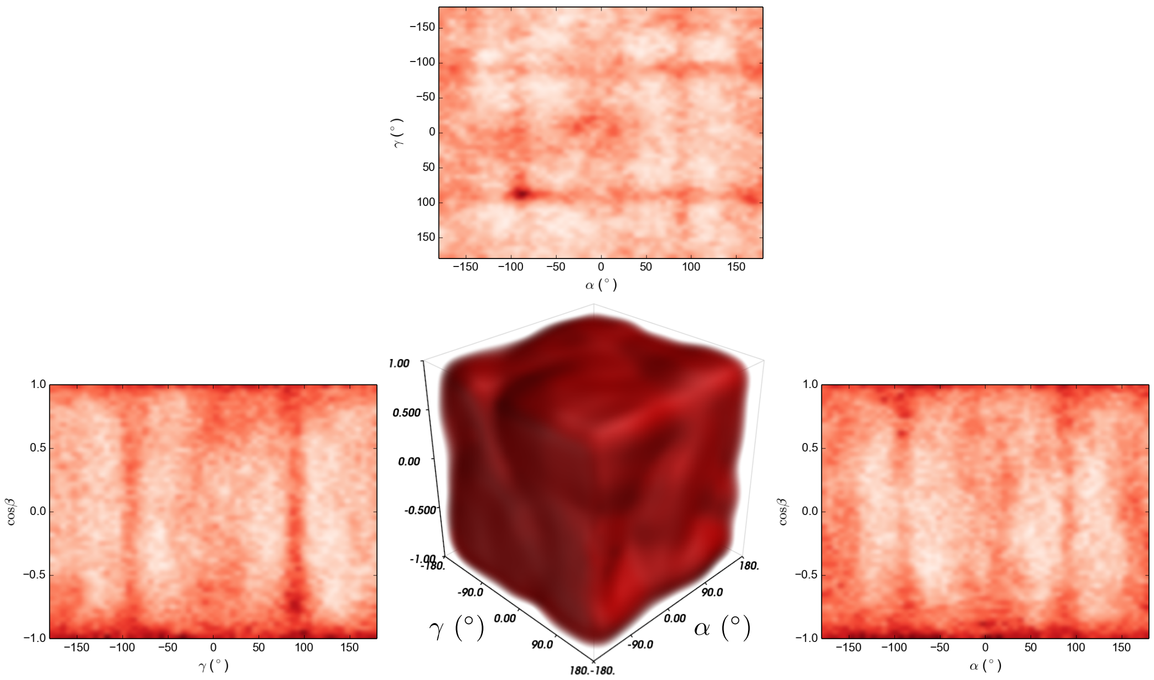

Figure 6.27: Perylene, third range, Euler angle correlations.

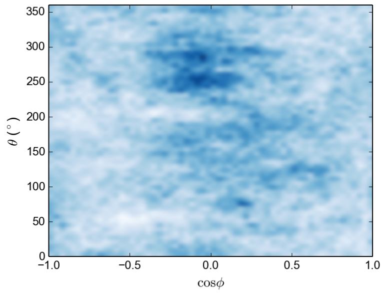

Figure 6.28: Perylene, third range, spherical polar coordinate correlations.

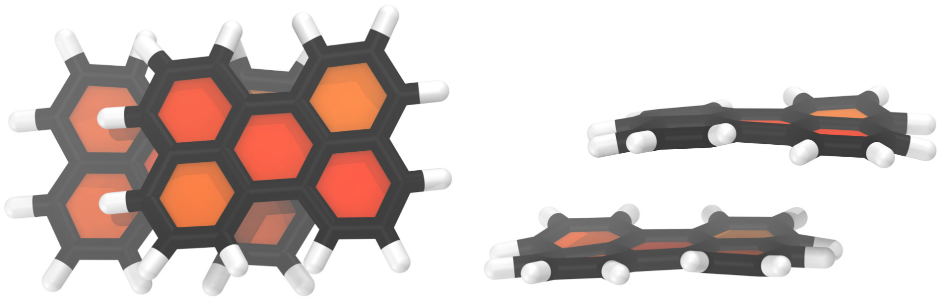

(a) Parallel alignment, top view. **(b)** Parallel alignment, side view.

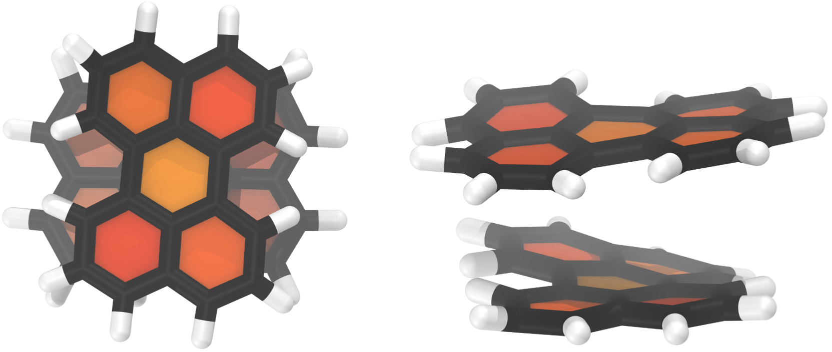

(c) Perpendicular alignment, top view. **(d)** Perpendicular alignment, side view.

Figure 6.29: Interaction of two perylene molecules at a separation of 3.4 Å–5.0 Å showing the approximately parallel arrangement of the molecules and either (a) and (b) a parallel, or (c) and (d) perpendicular alignment of the vectors along the length of the molecules.

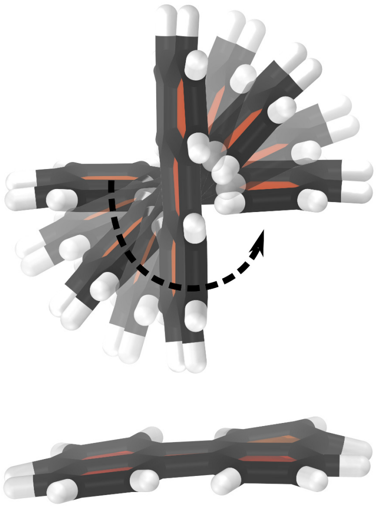

Figure 6.30: Interaction of two perylene molecules at a separation of 5.0 Å–7.0 Å showing the alignment of the vectors along the width of the molecules (in and out of the page) and no alignment of the molecular planes.

Spin Hamiltonian for the Triplet Pair State

Complete description of the spin Hamiltonain for singlet to triplet–triplet interaction may be found in Section 2.2.3.

In the dynamic model of TTA-UC (eq 6.13), the explicit forms of the generation Γ and annihilation Λ matrices are

$$\Gamma_{u,v} = \begin{cases} \frac{1}{9}, & \text{if } u = v \\ 0, & \text{otherwise} \end{cases} \tag{6.29}$$

and

$$\Lambda_{u,v} = \begin{cases} k_\mathrm{S}, & \text{if } u = v = 1 \\ k_\mathrm{T}, & \text{if } u = v = 2,3,4 \\ k_\mathrm{Q}, & \text{if } u = v = 5,6,7,8,9 \\ 0, & \text{otherwise} \end{cases} \tag{6.30}$$

Parametrization of Rubrene

The singlet k_{S_0} and triplet k_{T_0} decay channel coefficients were determined by fitting to experimental data of rubrene emitters in toluene solution.[359] The time-resolved experiments showed the population of excited triplet-state emitters decayed through bimolecular pathways at a rate of $k_2 \approx 1 \times 10^8\,\mathrm{M}^{-1}\,\mathrm{s}^{-1}$ and the efficiency of the bimolecular quenching to form the emissive singlet state was $\eta_\mathrm{conv} = 0.6$, independent of sensitizer or emitter concentration.

The equation describing the interaction of two excited triplet-state emitters is

$$^3\mathrm{E}^* + {}^3\mathrm{E}^* \underset{k_{-1}}{\overset{k_1}{\rightleftarrows}} \begin{cases} ^1[\mathrm{E}\cdots\mathrm{E}]^* \xrightarrow{k_\mathrm{S}} {}^1\mathrm{E} + {}^1\mathrm{E}^* \\ ^3[\mathrm{E}\cdots\mathrm{E}]^* \xrightarrow{k_\mathrm{T}} {}^1\mathrm{E} + {}^3\mathrm{E}^{**} \\ ^5[\mathrm{E}\cdots\mathrm{E}]^* \end{cases} \tag{6.31}$$

thus the proportion of bimolecular quenching of triplet emitters to form the singlet state is

$$\eta_\mathrm{conv} = 0.6 = \frac{k_\mathrm{S}}{k_\mathrm{S} + \frac{1}{2}k_\mathrm{T}}, \tag{6.32}$$

as the decay through the quintet channel is considered negligible and the triplet channel pathway only results in destruction of a single triplet from the triplet-pair. The overall rate γ_S of formation of the emissive singlet state from the triplet-pair

$$^3\mathrm{E}^* + {}^3\mathrm{E}^* \xrightarrow{\gamma_\mathrm{S}} {}^1\mathrm{E} + {}^1\mathrm{E}^* \tag{6.33}$$

is calculated in our model by

$$\gamma_\mathrm{S} = \frac{k_1}{9} \sum_{l=1}^{9} \frac{k_\mathrm{S}|C_\mathrm{S}^l|^2}{k_{-1} + k_\mathrm{S}|C_\mathrm{S}^l|^2 + k_\mathrm{T}|C_\mathrm{T}^l|^2} \tag{6.34}$$

where $|C_\mathrm{S}^l|^2$ and $|C_\mathrm{T}^l|^2$ are the singlet and triplet character of the nine triplet-pair states, respectively. When $k_1 = 1$ and $k_{-1} = 0$, then $\gamma_\mathrm{S} = k_\mathrm{S}$ and $\gamma_\mathrm{T} = k_\mathrm{T} = 1 - \gamma_\mathrm{S}$. Substituting into eq 6.32 gives $\gamma_\mathrm{S} = 3/7$ under these conditions. The ratio of k_S to k_T can then be found by performing a TTA-UC simulation with $k_1 = 1$, $k_{-1} = 0$,

$k_{\mathrm{T}} = 1$ and fitting k_{S} so that $\gamma_{\mathrm{S}} = 3/7$ at zero magnetic field strength. The relative orientation of the two emitters during a collision will modulate the magnitudes of $|C^l_{\mathrm{S}}|^2$ and $|C^l_{\mathrm{T}}|^2$. If random collision orientations is assumed and so the TTA-UC simulation is performed averaging over many unique orientations then this gives a $k_{\mathrm{S}} : k_{\mathrm{T}}$ ratio of 4.25.

For our simulations we assume the saturation limit where the excitation of the sensitizer, triplet energy transfer to the emitter and radiative decay of the excited singlet emitter are rapid compared to the triplet-state emitter lifetime, thus all emitters are in the excited triplet state. Using the concentration of rubrene from the molecular dynamics simulations gives $\alpha = \gamma_{\mathrm{S}} + \frac{1}{2}\gamma_{\mathrm{T}} = k_2[{}^3E^*] = 2.3 \times 10^{-3}\,\mathrm{ns}^{-1}$. Running the TTA-UC simulation of rubrene with parameters and molecular geometries obtained from the molecular dynamics simulations and scaling k_{S_0} and k_{T_0} so that $\gamma_{\mathrm{S}} + \frac{1}{2}\gamma_{\mathrm{T}} = 2.3 \times 10^{-3}\,\mathrm{ns}^{-1}$ gives the required parameters $k_{\mathrm{S}_0} = 2.66 \times 10^{8}\,\mathrm{ns}^{-1}$ and $k_{\mathrm{T}_0} = 6.25 \times 10^{7}\,\mathrm{ns}^{-1}$.

CHAPTER 7

Conclusion

7.1 Summary and Future Directions

This thesis investigated several aspects of structure and morphology on the electronic properties of organic semiconductors. Experimental and computational techniques were used to probe exciton relaxation, dissociation, transport and fission/fusion processes. An emphasis was made on improving the understanding of fundamental processes for organic solar cells, but many theoretical aspects are generally applicable to other organic optoelectronic applications.

Chapter 3 demonstrated a pump-push-probe transient absorption technique applied to the conjugated polymer poly(3-hexylthiophene) (P3HT) in solution. By targeting the excited-state absorption (ESA) band of the pump-induced exciton with a secondary excitation, high-energy excitons were generated. As these “hot” excitons were produced independently from the initial pump excitation, their spectral signatures were able to be easily isolated from the thermalised exciton population.

The pump pulse generated the initial S_1 singlet exciton population, characterised by a broad ESA band in the near infra-red (NIR). The excitons relaxed through a combination of excitonic energy transfer (EET) and torsional motions that acted to planarise the polymer backbone, although EET was restricted to intrachain movement due to the individual chains being well isolated in solution. After sufficient time for relaxation, the push pulse arrived, targeting the ESA band to promote the excitons to a high-energy S_n state with a greater degree of delocalisation. The majority of the high-energy excitons decayed rapidly back to the S_1 state within approximately 160 fs, with the possibility of localising on a new segment of the polymer chain. Excitons which localised on a previously unvisited segment caused further planarisation of the chromophore, and this additional relaxation was observed over several picoseconds. A proportion of the high-energy, delocalised excitons were able to overcome their binding energy and dissociate into free charge carriers. The electron and hole-polaron were still restricted to the same isolated polymer chain, so recombination occurred rapidly. This was visible as a permanent depletion in the S_1 exciton population and a recovery in ground-state population. Approximately 11% of excitons were observed to dissociate in this way, and the longest push wavelength used (1200 nm) indicates an upper bound to the exciton binding energy of 1 eV.

Future experiments using the pump-push-probe technique could further investigate the relaxation processes of hot excitons in a variety of conjugated polymer systems. Under the same solution-phase conditions that provides isolated polymer chains, the role of torsional relaxation may be studied by substitution of stiffer conjugated polymers such as poly(phenylenevinylene)s (PPVs) or polyfluorenes. Alternatively, the spatial extent of the push-induced exciton delocalisation could be tested through the use of a series of polymer or oligomer chain lengths or donor-acceptor type oligomers. Measuring the push-induced exciton dissociation as a function of wavelength would provide interesting data on the magnitude and distribution of exciton binding energies. Experiments on solid films or aggregates such as nanoparticles or nanofibres would introduce interchain interactions and allow the introduction of electron acceptors such as phenyl-C_{61}-butyric acid methyl ester (PCBM). The ability for any generated charge carriers to be better separated and stabilised across a polymer aggregate will result in a longer-lived transient absorption signature that should be directly observable in the experiments. This would provide definitive evidence of the push-induced charge carrier generation and support the interpretation of the solution-phase data. Introduction of electron acceptor materials into the polymer system could reveal information on the role of hot exciton dissociation at the donor-acceptor interfaces of organic photovoltaics.

Chapter 4 compared the optical properties of well-solvated P3HT chains and P3HT nanofibre aggregates, explaining the significant differences on a molecular level using detailed exciton transport simulations. An accurate coarse-grained molecular dynamics (MD) model of P3HT was used to obtain realistic structures of both free chains in a good solvent and nanofibre aggregates formed in a marginal solvent. A Frenkel–Holstein exciton model was applied to determine the sites and energies of the polymer chromophores, and a Monte Carlo exciton transport simulation was used to produce simulated steady-state and time-resolved spectroscopic data. This mesoscale method demonstrated the ability to simulate large polymer systems at a scale relevant to optoelectronic devices, while retaining the detail required to represent the effect of molecular-level morphology on the optical and electronic properties.

The simulations gave reasonable quantitative agreement to steady-state and time-resolved absorption and fluorescence experiments, showing the model was able to adequately capture the energies of the polymer chromophores and the dynamics of exciton mobility. Exciton diffusion length in the nanofibres was found to be approximately 8 nm, generally consisting of around 2–5 hopping events. Interchain exciton migration across the chain stacks was preferred, rather than intrachain transport along the chain length. Absorption of the simulated 400-nm laser light occurred throughout the nanofibre, with a slight preference for absorption at the more disordered regions at the nanofibre surface. Exciton migration tended to be toward the heart of the aggregates, where the more ordered, crystalline nature of the chains resulted in lower-energy chromophores. These acted to trap the exciton until radiative decay occurred. The phenomena of exciton funnelling towards the core of the aggregate was able to explain why aqueous polymer nanoparticles show such unusually high fluorescence quantum yields, as excitons would be effectively protected from the aqueous environment. In organic solar cells, the exciton funnelling away from the donor-acceptor interface may explain the relatively poor performance of nanofibre-based cells, where the favourable polymer domain sizes and higher charge carrier mobility would normally be expected to enhance performance relative to the typical bulk-heterojunction cell. Time-resolved fluorescence anisotropy experiments indicated that both the free chains and P3HT nanofibres showed a similar rate of fluorescence depolarisation, which was explained by noting that although the free chains are more disordered, the exciton migration is limited due to the isolated nature of the chains in solution. Conversely, in the nanofibre aggregates, the greater exciton mobility is offset by the more ordered alignment of the chromophores, which acts to better preserve the exciton transition dipole moment during migration.

The Frenkel–Holstein exciton model used in the simulations determines chromophore locations and energy considering only the intrachain, nearest-neighbour coupling between monomers. This simplification is valid for the isolated and extended nature of solvated polymer chains, but for condensed phases such as nanofibres or solid films, consideration of the intermolecular coupling becomes important. In principle, it is possible to introduce non-nearest-neighbour coupling terms in the Frenkel-Holstein Hamiltonian, but whether extending the model to easily handle cross-chain chromophores while retaining a low computational cost is a question for further research. The lack of a realistic and reliable model of nonradiative exciton decay was not expected to affect results on the relatively short time scales of exciton migration, but may be a significant source of error for simulations over longer durations. While a simplistic model based on the energy gap law could be implemented easily, parameters would need to be estimated based on experimentally measured exciton lifetimes. Development of a model of nonradiative exciton decay that considers factors such as the polymer environment, excited-state geometry changes and interchain interactions would be a challenging but worthwhile endeavour. Simulation of donor–acceptor blends would be a logical extension of the presented model. Introduction of electron acceptor sites that would act to dissociate the exciton would give a way to study not only the exciton mobility, but would also be the beginning of simulating the morphology-dependent current generation of an organic solar cell. Attempting to experimentally verify that excitons are funnelled towards low-energy trap sites at the core of the P3HT nanofibres may be possible through an excitation-power-dependent fluorescence study. With increasing excitation power, exciton density increases and exciton–exciton annihilation becomes a significant quenching pathway. If a funnelling effect is occurring, then this bimolecular decay should be enhanced compared to what would be expected through random exciton diffusion. Finally, in the model presented, the polymer conformation and exciton motion are completely decoupled, in that the structure is determined purely through the classical MD simulations and a static polymer conformation is used in the quantum mechanical exciton transport simulations. In reality this is not the case, with there often being a measurable difference in ground and excited-state geometries in conjugated polymers. The computational cost of closely coupling the molecular dynamics to the exciton motion would be extreme in the large systems simulated here, but could be considered if some method of simplification or optimisation could be developed.

The role of disorder in small-molecule semiconductor films was investigated in Chapter 5, revealing how the rate of singlet-exciton fission and triplet-exciton fusion processes are affected by the relative orientation of adjacent chromophore sites. A quantum mechanical model was presented which extended the historical theory of triplet exciton spin interactions pioneered by Merrifield, accounting for triplet exciton interactions in non-crystalline solids where the exciton sites are not necessarily mutually oriented. The model corrected the current literature understanding of these disordered systems and clarified the theoretical possibility of using the time-resolved fluorescence response to an applied magnetic field as a probe of disorder in such films.

The simulations showed that in the absence of an applied magnetic field, a disordered rubrene film was expected to show a diminished intensity of prompt fluorescence and enhanced delayed fluorescence compared to a crystalline film due to the greater degree of wavefunction overlap between the triplet-pair and singlet exciton states. As the crossing between the singlet and triplet-pair states was enhanced, the initial population of singlet excitons was depleted as the excitation was able to hide in the dark triplet states, observed as a reduction in the prompt fluorescence intensity. At later times, the return crossing from the triplet-pair to singlet exciton states caused the observed increase in delayed fluorescence. With the application of a strong magnetic field, the simulations showed that both the disordered and crystalline films were expected to display an enhancement of prompt fluorescence at the expense of the delayed fluorescence intensity relative to the behaviour in the absence of the magnetic field. The strong magnetic field acted to force the alignment of the spins, reducing the singlet and triplet-pair wavefunction overlap and restricting the crossing between the states. Interestingly, in the presence of intermediate-strength magnetic fields it was predicted that the ordered and crystalline rubrene films should show opposite behaviour, with the prompt fluorescence intensity enhanced in the disordered film but diminished in the crystalline film relative to zero-field. The implication of the simulation result is that studying the response of the time-resolved fluorescence to applied magnetic fields may be able to probe the degree of disorder in organic semiconductor films.

Chapter 6 studied the triplet fusion process in the highly disordered environment of a solution-phase system, in the context of improving solar cell efficiency through the incorporation of a triplet–triplet annihilation upconversion (TTA-UC) layer. Several properties of emitter molecules were examined to determine their influence on the photochemical upconversion process. The effects of diffusion rate, molecular shape, and collision geometry were studied using data obtained from MD simulations of rubrene or perylene emitters in explicit solvent coupled with the quantum mechanical description of the triplet–triplet spin interactions presented in Chapter 5. The model showed that the triplet exciton energy transfer required for annihilation was primarily assisted by the close contact of the polyaromatic core of the emitters during collisions. For molecules where this is the case, the upconversion process will then become diffusion limited, favouring small molecules with fast translational diffusion rates. Interestingly, as rapid diffusion will also reduce the collision duration available for the annihilation process to occur, upconversion efficiency should not be expected to scale linearly with the diffusion rate. Similarly, molecular structure that encourages some amount of adheration to extend collision duration can be beneficial. The precise orientation of the emitters during collisions was found to be influential, but we estimated the maximum enhancement in upconversion efficiency due to orientation to be approximately 30%, far outweighed by the effects of separation distance and diffusion rate. Although positive effects of magnetic fields have been observed in solid-phase TTA-UC systems, this should not be expected in high-temperature solutions, where the rapid tumbling of the molecules acts as a source of spin relaxation. By coupling the explicit trajectories of the emitter molecules from the MD simulations with a dynamic model of the triplet–triplet spin interactions, this mechanism of spin relaxation was shown with unprecedented detail. The model showed that the motion of the emitter pair during a collision is sufficient to cause mixing of the spin-states. Applied magnetic fields act only to reduce the efficiency of this mixing by forcing the alignment of the spins, resulting in an exclusively negative effect on the upconversion process.

The results presented in Chapter 6 highlight the difficulties faced when designing the ideal emitter for a solution-based TTA-UC system, in which several of the independent optimisations that were identified are not necessarily mutually compatible. Although the focus was on solution behaviour, the theories presented are also mostly applicable to the solid-state. In solid systems, the triplet-pair is formed through exciton migration rather than physical transport of the molecules, removing the requirement to optimise the emitter for maximum diffusion rate through solution. Where the emitter sites are fixed in place, such as a polymer or metal organic framework, optimising structure to ensure favourable emitter-pair geometry should be possible and may show noticeable benefits to the TTA-UC efficiency. Solid-state device performance could be simulated by combining a Monte-Carlo style exciton migration simulation like that presented in Chapter 4 with the triplet-fusion rates determined through the theory discussed in Chapters 5 and 6, which could provide a powerful tool to assist the design of future solid-state TTA-UC devices.

References

[1] Tapping, P. C.; Kee, T. W. Optical Pumping of Poly(3-hexylthiophene) Singlet Excitons Induces Charge Carrier Generation. *J. Phys. Chem. Lett.* **2014**, *5*, 1040–1047.

[2] Tapping, P. C.; Clafton, S. N.; Schwarz, K. N.; Kee, T. W.; Huang, D. M. Molecular-Level Details of Morphology-Dependent Exciton Migration in Poly(3-hexylthiophene) Nanostructures. *J. Phys. Chem. C* **2015**, *119*, 7047–7059.

[3] Tapping, P. C.; Huang, D. M. Comment on "Magnetic Field Effects on Singlet Fission and Fluorescence Decay Dynamics in Amorphous Rubrene". *J. Phys. Chem. C* **2016**, *120*, 25151–25157.

[4] Tapping, P. C.; Blacket, S.; Ackling, S.; Danos, A.; Schmidt, T. W.; Huang, D. M. Molecular Understanding of Photochemical Upconversion for Efficient Solar Cells. **2016**, Manuscript in preparation.

[5] Yang, J.; Wen, X.; Xia, H.; Sheng, R.; Ma, Q.; Kim, J.; Tapping, P. C.; Harada, T.; Kee, T. W.; Huang, F.; Cheng, Y.-B.; Green, M.; Ho-Baillie, A.; Huang, S.; Shrestha, S.; Patterson, R.; Conibeer, G. Exploring Hot Carrier Thermalization in Perovskites by Ultrafast Optical Characterization. *Nat. Commun.* **2017**, Accepted for publication. DOI: 10.1038/ncomms14120.

[6] Cao, W.; Lin, Y.; Patterson, R.; Wen, X.; Tapping, P. C.; Kee, T. W.; Veetil, B. P.; Zhang, P.; Zhang, Z.; Zhang, Q.; Reece, P.; Bremner, S.; Shrestha, S.; Conibeer, G. Difference in Hot Carrier Cooling Rate between Langmuir–Blodgett and Drop Cast PbS QDs Films Due to Strong Electron–Phonon Coupling. **2017**, Manuscript submitted for publication.

[7] Rockett, A. *The Materials Science of Semiconductors*; Springer, 2008.

[8] Roothaan, C. C. J. New Developments in Molecular Orbital Theory. *Rev. Mod. Phys.* **1951**, *23*, 69–89.

[9] Anthony, J. The Larger Acenes: Versatile Organic Semiconductors. *Angew. Chem.* **2008**, *47*, 452–483.

[10] Gsänger, M.; Bialas, D.; Huang, L.; Stolte, M.; Würthner, F. Organic Semiconductors based on Dyes and Color Pigments. *Adv. Mater.* **2016**, *28*, 3615–3645.

[11] Pron, A.; Rannou, P. Processible Conjugated Polymers: From Organic Semiconductors to Organic Metals and Superconductors. *Prog. Polym. Sci.* **2002**, *27*, 135–190.

[12] Schmid, P. E. Optical Absorption in Heavily Doped Silicon. *Phys. Rev. B* **1981**, *23*, 5531–5536.

[13] Nollau, A.; Pfeiffer, M.; Fritz, T.; Leo, K. Controlled n-Type Doping of a Molecular Organic Semiconductor: Naphthalenetetracarboxylic Dianhydride (NTCDA) Doped with Bis(ethylenedithio)-tetrathiafulvalene (BEDT-TTF). *J. Appl. Phys.* **2000**, *87*, 4340–4343.

[14] Pfeiffer, M.; Beyer, A.; Fritz, T.; Leo, K. Controlled Doping of Phthalocyanine Layers by Cosublimation with Acceptor Molecules: A Systematic Seebeck and Conductivity Study. *Appl. Phys. Lett.* **1998**, *73*, 3202–3204.

[15] Kepler, R. G.; Bierstedt, P. E.; Merrifield, R. E. Electronic Conduction and Exchange Interaction in a New Class of Conductive Organic Solids. *Phys. Rev. Lett.* **1960**, *5*, 503–504.

[16] Roncali, J. Synthetic Principles for Bandgap Control in Linear π-Conjugated Systems. *Chem. Rev.* **1997**, *97*, 173–206.

[17] Roncali, J. Molecular Engineering of the Band Gap of π-Conjugated Systems: Facing Technological Applications. *Macromol. Rapid Commun.* **2007**, *28*, 1761–1775.

[18] Shoaee, S.; Clarke, T. M.; Huang, C.; Barlow, S.; Marder, S. R.; Heeney, M.; McCulloch, I.; Durrant, J. R. Acceptor Energy Level Control of Charge Photogeneration in Organic Donor/Acceptor Blends. *J. Am. Chem. Soc.* **2010**, *132*, 12919–12926.

[19] Liu, L.; Eisenbrandt, P.; Roland, T.; Polkehn, M.; Schwartz, P.-O.; Bruchlos, K.; Omiecienski, B.; Ludwigs, S.; Leclerc, N.; Zaborova, E.; Leonard, J.; Mery, S.; Burghardt, I.; Haacke, S. Controlling Charge Separation and Recombination by Chemical Design in Donor–Acceptor Dyads. *Phys. Chem. Chem. Phys.* **2016**, *18*, 18536–18548.

[20] Gupta, S. K.; Jha, P.; Singh, A.; Chehimi, M. M.; Aswal, D. K. Flexible Organic Semiconductor Thin Films. *J. Mater. Chem. C* **2015**, *3*, 8468–8479.

[21] Yao, Y.; Dong, H.; Hu, W. Charge Transport in Organic and Polymeric Semiconductors for Flexible and Stretchable Devices. *Adv. Mater.* **2016**, *28*, 4513–4523.

[22] Würthner, F.; Schmidt, R. Electronic and Crystal Engineering of Acenes for Solution-Processible Self-Assembling Organic Semiconductors. *ChemPhysChem* **2006**, *7*, 793–797.

[23] Brotas, G.; Costa, C.; Dias, S. I. G.; Costa, P. M. M.; Di Paolo, R. E.; Martins, J. a.; Farinhas, J.; Alcácer, L.; Morgado, J.; Matos, M.; Charas, A. Solution-Processable Donor–Acceptor–Donor Oligomers with Cross-Linkable Functionality. *Macromol. Chem. Phys.* **2015**, *216*, 519–529.

[24] Burroughes, J. H.; Jones, C. A.; Friend, R. H. New Semiconductor Device Physics in Polymer Diodes and Transistors. *Nature* **1988**, *335*, 137–141.

[25] Walzer, K.; Maennig, B.; Pfeiffer, M.; Leo, K. Highly Efficient Organic Devices Based on Electrically Doped Transport Layers. *Chem. Rev.* **2007**, *107*, 1233–1271.

[26] Mas-Torrent, M.; Rovira, C. Novel Small Molecules for Organic Field-Effect Transistors: Towards Processability and High Performance. *Chem. Soc. Rev.* **2008**, *37*, 827–838.

[27] Aga, R.; Lombardi, J.; Bartsch, C.; Heckman, E. Performance of a Printed Photodetector on a Paper Substrate. *IEEE Photon. Technol. Lett.* **2014**, *26*, 305–308.

[28] Pace, G.; Grimoldi, A.; Sampietro, M.; Natali, D.; Caironi, M. Printed Photodetectors. *Semicond. Sci. Technol.* **2015**, *30*, 104006.

[29] Gather, M.; Köhnen, A.; Falcou, A.; Becker, H.; Meerholz, K. Solution-Processed Full-Color Polymer Organic Light-Emitting Diode Displays Fabricated by Direct Photolithography. *Adv. Funct. Mater.* **2007**, *17*, 191–200.

[30] Sekitani, T.; Nakajima, H.; Maeda, H.; Fukushima, T.; Aida, T.; Hata, K.; Someya, T. Stretchable Active-Matrix Organic Light-Emitting Diode Display Using Printable Elastic Conductors. *Nat. Mater.* **2009**, *8*, 494–499.

[31] Geffroy, B.; le Roy, P.; Prat, C. Organic Light-emitting Diode (OLED) Technology: Materials, Devices and Display Technologies. *Polym. Int.* **2006**, *55*, 572–582.

[32] Wu, Y.-L.; Chen, C.-Y.; Huang, Y.-H.; Lu, Y.-J.; Chou, C.-H.; Wu, C.-C. Highly Efficient Tandem Organic Light-emitting Devices Utilizing The Connecting Structure Based on n-Doped Electron-transport Layer/HATCN/hole-transport Layer. *Appl. Opt.* **2014**, *53*, E1–E6.

[33] Hoppe, H.; Sariciftci, N. S. Organic Solar Cells: An Overview. *J. Mater. Res.* **2004**, *19*, 1924–1945.

[34] Günes, S.; Neugebauer, H.; Sariciftci, N. S. Conjugated Polymer-Based Organic Solar Cells. *Chem. Rev.* **2007**, *107*, 1324–1338.

[35] Clarke, T. M.; Durrant, J. R. Charge Photogeneration in Organic Solar Cells. *Chem. Rev.* **2010**, *110*, 6736–6767.

[36] Rogers, J. A.; Bao, Z.; Baldwin, K.; Dodabalapur, A.; Crone, B.; Raju, V. R.; Kuck, V.; Katz, H.; Amundson, K.; Ewing, J.; Drzaic, P. Paper-like Electronic Displays: Large-Area Rubber-Stamped Plastic Sheets of Electronics and Microencapsulated Electrophoretic Inks. *Proc. Natl. Acad. Sci. USA* **2001**, *98*, 4835–4840.

[37] Zhang, Z.; Guo, K.; Li, Y.; Li, X.; Guan, G.; Li, H.; Luo, Y.; Zhao, F.; Zhang, Q.; Wei, B.; Pei, Q.; Peng, H. A Colour-Tunable, Weavable Fibre-Shaped Polymer Light-Emitting Electrochemical Cell. *Nat. Photon.* **2015**, *9*, 233–238.

[38] Papaiordanidou, M.; Takamatsu, S.; Rezaei-Mazinani, S.; Lonjaret, T.; Martin, A.; Ismailova, E. Cutaneous Recording and Stimulation of Muscles Using Organic Electronic Textiles. *Adv. Healthc. Mater.* **2016**,

[39] Kim, H. M.; Kang, H. W.; Hwang, D. K.; Lim, H. S.; Ju, B.-K.; Lim, J. A. Metal–Insulator–Semiconductor Coaxial Microfibers Based on Self-Organization of Organic Semiconductor:Polymer Blend for Weavable, Fibriform Organic Field-Effect Transistors. *Adv. Funct. Mater.* **2016**, *26*, 2706–2714.

[40] Görrn, P.; Sander, M.; Meyer, J.; Kröger, M.; Becker, E.; Johannes, H.-H.; Kowalsky, W.; Riedl, T. Towards See-Through Displays: Fully Transparent Thin-Film Transistors Driving Transparent Organic Light-Emitting Diodes. *Adv. Mater.* **2006**, *18*, 738–741.

[41] Park, J. W.; Shin, D. C.; Park, S. H. Large-area OLED Lightings and Their Applications. *Semicond. Sci. Technol.* **2011**, *26*, 034002.

[42] Rowell, M. W.; McGehee, M. D. Transparent Electrode Requirements for Thin Film Solar Cell Modules. *Energy Environ. Sci.* **2011**, *4*, 131–134.

[43] Chen, C.-C.; Dou, L.; Zhu, R.; Chung, C.-H.; Song, T.-B.; Zheng, Y. B.; Hawks, S.; Li, G.; Weiss, P. S.; Yang, Y. Visibly Transparent Polymer Solar

Cells Produced by Solution Processing. *ACS Nano* **2012**, *6*, 7185–7190.

[44] Laaperi, A. OLED Lifetime Issues From a Mobile-Phone-industry Point of View. *J. Soc. Inf. Disp.* **2008**, *16*, 1125–1130.

[45] Scharber, M.; Sariciftci, N. Efficiency of Bulk-Heterojunction Organic Solar Cells. *Prog. Polym. Sci.* **2013**, *38*, 1929–1940.

[46] Krebs, F. C. Polymer Solar Cell Modules Prepared Using Roll-to-Roll Methods: Knife-Over-Edge Coating, Slot-Die Coating And Screen Printing. *Sol. Energ. Mat. Sol. Cells* **2009**, *93*, 465–475.

[47] Søndergaard, R.; Hösel, M.; Angmo, D.; Larsen-Olsen, T. T.; Krebs, F. C. Roll-to-Roll Fabrication of Polymer Solar Cells. *Mater. Today* **2012**, *15*, 36–49.

[48] Carlé, J. E.; Andersen, T. R.; Helgesen, M.; Bundgaard, E.; Jørgensen, M.; Krebs, F. C. A Laboratory Scale Approach to Polymer Solar Cells Using One Coating/Printing Machine, Flexible Substrates, No ITO, No Vacuum and No Spincoating. *Sol. Energ. Mat. Sol. Cells* **2013**, *108*, 126–128.

[49] Shaheen, S. E.; Radspinner, R.; Peyghambarian, N.; Jabbour, G. E. Fabrication of Bulk Heterojunction Plastic Solar Cells by Screen Printing. *Appl. Phys. Lett.* **2001**, *79*, 2996–2998.

[50] Vangeneugden, D. L.; Vanderzande, D. J. M.; Salbeck, J.; van Hal, P. A.; Janssen, R. A. J.; Hummelen, J. C.; Brabec, C. J.; Shaheen, S. E.; Sariciftci, N. S. Synthesis and Characterization of a Poly(1,3-dithienylisothianaphthene) Derivative for Bulk Heterojunction Photovoltaic Cells. *J. Phys. Chem. B* **2001**, *105*, 11106–11113.

[51] Li, G.; Shrotriya, V.; Yao, Y.; Huang, J.; Yang, Y. Manipulating Regioregular Poly(3-hexylthiophene) : [6,6]-phenyl-C61-butyric Acid Methyl Ester Blends — Route Towards High Efficiency Polymer Solar Cells. *J. Mater. Chem.* **2007**, *17*, 3126–3140.

[52] Roncali, J. Molecular Bulk Heterojunctions: An Emerging Approach to Organic Solar Cells. *Acc. Chem. Res.* **2009**, *42*, 1719–1730.

[53] Brabec, C. J.; Gowrisanker, S.; Halls, J. J. M.; Laird, D.; Jia, S.; Williams, S. P. Polymer-Fullerene Bulk-Heterojunction Solar Cells. *Adv. Mater.* **2010**, *22*, 3839–3856.

[54] Tumbleston, J. R.; Collins, B. A.; Yang, L.; Stuart, A. C.; Gann, E.; Ma, W.; You, W.; Ade, H. The Influence of Molecular Orientation on Organic Bulk Heterojunction Solar Cells. *Nat. Photon.* **2014**, *8*, 385–391.

[55] Green, M. A.; Emery, K.; Hishikawa, Y.; Warta, W.; Dunlop, E. D. Solar Cell Efficiency Tables (Version 48). *Prog. Photovolt: Res. Appl.* **2016**, *24*, 905–913.

[56] Shockley, W.; Queisser, H. J. Detailed Balance Limit of Efficiency of p-n Junction Solar Cells. *J. Appl. Phys.* **1961**, *32*, 510–519.

[57] Piris, J.; Dykstra, T. E.; Bakulin, A. A.; van, P. H. M., Loosdrecht; Knulst, W.; Trinh, M. T.; Schins, J. M.; Siebbeles, L. D. A. Photogeneration and Ultrafast Dynamics of Excitons and Charges in P3HT/PCBM Blends. *J. Phys. Chem. C* **2009**, *113*, 14500–14506.

[58] Guo, J.; Ohkita, H.; Benten, H.; Ito, S. Charge Generation and Recombination Dynamics in Poly(3-hexylthiophene)/Fullerene Blend Films with Different Regioregularities and Morphologies. *J. Am. Chem. Soc.* **2010**, *132*, 6154–6164.

[59] Byers, J. C.; Ballantyne, S.; Rodionov, K.; Mann, A.; Semenikhin, O. A. Mechanism of Recombination Losses in Bulk Heterojunction P3HT:PCBM Solar Cells Studied Using Intensity Modulated Photocurrent Spectroscopy. *ACS Appl. Mater. Interfaces* **2011**, *3*, 392–401.

[60] Honda, S.; Nogami, T.; Ohkita, H.; Benten, H.; Ito, S. Improvement of the Light-Harvesting Efficiency in Polymer/Fullerene Bulk Heterojunction Solar Cells by Interfacial Dye Modification. *ACS Appl. Mater. Interfaces* **2009**, *1*, 804–810.

[61] Schwartz, B. J. Conjugated Polymers as Molecular Materials: How Chain Conformation and Film Morphology Influence Energy Transfer and Interchain Interactions. *Annu. Rev. Phys. Chem.* **2003**, *54*, 141.

[62] Ma, W.; Yang, C.; Gong, X.; Lee, K.; Heeger, A. Thermally Stable, Efficient Polymer Solar Cells with Nanoscale Control of the Interpenetrating Network Morphology. *Adv. Funct. Mater.* **2005**, *15*, 1617–1622.

[63] McNeill, C. R.; Westenhoff, S.; Groves, C.; Friend, R. H.; Greenham, N. C. Influence of Nanoscale Phase Separation on the Charge Generation Dynamics and Photovoltaic Performance of Conjugated Polymer Blends: Balancing Charge Generation and Separation. *J. Phys. Chem. C* **2007**, *111*, 19153–19160.

[64] Ameri, T.; Dennler, G.; Waldauf, C.; Denk, P.; Forberich, K.; Scharber, M. C.; Brabec, C. J.; Hingerl, K. Realization, Characterization, and Optical Modeling of Inverted Bulk-Heterojunction Organic Solar Cells. *J. Appl. Phys.* **2008**, *103*, 084506.

[65] Nelson, C. A.; Monahan, N. R.; Zhu, X. Y. Exceeding the Shockley–Queisser Limit in Solar Energy Conversion. *Energy Environ. Sci.* **2013**, *6*, 3508–3519.

[66] Schulze, T. F.; Cheng, Y. Y.; Fueckel, B.; MacQueen, R. W.; Danos, A.; Davis, N. J. L. K.; Tayebjee, M. J. Y.; Khoury, T.; Clady, R. G. C. R.; Ekins-Daukes, N. J.; Crossley, M. J.; Stannowski, B.; Lips, K.; Schmidt, T. W. Photochemical Upconversion Enhanced Solar Cells: Effect of a Back Reflector. *Aust. J. Chem.* **2012**, *65*, 480–485.

[67] Tayebjee, M. J. Y.; McCamey, D. R.; Schmidt, T. W. Beyond Shockley–Queisser: Molecular Approaches to High-Efficiency Photovoltaics. *J. Phys. Chem. Lett.* **2015**, *6*, 2367–2378.

[68] Saxman, A.; Liepins, R.; Aldissi, M. Polyacetylene: Its Synthesis, Doping and Structure. *Prog. Polym. Sci.* **1985**, *11*, 57–89.

[69] North, A. M.; Ross, D. A. Singlet Energy Migration Down Conjugated Polymer Chains. *J. Polym. Sci. Polym. Symp.* **1976**, *55*, 259–267.

[70] Chiang, C. K.; Fincher, C. R.; Park, Y. W.; Heeger, A. J.; Shirakawa, H.; Louis, E. J.; Gau, S. C.; MacDiarmid, A. G. Electrical Conductivity in Doped Polyacetylene. *Phys. Rev. Lett.* **1977**, *39*, 1098–1101.

[71] Shirakawa, H.; Louis, E. J.; MacDiarmid, A. G.; Chiang, C. K.; Heeger, A. J. Synthesis of Electrically Conducting Organic Polymers: Halogen Derivatives of

Polyacetylene. *J. Chem. Soc. Chem. Commun.* **1977**, *0*, 578–580.

[72] Nobelprize.org, The Nobel Prize in Chemistry. 2000; Accessed June 2016.

[73] Elsenbaumer, R.; Jen, K.; Oboodi, R. Processible and Environmentally Stable Conducting Polymers. *Synth. Met.* **1986**, *15*, 169–174.

[74] Zhao, M.-T.; Singh, B. P.; Prasad, P. N. A Systematic Study of Polarizability and Microscopic Third-Order Optical Nonlinearity in Thiophene Oligomers. *J. Chem. Phys.* **1988**, *89*, 5535–5541.

[75] Hotta, S.; Soga, M.; Sonoda, N. Novel Organosynthetic Routes to Polythiophene and its Derivatives. *Synth. Met.* **1988**, *26*, 267–279.

[76] Heffner, G. W.; Pearson, D. S. Molecular Characterization of Poly(3-hexylthiophene). *Macromolecules* **1991**, *24*, 6295–6299.

[77] Dang, M. T.; Hirsch, L.; Wantz, G. P3HT:PCBM, Best Seller in Polymer Photovoltaic Research. *Adv. Mater.* **2011**, *23*, 3597–3602.

[78] Zhao, B.; He, Z.; Cheng, X.; Qin, D.; Yun, M.; Wang, M.; Huang, X.; Wu, J.; Wu, H.; Cao, Y. Flexible Polymer Solar Cells with Power Conversion Efficiency of 8.7%. *J. Mater. Chem. C* **2014**, *2*, 5077–5082.

[79] You, J.; Dou, L.; Yoshimura, K.; Kato, T.; Ohya, K.; Moriarty, T.; Emery, K.; Chen, C.-C.; Gao, J.; Li, G.; Yang, Y. A Polymer Tandem Solar Cell With 10.6% Power Conversion Efficiency. *Nat. Commun.* **2013**, *4*, 1446.

[80] Burroughes, J. H.; Bradley, D. D. C.; Brown, A. R.; Marks, R. N.; Mackay, K.; Friend, R. H.; Burns, P. L.; Holmes, A. B. Light-Emitting Diodes Based on Conjugated Polymers. *Nature* **1990**, *347*, 539–541.

[81] Parker, I. D. Carrier Tunneling and Device Characteristics in Polymer Light-Emitting Diodes. *J. Appl. Phys.* **1994**, *75*, 1656–1666.

[82] Chen, T. A.; Rieke, R. D. The First Regioregular Head-to-Tail Poly(3-hexylthiophene-2,5-diyl) and a Regiorandom Isopolymer: Nickel Versus Palladium Catalysis of 2(5)-bromo-5(2)-(bromozincio)-3-hexylthiophene Polymerization. *J. Am. Chem. Soc.* **1992**, *114*, 10087–10088.

[83] Chen, T.-A.; Wu, X.; Rieke, R. D. Regiocontrolled Synthesis of Poly(3-alkylthiophenes) Mediated by Rieke Zinc: Their Characterization and Solid-State Properties. *J. Am. Chem. Soc.* **1995**, *117*, 233–244.

[84] Bidan, G.; De Nicola, A.; Enée, V.; Guillerez, S. Synthesis and UV–Visible Properties of Soluble Regioregular Oligo(3-octylthiophenes), Monomer to Hexamer. *Chem. Mater.* **1998**, *10*, 1052–1058.

[85] Howard, I. A.; Mauer, R.; Meister, M.; Laquai, F. Effect of Morphology on Ultrafast Free Carrier Generation in Polythiophene:Fullerene Organic Solar Cells. *J. Am. Chem. Soc.* **2010**, *132*, 14866–14876.

[86] Hu, D.; Yu, J.; Wong, K.; Bagchi, B.; Rossky, P. J.; Barbara, P. F. Collapse of Stiff Conjugated Polymers with Chemical Defects into Ordered, Cylindrical Conformations. *Nature* **2000**, *405*, 1030–1033.

[87] Schenning, A. P. H. J.; Meijer, E. W. Supramolecular Electronics; Nanowires from Self-Assembled Pi-Conjugated Systems. *Chem. Commun.* **2005**, 3245–3258.

[88] Park, D.; Kim, B.; Jang, M.; Bae, K.; Lee, S.; Joo, J. Synthesis and Characterization of Polythiophene and Poly(3-methylthiophene) Nanotubes and Nanowires. *Synth. Met.* **2005**, *153*, 341–344.

[89] Wu, C.; Szymanski, C.; McNeill, J. Preparation and Encapsulation of Highly Fluorescent Conjugated Polymer Nanoparticles. *Langmuir* **2006**, *22*, 2956–2960.

[90] Samitsu, S.; Shimomura, T.; Heike, S.; Hashizume, T.; Ito, K. Effective Production of Poly(3-alkylthiophene) Nanofibers by means of Whisker Method using Anisole Solvent: Structural, Optical, and Electrical Properties. *Macromolecules* **2008**, *41*, 8000–8010.

[91] Pecher, J.; Mecking, S. Nanoparticles of Conjugated Polymers. *Chem. Rev.* **2010**, *110*, 6260–6279.

[92] Sun, S.; Salim, T.; Wong, L. H.; Foo, Y. L.; Boey, F.; Lam, Y. M. A New Insight into Controlling Poly(3-hexylthiophene) Nanofiber Growth Through a Mixed-Solvent Approach for Organic Photovoltaics Applications. *J. Mater. Chem.* **2011**, *21*, 377–386.

[93] Roehling, J. D.; Arslan, I.; Moule, A. J. Controlling Microstructure in Poly(3–hexylthiophene) Nanofibers. *J. Mater. Chem.* **2012**, *22*, 2498–2506.

[94] Barford, W.; Marcus, M. Theory of Optical Transitions in Conjugated Polymers. I. Ideal Systems. *J. Chem. Phys.* **2014**, *141*, 164101.

[95] Barford, W.; Tozer, O. R. Theory of Exciton Transfer and Diffusion in Conjugated Polymers. *J. Chem. Phys.* **2014**, *141*, 164103.

[96] Marcus, M.; Tozer, O. R.; Barford, W. Theory of Optical Transitions in Conjugated Polymers. II. Real Systems. *J. Chem. Phys.* **2014**, *141*, 164102.

[97] Ghosh, S.; Rasmusson, J.; Inganäs, O. Supramolecular Self-Assembly for Enhanced Conductivity in Conjugated Polymer Blends: Ionic Crosslinking in Blends of Poly(3,4-ethylenedioxythiophene)-Poly(styrenesulfonate) and Poly(vinylpyrrolidone). *Adv. Mater.* **1998**, *10*, 1097–1099.

[98] Aasmundtveit, K. E.; Samuelsen, E. J.; Pettersson, L. A. A.; Inganäs, O.; Johansson, T.; Feidenhans, R. Structure of Thin Films of Poly(3,4-ethylenedioxythiophene). *Synth. Met.* **1999**, *101*, 561–564.

[99] Gross, M.; Muller, D. C.; Nothofer, H. G.; Scherf, U.; Neher, D.; Brauchle, C.; Meerholz, K. Improving the Performance of Doped Pi-Conjugated Polymers for use in Organic Light-Emitting Diodes. *Nature* **2000**, *405*, 661–665.

[100] Saito, Y.; Kitamura, T.; Wada, Y.; Yanagida, S. Poly(3,4-ethylenedioxythiophene) as a Hole Conductor in Solid State Dye Sensitized Solar Cells. *Synth. Met.* **2002**, *131*, 185–187.

[101] Andersson, P.; Nilsson, D.; Svensson, P.-O.; Chen, M.; Malmström, A.; Remonen, T.; Kugler, T.; Berggren, M. Active Matrix Displays Based on All-Organic Electrochemical Smart Pixels Printed on Paper. *Adv. Mater.* **2002**, *14*, 1460–1464.

[102] Kim, E.-G.; Brédas, J.-L. Electronic Evolution of Poly(3,4-ethylenedioxythiophene) (PEDOT): From the Isolated Chain to the Pristine and Heavily Doped Crystals. *J. Am. Chem. Soc.* **2008**, *130*, 16880–16889.

[103] Sternlicht, H.; McConnell, H. M. Paramagnetic Excitons in Molecular Crystals. *J. Chem. Phys.* **1961**, *35*, 1793–1800.

[104] Davydov, A. S. The Theory of Molecular Excitons. *Sov. Phys. Usp.* **1964**, *7*, 145.

[105] Hochstrasser, R. M. Electronic Spectra of Organic Molecules. *Annu. Rev. Phys. Chem.* **1966**, *17*, 457–480.

[106] Avakian, P.; Merrifield, R. E. Triplet Excitons in Anthracene Crystals — A Review. *Mol. Cryst.* **1968**, *5*, 37–77.

[107] Powell, R. C.; Soos, Z. G. Singlet Exciton Energy Transfer in Organic Solids. *J. Lumin.* **1975**, *11*, 1–45.

[108] Pope, M.; Swenberg, C. E. Electronic Processes in Organic Solids. *Annu. Rev. Phys. Chem.* **1984**, *35*, 613–655.

[109] Tang, C. W.; Albrecht, A. C. Photovoltaic Effects of Metal–Chlorophyll-A–Metal Sandwich Cells. *J. Chem. Phys.* **1975**, *62*, 2139–2149.

[110] Yakimov, A.; Forrest, S. R. High Photovoltage Multiple-Heterojunction Organic Solar Cells Incorporating Interfacial Metallic Nanoclusters. *Appl. Phys. Lett.* **2002**, *80*, 1667–1669.

[111] Xue, J.; Uchida, S.; Rand, B. P.; Forrest, S. R. 4.2% Efficient Organic Photovoltaic Cells with Low Series Resistances. *Appl. Phys. Lett.* **2004**, *84*, 3013–3015.

[112] Uchida, S.; Xue, J.; Rand, B. P.; Forrest, S. R. Organic Small Molecule Solar Cells with a Homogeneously Mixed Copper Phthalocyanine:C_{60} Active Layer. *Appl. Phys. Lett.* **2004**, *84*, 4218–4220.

[113] Mishra, A.; Bäuerle, P. Small Molecule Organic Semiconductors on the Move: Promises for Future Solar Energy Technology. *Angew. Chem. Int. Ed.* **2012**, *51*, 2020–2067.

[114] Karsten, B. P.; Bouwer, R. K. M.; Hummelen, J. C.; Williams, R. M.; Janssen, R. A. J. Charge Separation and Recombination in Small Band Gap Oligomer–Fullerene Triads. *J. Phys. Chem. B* **2010**, *114*, 14149–14156.

[115] Kanal, F.; Ruetzel, S.; Lu, H.; Moos, M.; Holzapfel, M.; Brixner, T.; Lambert, C. Measuring Charge-Separation Dynamics via Oligomer Length Variation. *J. Phys. Chem. C* **2014**, *118*, 23586–23598.

[116] Tang, C. W.; VanSlyke, S. A. Organic Electroluminescent Diodes. *Appl. Phys. Lett.* **1987**, *51*, 913–915.

[117] Huang, J.; Pfeiffer, M.; Werner, A.; Blochwitz, J.; Leo, K.; Liu, S. Low-Voltage Organic Electroluminescent Devices Using p-i-n Structures. *Appl. Phys. Lett.* **2002**, *80*, 139–141.

[118] Tsuboyama, A.; Iwawaki, H.; Furugori, M.; Mukaide, T.; Kamatani, J.; Igawa, S.; Moriyama, T.; Miura, S.; Takiguchi, T.; Okada, S.; Hoshino, M.; Ueno, K. Homoleptic Cyclometalated Iridium Complexes with Highly Efficient Red Phosphorescence and Application to Organic Light-Emitting Diode. *J. Am. Chem. Soc.* **2003**, *125*, 12971–12979.

[119] He, G.; Schneider, O.; Qin, D.; Zhou, X.; Pfeiffer, M.; Leo, K. Very High-Efficiency and Low Voltage Phosphorescent Organic Light-Emitting Diodes

Based on a p-i-n Junction. *J. Appl. Phys.* **2004**, *95*, 5773–5777.

[120] Endo, A.; Ogasawara, M.; Takahashi, A.; Yokoyama, D.; Kato, Y.; Adachi, C. Thermally Activated Delayed Fluorescence from Sn^{4+}-Porphyrin Complexes and Their Application to Organic Light Emitting Diodes — A Novel Mechanism for Electroluminescence. *Adv. Mater.* **2009**, *21*, 4802–4806.

[121] Endo, A.; Sato, K.; Yoshimura, K.; Kai, T.; Kawada, A.; Miyazaki, H.; Adachi, C. Efficient Up-conversion of Triplet Excitons into a Singlet State and its Application for Organic Light Emitting Diodes. *Appl. Phys. Lett.* **2011**, *98*.

[122] Zhang, Q.; Li, J.; Shizu, K.; Huang, S.; Hirata, S.; Miyazaki, H.; Adachi, C. Design of Efficient Thermally Activated Delayed Fluorescence Materials for Pure Blue Organic Light Emitting Diodes. *J. Am. Chem. Soc.* **2012**, *134*, 14706–14709.

[123] Dias, F. B.; Bourdakos, K. N.; Jankus, V.; Moss, K. C.; Kamtekar, K. T.; Bhalla, V.; Santos, J.; Bryce, M. R.; Monkman, A. P. Triplet Harvesting with 100% Efficiency by Way of Thermally Activated Delayed Fluorescence in Charge Transfer OLED Emitters. *Adv. Mater.* **2013**, *25*, 3707–3714.

[124] Zhang, Q.; Li, B.; Huang, S.; Nomura, H.; Tanaka, H.; Adachi, C. Efficient Blue Organic Light Emitting Diodes Employing Thermally Activated Delayed Fluorescence. *Nat. Photon.* **2014**, *8*, 326–332.

[125] Coropceanu, V.; Cornil, J.; da Silva Filho, D. A.; Olivier, Y.; Silbey, R.; Brédas, J.-L. Charge Transport in Organic Semiconductors. *Chem. Rev.* **2007**, *107*, 926–952.

[126] de Boer, R. W. I.; Klapwijk, T. M.; Morpurgo, A. F. Field-Effect Transistors on Tetracene Single Crystals. *Appl. Phys. Lett.* **2003**, *83*, 4345–4347.

[127] Podzorov, V.; Pudalov, V. M.; Gershenson, M. E. Field-effect Transistors on Rubrene Single Crystals with Parylene Gate Insulator. *Appl. Phys. Lett.* **2003**, *82*, 1739–1741.

[128] Podzorov, V.; Sysoev, S. E.; Loginova, E.; Pudalov, V. M.; Gershenson, M. E. Single-crystal Organic Field Effect Transistors with the Hole Mobility $\sim$8 cm^2/V s. *Appl. Phys. Lett.* **2003**, *83*, 3504–3506.

[129] de Boer, R. W. I.; Gershenson, M. E.; Morpurgo, A. F.; Podzorov, V. Organic Single-Crystal Field-Effect Transistors. *Phys. Status Solidi (A)* **2004**, *201*, 1302–1331.

[130] Reese, C.; Bao, Z. Organic Single-Crystal Field-Effect Transistors. *Mater. Today* **2007**, *10*, 20–27.

[131] Chen, Z.; Müller, P.; Swager, T. M. Syntheses of Soluble, π-Stacking Tetracene Derivatives. *Org. Lett.* **2006**, *8*, 273–276.

[132] Hasegawa, T.; Takeya, J. Organic Field-effect Transistors Using Single Crystals. *Sci. Technol. Adv. Mater.* **2009**, *10*, 024314.

[133] Hummelen, J. C.; Knight, B. W.; LePeq, F.; Wudl, F.; Yao, J.; Wilkins, C. L. Preparation and Characterization of Fulleroid and Methanofullerene Derivatives. *J. Org. Chem.* **1995**, *60*, 532–538.

[134] Yu, G.; Heeger, A. J. Polymer-C60 Charge-Transfer Blends: Enhanced Pho-

tosensitivity via a Bicontinuous Network of Donor/Acceptor Heterojunctions. *Fullerenes and Photon. III* **1996**, *2854*, 123–128.

[135] Beljonne, D.; Pourtois, G.; Silva, C.; Hennebicq, E.; Herz, L. M.; Friend, R. H.; Scholes, G. D.; Setayesh, S.; Müllen, K.; Brèdas, J. L. Interchain vs. Intrachain Energy Transfer in Acceptor-Capped Conjugated Polymers. *Proc. Natl. Acad. Sci. USA* **2002**, *99*, 10982–10987.

[136] Frenkel, J. On the Transformation of Light into Heat in Solids. I. *Phys. Rev.* **1931**, *37*, 17–44.

[137] Frenkel, J. On the Transformation of Light into Heat in Solids. II. *Phys. Rev.* **1931**, *37*, 1276–1294.

[138] Kasha, M. Energy Transfer Mechanisms and the Molecular Exciton Model for Molecular Aggregates. *Radiat. Res.* **1963**, *20*, 55–70.

[139] Kasha, M.; Rawls, H.; El-Bayoumi, M. The Exciton Model in Molecular Spectroscopy. *Pure Appl. Chem* **1965**, *11*, 371–392.

[140] Abe, S.; Yu, J.; Su, W. P. Singlet and Triplet Excitons in Conjugated Polymers. *Phys. Rev. B* **1992**, *45*, 8264–8271.

[141] Kaake, L. G.; Barbara, P. F.; Zhu, X.-Y. Intrinsic Charge Trapping in Organic and Polymeric Semiconductors: A Physical Chemistry Perspective. *J. Phys. Chem. Lett.* **2010**, *1*, 628–635.

[142] Busby, E.; Carroll, E. C.; Chinn, E. M.; Chang, L.; Moule, A. J., A. J.e; Larsen, D. S. Excited-State Self-Trapping and Ground-State Relaxation Dynamics in Poly(3-hexylthiophene) Resolved with Broadband Pump-Dump-Probe Spectroscopy. *J. Phys. Chem. Lett.* **2011**, *2*, 2764–2769.

[143] Barford, W.; Lidzey, D. G.; Makhov, D. V.; Meijer, A. J. H. Exciton Localization in Disordered Poly(3-hexylthiophene). *J. Chem. Phys.* **2010**, *133*, 044504.

[144] Makhov, D. V.; Barford, W. Local Exciton Ground States in Disordered Polymers. *Phys. Rev. B* **2010**, *81*, 165201.

[145] Barford, W.; Trembath, D. Exciton Localization in Polymers with Static Disorder. *Phys. Rev. B* **2009**, *80*, 165418.

[146] Knupfer, M. Exciton Binding Energies in Organic Semiconductors. *Appl. Phys. A* **2003**, *77*, 623–626.

[147] Arkhipov, V. I.; Emelianova, E. V.; Bässler, H. Hot Exciton Dissociation in a Conjugated Polymer. *Phys. Rev. Lett.* **1999**, *82*, 1321–1324.

[148] Haugeneder, A.; Neges, M.; Kallinger, C.; Spirkl, W.; Lemmer, U.; Feldmann, J.; Scherf, U.; Harth, E.; Gügel, A.; Müllen, K. Exciton Diffusion and Dissociation in Conjugated Polymer/Fullerene Blends and Heterostructures. *Phys. Rev. B* **1999**, *59*, 15346–15351.

[149] Holstein, T. Studies of Polaron Motion: Part I. The Molecular-Crystal Model. *Ann. Phys.* **1959**, *8*, 325–342.

[150] Holstein, T. Studies of Polaron Motion: Part II. The “Small” Polaron. *Ann. Phys.* **1959**, *8*, 343–389.

[151] Friedman, L.; Holstein, T. Studies of Polaron Motion: Part III. The Hall Mobility of the Small Polaron. *Ann. Phys.* **1963**, *21*, 494–549.

[152] Appel, J. In *Solid State Physics*; Frederick Seitz, D. T., Ehrenreich, H., Eds.; Academic Press, 1968; Vol. 21; pp 193–391.

[153] Emin, D.; Holstein, T. Studies of Small-Polaron Motion IV. Adiabatic Theory of the Hall Effect. *Ann. Phys.* **1969**, *53*, 439–520.

[154] Hwang, I.; Scholes, G. D. Electronic Energy Transfer and Quantum-Coherence in Conjugated Polymers. *Chem. Mater.* **2011**, *23*, 610–620.

[155] Forster, T. 10th Spiers Memorial Lecture. Transfer Mechanisms of Electronic Excitation. *Discuss. Faraday Soc.* **1959**, *27*, 7–17.

[156] *Compendium of Chemical Terminology*, 2nd ed.; International Union of Pure and Applied Chemistry, 2014.

[157] Song, Y.; Clafton, S. N.; Pensack, R. D.; Kee, T. W.; Scholes, G. D. Vibrational Coherence Probes the Mechanism of Ultrafast Electron Transfer in Polymer–Fullerene Blends. *Nat. Commun.* **2014**, *5*, 4933.

[158] Collini, E.; Scholes, G. D. Coherent Intrachain Energy Migration in a Conjugated Polymer at Room Temperature. *Science* **2009**, *323*, 369–373.

[159] Collini, E.; Scholes, G. D. Electronic and Vibrational Coherences in Resonance Energy Transfer along MEH-PPV Chains at Room Temperature. *J. Phys. Chem. A* **2009**, *113*, 4223–4241.

[160] Barford, W.; Bittner, E. R.; Ward, A. Exciton Dynamics in Disordered Poly(p-phenylenevinylene). 2. Exciton Diffusion. *J. Phys. Chem. A* **2012**, *116*, 10319–10327.

[161] Beljonne, D.; Hennebicq, E.; Daniel, C.; Herz, L. M.; Silva, C.; Scholes, G. D.; Hoeben, F. J. M.; Jonkheijm, P.; Schenning, A. P. H. J.; Meskers, S. C. J.; Phillips, R. T.; Friend, R. H.; Meijer, E. W. Excitation Migration along Oligophenylenevinylene-Based Chiral Stacks: Delocalization Effects on Transport Dynamics. *J. Phys. Chem. B* **2005**, *109*, 10594–10604.

[162] Beenken, W. J. D.; onu Pullerits, T. Excitonic Coupling in Polythiophenes: Comparison of Different Calculation Methods. *J. Chem. Phys.* **2004**, *120*, 2490–2495.

[163] Hennebicq, E.; Pourtois, G.; Scholes, G. D.; Herz, L. M.; Russell, D. M.; Silva, C.; Setayesh, S.; Grimsdale, A. C.; Müllen, K.; Brédas, J.-L.; Beljonne, D. Exciton Migration in Rigid-Rod Conjugated Polymers: An Improved Förster Model. *J. Am. Chem. Soc.* **2005**, *127*, 4744–4762.

[164] Barford, W. Exciton Transfer Integrals Between Polymer Chains. *J. Chem. Phys.* **2007**, *126*, 134905.

[165] Dexter, D. L. A Theory of Sensitized Luminescence in Solids. *J. Chem. Phys.* **1953**, *21*, 836–850.

[166] Swenberg, C. E.; Geacintov, N. E. In *Organic Molecular Photophysics*; Birks, J. B., Ed.; Wiley & Sons, Bristol, 1973; Chapter 10, pp 481–564.

[167] Sanders, S. N.; Kumarasamy, E.; Pun, A. B.; Trinh, M. T.; Choi, B.; Xia, J.; Taffet, E. J.; Low, J. Z.; Miller, J. R.; Roy, X.; Zhu, X.-Y.; Steigerwald, M. L.;

Sfeir, M. Y.; Campos, L. M. Quantitative Intramolecular Singlet Fission in Bipentacenes. *J. Am. Chem. Soc.* **2015**, *137*, 8965–8972.

[168] Singh-Rachford, T. N.; Castellano, F. N. Low Power Visible-to-UV Upconversion. *J. Phys. Chem. A* **2009**, *113*, 5912–5917.

[169] Singh-Rachford, T. N.; Castellano, F. N. Triplet Sensitized Red-to-Blue Photon Upconversion. *J. Phys. Chem. Lett.* **2010**, *1*, 195–200.

[170] Wu, W.; Guo, H.; Wu, W.; Ji, S.; Zhao, J. Organic Triplet Sensitizer Library Derived from a Single Chromophore (BODIPY) with Long-Lived Triplet Excited State for Triplet–Triplet Annihilation Based Upconversion. *J. Org. Chem.* **2011**, *76*, 7056–7064.

[171] Gray, V.; Dzebo, D.; Abrahamsson, M.; Albinsson, B.; Moth-Poulsen, K. Triplet-triplet Annihilation Photon-upconversion: Towards Solar Energy Applications. *Phys. Chem. Chem. Phys.* **2014**, *16*, 10345–10352.

[172] Kido, J.; Iizumi, Y. Fabrication of Highly Efficient Organic Electroluminescent Devices. *Appl. Phys. Lett.* **1998**, *73*, 2721–2723.

[173] Tokito, S.; Iijima, T.; Suzuri, Y.; Kita, H.; Tsuzuki, T.; Sato, F. Confinement of Triplet Energy on Phosphorescent Molecules for Highly-Efficient Organic Blue-Light-Emitting Devices. *Appl. Phys. Lett.* **2003**, *83*, 569–571.

[174] Yersin, H.; Rausch, A. F.; Czerwieniec, R.; Hofbeck, T.; Fischer, T. The Triplet State of Organo-transition Metal Compounds. Triplet Harvesting and Singlet Harvesting for Efficient OLEDs. *Coord. Chem. Rev.* **2011**, *255*, 2622–2652.

[175] Bai, J.; Chen, P.; Lei, Y.; Zhang, Y.; Zhang, Q.; Xiong, Z.; Li, F. Studying Singlet Fission and Triplet Fusion by Magneto-Electroluminescence Method in Singlet–Triplet Energy-Resonant Organic Light-Emitting Diodes. *Org. Electron.* **2014**, *15*, 169–174.

[176] Congreve, D. N.; Lee, J.; Thompson, N. J.; Hontz, E.; Yost, S. R.; Reusswig, P. D.; Bahlke, M. E.; Reineke, S.; Van Voorhis, T.; Baldo, M. A. External Quantum Efficiency Above 100% in a Singlet-Exciton-Fission-Based Organic Photovoltaic Cell. *Science* **2013**, *340*, 334–337.

[177] Bielecka, U.; Janus, K.; Bartkowiak, W. Nanoaggregation of P3HT in Chloroform Anisole Solution: Relationship Between Morphology and Electrical Properties. *Proc. SPIE* **2014**, *9185*, 91850E–91850E–7.

[178] Clafton, S. N.; Beattie, D. A.; Mierczynska-Vasilev, A.; Acres, R. G.; Morgan, A. C.; Kee, T. W. Chemical Defects in the Highly Fluorescent Conjugated Polymer Dots. *Langmuir* **2010**, *26*, 17785–17789.

[179] Hu, Z.; Tenery, D.; Bonner, M. S.; Gesquiere, A. J. Correlation Between Spectroscopic and Morphological Properties of Composite P3HT/PCBM Nanoparticles Studied by Single Particle Spectroscopy. *J. Lumin.* **2010**, *130*, 771–780.

[180] Clafton, S. N.; Huang, D. M.; Massey, W. R.; Kee, T. W. Femtosecond Dynamics of Excitons and Hole-Polarons in Composite P3HT/PCBM Nanoparticles. *J. Phys. Chem. B* **2013**, *117*, 4626–4633.

[181] Moulé, A. J.; Bonekamp, J. B.; Meerholz, K. The Effect of Active Layer Thickness and Composition on the Performance of Bulk-Heterojunction Solar Cells. *J. Appl.*

Phys. **2006**, *100*, 094503.

[182] Bagui, A.; Iyer, S. Effect of Solvent Annealing in the Presence of Electric Field on P3HT:PCBM Films Used in Organic Solar Cells. *IEEE Trans. Electron Devices* **2011**, *58*, 4061–4066.

[183] Kniepert, J.; Lange, I.; van der Kaap, N. J.; Koster, L. J. A.; Neher, D. A Conclusive View on Charge Generation, Recombination, and Extraction in As-Prepared and Annealed P3HT:PCBM Blends: Combined Experimental and Simulation Work. *Adv. Energy Mater.* **2014**, *4*, 1301401.

[184] Peet, J.; Kim, J. Y.; Coates, N. E.; Ma, W. L.; Moses, D.; Heeger, A. J.; Bazan, G. C. Efficiency Enhancement in Low-Bandgap Polymer Solar Cells by Processing with Alkane Dithiols. *Nat. Mater.* **2007**, *6*, 497–500.

[185] Lee, J. K.; Ma, W. L.; Brabec, C. J.; Yuen, J.; Moon, J. S.; Kim, J. Y.; Lee, K.; Bazan, G. C.; Heeger, A. J. Processing Additives for Improved Efficiency from Bulk Heterojunction Solar Cells. *J. Am. Chem. Soc.* **2008**, *130*, 3619–3623.

[186] Vanlaeke, P.; Swinnen, A.; Haeldermans, I.; Vanhoyland, G.; Aernouts, T.; Cheyns, D.; Deibel, C.; DaHaen, J.; Heremans, P.; Poortmans, J.; Manca, J. P3HT/PCBM Bulk Heterojunction Solar Cells: Relation Between Morphology and Electro-Optical Characteristics. *Sol. Energ. Mat. Sol. Cells* **2006**, *90*, 2150–2158.

[187] Adachi, T.; Lakhwani, G.; Traub, M. C.; Ono, R. J.; Bielawski, C. W.; Barbara, P. F.; Vanden Bout, D. A. Conformational Effect on Energy Transfer in Single Polythiophene Chains. *J. Phys. Chem. B* **2012**, *116*, 9866–9872.

[188] Chen, K.; Barker, A. J.; Reish, M. E.; Gordon, K. C.; Hodgkiss, J. M. Broadband Ultrafast Photoluminescence Spectroscopy Resolves Charge Photogeneration via Delocalized Hot Excitons in Polymer:Fullerene Photovoltaic Blends. *J. Am. Chem. Soc.* **2013**, *135*, 18502–18512.

[189] Spano, F. C. Temperature Dependent Exciton Emission from Herringbone Aggregates of Conjugated Oligomers. *J. Chem. Phys.* **2004**, *120*, 7643–7658.

[190] Spano, F. C. Modeling Disorder in Polymer Aggregates: The Optical Spectroscopy of Regioregular Poly(3-hexylthiophene) Thin Films. *J. Chem. Phys.* **2005**, *122*, 234701.

[191] Spano, F. C. Absorption in Regio-Regular Poly(3-hexylthiophene) Thin Films: Fermi Resonances, Interband Coupling and Disorder. *J. Chem. Phys.* **2006**, *325*, 22–35.

[192] Yamagata, H.; Spano, F. C. Interplay Between Intrachain and Interchain Interactions in Semiconducting Polymer Assemblies: The HJ-Aggregate Model. *J. Chem. Phys.* **2012**, *136*, 184901.

[193] Martin, T. P.; Wise, A. J.; Busby, E.; Gao, J.; Roehling, J. D.; Ford, M. J.; Larsen, D. S.; Moulé, A. J.; Grey, J. K. Packing Dependent Electronic Coupling in Single Poly(3-hexylthiophene) H- and J-Aggregate Nanofibers. *J. Phys. Chem. B* **2012**, *117*, 4478–4487.

[194] Niles, E. T.; Roehling, J. D.; Yamagata, H.; Wise, A. J.; Spano, F. C.; Moulé, A. J.; Grey, J. K. J-Aggregate Behavior in Poly(3-hexylthiophene) Nano-

fibers. *J. Phys. Chem. Lett.* **2012**, *3*, 259–263.

[195] Baghgar, M.; Labastide, J. A.; Bokel, F.; Hayward, R. C.; Barnes, M. D. Effect of Polymer Chain Folding on the Transition from H- to J-Aggregate Behavior in P3HT Nanofibers. *J. Phys. Chem. C* **2014**, *118*, 2229–2235.

[196] Mu, H.; Shen, H.; Klotzkin, D. Dependence of Film Morphology on Deposition Rate in ITO/TPD/Alq_3/Al Organic Luminescent Diodes. *Solid-State Electron.* **2004**, *48*, 2085–2088.

[197] Tak, Y.-H.; Kim, K.-B.; Park, H.-G.; Lee, K.-H.; Lee, J.-R. Criteria for ITO (Indium Tin Oxide) Thin Film as the Bottom Electrode of an Organic Light Emitting Diode. *Thin Solid Films* **2002**, *411*, 12–16.

[198] Chen, S.-Y.; Chu, T.-Y.; Chen, J.-F.; Su, C.-Y.; Chen, C. H. Stable Inverted Bottom-emitting Organic Electroluminescent Devices with Molecular Doping and Morphology Improvement. *Appl. Phys. Lett.* **2006**, *89*, 053518.

[199] Thomschke, M.; Hofmann, S.; Olthof, S.; Anderson, M.; Kleemann, H.; Schober, M.; Lüssem, B.; Leo, K. Improvement of Voltage and Charge Balance in Inverted Top-Emitting Organic Electroluminescent Diodes Comprising Doped Transport Layers by Thermal Annealing. *Appl. Phys. Lett.* **2011**, *98*, 083304.

[200] Dillon, R. J.; Piland, G. B.; Bardeen, C. J. B. Different Rates of Singlet Fission in Monoclinic versus Orthorhombic Crystal Forms of Diphenylhexatriene. *J. Am. Chem. Soc.* **2013**, *135*, 17278–17281.

[201] Zirzlmeier, J.; Lehnherr, D.; Coto, P. B.; Chernick, E. T.; Casillas, R.; Basel, B. S.; Thoss, M.; Tykwinski, R. R.; Guldi, D. M. Singlet Fission in Pentacene Dimers. *Proc. Natl. Acad. Sci. USA* **2015**, *112*, 5325–5330.

[202] Lukman, S.; Musser, A. J.; Chen, K.; Athanasopoulos, S.; Yong, C. K.; Zeng, Z.; Ye, Q.; Chi, C.; Hodgkiss, J. M.; Wu, J.; Friend, R. H.; Greenham, N. C. Tuneable Singlet Exciton Fission and Triplet–Triplet Annihilation in an Orthogonal Pentacene Dimer. *Adv. Funct. Mater.* **2015**, *25*, 5452–5461.

[203] Merrifield, R. E. Theory of Magnetic Field Effects on the Mutual Annihilation of Triplet Excitons. *J. Chem. Phys.* **1968**, *48*, 4318–4319.

[204] Johnson, R. C.; Merrifield, R. E. Effects of Magnetic Fields on the Mutual Annihilation of Triplet Excitons in Anthracene Crystals. *Phys. Rev. B* **1970**, *1*, 896–902.

[205] Merrifield, R. Magnetic Effects on Triplet Exciton Interactions. *Pure Appl. Chem.* **1971**, *27*, 481–498.

[206] Islangulov, R. R.; Kozlov, D. V.; Castellano, F. N. Low Power Upconversion Using MLCT Sensitizers. *Chem. Commun.* **2005**, 3776–3778.

[207] Singh-Rachford, T. N.; Castellano, F. N. Supra-Nanosecond Dynamics of a Red-to-Blue Photon Upconversion System. *Inorg. Chem.* **2009**, *48*, 2541–2548.

[208] Singh-Rachford, T. N.; Castellano, F. N. Photon Upconversion Based on Sensitized Triplet–Triplet Annihilation. *Coord. Chem. Rev.* **2010**, *254*, 2560–2573.

[209] Mani, T.; Vinogradov, S. A. Magnetic Field Effects on Triplet–Triplet Annihilation in Solutions: Modulation of Visible/NIR Luminescence. *J. Phys. Chem.*

Lett. **2013**, *4*, 2799–2804.

[210] Marcel, A.; vandeVen Martin,; Ulises, A. n. A.; Bernard, V. Fluorescence Anisotropy Measurements in Solution: Methods and Reference Materials. *Pure Appl. Chem.* **2013**, *85*, 589–608.

[211] Duffy, E.; Kowalczyk, P.; Jorgensen, W. Do Denaturants Interact with Aromatic Hydrocarbons in Water? *J. Am. Chem. Soc.* **1993**, *115*, 9271–9275.

[212] Jorgensen, W.; Maxwell, D.; TiradoRives, J. Development and Testing of the OPLS All-Atom Force Field on Conformational Energetics and Properties of Organic Liquids. *J. Am. Chem. Soc.* **1996**, *118*, 11225–11236.

[213] Rizzo, R.; Jorgensen, W. OPLS All-Atom Model for Amines: Resolution of the Amine Hydration Problem. *J. Am. Chem. Soc.* **1999**, *121*, 4827–4836.

[214] Price, M.; Ostrovsky, D.; Jorgensen, W. Gas-Phase and Liquid-State Properties of Esters, Nitriles, and Nitro Compounds with the OPLS-AA Force Field. *J. Comput. Chem.* **2001**, *22*, 1340–1352.

[215] Jorgensen, W.; McDonald, N. Development of an All-Atom Force Field for Geterocycles. Properties of Liquid Pyridine and Diazenes. *J. Mol. Struct.* **1998**, *424*, 145–155.

[216] Dahlgren, M. K.; Schyman, P.; Tirado-Rives, J.; Jorgensen, W. L. Characterization of Biaryl Torsional Energetics and its Treatment in OPLS All-Atom Force Fields. *J. Chem. Inf. Model.* **2013**, *53*, 1191–1199.

[217] Schwarz, K. N.; Kee, T. W.; Huang, D. M. Coarse-Grained Simulations of the Solution-Phase Self-Assembly of Poly(3-hexylthiophene) Nanostructures. *Nanoscale* **2013**, *5*, 2017–2027.

[218] Huang, L.; Liao, Q.; Shi, Q.; Fu, H.; Ma, J.; Yao, J. Rubrene Micro-Crystals from Solution Routes: Their Crystallography, Morphology and Optical Properties. *J. Mater. Chem.* **2010**, *20*, 159–166.

[219] Avakian, P. Influence of Magnetic Fields on Luminescence Involving Triplet Excitons. *Pure Appl. Chem.* **1974**, *37*, 1–19.

[220] Brabec, C.; Sariciftci, N.; Hummelen, J. Plastic Solar Cells. *Adv. Funct. Mater.* **2001**, *11*, 15–26.

[221] Li, G.; Shrotriya, V.; Huang, J.; Yao, Y.; Moriarty, T.; Emery, K.; Yang, Y. High-Efficiency Solution Processable Polymer Photovoltaic Cells by Self-Organization of Polymer Blends. *Nat. Mater.* **2005**, *4*, 864–868.

[222] Guenes, S.; Neugebauer, H.; Sariciftci, N. S. Conjugated Polymer-Based Organic Solar Cells. *Chem. Rev.* **2007**, *107*, 1324–1338.

[223] Thompson, B. C.; Fréchet, J. M. J. Organic Photovoltaics — Polymer-Fullerene Composite Solar Cells. *Angew. Chem., Int. Ed.* **2008**, *47*, 58–77.

[224] Spano, F. C. The Spectral Signatures of Frenkel Polarons in H- and J-Aggregates. *Acc. Chem. Res.* **2009**, *43*, 429–439.

[225] Kim, J. S.; Lee, J. H.; Park, J. H.; Shim, C.; Sim, M.; Cho, K. High-Efficiency Organic Solar Cells Based on Preformed Poly(3-hexylthiophene) Nanowires. *Adv. Funct. Mater.* **2011**, *21*, 480–486.

[226] Li, H.; Li, J.; Xu, Q.; Hu, X. Poly(3-hexylthiophene)/TiO_2 Nanoparticle-Functionalized Electrodes for Visible Light and Low Potential Photoelectrochemical Sensing of Organophosphorus Pesticide Chlopyrifos. *Anal. Chem.* **2011**, *83*, 9681–9686.

[227] Hu, Z.; Gesquiere, A. J. Charge Trapping and Storage by Composite P3HT/$PC_{60}BM$ Nanoparticles Investigated by Fluorescence-Voltage/Single Particle Spectroscopy. *J. Am. Chem. Soc.* **2011**, *133*, 20850–20856.

[228] Lee, S.-H.; Kim, D.-H.; Kim, J.-H.; Lee, G.-S.; Park, J.-G. Effect of Metal-Reflection and Surface-Roughness Properties on Power-Conversion Efficiency for Polymer Photovoltaic Cells. *J. Phys. Chem. C* **2009**, *113*, 21915–21920.

[229] Lee, S.-H.; Kim, J.-H.; Shim, T.-H.; Park, J.-G. Effect of Interface Thickness on Power Conversion Efficiency of Polymer Photovoltaic Cells. *Electron. Mater. Lett.* **2009**, *5*, 47–50.

[230] Marsh, R. A.; Hodgkiss, J. M.; Albert-Seifried, S.; Friend, R. H. Effect of Annealing on P3HT:PCBM Charge Transfer and Nanoscale Morphology Probed by Ultrafast Spectroscopy. *Nano Lett.* **2010**, *10*, 923–930.

[231] Kirkpatrick, J.; Keivanidis, P. E.; Bruno, A.; Ma, F.; Haque, S. A.; Yarstev, A.; Sundstrom, V.; Nelson, J. Ultrafast Transient Optical Studies of Charge Pair Generation and Recombination in Poly(3-hexylthiophene) (P3HT):[6,6]Phenyl C_{61} Butyric Methyl Acid Ester (PCBM) Blend Films. *J. Phys. Chem. B* **2011**, *115*, 15174–15180.

[232] Banerji, N.; Cowan, S.; Vauthey, E.; Heeger, A. J. Ultrafast Relaxation of the Poly(3-hexylthiophene) Emission Spectrum. *J. Phys. Chem. C* **2011**, *115*, 9726–9739.

[233] Ferreira, B.; da Silva, P. F.; Seixas de Melo, J. S.; Pina, J.; Maçanita, A. Excited-State Dynamics and Self-Organization of Poly(3-hexylthiophene) (P3HT) in Solution and Thin Films. *J. Phys. Chem. B* **2012**, *116*, 2347–2355.

[234] Wells, N. P.; Boudouris, B. W.; Hillmyer, M. A.; Blank, D. A. Intramolecular Exciton Relaxation and Migration Dynamics in Poly(3-hexylthiophene). *J. Phys. Chem. C* **2007**, *111*, 15404–15414.

[235] Cook, S.; Furube, A.; Katoh, R. Analysis of the Excited States of Regioregular Polythiophene P3HT. *Energ. Environ. Sci.* **2008**, *1*, 294–299.

[236] Parkinson, P.; Muller, C.; Stingelin, N.; Johnston, M. B.; Herz, L. M. Role of Ultrafast Torsional Relaxation in the Emission from Polythiophene Aggregates. *J. Phys. Chem. Lett.* **2010**, *1*, 2788–2792.

[237] Wells, N. P.; Blank, D. A. Correlated Exciton Relaxation in Poly(3-hexylthiophene). *Phys. Rev. Lett.* **2008**, *100*, 086403.

[238] Guo, J.; Ohkita, H.; Yokoya, S.; Benten, H.; Ito, S. Bimodal Polarons and Hole Transport in Poly(3-hexylthiophene):Fullerene Blend Films. *J. Am. Chem. Soc.* **2010**, *132*, 9631–9637.

[239] Grancini, G.; Maiuri, M.; Fazzi, D.; Petrozza, A.; Egelhaaf, H.-J.; Brida, D.; Cerullo, G.; Lanzani, G. Hot Exciton Dissociation in Polymer Solar Cells. *Nat. Mater.* **2013**, *12*, 29–33.

[240] Gélinas, S.; Rao, A.; Kumar, A.; Smith, S. L.; Chin, A. W.; Clark, J.; van der Poll, T. S.; Bazan, G. C.; Friend, R. H. Ultrafast Long-Range Charge Separation in Organic Semiconductor Photovoltaic Diodes. *Science* **2014**, *343*, 512–516.

[241] Kaake, L. G.; Moses, D.; Heeger, A. J. Coherence and Uncertainty in Nanostructured Organic Photovoltaics. *J. Phys. Chem. Lett.* **2013**, *4*, 2264–2268.

[242] Clark, J.; Nelson, T.; Tretiak, S.; Cirmi, G.; Lanzani, G. Femtosecond Torsional Relaxation. *Nat. Phys.* **2012**, *8*, 225–231.

[243] Bakulin, A. A.; Rao, A.; Pavelyev, V. G.; van Loosdrecht, P. H. M.; Pshenichnikov, M. S.; Niedzialek, D.; Cornil, J.; Beljonne, D.; Friend, R. H. The Role of Driving Energy and Delocalized States for Charge Separation in Organic Semiconductors. *Science* **2012**, *335*, 1340–1344.

[244] Gadermaier, C.; Cerullo, G.; Sansone, G.; Leising, G.; Scherf, U.; Lanzani, G. Time-Resolved Charge Carrier Generation from Higher Lying Excited States in Conjugated Polymers. *Phys. Rev. Lett.* **2002**, *89*, 117402.

[245] Kraabel, B.; Moses, D.; Heeger, A. J. Direct Observation of the Intersystem Crossing in Poly(3-octylthiophene). *J. Chem. Phys.* **1995**, *103*, 5102–5108.

[246] Guo, J.; Ohkita, H.; Benten, H.; Ito, S. Near-IR Femtosecond Transient Absorption Spectroscopy of Ultrafast Polaron and Triplet Exciton Formation in Polythiophene Films with Different Regioregularities. *J. Am. Chem. Soc.* **2009**, *131*, 16869–16880.

[247] Westenhoff, S.; Beenken, W. J. D.; Yartsev, A.; Greenham, N. C. Conformational Disorder of Conjugated Polymers. *J. Chem. Phys.* **2006**, *125*, 154903.

[248] Yu, W.; Zhou, J.; Bragg, A. E. Exciton Conformational Dynamics of Poly(3-hexylthiophene) (P3HT) in Solution from Time-Resolved Resonant-Raman Spectroscopy. *J. Phys. Chem. Lett.* **2012**, *3*, 1321–1328.

[249] Trotzky, S.; Hoyer, T.; Tuszynski, W.; Lienau, C.; Paris, J. Femtosecond Upconversion Technique for Probing the Charge Transfer in a P3HT:PCBM Blend via Photoluminescence Quenching. *J. Phys. D: Appl. Phys.* **2009**, *42*, 055105.

[250] Gao, B.-R.; Wang, H.-Y.; Wang, H.; Yang, Z.-Y.; Wang, L.; Jiang, Y.; Hao, Y.-W.; Chen, Q.-D.; Sun, H.-B. Investigation of Polaron Pair Dynamics in Poly(3-hexylthiophene) Film by Time Resolved Spectroscopy. *IEEE J. Quantum. Electron.* **2012**, *48*, 425–432.

[251] Stagira, S.; Nisoli, M.; Lanzani, G.; De Silvestri, S.; Cassano, T.; Tommasi, R.; Babudri, F.; Farinola, G. M.; Naso, F. Intrachain Charge Generation and Recombination in Alkoxy-Substituted Poly-(*p*-phenylenevinylene) Films. *Phys. Rev. B* **2001**, *64*, 205205.

[252] Harrison, M. G.; Grüner, J.; Spencer, G. C. W. Analysis of the Photocurrent Action Spectra of MEH-PPV Polymer Photodiodes. *Phys. Rev. B* **1997**, *55*, 7831–7849.

[253] Hendry, E.; Koeberg, M.; Schins, J. M.; Siebbeles, L. D. A.; Bonn, M. Ultrafast Charge Generation in a Semiconducting Polymer Studied with THz Emission Spectroscopy. *Phys. Rev. B* **2004**, *70*, 033202.

[254] Miranda, P. B.; Moses, D.; Heeger, A. J. Ultrafast Photogeneration of Charged

Polarons in Conjugated Polymers. *Phys. Rev. B* **2001**, *64*, 081201.

[255] Moses, D.; Dogariu, A.; Heeger, A. J. Ultrafast Photoinduced Charge Generation in Conjugated Polymers. *Chem. Phys. Lett.* **2000**, *316*, 356–360.

[256] Moore, E. E.; Yaron, D. An Explicit-Solvent Dynamic-Dielectric Screening Model of Electron-Hole Interactions in Conjugated Polymers. *J. Chem. Phys.* **1998**, *109*, 6147–6156.

[257] van der Horst, J.-W.; Bobbert, P. A.; de Jong, P. H. L.; Michels, M. A. J.; Brocks, G.; Kelly, P. J. Ab Initio Prediction of the Electronic and Optical Excitations in Polythiophene: Isolated Chains Versus Bulk Polymer. *Phys. Rev. B* **2000**, *61*, 15817–15826.

[258] Barford, W.; Bursill, R. J.; Yaron, D. Dynamical Model of the Dielectric Screening of Conjugated Polymers. *Phys. Rev. B* **2004**, *69*, 155203.

[259] Deibel, C.; Mack, D.; Gorenflot, J.; Schöll, A.; Krause, S.; Reinert, F.; Rauh, D.; Dyakonov, V. Energetics of Excited States in the Conjugated Polymer Poly(3-hexylthiophene). *Phys. Rev. B* **2010**, *81*, 085202.

[260] Takeda, N.; Asaoka, S.; Miller, J. R. Nature and Energies of Electrons and Holes in a Conjugated Polymer, Polyfluorene. *J. Am. Chem. Soc.* **2006**, *128*, 16073–16082.

[261] Jimenez, R.; Fleming, G. R.; Kumar, P. V.; Maroncelli, M. Femtosecond Solvation Dynamics of Water. *Nature* **1994**, *369*, 471–473.

[262] Stratt, R. M.; Cho, M. The Short-Time Dynamics of Solvation. *J. Chem. Phys.* **1994**, *100*, 6700–6708.

[263] Rosenthal, S. J.; Xie, X.; Du, M.; Fleming, G. R. Femtosecond Solvation Dynamics in Acetonitrile: Observation of the Inertial Contribution to the Solvent Response. *J. Chem. Phys.* **1991**, *95*, 4715–4718.

[264] Labastide, J. A.; Baghgar, M.; McKenna, A.; Barnes, M. D. Time- and Polarization-Resolved Photoluminescence Decay from Isolated Polythiophene (P3HT) Nanofibers. *J. Phys. Chem. C* **2012**, *116*, 23803–23811.

[265] Andersson, P. O.; Gillbro, T. Photophysics and Dynamics of the Lowest Excited Singlet State in Long Substituted Polyenes with Implications to the Very Long-Chain Limit. *J. Chem. Phys.* **1995**, *103*, 2509–2519.

[266] Perepichka, I.; Perepichka, D.; Meng, H.; Wudl, F. Light-Emitting Polythiophenes. *Adv. Mater.* **2005**, *17*, 2281–2305.

[267] Mulligan, C. J.; Bilen, C.; Zhou, X.; Belcher, W. J.; Dastoor, P. C. Levelised Cost of Electricity for Organic Photovoltaics. *Sol. Energ. Mat. Sol. Cells* **2015**, *133*, 26–31.

[268] Pivrikas, A.; Neugebauer, H.; Sariciftci, N. S. Influence of Processing Additives to Nano-Morphology and Efficiency of Bulk-Heterojunction Solar Cells: A Comparative Review. *Sol. Energ.* **2011**, *85*, 1226–1237.

[269] Beljonne, D.; Cornil, J.; Muccioli, L.; Zannoni, C.; Brédas, J.-L.; Castet, F. Electronic Processes at Organic–Organic Interfaces: Insight from Modeling and Implications for Opto-electronic Devices. *Chem. Mater.* **2011**, *23*, 591–609.

[270] Darling, S. B. Isolating the Effect of Torsional Defects on Mobility and Band Gap in Conjugated Polymers. *J. Phys. Chem. B* **2008**, *112*, 8891–8895.

[271] Dykstra, T. E.; Hennebicq, E.; Beljonne, D.; Gierschner, J.; Claudio, G.; Bittner, E. R.; Knoester, J.; Scholes, G. D. Conformational Disorder and Ultrafast Exciton Relaxation in PPV–Family Conjugated Polymers. *J. Phys. Chem. B* **2009**, *113*, 656–667.

[272] Singh, J.; Bittner, E. R.; Beljonne, D.; Scholes, G. D. Fluorescence Depolarization in Poly[2-methoxy-5-((2-ethylhexyl)oxy)-1,4-phenylenevinylene]: Sites Versus Eigenstates Hopping. *J. Chem. Phys.* **2009**, *131*, 194905.

[273] Cheung, D. L.; McMahon, D. P.; Troisi, A. A Realistic Description of the Charge Carrier Wave Function in Microcrystalline Polymer Semiconductors. *J. Am. Chem. Soc.* **2009**, *131*, 11179–11186.

[274] Munoz-Losa, A.; Curutchet, C.; Galvan, I. F.; Mennucci, B. Quantum Mechanical Methods Applied to Excitation Energy Transfer: A Comparative Analysis on Excitation Energies and Electronic Couplings. *J. Chem. Phys.* **2008**, *129*, 034104.

[275] Rühle, V.; Lukyanov, A.; May, F.; Schrader, M.; Vehoff, T.; Kirkpatrick, J.; Baumeier, B.; Andrienko, D. Microscopic Simulations of Charge Transport in Disordered Organic Semiconductors. *J. Chem. Theory Comput.* **2011**, *7*, 3335–3345.

[276] Denis, J.-C.; Schumacher, S.; Galbraith, I. Quantitative Description of Interactions Between Linear Organic Chromophores. *J. Chem. Phys.* **2012**, *137*, 224102.

[277] Groves, C. Developing Understanding of Organic Photovoltaic Devices: Kinetic Monte Carlo Models of Geminate and Non-Geminate Recombination, Charge Transport and Charge Extraction. *Energy Environ. Sci.* **2013**, *6*, 3202–3217.

[278] Kordt, P.; Stenzel, O.; Baumeier, B.; Schmidt, V.; Andrienko, D. Parametrization of Extended Gaussian Disorder Models from Microscopic Charge Transport Simulations. *J. Chem. Theory Comput.* **2014**, *10*, 2508–2513.

[279] Noriega, R.; Salleo, A.; Spakowitz, A. J. Chain Conformations Dictate Multiscale Charge Transport Phenomena in Disordered Semiconducting Polymers. *Proc. Natl. Acad. Sci. USA* **2013**, *110*, 16315–16320.

[280] Bittner, E. R.; Silva, C. Noise-Induced Quantum Coherence Drives Photo-Carrier Generation Dynamics at Polymeric Semiconductor Heterojunctions. *Nat. Commun.* **2014**, *5*, 3119.

[281] Maturová, K.; van Bavel, S. S.; Wienk, M. M.; Janssen, R. J.; Kemerink, M. Description of the Morphology Dependent Charge Transport and Performance of Polymer:Fullerene Bulk Heterojunction Solar Cells. *Adv. Funct. Mater.* **2011**, *21*, 261–269.

[282] Nam, Y. M.; Huh, J.; Ho Jo, W. Optimization of Thickness and Morphology of Active Layer for High Performance of Bulk-Heterojunction Organic Solar Cells. *Sol. Energy Mater. Sol. Cells* **2010**, *94*, 1118–1124.

[283] Grage, M. M.-L.; Zaushitsyn, Y.; Yartsev, A.; Chachisvilis, M.; Sundström, V.; Pullerits, T. o. Ultrafast Excitation Transfer and Trapping in a Thin Polymer Film. *Phys. Rev. B* **2003**, *67*, 205207.

[284] Westenhoff, S.; Daniel, C.; Friend, R. H.; Silva, C.; Sundstrom, V.; Yartsev, A. Exciton Migration in a Polythiophene: Probing the Spatial and Energy Domain by Line-Dipole Förster-Type Energy Transfer. *J. Chem. Phys.* **2005**, *122*, 094903.

[285] Tozer, O. R.; Barford, W. Exciton Dynamics in Disordered Poly(p-phenylenevinylene). 1. Ultrafast Interconversion and Dynamical Localization. *J. Phys. Chem. A* **2012**, *116*, 10310–10318.

[286] Carbone, P.; Troisi, A. Charge Diffusion in Semiconducting Polymers: Analytical Relation between Polymer Rigidity and Time Scales for Intrachain and Interchain Hopping. *J. Phys. Chem. Lett.* **2014**, *5*, 2637–2641.

[287] Onoda, M.; Tada, K.; Zakhidov, A.; Yoshino, K. Photoinduced Charge Separation in Photovoltaic Cell with Heterojunction of p- and n-Type Conjugated Polymers. *Thin Solid Films* **1998**, *331*, 76–81.

[288] Ihn, K. J.; Moulton, J.; Smith, P. Whiskers of Poly(3-alkylthiophene)s. *J. Polym. Sci. B Polym. Phys.* **1993**, *31*, 735–742.

[289] Chernyak, V.; Poliakov, E. Y.; Tretiak, S.; Mukamel, S. Two-Exciton States and Spectroscopy of Phenylacetylene Dendrimers. *J. Chem. Phys.* **1999**, *111*, 4158–4168.

[290] Avgin, I.; Huber, D. Excitons in Disordered Polymers. *J. Lumin.* **2007**, *122–123*, 389–392.

[291] Malyshev, A. V.; Malyshev, V. A. Statistics of Low Energy Levels of a One-Dimensional Weakly Localized Frenkel Exciton: A Numerical Study. *Phys. Rev. B* **2001**, *63*, 195111.

[292] Barford, W.; Boczarow, I.; Wharram, T. Ultrafast Dynamical Localization of Photoexcited States in Conformationally Disordered Poly(p-phenylenevinylene). *J. Phys. Chem. A* **2011**, *115*, 9111–9119.

[293] King, S.; Vaughan, H.; Monkman, A. Orientation of Triplet and Singlet Transition Dipole Moments in Polyfluorene, Studied by Polarised Spectroscopies. *Chem. Phys. Lett.* **2007**, *440*, 268–272.

[294] Köse, M. E. Evaluation of Excitonic Coupling and Charge Transport Integrals in P3HT Nanocrystal. *J. Phys. Chem. C* **2011**, *115*, 13076–13082.

[295] Gierschner, J.; Mack, H.-G.; Lüer, L.; Oelkrug, D. Fluorescence and Absorption Spectra of Oligophenylenevinylenes: Vibronic Coupling, Band Shapes, and Solvatochromism. *J. Chem. Phys.* **2002**, *116*, 8596–8609.

[296] Scholes, G. D. Long-Range Resonance Energy Transfer In Molecular Systems. *Annu. Rev. Phys. Chem.* **2003**, *54*, 57–87.

[297] Morfa, A. J.; Barnes, T. M.; Ferguson, A. J.; Levi, D. H.; Rumbles, G.; Rowlen, K. L.; van de Lagemaat, J. Optical Characterization of Pristine Poly(3-hexylthiophene) Films. *J. Polym. Sci. B Polym. Phys.* **2011**, *49*, 186–194.

[298] Englman, R.; Jortner, J. The Energy Gap Law for Radiationless Transitions in Large Molecules. *Mol. Phys.* **1970**, *18*, 145–164.

[299] Dimitrov, S. D.; Schroeder, B. C.; Nielsen, C. B.; Bronstein, H.; Fei, Z.; McCulloch, I.; Heeney, M.; Durrant, J. R. Singlet Exciton Lifetimes in Conjugated

Polymer Films for Organic Solar Cells. *Polymers* **2016**, *8*, 14.

[300] Linton, J.; Frank, C.; Rughooputh, S. Fluorescence Studies of Poly(3-hexylthiophene) Solutions. *Synth. Met.* **1989**, *28*, 393–398.

[301] Albert-Seifried, S.; Ko, D.-H.; Huttner, S.; Kanimozhi, C.; Patil, S.; Friend, R. H. Efficiency Limitations in a Low Band-gap Diketopyrrolopyrrole-Based Polymer Solar Cell. *Phys. Chem. Chem. Phys.* **2014**, *16*, 6743–6752.

[302] Huang, Y.-C.; Lu, T.-C.; Huang, C.-I. Exploring the Correlation Between Molecular Conformation and UV-Visible Absorption Spectra of Two-Dimensional Thiophene-Based Conjugated Polymers. *Polymer* **2013**, *54*, 6489–6499.

[303] Oliveira, E. F.; Lavarda, F. C. Effect of the Length of Alkyl Side Chains in the Electronic Structure of Conjugated Polymers. *Mater. Res.* **2015**, *17*, 1369–1374.

[304] Brown, P. J.; Thomas, D. S.; Köhler, A.; Wilson, J. S.; Kim, J.-S.; Ramsdale, C. M.; Sirringhaus, H.; Friend, R. H. Effect of Interchain Interactions on the Absorption and Emission of Poly(3-hexylthiophene). *Phys. Rev. B* **2003**, *67*, 64203.

[305] Tsoi, W. C.; James, D. T.; Kim, J. S.; Nicholson, P. G.; Murphy, C. E.; Bradley, D. D. C.; Nelson, J.; Kim, J.-S. The Nature of In-Plane Skeleton Raman Modes of P3HT and Their Correlation to the Degree of Molecular Order in P3HT:PCBM Blend Thin Films. *J. Am. Chem. Soc.* **2011**, *133*, 9834–9843.

[306] Spano, F. C.; Silva, C. H- and J-Aggregate Behavior in Polymeric Semiconductors. *Annu. Rev. Phys. Chem.* **2014**, *65*, 477–500.

[307] Meier, H.; Stalmach, U.; Kolshorn, H. Effective Conjugation Length and UV/Vis Spectra of Oligomers. *Acta Polym.* **1997**, *48*, 379–384.

[308] Gierschner, J.; Cornil, J.; Egelhaaf, H.-J. Optical Bandgaps of π-Conjugated Organic Materials at the Polymer Limit: Experiment and Theory. *Adv. Mater.* **2007**, *19*, 173–191.

[309] Izumi, T.; Kobashi, S.; Takimiya, K.; Aso, Y.; Otsubo, T. Synthesis and Spectroscopic Properties of a Series of β-Blocked Long Oligothiophenes up to the 96-mer: Revaluation of Effective Conjugation Length. *J. Am. Chem. Soc.* **2003**, *125*, 5286–5287.

[310] Xie, Y.; Li, Y.; Xiao, L.; Qiao, Q.; Dhakal, R.; Zhang, Z.; Gong, Q.; Galipeau, D.; Yan, X. Femtosecond Time-Resolved Fluorescence Study of P3HT/PCBM Blend Films. *J. Phys. Chem. C* **2010**, *114*, 14590–14600.

[311] Sim, M.; Shin, J.; Shim, C.; Kim, M.; Jo, S. B.; Kim, J.-H.; Cho, K. Dependence of Exciton Diffusion Length on Crystalline Order in Conjugated Polymers. *J. Phys. Chem. C* **2014**, *118*, 760–766.

[312] Ester, M.; Kriegel, H.-P.; S, J.; Xu, X. A Density-Based Algorithm for Discovering Clusters in Large Spatial Databases with Noise. *Proc. of 2nd In. Conf. on Knowledge Discovery and Data Mining* **1996**, *96*, 226–231.

[313] Kurniawan, M.; Salim, T.; Tai, K. F.; Sun, S.; Sie, E. J.; Wu, X.; Yeow, E. K. L.; Huan, C. H. A.; Lam, Y. M.; Sum, T. C. Carrier Dynamics in Polymer Nanofiber:Fullerene Solar Cells. *J. Phys. Chem. C* **2012**, *116*, 18015–18022.

[314] Solanki, A.; Wu, B.; Salim, T.; Yeow, E. K. L.; Lam, Y. M.; Sum, T. C. Performance Improvements in Polymer Nanofiber/Fullerene Solar Cells with External Electric Field Treatment. *J. Phys. Chem. C* **2014**, *118*, 11285–11291.

[315] He, Z.; Zhong, C.; Su, S.; Xu, M.; Wu, H.; Cao, Y. Enhanced Power-Conversion Efficiency in Polymer Solar Cells Using an Inverted Device Structure. *Nat. Photon.* **2012**, *6*, 591–595.

[316] Wu, C.; Bull, B.; Szymanski, C.; Christensen, K.; McNeill, J. Multicolor Conjugated Polymer Dots for Biological Fluorescence Imaging. *ACS Nano* **2008**, *2*, 2415–2423.

[317] Bagchi, B. Photochemical Funnel in Stiff Conjugated Polymers: Interplay Between Defect Mediated Polymer Conformations, Side Chain Interactions and Resonance Energy Transfer. *Annu. Rep. Prog. Chem., Sect. C: Phys. Chem.* **2013**, *109*, 36–64.

[318] Ruseckas, A.; Wood, P.; Samuel, I. D. W.; Webster, G. R.; Mitchell, W. J.; Burn, P. L.; Sundström, V. Ultrafast Depolarization of the Fluorescence in a Conjugated Polymer. *Phys. Rev. B* **2005**, *72*, 115214.

[319] Yang, X.; Dykstra, T.; Scholes, G. Photon–Echo Studies of Collective Absorption and Dynamic Localization of Excitation in Conjugated Polymers and Oligomers. *Phys. Rev. B* **2005**, *71*, 045203.

[320] Beenken, W. J. D.; Pullerits, T. Spectroscopic Units in Conjugated Polymers: A Quantum Chemically Founded Concept? *J. Phys. Chem. B* **2004**, *108*, 6164–6169.

[321] Piland, G. B.; Burdett, J. J.; Kurunthu, D.; Bardeen, C. J. Magnetic Field Effects on Singlet Fission and Fluorescence Decay Dynamics in Amorphous Rubrene. *J. Phys. Chem. C* **2013**, *117*, 1224–1236.

[322] Smith, M. B.; Michl, J. Singlet Fission. *Chem. Rev.* **2010**, *110*, 6891–6936.

[323] Mezyk, J.; Tubino, R.; Monguzzi, A.; Mech, A.; Meinardi, F. Effect of an External Magnetic Field on the Up-Conversion Photoluminescence of Organic Films: The Role of Disorder in Triplet-Triplet Annihilation. *Phys. Rev. Lett.* **2009**, *102*, 087404.

[324] Yarmus, L.; Rosenthal, J.; Chopp, M. EPR of Triplet Excitions in Tetracene Crystals: Spin Polarization and the Role of Singlet Exciton Fission. *Chem. Phys. Lett.* **1972**, *16*, 477–481.

[325] Shankar, R. *Principles of Quantum Mechanics*, 2nd ed.; Springer: New York, 1994.

[326] Steiner, U. E.; Ulrich, T. Magnetic Field Effects in Chemical Kinetics and Related Phenomena. *Chem. Rev.* **1989**, *89*, 51–147.

[327] Schmidt, T. W.; Castellano, F. N. Photochemical Upconversion: The Primacy of Kinetics. *J. Phys. Chem. Lett.* **2014**, *5*, 4062–4072.

[328] Avakian, P.; Groff, R.; Kellogg, R.; Merrifield, R.; Suna, A. In *Organic Scintillators and Scintillation Counting*; Horrocks, D. L., Peng, C.-T., Eds.; Academic Press, 1971; pp 499–510.

[329] Campbell, R.; Robertson, J. M.; Trotter, J. The Crystal Structure of Hexacene, and a Revision of the Crystallographic Data for Tetracene. *Acta Crystallogr.* **1962**, *15*, 289–290.

[330] Scafetta, N.; Willson, R. C. ACRIM Total Solar Irradiance Satellite Composite Validation Versus Tsi Proxy Models. *Astrophys. Space Sci.* **2014**, *350*, 421–442.

[331] Jean, J.; Brown, P. R.; Jaffe, R. L.; Buonassisi, T.; Bulovic, V. Pathways for Solar Photovoltaics. *Energy Environ. Sci.* **2015**, *8*, 1200–1219.

[332] Guo, S.; Wu, W.; Guo, H.; Zhao, J. Room-Temperature Long-Lived Triplet Excited States of Naphthalenediimides and Their Applications as Organic Triplet Photosensitizers for Photooxidation and Triplet–Triplet Annihilation Upconversions. *J. Org. Chem.* **2012**, *77*, 3933–3943.

[333] Simon, Y. C.; Weder, C. Low-Power Photon Upconversion Through Triplet-Triplet Annihilation in Polymers. *J. Mater. Chem.* **2012**, *22*, 20817–20830.

[334] Mahato, P.; Monguzzi, A.; Yanai, N.; Yamada, T.; Kimizuka, N. Fast and Long-Range Triplet Exciton Diffusion in Metal-Organic Frameworks for Photon Upconversion at Ultralow Excitation Power. *Nat. Mater.* **2015**, *14*, 924–930.

[335] Monguzzi, A.; Mauri, M.; Frigoli, M.; Pedrini, J.; Simonutti, R.; Larpent, C.; Vaccaro, G.; Sassi, M.; Meinardi, F. Unraveling Triplet Excitons Photophysics in Hyper-Cross-Linked Polymeric Nanoparticles: Toward the Next Generation of Solid-State Upconverting Materials. *J. Phys. Chem. Lett.* **2016**, *7*, 2779–2785.

[336] Cheng, Y. Y.; Khoury, T.; Clady, R. G. C. R.; Tayebjee, M. J. Y.; Ekins-Daukes, N. J.; Crossley, M. J.; Schmidt, T. W. On the Efficiency Limit of Triplet-Triplet Annihilation for Photochemical Upconversion. *Phys. Chem. Chem. Phys.* **2010**, *12*, 66–71.

[337] Suna, A. Kinematics of Exciton–Exciton Annihilation in Molecular Crystals. *Phys. Rev. B* **1970**, *1*, 1716–1739.

[338] Wyrsch, D.; Labhart, H. Magnetic Field Effects on p-Type Delayed Fluorescence of 1,2-Benzanthracene in Solution. *Chem. Phys. Lett.* **1971**, *8*, 217–219.

[339] Iwasaki, Y.; Maeda, K.; Murai, H. Time-Domain Observation of External Magnetic Field Effects on the Delayed Fluorescence of N,N,N′,N′-tetramethyl-1,4-phenylenediamine in Alcoholic Solution. *J. Phys. Chem. A* **2001**, *105*, 2961–2966.

[340] Yokoyama, K.; Wakikawa, Y.; Miura, T.; ichi Fujimori, J.; Ito, F.; Ikoma, T. Solvent Viscosity Effect on Triplet–Triplet Pair in Triplet Fusion. *J. Phys. Chem. B* **2015**, *119*, 15901–15908.

[341] Atkins, P.; Evans, G. Electron Spin Polarization in a Rotating Triplet. *Mol. Phys.* **1974**, *27*, 1633–1644.

[342] Atkins, P.; Evans, G. Magnetic Field Effects on Chemiluminescent Fluid Solutions. *Mol. Phys.* **1975**, *29*, 921–935.

[343] Redfield, A. In *Advances in Magnetic Resonance*; Waugh, J. S., Ed.; Advances in Magnetic and Optical Resonance; Academic Press, 1965; Vol. 1; pp 1–32.

[344] Lendi, K.; Gerber, P.; Labhart, H. Influence of a Magnetic Field on Delayed Fluorescence of Aromatic Hydrocarbonsin Solution: II. A Theoretical Approach.

Chem. Phys. **1976**, *18*, 449–468.

[345] Plimpton, S. Fast Parallel Algorithms for Short-Range Molecular-Dynamics. *J. Comput. Phys.* **1995**, *117*, 1–19.

[346] Brown, W. M.; Wang, P.; Plimpton, S. J.; Tharrington, A. N. Implementing Molecular Dynamics on Hybrid High Performance Computers — Short Range Forces. *Comp. Phys. Comm.* **2011**, *182*, 898–911.

[347] Brown, W. M.; Kohlmeyer, A.; Plimpton, S. J.; Tharrington, A. N. Implementing Molecular Dynamics on Hybrid High Performance Computers — Particle-Particle Particle-Mesh. *Comp. Phys. Comm.* **2012**, *183*, 449–459.

[348] Brown, W. M.; Masako, Y. Implementing Molecular Dynamics on Hybrid High Performance Computers - Three-Body Potentials. *Comp. Phys. Comm.* **2013**, *184*, 2785–2793.

[349] Ufimtsev, I. S.; Martinez, T. J. Quantum Chemistry on Graphical Processing Units. 3. Analytical Energy Gradients, Geometry Optimization, and First Principles Molecular Dynamics. *J. Chem. Theory Comput.* **2009**, *5*, 2619–2628.

[350] Grimme, S.; Antony, J.; Ehrlich, S.; Krieg, H. A Consistent and Accurate Ab Initio Parametrization of Density Functional Dispersion Correction (DFT-D) for the 94 Elements H–Pu. *J. Chem. Phys.* **2010**, *132*, 154104–1–20.

[351] Hoover, W. G. Constant-Pressure Equations Of Motion. *Phys. Rev. A* **1986**, *34*, 2499–2500.

[352] Plimpton, S. J.; Pollock, R.; Stevens, M. Particle-Mesh Ewald and rRESPA for Parallel Molecular Dynamics Simulations. Proceedings of the Eighth SIAM Conference on Parallel Processing for Scientific Computing. Minneapolis, MN, 1997.

[353] Hockney, R. W.; Eastwood, J. W. *Computer Simulation Using Particles*; Taylor & Francis: Bristol, 1988.

[354] Ryckaert, J. P.; Ciccotti, G.; Berendsen, H. J. C. Numerical Integration of the Cartesian Equations of Motion of a System with Constraints: Molecular Dynamics of *n*-alkanes. *J. Comput. Phys.* **1977**, *23*, 327–341.

[355] Groff, R. P.; Avakian, P.; Merrifield, R. E. Coexistence of Exciton Fission and Fusion in Tetracene Crystals. *Phys. Rev. B* **1970**, *1*, 815–817.

[356] Closs, G. L.; Piotrowiak, P.; MacInnis, J. M.; Fleming, G. R. Determination of Long-Distance Intramolecular Triplet Energy-Transfer Rates. Quantitative Comparison with Electron Transfer. *J. Am. Chem. Soc.* **1988**, *110*, 2652–2653.

[357] Closs, G. L.; Johnson, M. D.; Miller, J. R.; Piotrowiak, P. A Connection Between Intramolecular Long-Range Electron, Hole, and Triplet Energy Transfers. *J. Am. Chem. Soc.* **1989**, *111*, 3751–3753.

[358] Curutchet, C.; Voityuk, A. A. Distance Dependence of Triplet Energy Transfer in Water and Organic Solvents: A QM/MD Study. *J. Phys. Chem. C* **2012**, *116*, 22179–22185.

[359] Cheng, Y. Y.; Fückel, B.; Khoury, T.; Clady, R. G. C. R.; Tayebjee, M. J. Y.; Ekins-Daukes, N. J.; Crossley, M. J.; Schmidt, T. W. Kinetic Analysis of Photochemical Upconversion by Triplet-Triplet Annihilation: Beyond Any Spin Sta-

tistical Limit. *J. Phys. Chem. Lett.* **2010**, *1*, 1795–1799.

[360] Lewitzka, F.; Löhmannsröben, H.-G. Investigation of Triplet Tetracene and Triplet Rubrene in Solution. *Z. Physik. Chem.* **1986**, *150*, 69–86.

[361] Hoseinkhani, S.; Tubino, R.; Meinardi, F.; Monguzzi, A. Achieving the Photon Up-Conversion Thermodynamic Yield Upper Limit by Sensitized Triplet–Triplet Annihilation. *Phys. Chem. Chem. Phys.* **2015**, *17*, 4020–4024.

[362] Ortega, A.; Amorós, D.; de la Torre, J. G. Prediction of Hydrodynamic and Other Solution Properties of Rigid Proteins from Atomic- and Residue-Level Models. *Biophys. J.* **2011**, *101*, 892–898.

[363] McLinden, M. O.; Splett, J. D. A Liquid Density Standard Over Wide Ranges of Temperature and Pressure Based on Toluene. *Journal of Research of NIST* **2008**, *113*, 29–67.

[364] O'Reilly, D.; Peterson, E. Self-Diffusion Coefficients and Rotational Correlation Times in Polar Liquids. 3. Toluene. *J. Chem. Phys.* **1972**, *56*, 2262–2266.

[365] Hejtmanek, V.; Schneider, P. Diffusion-Coefficients of Some Large Organic-Molecules in Acetone, Cyclohexane, and Toluene. *J. Chem. Eng. Data* **1993**, *38*, 407–409.

[366] Sturz, L.; Dölle, A. Anisotropic Reorientational Dynamics of Toluene in Neat Liquid. A ^{13}C Nuclear Magnetic Relaxation Study. *J. Phys. Chem. A* **2001**, *105*, 5055–5060.